Development of the source calibration system of the STEREO experiment and search for sterile neutrinos at the ILL

Luis Manzanillas

Communauté
UNIVERSITÉ Grenoble Alpes

THÈSE

Pour obtenir le grade de

DOCTEUR DE LA COMMUNAUTÉ UNIVERSITÉ GRENOBLE ALPES

Spécialité : Physique Subatomique et Astroparticules

Arrêté ministériel : 25 mai 2016

Présentée par

Luis MANZANILLAS

Thèse dirigée par **Dominique DUCHESNEAU**

préparée au sein du **Laboratoire Laboratoire d'Annecy-le-Vieux de Physique des Particules**
dans **l'École Doctorale Physique**

Développement du système de calibration par sources de l'expérience STEREO et recherche de neutrinos stériles auprès de l'ILL

Development of the source calibration system of the STEREO experiment and search for sterile neutrinos at the ILL

Thèse soutenue publiquement le **10 octobre 2016**,
devant le jury composé de :

Monsieur Dominique DUCHESNEAU
DIRECTEUR DE RECHERCHE, LAPP/CNRS/IN2P3, Directeur de thèse
Madame Alessandra TONAZZO
PROFESSEURE, APC, Rapporteur
Monsieur Alain LETOURNEAU
DIRECTEUR DE RECHERCHE, CEA, Rapporteur
Monsieur Eric BAUSSAN
MAITRE DE CONFERENCE, IPHC, Examinateur
Monsieur Giovanni LAMANNA
DIRECTEUR DE RECHERCHE, LAPP/CNRS/IN2P3, Président
Monsieur Pablo DEL AMO SANCHEZ
MAITRE DE CONFERENCE, Université Savoie Mont Blanc, Encadrant

A mi familia

Acknowledgments

C'est avec un grand plaisir que je finis ce manuscrit avec quelques lignes de remerciements envers les personnes qui ont contribué à l'achèvement de ce projet de thèse. Bien que ce manuscrit soit rédigé en anglais, je me permets d'utiliser le français afin de pouvoir pleinement remercier les nombreuses personnes qui ont participé tout au long de cette aventure.

Tout d'abord, je souhaite remercier toute la direction du LAPP pour m'avoir accepté au sein de cette établissement. Ce fût un réel plaisir d'effectuer ma thèse dans de tels lieux dans ce magnifique ville.

Je remercie chaleureusement Alain Letourneau et Alessandra Tonazzo pour avoir accepté sans hésitation d'être rapporteurs de mon manuscrit, malgré la charge de travail supplémentaire que cela implique. Je remercie aussi Eric Baussan pour être partie de mon Jury de thèse. De la même façon je tiens à remercier Giovanni Lamanna, directeur du LAPP, qui m'a fait l'honneur de bien vouloir présider le Jury de ma soutenance de thèse.

Je tiens à remercier tout le groupe neutrino au LAPP, et particulièrement Dominique Duchesneau, mon directeur de thèse et Pablo del Amo Sanchez qui a encadré mon travail de thèse pendant ces trois dernières années. Merci pour toutes les corrections et observations au manuscrit, qui ont contribué à améliorer énormément la qualité de ce travail. Je ne peux oublier Eric Ragoucy et Wassila El Kanawati, que ont eu la gentillesse de lire plusieurs chapitres de ce thèse.

Bien entendu, je n'oublie pas le reste des membres du groupe Neutrino. Je pense notamment à Henri, Isabelle, Jean, Alberto, Laura; et aussi les plus jeunes du group neutrino: Thiabaud et Anne, je leur souhaite bon courage pour la suite, tout en sachant que ses thèses seront d'excellente qualité. Dans la collaboration STEREO, j'ai eu un grand plaisir de travailler avec des chercheurs extrêmement motivés à transmettre leurs connaissances et leur passion pour la physique. Je remercie ensuite David Lhuillier, directeur du projet STEREO.

Je remercie également tous les amis du LAPP, doctorants, post-docs et permanents, avec qui j'ai partagé beaucoup de choses, notamment le group de course à pied et randonnée, avec qui j'ai parcouru presque toutes les montagnes de la Haute Savoie, soit en marchant, soit en courant.

Je souhaite terminer ces remerciements en exprimant, ma plus grande gratitude envers ma famille. Ils m'ont donné les moyens de choisir ce que je voulais faire de

ma vie et m'ont toujours soutenu. Finalement, je termine ces lignes en remerciant Cintya, que toujours m'a soutenu et pour toute son aide à la préparation du pot de thèse.

ABSTRACT

The STEREO experiment has been proposed to give an unambiguous response to the hypothesis of a light sterile neutrino state ($\Delta m^2 \sim 1eV^2$) as the origin of the reactor antineutrino anomaly. Its goal is to confirm or reject this hypothesis by searching at short distance (9-11 m) for a neutrino oscillation pattern in the energy spectrum of the $\overline{\nu_e}$'s emitted by the research nuclear reactor of the Laue-Langevin Institute in Grenoble (France). To this end, the detector is composed of 2 tons of Gd-loaded liquid scintillator read out by an array of PMTs, and is segmented in 6 cells in the direction of the $\overline{\nu_e}$'s propagation. Antineutrinos are detected via the IBD process by observing a time correlated signal composed of a prompt energy deposit from a positron and a delayed signal produced by the neutron capture. Measuring small oscillations superimposed on the reactor antineutrino energy spectrum requires a good energy resolution and an excellent knowledge of the detector response. This manuscript presents a dedicated Geant4 simulation study of a calibration system based on radioactive sources. This system has been conceived to fulfill all the STEREO physics requirements: calibrating the energy scale and the neutron capture efficiency at the 2 % level, knowing the energy response in the reactor antineutrino energy spectrum (0-8 MeV), and characterizing the detector response in a broader sense (non-uniformities, non-linearity, particle identification, etc). To this end, we propose three calibration subsystems: one automated subsystem to move radioactive sources around the detector, whose main role is to calibrate the energy scale in each cell independently; a second subsystem to inter-calibrate the neutron capture efficiency between cells by moving an AmBe source under the detector; and finally, a third subsystem consisting in three manual calibration tubes inside the liquid scintillator, necessary to assess the absolute neutron capture efficiency inside three different cells. The final part of this manuscript is devoted to the study of the selection criteria, and the proposal of methods to reject the expected gamma background.

Keywords: Neutrino oscillations, sterile neutrinos, reactor antineutrino anomaly, STEREO experiment.

RÉSUMÉ

L'expérience STEREO a été proposé afin de donner une réponse sans ambiguïté à l'idée d'un état de neutrino stérile léger ($\Delta m^2 \sim 1eV^2$) comme l'origine de l'anomalie réacteur des antineutrinos. Le but de l'expérience est de confirmer ou de rejeter cette hypothèse en recherchant un patron d'oscillation à courte distance (9-11 m) dans le spectre en énergie des $\overline{\nu_e}$'s émis par le réacteur nucléaire de recherche de l'Institut Laue-Langevin à Grenoble (France). A cet effet, le détecteur est composé de 2 tonnes du liquide scintillant dopé au Gd et lu par un réseau de tubes photomultiplicateurs, et est segmenté en 6 cellules dans la direction de propagation des antineutrinos. Les $\overline{\nu_e}$'s sont détectés par le processus IBD en observant un signal corrélé dans le temps d'un dépôt d'énergie rapide d'un positron et un signal retardé produit par la capture d'un neutron. La mesure des petites oscillations deformant le spectre d'énergie des antineutrinos nécessite une bonne résolution en énergie et une excellente connaissance de la réponse du détecteur. Ce manuscrit présente une étude de simulation détaillée basée sur le logiciel Geant4 STEREO, ce qui a permis le développement du système de calibration par sources. Ce système a été conçu pour répondre à toutes les exigences physiques de STEREO: calibrer l'échelle de l'énergie et de l'efficacité de capture de neutrons au niveau de 2%, connaître la réponse en énergie dans le spectre d'énergie réacteur antineutrino (1-8 MeV), étudier et la caractériser la réponse et des non-uniformités du détecteur. A cet effet, on propose un système de calibration consistant en trois sous-systèmes: un sous-système automatisé pour déplacer des sources radioactives autour du détecteur pour calibrer l'échelle en énergie dans chaque cellule de manière indépendante. Un second sous-système pour déplacer une source AmBe sous le détecteur, dont l'objectif est d'inter-calibrer l'efficacité de capture de neutrons entre les cellules. Enfin, un troisième système manuel qui consistent en trois tubes de calibration placés à l'intérieur du liquide scintillante pour évaluer l'efficacité absolue de la capture des neutrons dans trois cellules différentes. La dernière partie de ce manuscrit est consacré à l'étude et la caractérisation du bruite de fond gamma et les signaux neutrino attendus.

MOTS CLÉS: oscillation du neutrino, neutrinos stériles, expérience STEREO, anomalie réacteur des antineutrinos.

Contents

List of Figures

List of Tables

- Chapter 1 -

Neutrinos

1.1 Introduction

The history of weak interactions started with the discovery of the radioactivity of uranium by Becquerel in 1896 [1]. Rutherford discovered three years later that these radioactive process emitted α and β particles. In 1914, Chadwick demonstrated that the β-spectrum was continuous in contrast to α and γ rays, whose energies take discrete values [2]. This result, which was confirmed later by Ellis and Wooster in 1927 [3], forced Pauli to propose the idea that the missing energy could be explained by the existence of a new particle [4] [1].

This was done in a famous letter that Pauli addressed to the participants of a nuclear conference in Tübingen. At that time, electrons and protons were considered as elementary particles and nuclei were considered as a bound state of protons and electrons. In this framework there were two fundamental problems:

1. The problem of the continuous β spectrum
2. The problem of the spin of some nuclei

Consider the reaction $(A, Z) \rightarrow (A, Z+1) + e^-$, which is allowed in the proton-electron model. Energy conservation tells us that the e^- should have a fixed kinetic energy given by $Q = (M_{A,Z} - M_{A,Z+1}) - m_e$. However, all the experiments showed a continuous β spectrum with the end point equal to Q. Pauli was the first who understood that if the energy and momentum conservation laws hold, one should postulate the existence of a new neutral particle, which Pauli called "neutron". After the discovery of the neutron by Chadwick in 1932 [6], Fermi renamed Pauli's new particle the "neutrino" [5, 7].

[1] Less conservative, Bohr suggested that the energy conservation law could be taken just in a statistical sense [5]

Pauli assumed that this new particle should have a mass of the order of magnitude of the electron mass and in any case not larger than 0.01 the proton mass. However, Fermi and Perrin independently concluded in 1933 that neutrinos could be massless particles [8, 9].

Another fundamental contribution was made by Fermi in 1934 when he proposed a theory for the β decays. Despite the success of Fermi's theory, that required a neutrino and predicted its interaction cross section, many theorists claimed that it would never be observed. As it turns out, they were wrong, and neutrinos were observed for the first time 22 years later, in 1956, by Reines and Cowan [10]. They placed a detector filled with liquid scintillator and surrounded by photo-multiplier tubes in the vicinity of the Savannah River nuclear reactor. For this discovery they were honored with the Nobel prize 40 years later. The detection principle used by Reines and Cowan is the same used today in different reactor neutrino experiments such as KamLAND, Double Chooz, Daya Bay and RENO. It is the so called inverse beta decay process (IBD). It will be also used in the STEREO experiment. In the IBD process an electron antineutrino interacts with a free proton leading to a positron plus a neutron ($\overline{\nu_e} + p \rightarrow n + e^+$).

The next important discovery was the violation of parity in weak interactions. Parity is a symmetry transformation that inverts all coordinates with respect to the origin, e.g. P: $\vec{x} \rightarrow -\vec{x}$, and was believed to be a symmetry of all interactions. It was also the case of charge conjugation, which reverses all charges of a particle p, transforming it into its antiparticle $\overline{p}$, i.e. $C|p>=|\overline{p}>$. In the 1950's, Kaon decays led Lee and Yang to review the evidence for parity conservation, and noted in 1956, that it was lacking not only in kaon decays but in all previously observed weak interactions[11]. In 1957, Wu's experiment showed that parity is not conserved in weak interactions [12].

Some symmetry was restored when Feynman and Gell-Man proposed the the $V-A$ theory of weak interactions [13]. It violated maximally both C and P symmetries but the combined CP symmetry (both charge reversal and space inversion) still held. The $V-A$ theory can be easily accommodated in the lepton sector by using the two massless neutrino components. This idea had been proposed by Weyl before, and rejected by Pauli precisely because it violate parity.

In 1958, the neutrino helicity was measured by Goldhaber, Grodzins and Sunyar [14]. Measuring the polarization of the γ emitted by the excited state of the ^{152}Sm obtained from the β decay of ^{152}Eu, they found that neutrinos always have negative helicity which means that neutrinos are left handed particles. Since as will see in section **??**, a mass term requires both a left and a right handed state. The absence of positive helicity implied a

massless neutrino.

Bruno Pontecorvo was the first who discussed the universality of all weak interactions (β decays as well as μ decays) [15]. Then, he proposed the existence of different neutrinos (electron and muon at that time). The proof of the existence of different type of neutrinos, showing that ν_μ and ν_e are different particles was done in 1962 by L.M. Lederman, M. Schwartz, J. Steinberger et al. in the Brookhaven experiment [16, 17]. The concept of lepton number appeared, with $L_e = +1$ for the e and ν_e and $L_\mu = +1$ for the μ and ν_μ.

The development of the electroweak theory predicted the existence of the new Gauge bosons Z and W. Associated with the neutral Z boson, neutral currents should exist. They were discovered in 1973 in the Gargamelle experiment using the proton synchrotron (PS) $\nu_\mu/\overline{\nu_\mu}$ beam at CERN [18]. After that, it was clear that the number of light neutrinos could be extracted by measuring the total decay width Γ_Z of the Z^0 resonance. In 1989, the number of light neutrino species was thus measured to be $N_\nu = 3.27 \pm 0.3$ by the ALEPH experiment at CERN, in excellent agreement with the theoretical expectation of three [19]. In 2000 a third neutrino (ν_τ) was finally observed by the first time in the DONUT experiment [20]. In 2006, the final electroweak measurements performed with data taken at the Z resonance by the experiments operating at the electron-positron colliders SLC and LEP reported $N_\nu = 2.9841 \pm 0.0083$ [21].

Within the Standard Model framework, neutrinos are massless particles. However with the development of solar neutrino experiments, a deficit in the measured solar neutrino flux with respect to the theoretical expectation (the so-called Standard Solar Model [22, 23]) was found, most notably by pioneer Ray Davis with the Homestake experiment in the late 1960's ([24] , 2002 Nobel Prize). This phenomena was called the solar neutrino anomaly [25]. Something similar was observed with atmospheric neutrinos by the experiments at Kamiokande [26], where the measured upward and downward ν_e fluxes were equal and consistent with the expectations, whereas the upward ν_μ flux was determined to be much lower than the downward ν_μ flux and the theoretical predictions (atmospheric neutrino anomaly [27]). Neutrino oscillations were proposed as the explanation to these deficits, i.e. that neutrinos can change of identity (flavor) during their propagation. This metamorphosis requires that neutrinos have mass, in contradiction with the SM picture. Pontecorvo presented the first intuitive understanding of the the two neutrino mixing and oscillation [28, 29]. The theory was then developed and formalized to the three neutrino framework as it will be shown in the next sections. The experimental proof of the neutrino oscillation hypothesis came in the late 1990's and early 2000's from the SuperKamiokande and SNO experiments [30, 31]. For this discovery, Takaaki Kajita and Arthur B. McDonald were honored with the physics Nobel prize in 2015. Neutrino oscillation have since

been observed in many other experiments, and most of the oscillation parameters have been measured (see Chapter 2).

Despite the success of the theory of neutrino oscillation, there are still many open questions in the field of neutrino physics. Since neutrinos are the only fundamental fermions with no electric charge, they have the possibility to be Majorana particles, which implies that neutrinos are their own antiparticles. This formalism will be presented in a later section. From oscillation experiments we know that neutrinos are massive particles, but we do not know the exact values of these masses, and we do not know which is the lightest mass state, nor the value of the CP violating phase.

The history of neutrino physics is a history based on anomalies and deficits. In recent years the flux of neutrinos emitted by nuclear reactors has been recalculated [32, 33]. When the measured fluxes were compared to the new calculations, the measurements showed a 6% deficit with respect to the expectations, this problem has been called the reactor antineutrino anomaly [34]. A possible explanation to this deficit could be the existence of a light sterile neutrino with a mass in the eV scale. Similar to what happen in the 90's (solar and atmospheric anomalies), neutrino oscillations could be the solution. Some of the reactor neutrinos could oscillate into this sterile neutrino state. In order to confirm or reject this hypothesis, several experiments have been proposed, among which is STEREO. In the next two years, STEREO (or another experiment) will provide us a definitive answer to this problem.

1.2 Neutrinos in the standard model

The Standard Model (SM) is the quantum field theory (QFT) describing the strong, weak and electromagnetic interactions of elementary particles. The basic principle of the SM is gauge invariance, i.e. invariance under local transformations generated by a so-called gauge group. The theory is based in the gauge group $SU(3)_c \otimes SU(2)_L \otimes U(1)_Y$. The subscripts C, L and Y denote color, left handed chirality, and weak hypercharge respectively [5, 35].

There are eight massless gluons corresponding to the eight generators of $SU(3)_C$, which mediate the strong interaction, and four electroweak gauge bosons, three of them are massive ($W^{\pm}$ and Z) and one is massless (γ), corresponding to the three generators of $SU(2)_L$ and the generator of $U(1)_Y$. The reason why three bosons are massive is the spontaneous symmetry breaking through the Higgs mechanism.

The electroweak part of the SM determines the interactions of neutrinos with other particles, this part is based in the symmetry $SU(2)_L \otimes U(1)_Y$. We can study this part separately from the strong interaction, because symmetry under color group is unbroken and there is no mixing between $SU(3)_C$ and $SU(2)_L \otimes U(1)_Y$.

In the framework of the SM, elementary particles are grouped in fermions and bosons. The firsts are divided in quarks and leptons, which constitute matter; bosons are force mediators. There are three generations of fermions with identical properties, except that they have different masses and the heavier generations are unstable under weak interaction. The existence of three families of fermions is unexplained in the standard model.

	1^{st}**generation**	2^{nd}**generation**	3^{rd}**generation**
quarks:	$\begin{pmatrix} u \\ d \end{pmatrix}_L$	$\begin{pmatrix} c \\ s \end{pmatrix}_L$	$\begin{pmatrix} t \\ b \end{pmatrix}_L$
	u_R, d_R	c_R, s_R	t_R, b_R
leptons:	$\begin{pmatrix} e \\ \nu_e \end{pmatrix}_L$	$\begin{pmatrix} \mu \\ \nu_\mu \end{pmatrix}_L$	$\begin{pmatrix} \tau \\ \nu_\tau \end{pmatrix}_L$
	e_R	μ_R	τ_R

Table 1.1: Fermions described by the standard model. Three families with the same properties except for different masses. Quarks participate to all interactions, while leptons participate to all interactions except to the strong interaction. There are no right handed neutrinos in the standard model, as deduced from the 1958 neutrino helicity experiment carried out by Goldhaber, Grodzins and Sunyar [14]

All the fermions of the standard model have spin 1/2, and then follow the Pauli exclusion principle. Gauge bosons have spin 1, while Higgs boson has spin 0. Quarks are the components of hadrons, and do not exist as free particles. Neutrinos are the only fundamental fermions with no electric charge.

There are 13 free independent parameters in the fermion sector of the standard model: six quark masses, three charged lepton masses, three quark mixing angles and one phase, neutrinos being massless in the framework of the standard model. The value of these parameters are not predicted by the model, so they must be determined by experimental measurements.

1.2.1 Masses in the Standard Model and Brout Englert Higgs Mechanism

In the Standard Model fermions are represented by the Dirac fields ψ. These can be expressed as a sum of a left-handed part ψ_L and a right-handed part ψ_R. In the Lagrangian of the SM these terms are written as $-\psi\overline{\psi}m$. However terms as $-\psi\overline{\psi}m$ are forbidden in

this Lagrangian because of Gauge invariance. If we consider this term, we can decompose it in its chiral states and so we have $m\overline{\psi}\psi = -m[\overline{\psi_L}\psi_R + \overline{\psi_R}\psi_L]$. Since left handed fermions form an isospin doublet and right handed fermions form an isospin singlet, they transform differently under $SU(2)_L \times U(1)_Y$

$$\begin{aligned} \text{left handed doublet} = \psi_L \rightarrow \psi_L^{'} &= e^{i\alpha T + i\beta Y}\psi_L \\ \text{right handed singlet} = \psi_R \rightarrow \psi_R^{'} &= e^{i\beta Y}\psi_R \end{aligned} \tag{1.2.1}$$

which means that a term like $m\overline{\psi}\psi$ is not invariant under $SU(2)_L \times U(1)_Y$ rotations. Since these terms are forbidden, fermions and gauge bosons are massless. Higgs mechanism can accommodate massive gauge bosons keeping gauge invariance. This mechanism can also give mass to the fermions.

Hence, a specific mechanism has to be implemented in order to give mass to fermions and bosons. It is the so called Brout-Englert-Higgs mechanism (BEH) [36, 37, 38, 39].

In the BEH mechanism, masses are generated by the spontaneous symmetry breaking of $SU(2)_L \times U(1)_Y$. This symmetry breaking is done by introducing a Higgs doublet of spin 0 and hypercharge 1

$$\Phi(x) = \begin{pmatrix} \Phi^+(x) \\ \Phi^0(x) \end{pmatrix} \tag{1.2.2}$$

where $\Phi^+(x)$ and $\Phi^0(x)$ represent a charged and a neutral scalar field. Then we need to add a potential $V(\Phi)$ that will spontaneously break the symmetry:

$$V(\Phi) = \mu^2(\Phi^\dagger\Phi) + \lambda(\Phi^\dagger\Phi)^2 \tag{1.2.3}$$

with $\mu^2 < 0$. The part added to the Lagrangian for the scalar field is:

$$L_{scalar} = (D^\mu(\Phi))^\dagger(D_\mu(\Phi)) - V(\Phi) \tag{1.2.4}$$

where D_μ is the covariant derivative associated to the $SU(2)_L \times U(1)_Y$ symmetry. The last step is the choice of a vacuum, this vacuum should spontaneously break the symmetry $SU(2)_L \times U(1)_Y$ but leaving invariant $U(1)_{EM}$, thus the photon remaining a massless particle. Then we can choose the vacuum as follow:

$$Vacuum = \Phi_0 = \frac{1}{\sqrt{2}}\begin{pmatrix} 0 \\ v + h \end{pmatrix} \tag{1.2.5}$$

this vacuum is neutral and has hypercharge 1.

Using the complex Higgs doublet, we can make a term in the Lagrangian that is a singlet under $SU(2)_L$ and $U(1)_Y$. Then, we can introduce a term like $-\lambda_f\overline{\psi}\Phi\psi$, where λ_f is the so called Yukawa coupling. This term is invariant under $SU(2)_L \times U(1)_Y$.

The mass term for fermions in the Lagrangian can be written as follow:

$$L_{\text{fermion mass}} = -\lambda_f[\overline{\psi}_L \Phi \psi_R + \overline{\psi}_R \overline{\Phi} \psi_L] \tag{1.2.6}$$

This term describes the interaction between the Higgs field and fermions. A fermion can acquire a finite mass if the doublet has a non zero expectation value. This is the case if $\Phi_0 = \frac{1}{\sqrt{2}}\begin{pmatrix} 0 \\ v+h \end{pmatrix}$. For the electron-higgs interaction we have

$$\begin{aligned} L_{H,e} &= -\lambda_e \frac{1}{\sqrt{2}} \left[(\overline{\nu}, \overline{e})_L \begin{pmatrix} 0 \\ v+h \end{pmatrix} e_R + \overline{e_R}(0, v+h) \begin{pmatrix} \nu \\ e \end{pmatrix}_L \right] \\ &= -\frac{\lambda_e (v+h)}{\sqrt{2}} [\overline{e_L} e_R + \overline{e_R} e_L] \\ &= -\frac{\lambda_e (v+h)}{\sqrt{2}} \overline{e} e \\ &= -\frac{\lambda_e v}{\sqrt{2}} \overline{e} e - \frac{\lambda_e h}{\sqrt{2}} \overline{e} e \end{aligned} \tag{1.2.7}$$

where the electron mass term is given by $m_e = \frac{\lambda_e v}{\sqrt{2}}$ and the electron-Higgs interaction $\frac{\lambda_e h}{\sqrt{2}} \propto m_e/v$. It is important to note that the electron mass is not predicted by the model since the Yukawa coupling λ_e is a free parameter, so it has to be determined by the experiment. It is also clear that the coupling of the Higgs boson to the electron is very weak compared to the coupling to the Gauge bosons or to the top quark, which are much more massive than the electron.

Finally in the most general case for the three charged leptons we have:

$$L_{H,L} = -\sum_{\alpha=e,\mu,\tau} \frac{\lambda^l_\alpha v}{\sqrt{2}} \overline{l_\alpha} l_\alpha - \sum_{\alpha=e,\mu,\tau} \frac{\lambda^l_\alpha}{\sqrt{2}} \overline{l_\alpha} l_\alpha h \tag{1.2.8}$$

where $l_\alpha \equiv l_{\alpha L} + l_{\alpha R}$ $(\alpha = e, \mu, \tau)$

As there are no right handed neutrinos in the SM, there are good reasons to think that neutrinos are massless particles. Indeed, neutrinos were assumed for a long time to be massless. Nevertheless, thanks to neutrino oscillation experiments, we know that neutrinos oscillate and therefore have mass. However their mass is tiny compared to the rest of fermions of the Standard Model.

1.3 Neutrinos beyond the standard model

Since Pauli's proposal, the mass of neutrinos has been the subject of intense experimental and theoretical investigations. The reason why neutrinos have a tiny mass is still unknown.

It is believed that the origin of the neutrino mass is a low energy manifestation of physics beyond the standard model [40, 41].

Since neutrinos are electrically neutral particles, two types of neutrino mass terms are possible: Dirac and Majorana. This is unlike all other SM fermions, which are electrically charged and can only have Dirac masses.

1.3.1 Dirac mass

The most straightforward way to include neutrino masses is to use the same Higgs mechanism that gives mass to quarks and charged leptons. In this case the simplest extension of the Standard Model is to allow the existence of right handed neutrinos. This model is called the "minimally extended Standard Model". Right handed neutrinos are different from the other fermions, because they are invariant under the symmetries of the standard model. Right handed neutrinos are called **sterile** neutrinos, because they do not participate in weak interactions [42]. Left handed neutrinos are called active.

Adding in the Lagrangian a new lepton term, we have

$$L_{H,L} = -\left(\frac{v+h}{\sqrt{2}}\right)\left[\overline{l'_L}\Lambda'^{l} l'_R + \overline{\nu'_L}\Lambda'^{\nu}\nu'_R\right] + H.c. \tag{1.3.1}$$

with the new right-handed neutrino array

$$\nu'_R \equiv \begin{pmatrix} \nu'_{eR} \\ \nu'_{\mu R} \\ \nu'_{\tau R} \end{pmatrix} \tag{1.3.2}$$

The matrices of charged lepton Yukawa couplings Λ^{l} and neutrino Yukawa couplings Λ'^{ν} can be diagonalized as follows:

$$V_L^{\nu\dagger}\Lambda'^{\nu}V_R^{\nu} = \Lambda^{\nu}, \text{ with } \Lambda^{\nu}_{kj} = \lambda^{\nu}_k\delta_{kj} \quad (k,j=1,2,3) \tag{1.3.3}$$

Defining the neutrino fields as

$$\nu_L = V_L^{\nu\dagger}\nu'_L \equiv \begin{pmatrix} \nu'_{1L} \\ \nu'_{2L} \\ \nu'_{3L} \end{pmatrix}, \quad \nu_R = V_R^{\nu\dagger}\nu'_R \equiv \begin{pmatrix} \nu'_{1R} \\ \nu'_{2R} \\ \nu'_{3R} \end{pmatrix} \tag{1.3.4}$$

and taking the Dirac neutrino fields $\nu_k = \nu_{kL} + \nu_{kR}, \quad (k=1,2,3)$, the Lagrangian can

be written as:

$$L_{H,L} = -\sum_{\alpha=e,\mu,\tau} \frac{\lambda^l_\alpha v}{\sqrt{2}} \overline{l_\alpha} l_\alpha - \sum_{k=1}^{3} \frac{\lambda^\nu_k v}{\sqrt{2}} \overline{\nu_k} \nu_k - \sum_{\alpha=e,\mu,\tau} \frac{\lambda^l_\alpha}{\sqrt{2}} \overline{l_\alpha} l_\alpha h - \sum_{k=1}^{3} \frac{\lambda^\nu_k}{\sqrt{2}} \overline{\nu_k} \nu_k h \tag{1.3.5}$$

Then, according to this Lagrangian, the neutrino mass is given by:

$$m_k = \frac{\lambda^\nu_k v}{\sqrt{2}} \quad (k = 1, 2, 3) \tag{1.3.6}$$

Massive Dirac neutrinos couple to the Higgs field through the two relevant terms in equation 1.3.5. Neutrino masses are proportional to v. The main problem of this mechanism is that there is no explanation for the huge difference between the masses of charged fermions and the masses of neutrinos.

Dirac particles come in four types, left handed and right handed particles and left handed and right handed antiparticles. Charged fermions can only have Dirac mass, however for neutral fermions it is not the case, since neutral fermions are allowed to have what is known as Majorana mass term, as we shall see next.

1.3.2 Majorana mass

The Dirac equation $(i\gamma^\mu \partial_\mu - m)\psi = 0$ for a fermion field $\psi = \psi_L + \psi_R$ is equivalent to the coupled equations [43, 44, 45]:

$$\begin{aligned} i\gamma^\mu \partial_\mu \psi_L &= m\psi_R \\ i\gamma^\mu \partial_\mu \psi_R &= m\psi_L \end{aligned} \tag{1.3.7}$$

The mass term couples the equations. If the field is massless, then we have:

$$\begin{aligned} i\gamma^\mu \partial_\mu \psi_L &= 0 \\ i\gamma^\mu \partial_\mu \psi_R &= 0 \end{aligned} \tag{1.3.8}$$

The equations 1.3.8 are called Weyl equations; ψ_L and ψ_R are Weyl spinors. Since at the time of the formulation of the modern $V - A$ theory of weak interactions there was no indication of the existence of a non-zero neutrino mass, and the only evidence at that time (1957) was the parity violation in weak interactions, and the participation of left handed neutrinos in weak interactions, Landau, Lee, Yang, and Salam proposed to describe neutrino interaction through a left handed Weyl spinor ν_L [45, 44, 43]. This is the usual formulation of the Standard Model.

In 1937, Ettore Majorana wondered if it is possible to make a right handed field from a left handed one and form a mass term [46].In the case of Majorana studied, the two equations of 1.3.7 are not independent. We want to obtain the first equation 1.3.7 from

the second one. In order to do that we take the Hermitian conjugate of the second equation 1.3.7 and using the properties of gamma matrices, we obtain

$$-i\partial_\mu \overline{\psi_R}\gamma^\mu = m\overline{\psi_L} \tag{1.3.9}$$

Now, in order to obtain the second equation of 1.3.7, we can take the transpose of 1.3.9, and using the property of the charge conjugation matrix that $C\gamma^{\mu T} = -\gamma^\mu C$, we get

$$i\gamma^\mu \partial_\mu C\overline{\psi_R}^T = mC\overline{\psi_L}^T \tag{1.3.10}$$

This equation has the same structure as the first equation of 1.3.7 and we can consider them identical if we set

$$\psi_R = \xi C\overline{\psi_L}^T \tag{1.3.11}$$

with ξ an arbitrary phase factor. This is the Majorana relation between ψ_R and ψ_L. Then, we can write the Dirac equation only in terms of the left handed field ψ_L

$$\psi = \psi_L + \psi_R = \psi_L + C\overline{\psi_L}^T \tag{1.3.12}$$

which implies

$$\psi^C = (\psi_L + C\overline{\psi_L}^T)^C = \psi \tag{1.3.13}$$

This Majorana condition implies that a Majorana particle is its own antiparticle. Clearly a Majorana particle can only be neutral because the charge conjugation operator flips the sign of the electric charge. The only fundamental fermions that can be Majorana particles are neutrinos. Also, the antineutrino is just the right handed component of the neutrino field: $\nu_R = \nu_L^C = C\overline{\nu}_L^T$

If neutrinos are Majorana particles, we can form a mass term only with the left handed field, since the necessary right handed field is just $\nu_L^C = C\overline{\nu_L}^T$, so we obtain

$$L_L^M = -\frac{1}{2}m\overline{\nu_L^C}\nu_L + h.c. \tag{1.3.14}$$

Dirac neutrinos have lepton number $L = +1$ and antineutrinos $L = -1$. Since the Majorana mass term couples neutrinos with antineutrinos, interactions involving Majorana neutrinos generally violate lepton number conservation by $\Delta L = \pm 2$.

1.3.3 The seesaw mechanism

If we consider a Dirac mass term for a single species of neutrinos we have

$$L_{Dirac} = -\frac{1}{2}m\overline{\nu_L}\nu_R + h.c. \tag{1.3.15}$$

which assumes the existence of a right handed neutrino field ν_R. Then, assuming that we can write a left handed and right handed Majorana mass terms, and using the charge conjugate fields, ν_L^C and ν_R^C, to form a new Dirac mass term $m_D\overline{\nu_L^C}\nu_R^C$, we can include all these terms to form a most general mass term. This is the main idea behind the Seesaw Mechanism [47, 48], explicitly we have

$$\begin{aligned} -L_{Seesaw} &= L_L^D + L_R^D + L_L^M + L_R^M + h.c. \\ &= \frac{1}{2}m_D\overline{\nu_R}\nu_L + \frac{1}{2}m_D\overline{\nu_L^C}\nu_R^C + \frac{1}{2}m_L\overline{\nu_L^C}\nu_L + \frac{1}{2}m_R\overline{\nu_R^C}\nu_R + h.c. \end{aligned} \tag{1.3.16}$$

which can be written in a matrix form as follows

$$L_{Seesaw} = -\frac{1}{2}\begin{pmatrix}\overline{\nu_L^C} & \overline{\nu_R}\end{pmatrix}\begin{pmatrix} m_L & m_D \\ m_D & m_R\end{pmatrix}\begin{pmatrix}\nu_L \\ \nu_R^C\end{pmatrix} + h.c. \tag{1.3.17}$$

with the mass matrix

$$M = \begin{pmatrix} m_L & m_D \\ m_D & m_R\end{pmatrix} \tag{1.3.18}$$

The Lagrangian has been written in terms of the chiral states ν_L and ν_R. These fields do not have a definite mass because of the non diagonal m_D terms in the mass matrix. These fields are not mass eigenstates, and therefore do not correspond to the physical particle. It means that the flavor eigenstates which couples to the Z and W bosons are a superposition of the mass eigenstates.

If we have mass eigenstates ν_1 and ν_2, we can rewrite the Lagrangian in terms of these mass eigenstates. In order to diagonalize the mass matrix, we need to look for a unitary matrix U, which transforms the left handed chiral fields into left handed components with a definite mass. Then we have

$$U^\dagger M U = M' \tag{1.3.19}$$

and

$$M' = \begin{pmatrix} m_1 & 0 \\ 0 & m_2\end{pmatrix} \tag{1.3.20}$$

Using the standard procedure to diagonalize a matrix, the masses m_1 and m_2 can be expressed in terms of m_L, m_R and m_D, then we have

$$m_{1,2} = \frac{1}{2}\left[(m_L + m_R) \pm \sqrt{(m_L - m_R)^2 + 4m_D^2}\right] \tag{1.3.21}$$

Finally, as we know that the standard model forbids the left handed Majorana term, we can set $m_L = 0$. With this choice and under the assumption of $m_R >> m_D$ we can

write

$$m_{1,2} = \frac{m_R}{2}\left[1 \pm \sqrt{1 + 4\frac{m_D^2}{m_R^2}}\right] \simeq \begin{cases} m_R & \text{For the heavy state} \\ -\dfrac{m_D^2}{m_R} & \text{For the light state} \end{cases} \tag{1.3.22}$$

This mechanism could explain the tiny mass of active neutrinos, because the right handed neutrino can be a heavy sterile state. However it does not say anything about the mass ordering.

1.4 Neutrino mixing and oscillation

1.4.1 Neutrino mixing

As we have seen in the previous section, in order to give masses to neutrinos, we need to add a mass term to the Lagrangian. This mass term induces a mixing between flavors, similar to the mixing in the quark sector. Given that the flavor eigenstates differ from the mass eigenstates, a mixing matrix U has been introduced and links mass eigenstates to flavor eigenstates. This means that a flavor eigenstate $\nu_\alpha \quad (\alpha = e, \mu, \tau)$ is a superposition of the mass eigenstates $\nu_k \quad (k = 1, 2, 3)$. The mixing matrix U is usually called U_{PMNS} (from Pontecorvo, Maki, Nakagawa, and Sakata).

$$\begin{pmatrix} \nu_e \\ \nu_\mu \\ \nu_\tau \end{pmatrix} = U_{PMNS} \begin{pmatrix} \nu_1 \\ \nu_2 \\ \nu_3 \end{pmatrix} \tag{1.4.1}$$

The matrix U_{PMNS} is a unitary matrix, so it has 9 independent coefficients

$$U_{PMNS} = \begin{pmatrix} U_{e1} & U_{e2} & U_{e3} \\ U_{\mu 1} & U_{\mu 2} & U_{\mu 3} \\ U_{\tau 1} & U_{\tau 2} & U_{\tau 3} \end{pmatrix} \tag{1.4.2}$$

The 9 parameters of the unitary matrix U_{PMNS} can be grouped in 3 mixing angles and 6 phases. These phases can be redefined to be absorbed into one Dirac phase (δ) and two Majorana phases (α, β) [49]. The most common parameterization of the matrix U_{PMNS} is the following:

$$U_{PMNS} = \begin{pmatrix} 1 & 0 & 0 \\ 0 & c_{23} & s_{23} \\ 0 & -s_{23} & c_{23} \end{pmatrix} \begin{pmatrix} c_{13} & 0 & s_{13}e^{-i\delta} \\ 0 & 1 & 0 \\ s_{13}e^{i\delta} & 0 & c_{13} \end{pmatrix} \begin{pmatrix} c_{12} & s_{12} & 0 \\ -s_{12} & c_{12} & 0 \\ 0 & 0 & 1 \end{pmatrix} \begin{pmatrix} i & 0 & 0 \\ 0 & e^{i\alpha} & 0 \\ 0 & 0 & e^{i\beta} \end{pmatrix} \tag{1.4.3}$$

where $c_{ij} = \cos\theta_{ij}$, $s_{ij} = \sin\theta_{ij}$, the three mixing angles are θ_{12}, θ_{23}, θ_{13}, and the phase δ is the CP phase in the leptonic sector.

The parameters of the PMNS matrix can all be determined through measurements of neutrino oscillations, as will be shown in the next section, except for the three Majorana phases. However, Majorana phases would manifest in other neutrino experiments, such as neutrino less double beta decay [47, 50].

1.4.2 Neutrino oscillations

According to the general theory of neutrino oscillations [42, 51, 52, 53], this is a pure quantum phenomena. Neutrinos are produced in charged current weak interactions in association with a charged lepton or anti-lepton of a defined flavor $l_\alpha^\mp$. A neutrino with a flavor α and momentum $\vec{p}$ does not have a well defined mass and can be written as a linear superposition of three states of mass ν_k. In general a neutrino flavor state ν_α is described by the mass eigenstate superposition

$$|\nu_\alpha\rangle = \sum_k U^*_{\alpha k} |\nu_k\rangle \quad (\alpha = e, \mu, \tau) \tag{1.4.4}$$

with U, the PMNS matrix. The unitary of the PMNS matrix comes from the fact that the three flavor eigenstates are orthogonal to each other (ditto for the mass eigenstates). In order to have orthonormal massive neutrino states and flavor states we need $\langle \nu_k \,|\, \nu_j \rangle = \delta_{kj}$ and $\langle \nu_\alpha \,|\, \nu_\beta \rangle = \delta_{\alpha\beta}$ respectively.

We have not limited the number of massive neutrinos in equation 1.4.4. However, we know that the number of active light neutrinos is three and correspond to the three charged leptons (e, μ, τ). Then, if there are more than three massive neutrinos, these additional neutrinos are sterile, because they do not participate in weak interactions and only interact through gravitational interaction or some unknown interaction beyond the Standard Model. Therefore, transitions of active flavor neutrinos into sterile neutrinos can be observed only via disappearance experiments.

Massive neutrinos states ν_k are eigenstates of the Hamiltonian $H\,|\nu_k\rangle = E_k\,|\nu_k\rangle$ with energy eigenvalues:

$$E_k = \sqrt{\vec{p}^2 + m_k^2} \tag{1.4.5}$$

For ultrarelativistic neutrinos we can write

$$E_k = \sqrt{\vec{p}^2 + m_k^2} \simeq |\vec{p}| + \frac{m_k^2}{2|\vec{p}|} \simeq E + \frac{m_k^2}{2E} \tag{1.4.6}$$

The Schrödinger equation $i\frac{d}{dt}\,|\nu_k(t)\rangle = H\,|\nu_k(t)\rangle$ implies that the time evolution of mass

eigenstates evolves as plane waves. Then, for a flavor state α at time $t = 0$ and its evolution we have

$$|\nu_\alpha(t)\rangle = \sum_k U^*_{\alpha k} e^{-iE_k t} |\nu_k\rangle \tag{1.4.7}$$

As U is a unitary matrix, the equation 1.4.4 can be inverted, and so we can write

$$|\nu_k\rangle = \sum_\alpha U_{\alpha k} |\nu_\alpha\rangle \tag{1.4.8}$$

Using this relation and equation 1.4.7, the flavor state can be expressed as

$$|\nu_\alpha(t)\rangle = \sum_{\beta=e,\mu,\tau} \left(\sum_k U^*_{\alpha k} e^{-iE_k t} U_{\beta k} \right) |\nu_\beta\rangle \tag{1.4.9}$$

The time evolution of a neutrino flavor α is described as a superposition of the different flavor states. Then, the transition probability from a flavor α into a flavor β is given by

$$P_{\nu_\alpha \to \nu_\beta}(t) = |\langle \nu_\beta | \nu_\alpha(t) \rangle|^2 = \sum_{k,j} U^*_{\alpha k} U_{\beta k} U_{\alpha j} U^*_{\beta j} e^{-i(E_k - E_j)t} \tag{1.4.10}$$

Using equation 1.4.6 we can find $E_k - E_j$, which gives

$$E_k - E_j \simeq \frac{m_k^2 - m_j^2}{2E} = \frac{\Delta m^2_{kj}}{2E} \tag{1.4.11}$$

If we consider that in neutrino experiments the time is not measured, and the fact that ultrarelativistic neutrinos propagate almost at the speed of light, then we can approximate $t = L$, where L is the so called baseline, and is simply the distance between the neutrino source and the detector. Putting all this together we have

$$P_{\nu_\alpha \to \nu_\beta}(L, E) = \sum_{k,j} U^*_{\alpha k} U_{\beta k} U_{\alpha j} U^*_{\beta j} e^{-i \dfrac{\Delta m^2_{kj} L}{2E}} \tag{1.4.12}$$

Using the unitary relations and separating real from imaginary parts, we can write

$$\begin{aligned} P_{\nu_\alpha \to \nu_\beta}(L, E) = \delta_{\alpha\beta} &- 4 \sum_{k>j} \Re\mathfrak{e}[U^*_{\alpha k} U_{\beta k} U_{\alpha j} U^*_{\beta j}] \sin^2 \left(\frac{\Delta m^2_{kj} L}{4E} \right) \\ &+ 2 \sum_{k>j} \Im\mathfrak{m}[U^*_{\alpha k} U_{\beta k} U_{\alpha j} U^*_{\beta j}] \sin \left(\frac{\Delta m^2_{kj} L}{2E} \right) \end{aligned} \tag{1.4.13}$$

The survival probability correspond to the case of $\alpha = \beta$, and the transition probability correspond to the case $\alpha \neq \beta$. Under the assumption of CPT conservation we have

$$P_{\nu_\alpha \to \nu_\beta} = P_{\overline{\nu}_\beta \to \overline{\nu}_\alpha} \tag{1.4.14}$$

Thus the oscillation probability in the case of antineutrinos is the same as in the case of neutrinos, except that the mixing matrix U has to be replaced by U^*. We can derive in a similar way the equation for antineutrinos, leading to

$$\begin{aligned} P_{\overline{\nu}_\alpha \to \overline{\nu}_\beta}(L,E) = \delta_{\alpha\beta} - 4\sum_{k>j} \Re\mathfrak{e}[U^*_{\alpha k}U_{\beta k}U_{\alpha j}U^*_{\beta j}] \sin^2\left(\frac{\Delta m^2_{kj}L}{4E}\right) \\ -2\sum_{k>j} \Im\mathfrak{m}[U^*_{\alpha k}U_{\beta k}U_{\alpha j}U^*_{\beta j}] \sin\left(\frac{\Delta m^2_{kj}L}{2E}\right) \end{aligned} \tag{1.4.15}$$

The only difference in the oscillation probability for antineutrinos given by the equation 1.4.15 from the neutrino's equation 1.4.13 is the sign of the imaginary part.

From previous equations we can find the neutrino oscillation phase as

$$\Phi_{kj} = \frac{\Delta m^2_{kj}L}{2E} \tag{1.4.16}$$

This result shows that the phase of neutrino oscillation is governed by Δm^2_{kj} which is a physical constant and can be determined experimentally by measuring the distance to the source L, and the energy of neutrinos or antineutrinos. The amplitude of the oscillation will be determined by the quadratic terms $U^*_{\alpha k}U_{\beta k}U_{\alpha j}U^*_{\beta j}$, which are constants of nature. Neutrino oscillation can only occur if $\Delta m^2_{kj} \neq 0$; in consequence at least one neutrino mass state must be different from 0. If the phase is equal to 2π, we can find the oscillation length

$$L^{osc}_{kj} = \frac{4\pi E}{\Delta m^2_{kj}L} \tag{1.4.17}$$

If we consider the case of survival probability $\alpha = \beta$, the quadratic products $U^*_{\alpha k}U_{\beta k}U_{\alpha j}U^*_{\beta j} = |U_{\alpha k}|^2|U_{\alpha j}|^2$, are reals and we can write the survival probability as

$$P_{\nu_\alpha \to \nu_\beta}(L,E) = 1 - 4\sum_{k>j} |U_{\alpha k}|^2|U_{\alpha j}|^2 \sin^2\left(\frac{\Delta m^2_{kj}L}{4E}\right) \tag{1.4.18}$$

Experimentally, we can perform two types of experiment. In a neutrino flux with a defined flavor α, we can look for the appearance of neutrinos of some flavor β. This kind of experiments are called appearance experiments. Alternatively, if we know the flux of neutrinos with flavor α, we can look for the disappearance of some of them, due to the oscillation into a β different flavor. These experiments are referred as disappearance experiments. The STEREO experiment is an antineutrino disappearance experiment.

1.4.2.1 Two flavor oscillations

We can consider the special case when only one squared mass splitting Δm^2_{kj} is important and the others can be neglected. This is the case of the atmospheric neutrino mixing ($\nu_\mu \to \nu_\tau$) where the ν_e plays almost no role. It is also appropriate for the solar case and for short baseline reactor antineutrino experiments. These approximations are possible because the mixing angle θ_{13} is very small and two of the mass states are very close compared to the third. In these cases we have two mass states ν_1 and ν_2, and two flavor ν_α and ν_β. Then, we have $\Delta m^2 = m_2^2 - m_1^2$. The only unitary matrix 2x2, is the rotation matrix, which rotates a vector in the flavor basis into a vector in the mass basis

$$U = \begin{pmatrix} \cos\theta & \sin\theta \\ -\sin\theta & \cos\theta \end{pmatrix} \tag{1.4.19}$$

Then, the flavor states can be expressed as

$$\begin{pmatrix} \nu_\alpha \\ \nu_\beta \end{pmatrix} = \begin{pmatrix} \cos\theta & \sin\theta \\ -\sin\theta & \cos\theta \end{pmatrix} \begin{pmatrix} \nu_1 \\ \nu_2 \end{pmatrix} \tag{1.4.20}$$

The angle θ is referred as the mixing angle. Inserting this mixing matrix in equation 1.4.13, and replacing Δm^2_{kj} by Δm^2, we can find the transition probability

$$P_{\nu_\alpha \to \nu_\beta}(L, E) = \sin^2 2\theta \sin^2\left(\frac{\Delta m^2 L}{4E}\right) \tag{1.4.21}$$

And for the survival probability, we can use the unitarity and get

$$P_{\nu_\alpha \to \nu_\alpha}(L, E) = 1 - \sin^2 2\theta \sin^2\left(\frac{\Delta m^2 L}{4E}\right) \tag{1.4.22}$$

If we measure E in MeV or GeV and respectively L in meters or Km, equation 1.4.22 can be expressed as

$$P_{\nu_\alpha \to \nu_\alpha}(L, E) = 1 - \sin^2 2\theta \sin^2\left(1.27\frac{\Delta m^2[eV^2]L[m]}{E[MeV]}\right) \tag{1.4.23}$$

- Chapter 2 -

Experimental status

The recent advances on both the theoretical and the experimental neutrino physics have made possible the measurements of most of the neutrino oscillation parameters. In particular, the confirmation of the neutrino oscillation phenomena implies that neutrinos are massive particles. However, the tiny value of their mass has complicated their determination.

These results showed an important difference between the mixing matrix in the quark sector, and the mixing matrix in the lepton sector. In particular, experiments found two large mixing angles θ_{12} (solar sector), θ_{23} (atmospheric sector) and one relatively small angle θ_{13} (reactor sector), which is still roughly as big as the biggest mixing angle in the quark sector.

All these observations can be interpreted in the framework of the minimal extension of the standard model with three massive neutrinos, usually referred as active neutrinos. Nevertheless, there exist many open questions about massive neutrinos mixing and the origin of their mass. Since neutrinos are massive particles, they can be Dirac or Majorana particles. Another open question is what is the scale of the absolute neutrino masses, and why are neutrino masses so tiny? An additional parameter that is still unknown is the value of the CP violating phase.

In spite of the success of the explanation of the experimental results by the neutrino oscillation framework, in recent years some anomalies have been detected, showing some deficits in short baseline experiments. These anomalies require the existence of at least one more light sterile neutrino, in order to explain the experimental results.

2.1 Neutrino oscillation parameters

The possibility of neutrino oscillations has been discussed nearby since neutrinos were discovered in 1956. However, it was only in 1998 that neutrino oscillation had the first experimental evidence from the SuperKamiokande experiment, then confirmed by the SNO experiment. The first experiment showed the disappearance of atmospheric muon neutrinos and the second experiment showed evidence of the conversion of electron neutrinos from the Sun into a different flavor. These two experiments were honored with the Nobel prize in 2015.

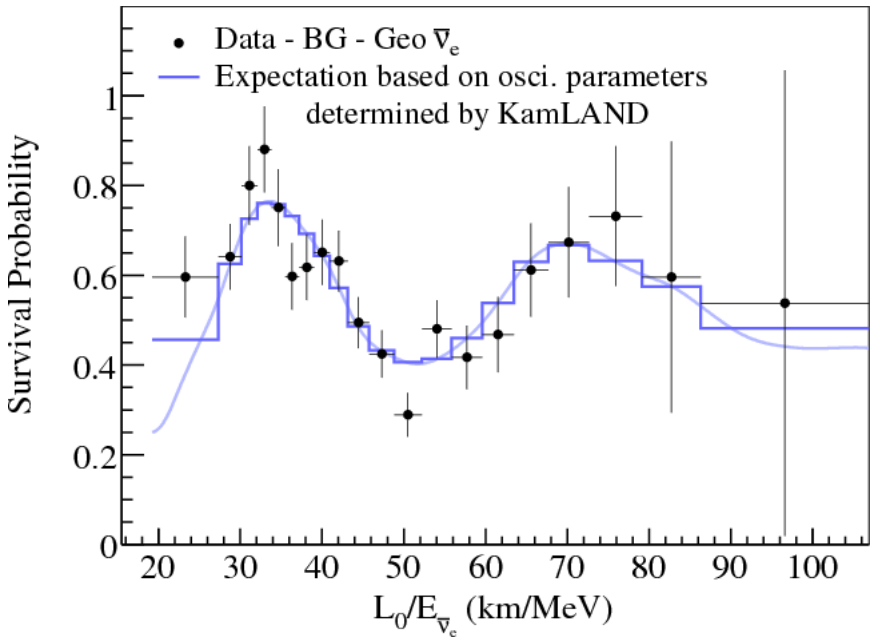

Figure 2.1: Results of the KamLAND experiment, which observes electron antineutrinos from nuclear reactor in Japan. Results shows the ratio expected versus predicted neutrino flux for a distance of 180 Km and cover all the energy spectra of neutrinos coming from nuclear reactors.[54]

Neutrino oscillation experiments provide two parameters: the mixing angle θ_{ij} and the oscillation frequency Δm^2_{ij}. Figure 2.1 shows the results of the KamLAND experiment, which has observed the disappearance of reactor antineutrinos at a distance of 180 Km. At this time, we know three mixing angles and two differences of squared masses. Depending of the oscillation phase given by Δm^2_{ij} and related to L/E, the sensitivity to some difference of masses appears. In general the effects given by the other parameters can be omitted, because there is a separation of a factor 30 between the different splits of masses. For this reason, the analysis can be often simplified to the two flavor oscillation framework.

According to these parameters, experiments can be classified in solar, atmospheric and

reactor (anti)neutrino experiments.

2.1.1 Solar neutrino sector

In stars the energy is produced via thermonuclear fusion. Indeed, the Sun is a very intense source of electron neutrinos with an energy of the order of 1 MeV. All the experiments showed a deficit of neutrinos comparing with the standard solar model prediction [23]. This anomaly was known as the solar neutrino problem.

The first experiment which pointed out the Solar neutrino problem was the Homestake experiment [24]. This was confirmed by other experiments as Kamiokande, Gallex, GNO, SAGE and Super-Kamiokande [55, 56, 57, 58]. All these experiments allow to detect only electron neutrinos, so they can only observe deficits. To confirm oscillations in the solar sector, a new experiment was needed, the SNO experiment [59]. This experiment showed that the deficit of electron neutrinos can be understood in terms of flavor conversion using oscillation theory. Indeed, the SNO experiment was able to detect not only electron neutrinos via charged currents, but also the three flavor of neutrinos via neutral currents [31]. The analysis showed that the total number of neutrinos is in good agreement with the prediction of the solar standard model.

The sector studied by solar electron neutrino experiments correspond to θ_{12}. The KamLAND experiment is a reactor antineutrino experiment located in the Kamioka mine in Japan. The experiment detects electron antineutrinos from nuclear reactors around the Kamioka mine at a mean distance of 180 Km [60]. The experiment is sensitive to Δm^2_{21} and θ_{12}, but also to the θ_{13} sector, which allows to constrain them.

KamLAND results have shown that only vacuum oscillation is not enough to explain all the neutrino deficit of solar neutrinos, showing that there are important effects of neutrino oscillation in matter that happen inside the Sun. It is called the matter effect or MSW effect [61]. Combining different solar experiments with KamLAND results, the actual values of the parameters in the so called solar sector have been determined (see figure 2.2) [54, 62].

$$\begin{aligned} \Delta m^2_{21} &= 7.58^{+0.22}_{-0.26} \times 10^{-5} eV^2 \\ \sin^2\theta_{12} &= 0.304^{+0.022}_{-0.016} \end{aligned} \tag{2.1.1}$$

2.1.2 Atmospheric neutrino sector

When cosmic rays arrive to the earth, they interact with the atmosphere. Cosmic rays are composed mostly by protons, and a small fraction of gammas, antiprotons, electrons,

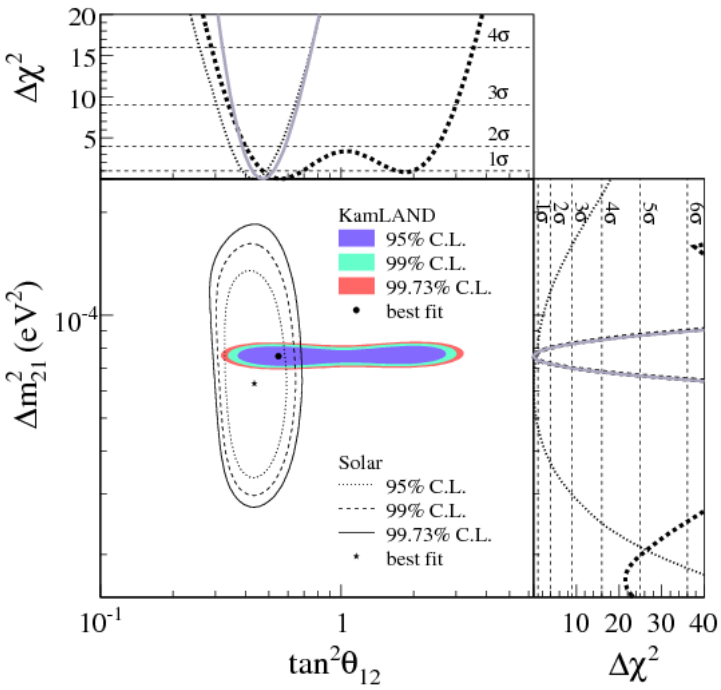

Figure 2.2: Determination of the solar neutrino oscillation parameters, combining KamLAND results with solar experiments. The solid and dotted lines shows the region allowed by solar experiments and the dashed region allowed by KamLAND [54].

positrons and heavy nuclei. The interaction of these particles with the atmosphere can produce hadronic showers, which contain pions and kaons. Pions and kaons then decay into muons and muon neutrinos of high energy. The muons decay then into electrons, electron neutrinos and muon neutrinos:

$$\begin{aligned} \pi^{\pm} &\rightarrow \mu^{\pm} + \nu_{\mu}(\overline{\nu_{\mu}}) \\ \mu^{\pm} &\rightarrow e^{\pm} + \nu_{e}(\overline{\nu_{e}}) + \nu_{\mu}(\overline{\nu_{\mu}}) \end{aligned} \tag{2.1.2}$$

At low energies (<1GeV), muons decay before hitting the earth's surface, at this energy the ratio between electron (anti)neutrinos and muon (anti)neutrinos is expected to be 2 [63]. The first indications of deviation of this ratio from a proportion 2:1 appeared with the IMB experiment, which studied the nucleon decay, giving origin to the so called atmospheric neutrino anomaly [64]. The deficit of neutrinos was confirmed by the Kamiokande experiment [65]. However other experiments like NUSEX and Frejus did not observe any deficit [66, 67]. The origin of this deficit was not clear and many interpretations were proposed: from Lorentz invariance violation, flavor changing neutral currents to neutrino decay and neutrino oscillations.

The definitive evidence was shown by the SuperKamiokande experiment, which is a second generation water Cherenkov detector, more than ten times larger than Kamiokande,

its predecessor. SuperKamiokande started operating in 1996, and after two years of data taking, reported the first results, confirming the atmospheric neutrino anomaly, and showing that there is a strong dependence of the observed muon neutrino flux with the neutrino direction [68].

The flux of neutrinos produced in the atmosphere is expected to be isotropic. For this reason the flux of neutrinos going up and going down in an underground detector like SuperKamiokande should be the same. SuperKamiokande showed that while electron neutrinos have almost no dependence on the zenith angle, down going muon neutrinos exceed significantly the flux of up going neutrinos. The interpretation of these results can be made in terms of oscillations. Muon neutrinos going up are produced in the opposite side of the earth and have to travel around of 12 000 Km before interacting. Some of these muon neutrinos apparently disappear in the way, while no indication of electron disappearance was found. The interpretation then is that muon neutrinos must have oscillated into tau neutrinos [69, 70].

Oscillation of muon neutrinos into tau neutrinos have been confirmed by accelerator experiments like K2K and MINOS [71, 72]. These experiments studied the flavor composition of muon neutrino flux produced in an accelerator, using a near and a far detector. The near detector allows to know with precision of the number of muon neutrinos going to the far detector, and then, with the information of energy and the distance, estimate the oscillation parameters. All these experiments are disappearance experiments, however results from the OPERA and T2K experiments show the appearance of tau and electron neutrinos respectively, in a pure muon neutrino flux [73, 74]

Combining atmospheric with reactor data (see figure 2.3), the global fit for the parameters in the atmospheric sector gives [75]

$$\begin{aligned} \Delta m^2_{31} &= 2.48^{+0.05}_{-0.07} \times 10^{-3} eV^2 \\ \sin^2\theta_{23} &= 0.567^{+0.032}_{-0.128} \end{aligned} \tag{2.1.3}$$

2.1.3 θ_{13} sector: Reactor and accelerator neutrinos

The observation of the energy spectrum of reactor antineutrinos shows an oscillation behavior. The first hints for a non-zero value of θ_{13} were revealed by comparing solar neutrino experiments with KamLAND (reactor neutrino experiment) [76, 77]. The Double Chooz experiment showed for the first time a non-zero value of θ_{13} [78], which was confirmed and measured with high precision by the Daya Bay and RENO experiments [79, 80]. T2K and MINOS also observed a non-zero value of θ_{13} in 2012 [74, 81].

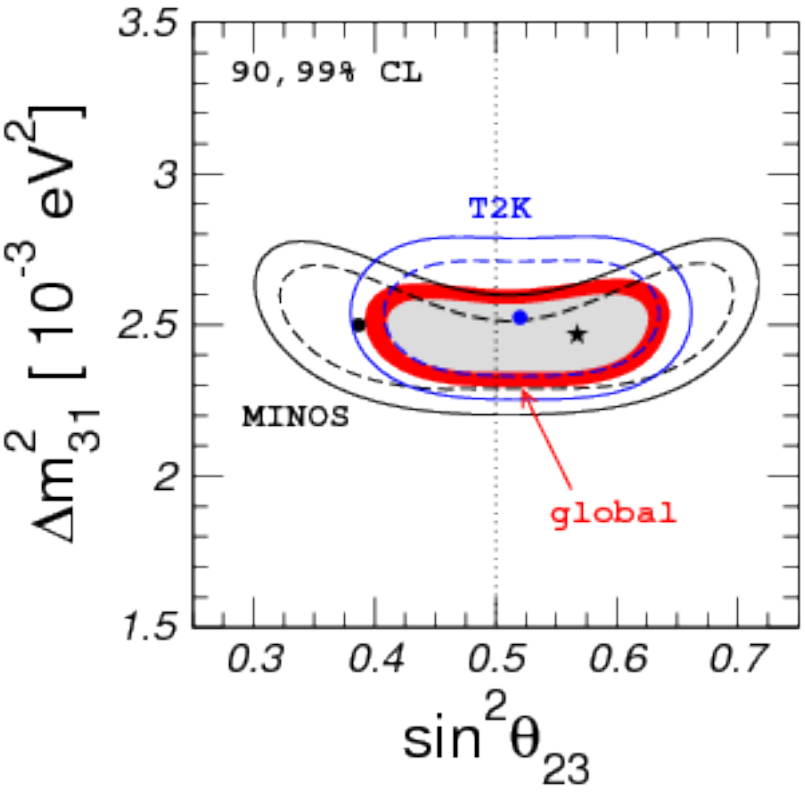

Figure 2.3: Determination of the atmospheric neutrino oscillation parameters. The black star shows the best fit value [75].

Reactor neutrino experiments are disappearance experiments. Detectors are placed at a distance of a few kilometers, and usually a near detector is used to estimate the absolute neutrino flux in the far detectors. The advantage of a reactor neutrino detector is that the construction of a neutrino beam is not needed, and detectors are not necessarily "large". Depending on the distance to the source, the solar component in the oscillation can be ignored. Thus, for "short" baseline experiments as Double Chooz, Daya Bay and RENO, the oscillation probability is given only by θ_{13} and Δm^2_{31}.

$$P_{survival} \approx 1 - \sin^2(2\theta_{13}) \sin^2\left(1.27\frac{\Delta m^2_{31} L}{E}\right) \tag{2.1.4}$$

where L is the distance from the detector to the source in meters and E is the neutrino energy in MeV. Furthermore, Δm^2_{31} has been constraint from atmospheric and accelerator neutrino experiments.

The global fit (see figure 2.4) for the parameters in the θ_{13} sector gives [82, 83]

$$\begin{aligned} \Delta m^2_{31} &= 2.457^{+0.047}_{-0.047} \times 10^{-3} eV^2 \\ \sin^2\theta_{13} &= 0.0214^{+0.0010}_{-0.0010} \end{aligned} \tag{2.1.5}$$

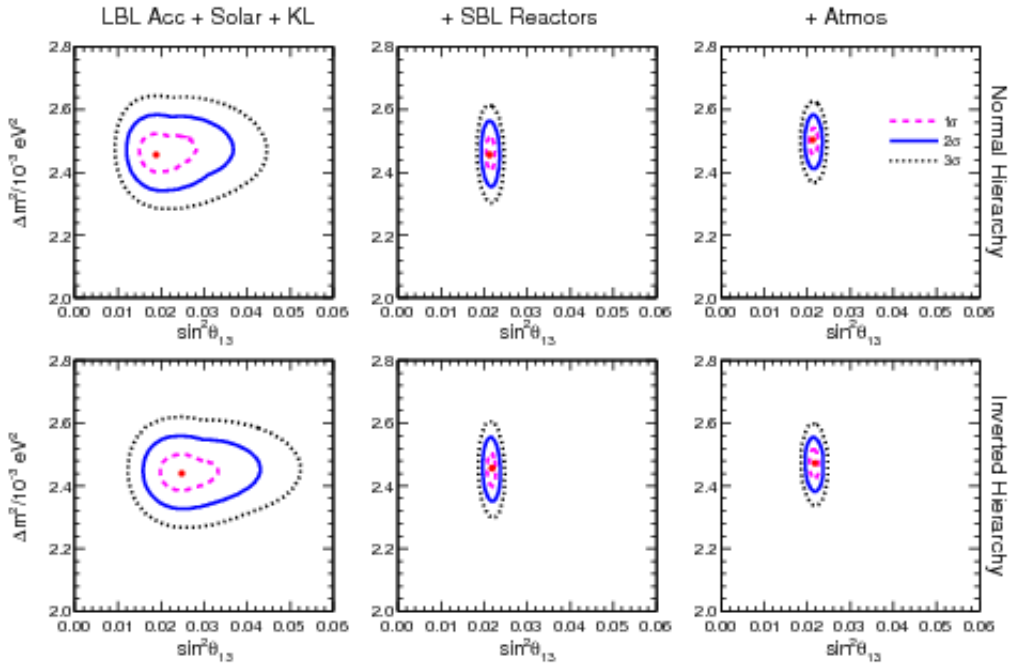

Figure 2.4: Bounds on θ_{13} combining different data. Red dots represent the best fit values [82].

2.2 Absolute neutrino masses

Oscillation experiments have proved not only that neutrino oscillates during their propagation; in addition these experiments prove that neutrinos are massive particles. Nevertheless, the absolute scale of neutrino masses is one of the biggest open question not only in neutrino physics, but also in astrophysics and cosmology. Experiments others than oscillations experiments are required to determine the value of neutrino masses.

Oscillation experiments only provide the differences between the squares of neutrino masses. The current knowledge of neutrino masses leads to the possibility that the solar neutrino doublet has a mean mass either smaller or larger than the remaining atmospheric neutrino [84, 85]. The first possibility is called normal hierarchy (NH) and inverted hierarchy (IH) for the second one (see figure 2.5). Neutrino mass hierarchy has an impact in experiments to determine the CP violating phase, and in experiments looking for the neutrino less double beta decay [86].

The most sensitive method to measure the neutrino mass is by observing the spectrum in the beta decay process. In the β-decay process a nucleus decay emitting an electron plus an antineutrino. The most known method to measure the neutrino mass via the beta decay process is the tritium decay.

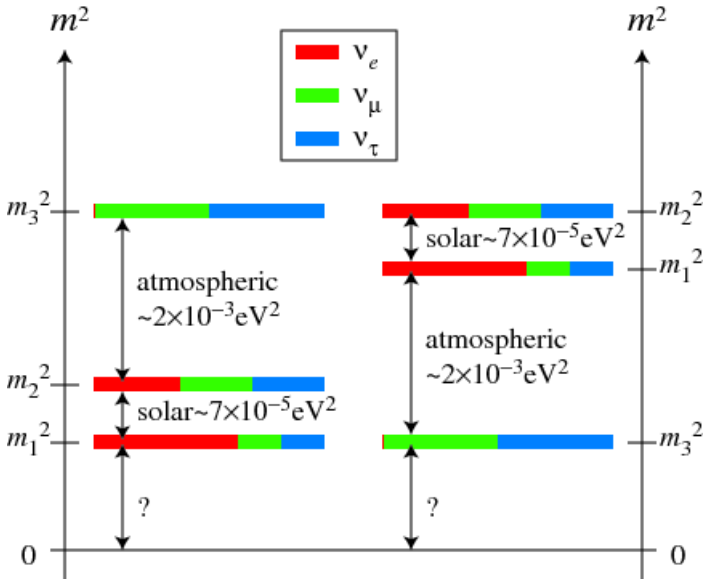

Figure 2.5: Neutrino mass hierarchy: There are two possible configurations for the neutrino mass hierarchy; normal and inverted. Actual neutrino oscillation experiments in the atmospheric sector only determine the absolute difference between the squared masses [87, 88].

The energy released in the β-decay is shared between the electron and the antineutrino. The energy spectrum of the electron according to Fermi theory is given by [89, 90]

$$\frac{dN}{dE} \propto p(E + m_e c^2)(Q - E)\sqrt{(Q - E)^2 - m_{\overline{\nu}_e}^2 c^4} \tag{2.2.1}$$

with E the electron energy, Q the end point energy, the electron mass m_e, and the average of the electron antineutrino mass $m_{\overline{\nu}_e}^2 = \sum |U_{ei}|^2 m_{\nu_i}^2$, which corresponds to the incoherent sum of neutrino mass eigenstates. The effect of the neutrino mass parameter is "significant" only in a very narrow region of the spectrum close to Q.

Tritium (^{3}H) decay is an ideal candidate for searching the effects of the neutrino mass in the spectrum end point as is shown in figure 2.6. On the one hand it has a small value of Q (18.6 keV) and then the relative magnitude of the effect is larger, and in the other hand, the one-electron atomic wave functions are well known.

The Mainz and Troitzk experiments have used tritium decay in the past [92, 93], they put an upper limit on the electron neutrino mass of 2.3 and 2.1 eV respectively. These two experiments have been merged in a new experiment called KATRIN, whose expected sensitivity is 0.2 eV [91].

The τ and μ neutrino masses can be determined by studying the kinematics in pion

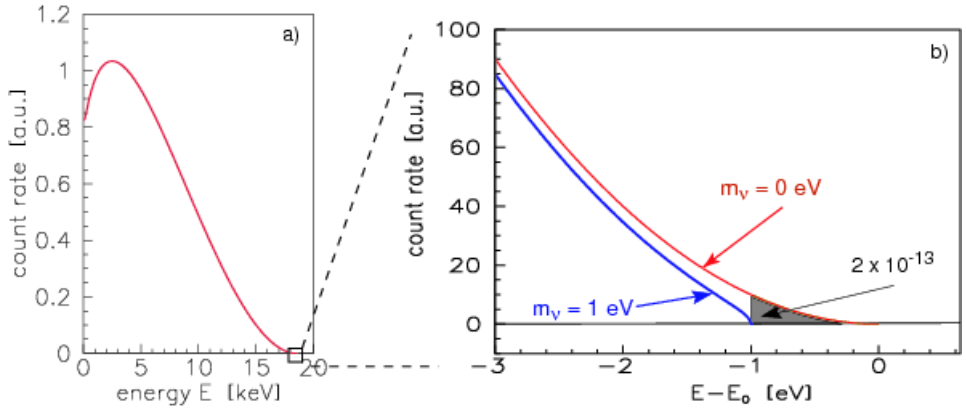

Figure 2.6: Tritium decay spectrum: On the left side the complete spectrum and on the right side the narrow region around the end point, in blue the beta spectrum in presence of a neutrino with a mass of 1 eV [91].

and tau decays. However, these experiments are much less stringent than those obtained by tritium decay experiments. The PSI and the ALEPH experiments found the upper limits [94, 95]:

$$m_{\nu_\mu} < 0.17 \text{ MeV and } m_{\nu_\tau} < 18.2 \text{ MeV} \tag{2.2.2}$$

In astrophysics and cosmology, neutrino masses are very important to describe the evolution of the universe. Because of the huge abundance of neutrinos, they contribute to the mass density of the universe [96, 97, 98]. The total mass of neutrinos affects the shape of the matter power spectrum of the cosmic microwave background (CMB). Depending on the data set, different upper limits on the sum of the three neutrino mass eigenstates has been obtained [99]. The most recent result has been obtained by the Plank collaboration, combining with other data, and they found [100]:

$$\sum m_\nu < 0.23 \text{ eV} \tag{2.2.3}$$

Thus, at the moment cosmology has established the strongest limit on this quantity.

2.3 Anomalies

Besides the great success of the three flavor oscillation theory, there are some anomalies in short baseline neutrino experiments that can not be explained in the three neutrino framework. These anomalies suggest that the picture could be incomplete and may be a signal of new physics, pointing to the existence of a light sterile neutrino. In the following we describe some of these anomalies.

2.3.1 The reactor antineutrino anomaly (RAA)

Nuclear reactors are the most intense and controlled source of neutrinos. For a typical reactor, the fission rate at the nuclear core with a thermal power P_{th} in GW is $0.3\times10^{20}P_{th}s^{-1}$, with 6 ν emitted per fission [101, 102], which leads to a neutrino flux in a 4π solid angle of 2×10^{20} neutrinos per second per GW of thermal power.

The antineutrino flux produced in nuclear reactors was reevaluated during the development of the last generation of neutrino oscillation experiments, which have measured θ_{13}. The predicted total flux was shifted of about +3% in a first study by Muller et al. [32] and was confirmed independently by Huber et al. [33]. This increase in the electron antineutrino flux, was followed by a reevaluation of the results of oscillation experiments at short baselines. Including the update half life of the neutron, off-equilibrium corrections, and the new antineutrino spectra and flux, a total deficit of around 7% (3σ) was found in data with respect to the theoretical calibrations (see figure 2.7). The discrepancy between the new predicted neutrino flux and the observed flux in these experiments has been called the reactor antineutrino anomaly [34].

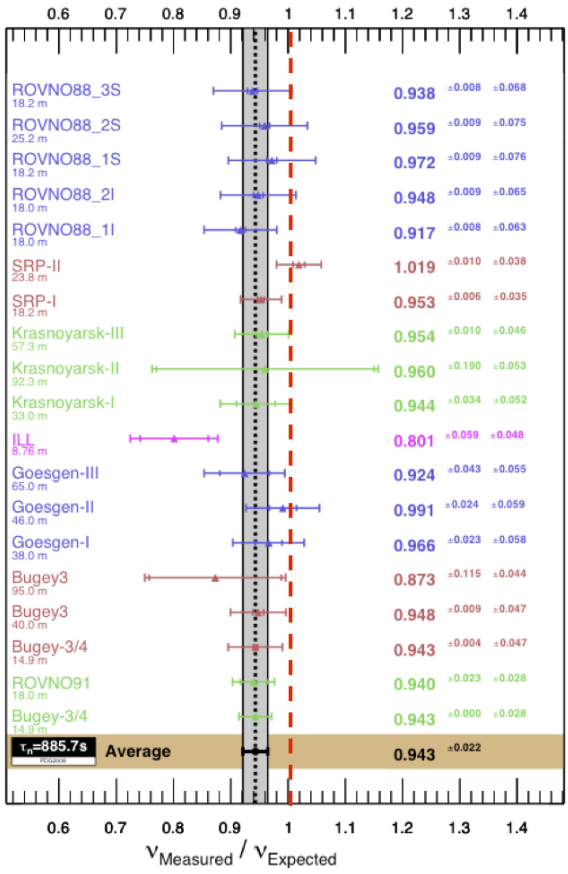

Figure 2.7: Predicted versus measured neutrino flux in reactor neutrino experiments at short baselines [103]. The dotted vertical line shows the expected flux.

2.3.2 The gallium anomaly

The radio-chemical solar experiments GALLEX [104, 105] and SAGE [106, 107] were calibrated using intense radioactive source of ^{51}Cr and ^{37}Ar placed inside the detector. Mono-energetic electron neutrinos produced by these sources are detected using the reaction

$$\nu_e + {}^{71}Ga \rightarrow {}^{71}Ge + e^- \tag{2.3.1}$$

These experiments reported a ratio between the measured and predicted events rates smaller than unity. The combined ratio gives an average of 0.86. Thus, the total deficit of events is 2.8σ smaller than the prediction as is shown in Figure 2.8, this has been called the gallium anomaly.

There are 4 (2) neutrino lines from the radioactive sources Cr (Ar). To compute the number of expected events, the cross sections predicted by Bahcall [108] were used. The uncertainties in these cross sections are large, because only the cross section for the transition $^{71}Ga \rightarrow ^{71}Ge$ into the ground state of ^{71}Ge is well known. While the transitions of ^{71}Ga to the two exited state of ^{71}Ge are inferred using nuclear models [109]. However, even taking into account all these uncertainties, is not enough to explain the total deficit [110].

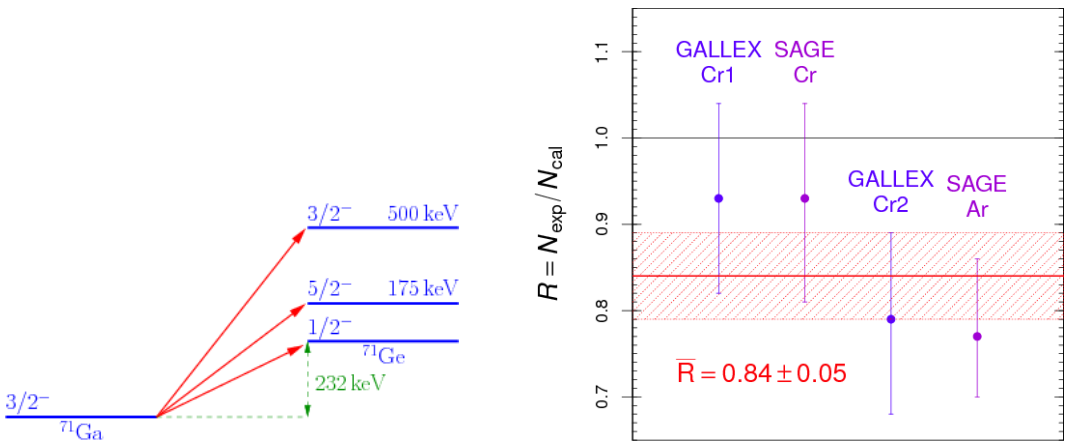

(a) $^{71}Ga \rightarrow ^{71}Ge$ (b) Ratios measured and predicted

Figure 2.8: (a) Transitions of ^{71}Ga to the ground and exited states of ^{71}Ge. (b) Ratios of the measured (N_{exp}) and calculated (N_{cal}) number of events during the calibration of the GALLEX and SAGE experiments using radioactive sources. [111]

2.4 Light sterile neutrino searches

In addition to the reactor antineutrino anomaly and the gallium anomaly, other discrepancies have been observed. The LSND experiment have reported an excess of 3.8σ of electron antineutrinos events in a beam of muon antineutrinos produced by muon decays at rest [112]

$$\mu^+ \to e^+ + \nu_e + \overline{\nu_\mu} \tag{2.4.1}$$

Electron antineutrinos are detected via the inverse beta decay process at a distance of 30 m. However, the KARMEN experiment did not report any excess in the channel $\overline{\nu_\mu} \to \overline{\nu_e}$ at a distance of 18 m [113, 114]. The MiniBooNE experiment was built to confirm the LSND data. Nevertheless, while the antineutrino data seems to confirm LSND excess, tension appears in the MiniBooNE neutrino data [115].

To explain all these anomalies, the existence of at least one additional sterile neutrino is required. Oscillation into a light sterile neutrino could explain the neutrino deficits observed in the RAA and the gallium anomaly [116, 117]. The best fit values for the oscillation parameters suggested by these anomalies are $\Delta m^2 > 1.5$ eV^2 and $\sin^2 2\theta = 0.14 \pm 0.08$ [103].

Global fits have been performed using all the short baseline data. However the fit results can drastically change depending on the data taken into account [111, 118]. Nevertheless, in the "pragmatic approach", in which the anomalous MiniBooNE data is omitted, the results seems pointing to the existence of a light sterile neutrino with a Δm^2_{41} in the eV scale.

In the 3+1 neutrino framework, the transition probability at short baseline experiments has the form of the equation 1.4.23, more precisely it takes the form [119]

$$P_{\nu_\alpha \to \nu_\beta} = \delta_{\alpha\beta} - 4|U_{\alpha 4}|^2 \left(\delta_{\alpha\beta} - |U_{\beta 4}|^2\right) \sin^2\left(\frac{\Delta m^2_{41} L}{4E}\right) \tag{2.4.2}$$

In the case of experiments at short baselines in nuclear reactors, which are disappearance experiments, the survival probability for electron antineutrinos becomes

$$P_{\overline{\nu_e} \to \overline{\nu_e}} = 1 - \sin^2 2\vartheta_{ee} \sin^2\left(\frac{\Delta m^2_{41} L}{4E}\right) \tag{2.4.3}$$

There is an important experimental program around the world to test the eV sterile neutrino hypothesis. In the near future many experiments will explore and test the existence of a light sterile neutrino at the eV scale. All these projects can be classified in different categories, according to the neutrino source. Most of the proposals will use nuclear reac-

tors as source of electron antineutrinos, but there are also projects which will use intense radioactive sources.

STEREO is a disappearance neutrino experiment and it will use as $\overline{\nu_e}$ source one of the most compact nuclear reactors around the world, the research nuclear reactor at the "Institute Laue-Langevin" (ILL) located in Grenoble (France). The distance from the center of the detector to the center of the reactor core will be only 10 m.

There are several experiments similar to STEREO, with identical or different detection techniques. All these projects have similar schedules. In table 2.1 a summary of some of these experiments is presented. One key parameter for the successful detection in these experiments is the baseline. The oscillation length induced by a sterile neutrino in the eV scale is only a few meters, and so the detector must be placed few meters away from the reactor core. In addition, the statistics to be accumulated needs to be large in order to cover all the RAA region. Fortunately, depending on the reactor power, it can be achieved in a relatively short period of time. In the case of STEREO, the acquisition time is expected to be 2 years (∼120 000 antineutrinos detected).

Project	P_{th} (MW)	M_{target} (tons)	L (m)	Depth (m.w.e)	Technology	Status
NUCIFER (FRA)[120]	70	0.8	7	13	LS	operating
STEREO (FRA)[121, 122]	57	1.75	9-12	18	LS (Gd)	in preparation
SoLid (BEL)[123, 124]	45-80	3	6-8	10	PS (Li)	in preparation
PROSPECT (USA)[125, 126]	85	3,10	7-12	few	LS (Li)	in preparation
NEOS (KOR) [127]	16400	1	25	10-23	LS (Gd)	in preparation
DANSS (RUS)[128, 129]	3000	0.9	10-12	50	PS (Gd)	in preparation
Neutrino-4 (RUS)[130, 131]	100	1.5	6-11	10	LS (Gd)	proposal
Poseidon (RUS)[132]	100	3	5-8	15	LS (Gd)	proposal
HANARO (KOR)[133]	30	0.5	6	few	LS (Gd)	proposal

Table 2.1: Reactor neutrino experiments in preparation or proposal to search for a light sterile neutrino.

From the point of view of the detector response, a good energy resolution is needed to cover higher values of Δm^2_{41}. On the other hand, due to small mixing angles, high statistics is required. Finally, given the neutron and gamma ambiance present in some of the nuclear plants, the amount of background can play a crucial role in these experiments.

- Chapter 3 -

The STEREO experiment

3.1 Introduction

The STEREO experiment was proposed in 2013, after the highlighting of the reactor antineutrino anomaly. The goal of the experiment is to confirm or reject the existence of a light sterile neutrino state ($\Delta m^2 \sim 1\text{eV}$) by searching at short baseline for a neutrino oscillation pattern in the energy spectrum of the antineutrinos emitted by the Institute Laue-Langevin (ILL) nuclear reactor at Grenoble.

In the following sections we first describe the concept of the STEREO experiment. Then, the experimental conditions of the ILL site are presented. Finally, the detector and its components are detailed.

3.2 Experimental concept

In order to observe an unambiguous signature of an oscillation induced by a light ($\Delta m^2 \sim 1\text{eV}^2$) sterile neutrino, the detector has to be very close to the neutrino source ($L \lesssim 10$ m) and both the energy and distance dependences of the oscillation formula must be probed by the experiment. Therefore, good energy and position resolutions are needed. Another way of constraining a sterile neutrino is to establish or reject the disappearance of the antineutrinos issued from the reactor core. This entails measuring their flux, and hence, knowing precisely the efficiency of the observing an antineutrino interaction. Finally, since the oscillation STEREO is seeking is a sinusoid of, at most, an amplitude of $\sim 10\%$ superimposed on the reactor antineutrino energy spectrum, high statistics are necessary.

The center of the STEREO detector will be placed 10 m away from the ILL nuclear

reactor core. The experiment uses two tons of Gd-loaded liquid scintillator read out by an array of PMTs to detect $\overline{\nu_e}$'s through the inverse beta decay process (IBD). It is segmented in the direction of the $\overline{\nu_e}$'s propagation into 6 37cm-long cells, which allows a determination of the interaction position better than 20 cm. This configuration allows STEREO to explore the energy and the baseline dependences of the oscillation (see figure 3.1). The ILL's is France's most compact nuclear reactor. The dimensions of its reactor core are 37 cm diameter and 80 cm height. They limit the precision of the baseline determination to $\sim$ 18 cm, a quantity that is still much smaller than the oscillation length, which is about 3 m for 3 MeV neutrinos (typical energy of detected reactor anti-neutrinos) and the best fit values of the oscillation parameters for the RAA. To increase the detection baselines, STEREO is a mobile detector. Thus the data taking will be performed at two distances, giving a total 3 m effective baseline detection to explore during the two years of operation. This data taking period, which amounts to 300 days of reactor ON data at a rate of about 400 detected neutrinos per day, will allow STEREO to accumulate ~120 000 events.

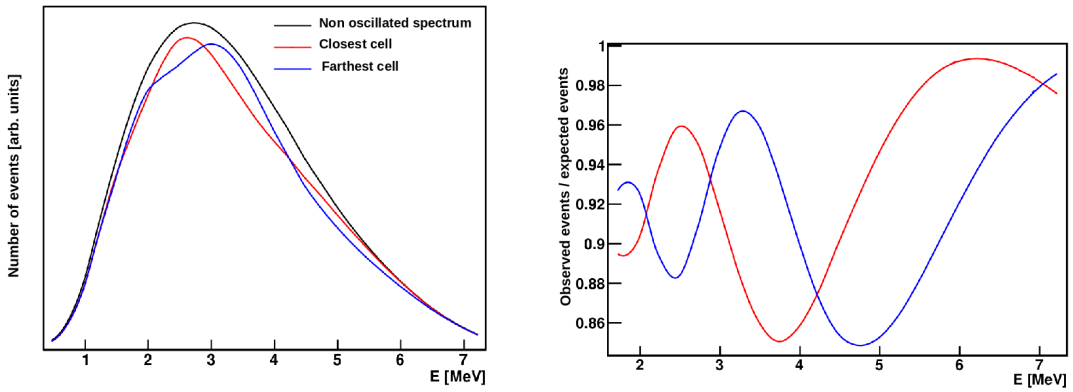

(a) Energy spectrum (b) Rate oscillated-non oscillated spectrum

Figure 3.1: (a) Predicted energy spectrum for antineutrinos (black), and deficit and distortion of the spectrum at different distances in the closest cell (red) and in the farthest cell (blue). (b) Ratio between the oscillated and non oscillated spectrum in the first cell (red) and in the farthest cell (blue).

Thanks to its liquid scintillator (LS) technology, the expected energy resolution in STEREO is about 12% at 2 MeV. In order to avoid escaping gammas to degrade the detector's energy resolution and neutron detection efficiency, an outer crown of liquid scintillator without Gd, called Gamma Catcher (GC), surrounds the Target. To accurately reconstruct the energy of antineutrinos, a radioactive source-based calibration system, and a LED-driven monitoring system have been designed.

The IBD process ($\overline{\nu_e} + p \rightarrow n + e^+$) through which antineutrinos interact in STEREO gives a very clear experimental signature: two energy deposits correlated in time. The first

one arises from the deposition of the positron's kinetic energy and its rapid annihilation. The second one is due to the capture of the neutron by a Gd nucleus after the thermalization and diffusion of the neutron, which lasts a few microseconds. This coincidence in time ($\lesssim 50\mu$s for STEREO) achieves a good background rejection. However, since the ILL nuclear reactor is used as a neutron source, a high gamma and neutron ambiance is present. These gammas and neutrons can interact in the detector and mimic a neutrino signal. Moreover STEREO will be placed at the Earth's surface and, as a consequence, is exposed to cosmic rays and the background they induce. To protect the detector from gammas and neutrons, a shielding composed of lead and polyethylene has been put in place around the instrument. The STEREO site has been also reinforced with neutron absorber materials and lead. As for the cosmic rays induced background, a muon detector is placed over the detector, which allows to tag the passage of a muon and reject it by applying a veto.

3.3 Detection principle

As was already said in the first chapter, according to the standard model, neutrinos interact only via the gravitational and electroweak interactions. The electroweak interaction can be mediated by a charged or a neutral current exchanging a $W^{\pm}$ or a Z respectively. The charged current interaction of a $\overline{\nu_e}$ with a proton, the so called inverse beta decay (IBD) process, yields a positron and a neutron:

$$\overline{\nu_e} + p \rightarrow e^+ + n \tag{3.3.1}$$

For the IBD to happen, however, the antineutrino energy has to be bigger than a threshold, whose value depends on the nucleus the proton is bounded to. If the nucleus is hydrogen's, the proton can be considered as a free particle. Using the energy conservation law and neglecting the $\overline{\nu_e}$ mass, this threshold is

$$E_{\overline{\nu_e}}^{\text{thres}} = \frac{(m_e + m_n)^2 - m_p^2}{2m_p} \simeq 1.806\text{MeV} \tag{3.3.2}$$

where m_e, m_p, and m_n are the electron, proton and neutron masses respectively. The threshold energy for other nuclei is much higher and in that case, the neutron will not be detected because it will remain attached to the nucleus. As a first approximation, the cross section for the IBD with a free proton can be written as [134]

$$\sigma^{(0)} = \frac{2\pi^2}{m_e^5 \tau_n f} E_{e^+}^{(0)} p_{e^+}^{(0)} \tag{3.3.3}$$

where τ_n is the measured neutron lifetime, f =1.7152 is the phase space factor, and includes the Coulomb, weak magnetism, recoil, and outer radiative corrections, but not the inner

radiative corrections [135]. The detected $\overline{\nu_e}$ spectrum can be obtained by multiplying the predicted reactor $\overline{\nu_e}$ energy spectrum by the IBD cross section, as shown in the figure 3.2.

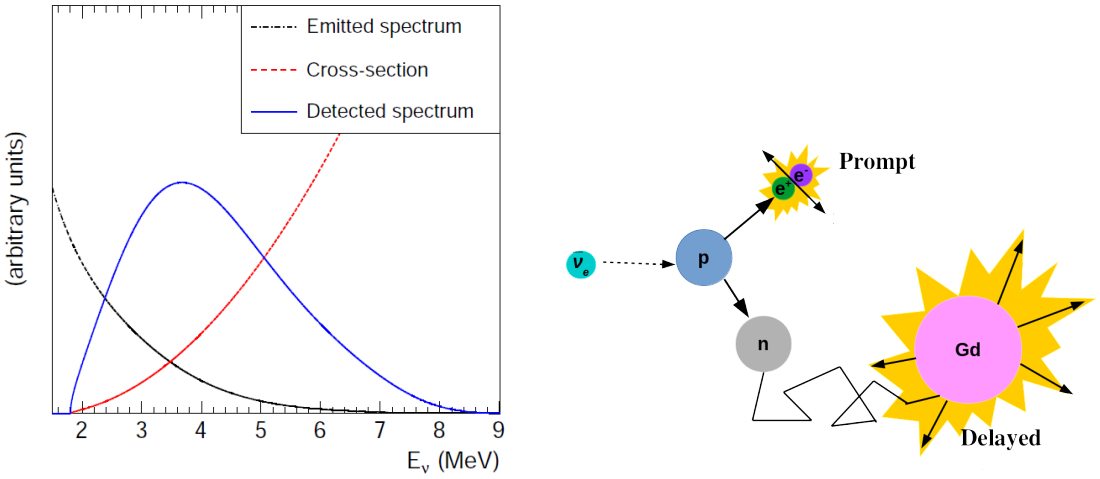

(a) $\overline{\nu_e}$ detected energy spectrum (b) IBD signature

Figure 3.2: (a) The detected $\overline{\nu_e}$ in the case of ^{235}U (blue). This shape is the result of folding the IBD cross section (red) and the $\overline{\nu_e}$ emitted spectrum (black). The energy threshold for the IBD is about 1.8 MeV. The spectrum reaches its maximum around 4 MeV and fades away around 8 MeV [32]. (b) The experimental IBD signature, the positron losses its energy and annihilates with an electron producing two back-to-back 511 keV gammas. The neutron thermalizes and then diffuses until it's captured a few microseconds later by a nucleus, usually Gd in the case of STEREO.

Using simple kinematics, the relation between the $\overline{\nu_e}$ energy and the positron energy can be obtained for the case of the IBD, leading to

$$E_{\overline{\nu_e}} = \frac{2m_p E_{e^+} + m_n^2 - m_p^2 - m_e^2}{2\left(m_p - E_{e^+} + \cos\theta\sqrt{E_{e^+}^2 - m_e^2}\right)} \tag{3.3.4}$$

where θ is the angle between the $\overline{\nu_e}$ and the e^+ direction. Taking into account that the proton mass is much higher than the positron energy, the last equation can be approximated as

$$E_{\overline{\nu_e}} = E_{e^+} + (m_n^2 - m_p^2) + \mathcal{O}(E_{e^+}/m_n) = E_{e^+} + \Delta + \mathcal{O}(E_{e^+}/m_n) \tag{3.3.5}$$

where Δ =1.293 MeV is the difference between the squared neutron and proton masses.

In a liquid scintillator detector like STEREO, the prompt visible energy corresponds to the positron's kinetic energy plus the energy liberated in the positron annihilation with

an electron. Thus the visible energy can be written as

$$E_{vis} = T_{e^+} + 2m_e = E_{e^+} + m_{e^-} \simeq E_{\overline{\nu_e}} - \Delta + m_e \simeq E_{\overline{\nu_e}} - 0.782\text{MeV} \tag{3.3.6}$$

The positron energy is almost instantaneously deposited in the liquid scintillator, and is detected together with the deposited energy of the two 511 keV gammas from its annihilation with an electron. The neutron produced in the IBD thermalizes and diffuses until it's captured by a nucleus some microseconds later. In a "pure" liquid scintillator, the neutron is usually captured on H. Nevertheless the STEREO liquid scintillator is doped with Gd, consequently most of the time the neutron is captured by this nucleus. The use of Gd has two advantages, on one hand the neutron capture cross section for Gd is the highest (σ =48770 barns [136]), which reduces considerably the neutron capture time and distance it diffuses, and on the other hand, its de-excitation produces a gamma cascade with a total energy of around 8 MeV, well above natural radioactivity signals and easily detected.

Thus the experimental signature looked for in STEREO is the coincidence of a prompt (2-8 MeV) and a delayed (5-10 MeV) signals in a time window of 50 μs.

3.4 Nuclear reactors as neutrino sources

Nuclear reactors are the most common man-controlled source of electron antineutrinos. Most of the reactors are of the type called pressurized water reactors (PWR). In France, all of the 58 reactors are of this type. In a PWR reactor, the fuel used is the uranium dioxide, which is enriched in its ^{235}U isotope at $\sim$3.5%. After the enrichment, the uranium is encapsulated in ceramic pellets that are inserted in a Zircaloy-4 tube. Each end of the tube is sealed by welding an end plug to form a fuel rod. The final fuel rods are grouped in fuel assemblies that then are used to build the reactor core. In addition, the core also contains movable control rods, which are made of a neutron absorber material (often silver, indium, cadmium or hafnium). By rising and lowering these control rods, the power output of the reactor can be controlled.

The chain reaction heats up the core at high temperature. A primary cooling system recovers this heat. The heat transfer fluid is pressurized water, which circulates inside the core. The temperature of the water is about 300°C, with an increase of about 40 °C between the entrance and the exit of the core. The water of the primary cooling system also plays the role of moderator, slowing down and helping to thermalize fast neutrons, sustaining the chain reaction. The chain reaction is usually controlled by injecting variable amounts of boron in the water of the primary cooling system.

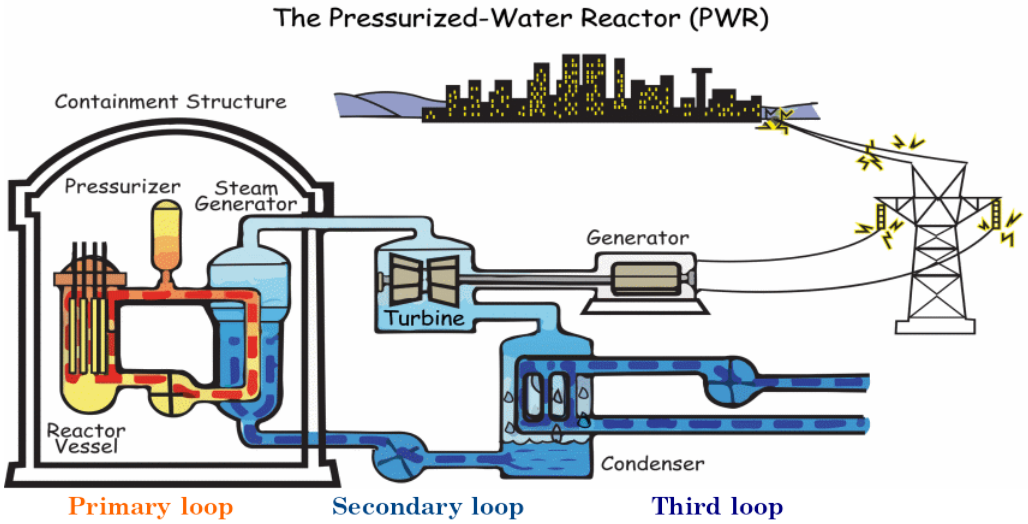

Figure 3.3: Pressurized Water Reactor (PWR) with the different loops of water for the cooling system [137]. In a PWR, the core is enclosed in a vessel that can withstand the 150-bar pressure of the primary circuit. This is a closed circuit of water whose high pressure, regulated by the pressurizer, maintains it in the liquid state in spite of its high temperature (approximately 280 °C at the core inlet, and 320 °C at the outlet). Water leaving the core is divided between three loops in 900 MWe reactors and four loops in 1300 or 1450 MWe reactors. Each loop has a steam generator and a primary coolant pump. Steam generators are heat exchangers in which the water in the primary circuit transfers its heat to the water in the secondary circuit. The water enters in liquid form and is converted to steam; the steam produced by each loop is collected to be sent to a series of high-pressure and then low-pressure turbines, directly coupled to the same shaft as the alternator. Finally, the steam is condensed and then taken up (in liquid form) by the secondary pumps and sent back to the steam generators. The condenser is also a heat exchanger. It is cooled by a third water circuit that is open to the environment.

The primary cooling loop transmits the heat to the water of a secondary cooling loop. This exchange is done through a vapor generator. The water of the secondary cooling system initially in liquid state then vaporizes and drives an assembly of turbines, which then drive a generator producing electricity. After the passage through the turbines, vapor is pressurized in a condenser in order to be transformed in liquid water to be used in a new cycle. The condenser is formed by thousands of tubes in which cooled by cold water previously collected from a river or the sea (this is called the third cooling loop).

The most common fuel used in reactors is uranium. The natural uranium is composed of three isotopes: ^{234}U at 0.0056%, ^{235}U at 0.72%, and ^{238}U at 99.27%. Only ^{235}U can be fissioned by thermal neutrons. On the other hand, ^{234}U and ^{238}U are fissile only under fast neutrons bombardment [138]. From the point of view of maintaining the chain reaction,

it is simpler to use moderated neutrons. The cross section of the ^{235}U for neutron capture is much higher in the thermal regime (600 barns) than in the fast regime (1 barn). The use of (light) water as moderator makes impossible the use of natural uranium to produce the chain reaction because of the high neutron capture cross section of the hydrogen (0.3 barns). Therefore, the fuel needs to be enriched in ^{235}U. Another option is using heavy water as moderator.

The thermal neutron capture by the ^{235}U produces an excited ^{236}U*, strongly unstable that quickly breaks in two fissile fragments. This reaction liberates about 200 MeV, and in average 2.5 neutrons are emitted [139]. Only one of these neutrons is moderated and can be used to sustain the chain reaction. The fission fragments are neutron rich so each fragment undergoes in average three β decays before attaining stability. A $\overline{\nu_e}$ is emitted in each β decay.

Thus each fission is accompanied approximately of 6 β decays, with an electron and an electron antineutrino produced in each decay. The neutrino flux in a 4π solid angle is 2×10^{20} neutrinos per second per GW of thermal power [102, 140]. There are four dominant isotopes ^{235}U, ^{239}Pu, ^{241}Pu and ^{238}U that contribute to the thermal power in a nuclear reactor; other isotopes contribute only at the 0.1 % level [141]. Thus, the electron and $\overline{\nu_e}$ spectrum is given by [142, 32]

$$S_{tot}(E) = \sum_k \alpha_k \times S_k(E), \quad k = {}^{235}\text{U, } {}^{238}\text{U, } {}^{239}\text{Pu, and } {}^{241}\text{Pu} \tag{3.4.1}$$

where the α_k is the number of fissions of the k^{th} isotope at the considered time, $S_k(E)$ is the corresponding β or $\overline{\nu_e}$ spectrum normalized to one fission, and E is the kinetic energy of the particle.

3.5 ILL ANTINEUTRINO SOURCE AND SPECTRA

The oscillation length induced by a sterile neutrino in the eV scale is about 3 meters for neutrinos of 3 MeV (typical energy of electron antineutrinos), so the source of neutrinos to search for such oscillation must be as compact as possible. The source of electron antineutrinos for the STEREO experiment is the ILL research nuclear reactor. Its core consists in a cylinder of 37 cm diameter and 80 cm height; this is the **most compact nuclear reactor in France** (c.f. the size of typical commercial nuclear reactors, ∼3 m diameter). The characteristics of the ILL site allow the installation of the detector at a distance of only 10 m between the center of the detector and center of the reactor core. There are in general 3 or 4 operating cycles per year, each cycle of the reactor lasting 50 days. During

the summer the inter-cycle pause is one month, while in winter it is three months.

The reactor $\overline{\nu_e}$ spectrum has been obtained in the eighties, the key ingredient being the measurements of the β spectra of ^{235}U, ^{239}Pu, and ^{241}Pu fissions at the ILL [143, 144, 145, 146]. These measurements were performed irradiating a Target with a thermal neutron flux, and then measuring the beta spectrum using the BILL magnetic spectrometer. The β spectrum of ^{238}U was obtained in the 2013 by a German group in Garching by irradiating Target foils of natural uranium with a thermal and a fast neutron beam and recording the β spectrum with a gamma suppressing electron telescope [147]. The β spectrum of fission products provides information of the associated $\overline{\nu_e}$ spectrum, since they are related by the energy conservation law

$$E_{\overline{\nu_e}} + E_{e^-} = Q_\beta + \Delta E^* = E_0 \tag{3.5.1}$$

where $E_{\overline{\nu_e}}$ is the $\overline{\nu_e}$ energy, E_{e^-} is the electron energy, Q_β is the difference of mass between the mother and the daughter nucleus, ΔE^* is the excitation energy of the nucleus, and E_0 is the end point energy. The electron and the $\overline{\nu_e}$ share the total energy E_0. The values taken by ΔE^* are quantized, and we speak of a β branch associated to each value of ΔE^*. During the preparation of the Double Chooz experiment, a new evaluation of the $\overline{\nu_e}$ spectrum was performed [32]; these results are shown in the figure 3.4

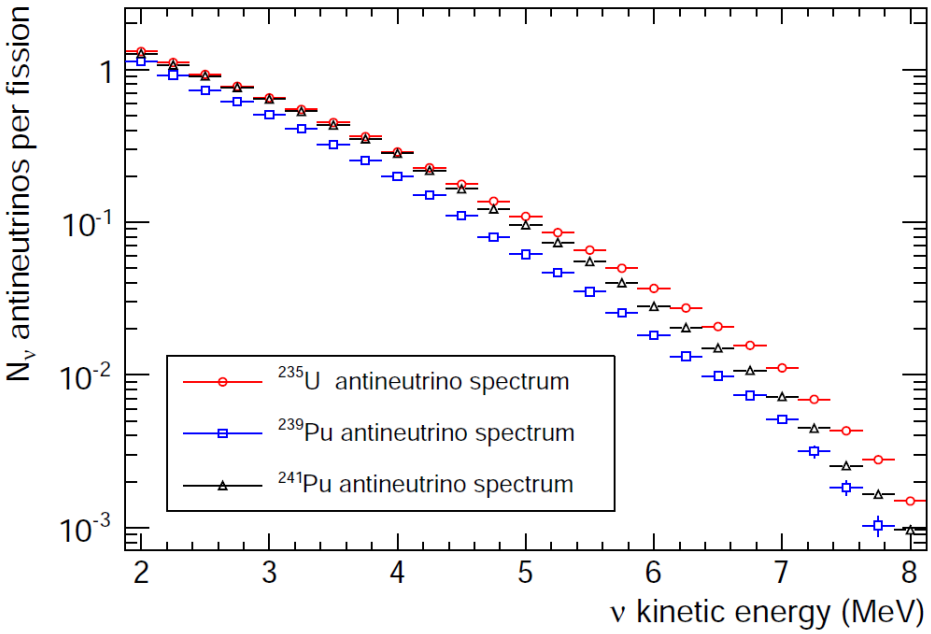

Figure 3.4: The new predicted spectra for $\overline{\nu_e}$ for ^{235}U, ^{239}Pu, and ^{241}Pu. The predictions rates are normalized to one fission [32].

The ILL reactor runs at a thermal power of 57 MW, which remains almost constant during the ON periods (with variations under the 1% level). The fuel element consists of

about 10 Kg of highly enriched (93%) ^{235}U. The almost pure ^{235}U core has the advantage that its β spectrum is the most precisely known and that contributions from other isotopes can be neglected. This will reduce the systematic uncertainties associated to the $\overline{\nu_e}$ spectrum prediction. A recent $\overline{\nu_e}$ spectrum prediction for the ILL reactor can be seen in Figure 3.2. The mean energy per fission for the ^{235}U is $E_{^{235}U} = 201.9 \pm 0.5$MeV; leading to a flux of 9.5×10^{18} $\overline{\nu_e}$ per second [101, 148]. The use of fuel highly enriched in ^{235}U also means that STEREO will be able to provide a new and most precisely measurement of the ^{235}U antineutrino energy spectrum which is essential for future reactor neutrino experiments [149, 150].

The ILL nuclear reactor core contains aluminum. It can be activated and emit $\overline{\nu_e}$'s with a maximum energy of 2.8 MeV. These neutrinos produce a visible energy just below the threshold of visible energy for STEREO (2 MeV) to accept a neutrino candidate.

3.6 ILL EXPERIMENTAL SITE

The latest experiment to detect $\overline{\nu_e}$ at the ILL was placed in the lowest floor at the B42 room (see figure 3.5), at a distance of 8.6 m away from the reactor core [148, 151]. STEREO will be placed at the case-mate PN3 at the exit of the H7 tube (see figure 3.6). This site has the advantage of being at the same level of the reactor core, which implies a smaller effective reactor core size than it was seen at the B42 room.

The distance between the casemate PN3 and the center of the reactor core is only 8 m. This site is located under a water channel, which is used to transfer the new and the spent reactor fuel from the outside to the reactor core and viceversa. This channel consists of a U-shaped structure made of 1.9 m thick concrete walls and filled with 6 m of water. It gives an additional protection to STEREO against cosmic muons, which constitutes an important source of background.

Around the PN3 casemate, there are different experiments that use intense neutron beams, which induce an important neutron and gamma background. However, to mitigate these backgrounds, the PN3 site has the advantage of supporting a weight of 10 t/m^2. Therefore the installation of heavy lead and polyethylene shieldings is possible. The experiment located in the IN20 hall, use Helmholtz coils generating intense magnetic fields (6-15 T). The PMTs gain could be perturbed by this field, and the light collection degraded. The impact of the magnetic field in the PMTs has been simulated using COMSOL software [152]. In order to reduce the effect of this magnetic field, a magnetic shielding has been designed, consisting in 10 mm of ARMCO soft iron around the whole setup (detector+ muon veto), 1.5 mm μ-metal around the inner detector (Target +GC),

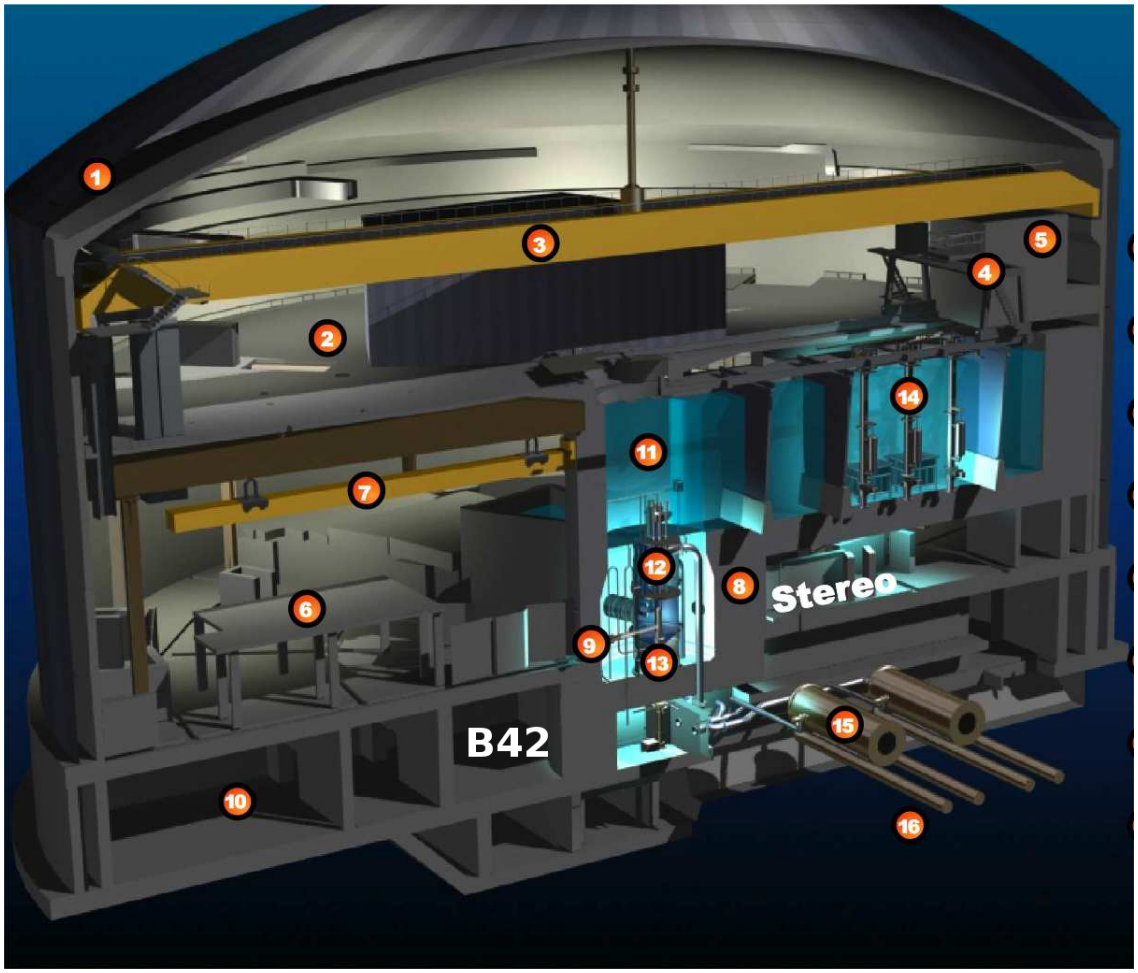

Figure 3.5: The ILL STEREO site. The latest neutrino experiment was placed in the room B42. STEREO will be placed at the casemate PN3 and thus benefits of the protection of a water channel.

and μ-metal cylinders around each PMT [153].

3.6.1 Background in the PN3 casemate

Any particle that could mimic a prompt or a delayed signal in STEREO is a potential background source. The ILL reactor producing the most intense continuous neutron flux in the world, an intense γ and neutron ambiance is present on site. Fast neutrons are produced in the reactor core; high energy gammas come either directly from the reactor core, or from the activation of the surrounding materials. In addition, cosmic muons can produce by spallation radioactive isotopes and fast neutrons. For this reason, one of the main challenges of the STEREO experiment is the evaluation and control of the background sources.

The background can be accidental or correlated, depending on the physical process associated. In the case of accidental background, the prompt and delayed signals have

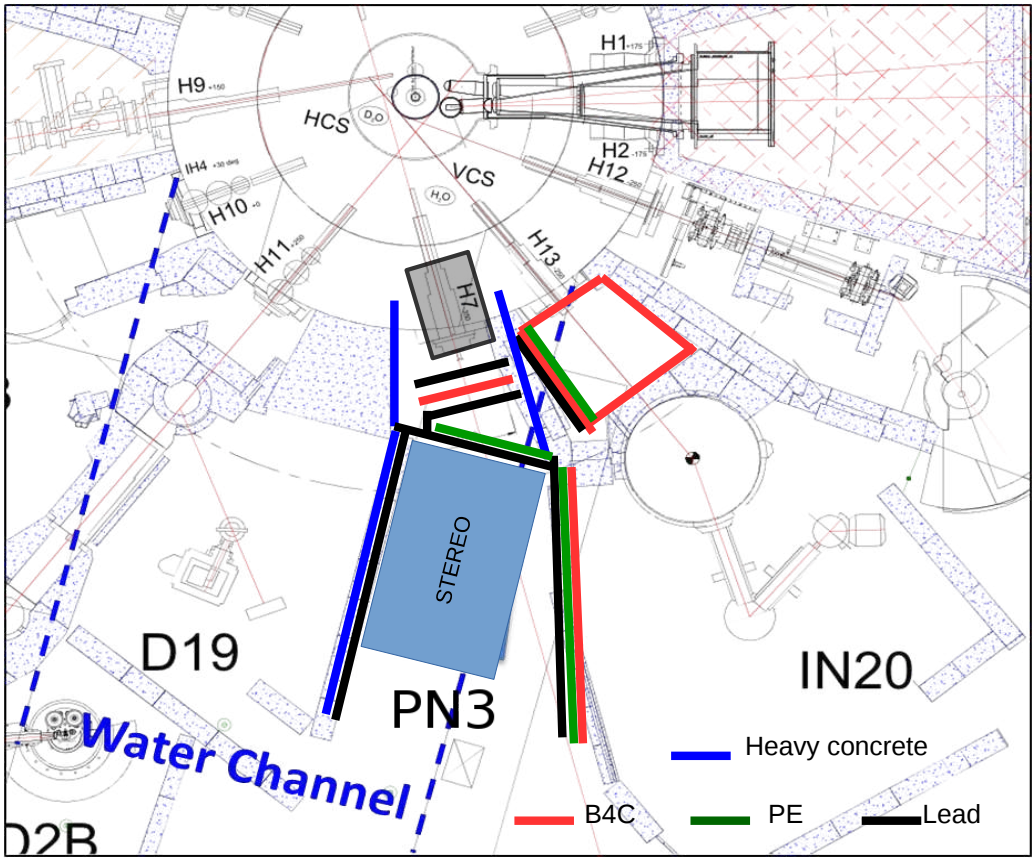

Figure 3.6: Plan of the ILL hall, that allows the installation of the STEREO experiment at a distance of only 10 m. STEREO will be placed in casemate PN3 at the end of the H7 tube.

an independent origin. The main contribution of accidentals is given by gamma rays, either produced by natural radioactivity or by neutron captures inside the detector or its vicinity. In the correlated background, the prompt and delayed signals have the same origin and it is dominated by cosmic rays. Cosmic rays can produce high energy neutrons by spallation on the materials surrounding the detector. If these penetrate in the LS Target, they will generate recoiling protons, that can mimic a prompt signal. The delayed signal is provided by the same neutron which thermalizes and diffuses until it's captured on Gd some microseconds later, giving a false signal strongly resembling the antineutrino signature.

3.6.1.1 Neutron background

The PN3 and IN20 casemates are located at the end of the H7 and H13 neutron lines respectively (see figure 3.6). These two line constitute the main source of neutrons coming from the reactor core. The neutron propagation from the reactor core over the H7 tube until the PN3 casemate has been simulated using MCNPX [154]. The neutron flux at

the end of the tube was estimated to be $3.4 \pm 0.02 \times 10^9$n/s cm^2. The plug initially used at the H7 tube contained Li. Measurements revealed an amount of fast neutrons (with an energy of several MeV) well in excess of the MCNPX prediction. It was found that fast neutrons can actually be produced in the Li energies up to 16 MeV by the following reactions: n(thermal) $+^6$ Li $\rightarrow^4$ He $+^3$ H and then ^{3}H $+^6$ Li $\rightarrow^8$ Be $+ n$(fast). In order to stop producing these fast neutrons and further suppress the reactor neutron flux, a new plug was designed. It is constituted of boral, lead and heavy concrete; by putting this plug at the exit of the H7 tube, the neutron flux was then reduced to 1.2×10^{-4}n/s cm^2. The details of this study can be found in the PhD thesis of M. Pequignot [155].

In the same way, the neutron flux at the exit of the H13 tube is very high. Even if this flux does not directly go in the PN3 room, neutrons can diffuse and potentially enter PN3. To protect the STEREO site, additional walls of polyethylene have been implemented, helped by B4C rubber sheets as shown in the figure 3.6. By using this additional protection most of the neutrons are thermalized and stopped before they are captured by nuclei like Fe, Al, Ni, Cr, etc producing high energy gammas. These gammas can produce a signal in the energy window for both prompt and delayed signals.

3.6.1.2 Gamma background

Gammas constitute another source of background and are responsible of accidental events. It can be generated in the reactor core, nevertheless the most dangerous gammas are produced by neutron captures in the materials surrounding the detector. Neutron captures on Fe, Al, Ni, Cr, etc can generate high energy gammas up to 10 MeV.

The measurements in the PN3 casemate site showed that the gamma flux comes mainly from the IN20 casemate (∼85%). The D19 casemate does not seem to have an important influence (13.5 %) in the counting rate, and the H7 tube, contributes only 1.5% [156]. During a campaign of measurements at the ILL using a Ge detector, some prominent gamma lines have been identified. Among these lines, we can find neutron captures on Fe (7.63, 7.65 MeV), Al (7.72 MeV), H (2.22 MeV) and positron annihilation (511 keV), among others.

By putting B4C in the walls around the Ge detector used, the rate of gammas decreased by a factor 1.4 (see figure 3.7). Nevertheless, the gamma lines coming from neutron captures on Fe were not affected. It indicates that these neutron captures on Fe are mostly happening in the walls around the PN3 casemate and not in the detector walls. In order to reduce the number of neutron captures on the heavy concrete walls, B4C has been put in the walls of the casemate of the H13 neutron beam shutter and the IN20 casemate. B4C has also been used in PN3 as the Pb shielding is supported by steel structures which

can also capture neutrons. Boron has a thermal neutron capture cross section of around 750 barns [157, 158], which prevents the neutron captures in other materials around the detector. In addition, when a boron nucleus absorbs a thermal neutron, it decays into Lithium plus an α particle, which stops in air after a few cm.

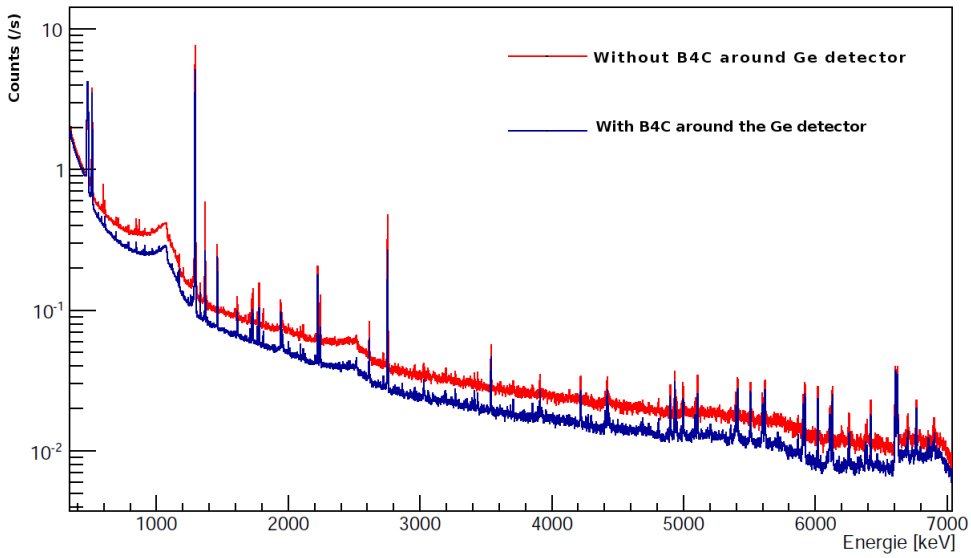

Figure 3.7: Gamma background in the PN3 casemate. The red spectrum shows the result of the measurement in the center of the casemate using a Ge detector. The blue spectrum shows the result by using a B4C protection around the same detector. The result shows a reduction of a factor 1.4 in the total rate, however the lines associated to neutron captures on Fe are not affected, which indicates that these captures are produced in the heavy concrete walls around the detector [155].

The gamma flux measured at the PN3 casemate before the installation of all the shieldings was 147 Hz/100 cm^2 for energies above 2 MeV [155].

3.6.1.3 Cosmic ray-induced background

Cosmic-ray muons constitute a very important source of correlated background for neutrino detection. The expected muon rate at STEREO's site is about 500 Hz. In organic liquid scintillators, muons and the subsequent shower products interact mostly on ^{12}C, the most abundant nucleus other than H [159, 160]. These interactions produce fast and slow neutrons and radioisotopes by spallation. Fast neutrons give rise to proton recoils, which can mimic a prompt signal. The same neutrons thermalize and diffuse to finally be captured on Gd imitating a neutrino signal by giving a false "Prompt-Delayed" coincidence. Further possibilities for "Prompt-Delayed" coincidence can be generated when two or more neutrons are induced by the same muon. A similar correlated signal can arise when the spallation results in certain radioisotopes (^{8}He, ^{9}Li, ^{11}Li) that undergo β decay

followed by neutron emission.

If the muon interacts directly with the detector or the muon veto, the muon signal can be easily identified. These events can be removed by stopping the acquisition for some time after the passage of the muon (e.g. 100 μs). However, it is also possible, that the interactions take place in the surrounding materials, most notably Pb from the shieldings. In this case, fast neutrons can go through the shielding and reach the Target, producing a correlated background.

The ILL reactor has the advantage of providing large periods of reactor OFF. In these periods, the cosmic-ray induced background can be precisely measured and then, subtracted from the reactor ON data. For fast neutrons, the way in which light is emitted when heavy particles interact in the liquid scintillator gives an additional handle: it is different from the case of e^-/e^+ or gamma interaction and can be used to identify them. In the case of recoiling protons, the decay time of the light emission is expected to be longer. This technique is called pulse shape discrimination (PSD) [161, 162] (see section 3.7.3).

3.7 The STEREO scintillating liquids

The gadolinium loaded organic liquid scintillator is a crucial component in the STEREO experiment. The atoms of hydrogen act as free "protons" and serve as Target for the IBD reaction. On the other hand, Gd atoms are responsible of producing a clear delayed signal in a short period of time thanks to the large neutron capture cross section. Furthermore, neutron capture on Gd produces a cascade of gammas with a total energy of 8 MeV, much higher than natural radioactivity's, which is below 3.5 MeV. Finally, its high light yield is a necessary condition to achieve a good energy resolution.

The STEREO liquid scintillator is composed of several materials: The base of the liquid consists in an aromatic solvent, whose molecules feature one or more ring systems. For STEREO, the solvent is made of 75% LAB (Linear Alkyl Benzene $C_{18}H_{30}$), 20% PXE (phenyl–1–xylylethan $C_{16}H_{18}$), and 5% DIN (di-isopropylnaphthalene $C_{16}H_{20}$). The use of PXE improves the light yield while the use of DIN improves the PSD. The solvents emission spectrum usually peaks in the UV range (around 300 nm), whereas the PMTs are most sensitive at wavelengths of 420 nm. Thus fluors are added to shift the emission peak towards the near UV and blue wavelength ranges. The solute includes 7g/l PPO as primary fluor and 20 mg/l of bis-MSB as secondary fluor. The role of primary fluors is to acquire energy by non radiative transfer from the excited solvent molecules, and emit light in longer wavelengths than the solvent. Secondary fluors on the other hand, absorb

far UV light emitted by the solvent and re-emit it in the near UV-blue range (this is called wavelength shifting). The expected attenuation length for photons of 430 nm is about 5 meters, while the light yield is planned to be 6000 photons per MeV. Finally, a gadolinium complex of 0.2 % Gd + 1% THF (tetrahydrofuran C_4H_8O) is added to dope the liquid in the Target, the GC's liquid scintillator being free from gadolinium.

3.7.1 Interaction of particles in the liquid scintillator

When a charged particle interacts with the scintillator material, the electromagnetic interaction is responsible for its energy loss. The electromagnetic interaction can be either with electrons or with the atomic nucleus. However, at low energy ($\sim$ MeV), the interaction with electrons is predominant. The interaction of charged particles with matter produces the excitation or ionization of the molecules.

The energy loss of electrons is given by the Bethe-Bloch formula [163, 164, 165]

$$-\frac{dE}{dx} = 4\pi N_A r_e^2 m_e c^2 \frac{Z}{A}\frac{1}{\beta^2}\left[\ln\frac{\gamma m_e c^2 \beta\sqrt{\gamma-1}}{\sqrt{2}I} + \frac{1}{2}(1-\beta^2) - \frac{2\gamma-1}{2\gamma^2}\ln 2 + \frac{1}{16}\left(\frac{\gamma-1}{\gamma}\right)^2\right] \tag{3.7.1}$$

where N_A is the Avogadro number, r_e is the electron radius, Z, A are the atomic and weight numbers of the absorber, I is the mean excitation energy, characteristic of the absorber material. The energy of the detected positrons in STEREO ranges from 1 to 8 MeV, which means that they lose their energy mostly by ionization.

For high energy particles, an additional contribution to the energy loss is present, the Bremsstrahlung effect. This effect consists in the emission of photons by the deceleration of charged particles due to the influence of the Coulomb field of the nuclei [166]. Besides the Bremsstrahlung effect, at high energy, e^-/e^+ pair production participates in the energy loss of charged particles. Both processes contribute to the energy leaks that are observed in the neutrino signal (see section 5.4).

If the particle moves faster than the speed of light in the medium, it radiates light through the Cerenkov effect [167]. However the energy loss given by Cerenkov radiation is much smaller than the energy loss produced by collision or Bremsstrahlung.

In a similar way, the interaction of photons with matter depends on their energy. In contrast to charged particles, photons can be either completely absorbed (photoelectric effect, pair production) or scattered with a large angle (Compton effect) when they interact with matter.

In the photoelectric effect, the photon is completely absorbed. The energy required for the photoelectric effect is at least the ionization energy of the electrons. The recoil momentum of this interaction is taken by the atomic nucleus. If the photon has enough energy, it can eject electrons from the inner shells of the atom. In the non relativistic limit, the photoelectric cross section is given by the Born approximation [168]

$$\sigma_{photo} = \left(\frac{32}{\varepsilon^7}\right)^{1/2} \alpha^4 Z^5 \sigma_{Th}^e \quad [\mathrm{cm}^2/\mathrm{atom}] \tag{3.7.2}$$

where $\varepsilon = E_\gamma / m_e c^2$, σ_{Th}^e is the Thomson cross section for elastic scattering of photons on electrons. The photoelectric effect is dominant at low energies. For liquid scintillator in particular, below 50 keV most of the interactions are produced by photoelectric effect.

For higher energy, the Compton effect where photons scatter off electrons, becomes more important. In a liquid scintillator, photons with energies ranging from 50 keV to about 20 MeV interact mostly by this effect. The Compton cross section is given by the Klein-Nishina formula [169, 170]

$$\sigma_{\mathrm{KN}} = 2\pi r_0^2 \left\{ \frac{1+k}{k^2} \left[\frac{2(1+k)}{1+2k} - \frac{\ln(1+2k)}{k} \right] + \frac{\ln(1+2k)}{2k} - \frac{1+3k}{(1+2k)^2} \right\} \tag{3.7.3}$$

with $k = \frac{h\nu}{m_e c^2}$. The maximum energy transferred to electrons via Compton scattering "Compton edge" is given by

$$E_{\mathrm{Compton}} = E_{\mathrm{T}}(\max) = E \left(1 - \frac{1}{1 + \frac{2E}{m_e c^2}} \right) \tag{3.7.4}$$

with E the energy of the incident photon. Figure 3.8 shows the energy transferred to electrons by 2.2 MeV gammas, the maximum energy transferred can be estimated with equation 3.7.4 to about 1.97 MeV. Figure 3.8 shows that, to first order, gamma's interaction with the LS is equivalent to that of the corresponding e^-/e^+ distribution, which can be predicted with help of the simulation.

Finally, at high energy, pair production becomes the dominant effect. In this case, an electron-positron pair is produced in the Coulomb field of the nucleus.

In STEREO, the prompt signal is produced by the positron and the two 511 keV gammas from its annihilation within the liquid scintillator. As a first approximation, it can be considered that the loss of the positron's kinetic energy happens exactly as if it were an electron. Then, for the purposes of calibration and modeling of the detector response, a positron is just "an electron with two 511 keV annihilation gammas". The delayed signal

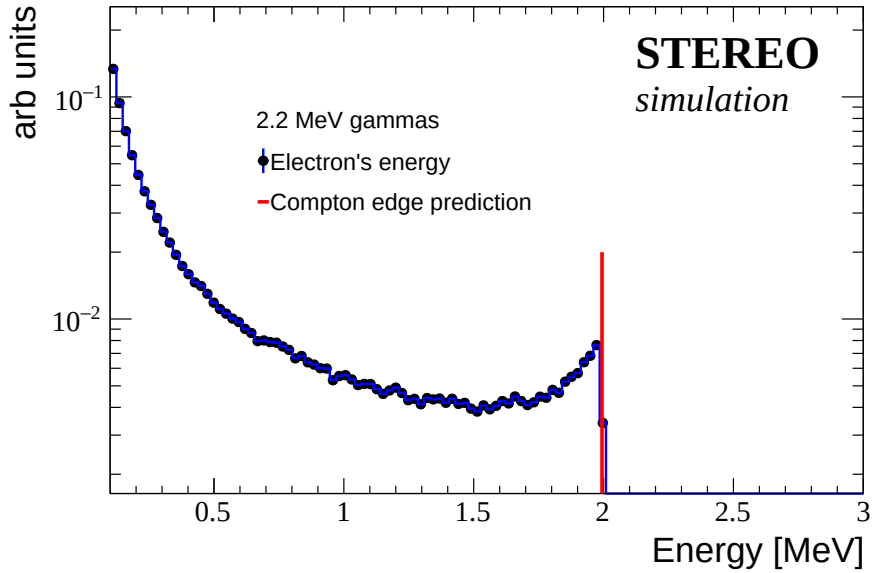

Figure 3.8: e^-/e^+ distribution as a function of the energy generated by interaction of 2.2 MeV gammas in the LS. The maximum energy transferred for these gammas is about 1.994 MeV (vertical red line in the plot).

is originated by the interaction of gammas from the 8 MeV Gd gamma cascade. All these gammas are in the energy range between 0.511 to 7 MeV, and they interact mostly via the Compton effect, producing plenty of electrons of low energy.

The typical distance of conversion for gammas of about 1 MeV in a LS is about 16 cm, while for gammas of 511 keV is about 14 cm. Alphas lose their energy in the LS in a few micrometers, and protons (∼MeV) in a few dozens of micrometers. On the other hand, neutrons thermalize in the LS in a few millimeters (∼keV) or centimeters (∼MeV) depending on their energy, but they can diffuse, so the distance between the emission point and the point of capture in the STEREO liquid scintillator is about 10 cm. Finally for positrons of a few MeV the distance of interaction in the LS before lose all their energy is a few millimeters.

3.7.2 Scintillation mechanism and non-linearity

A charged particle passing across the scintillator excites its molecules. Some of these molecules will release a small fraction of this energy as optical photons. In a liquid scintillator, molecules contain benzene rings, which can be excited into their singlet or triplet states. The primary excitation occurs mostly in the liquid solvents, then the excitation energy migrates from one solvent molecule to its neighbor solvent molecule, till this energy is transferred to the solute molecules. It re-emits this energy as light [173]. The singlet

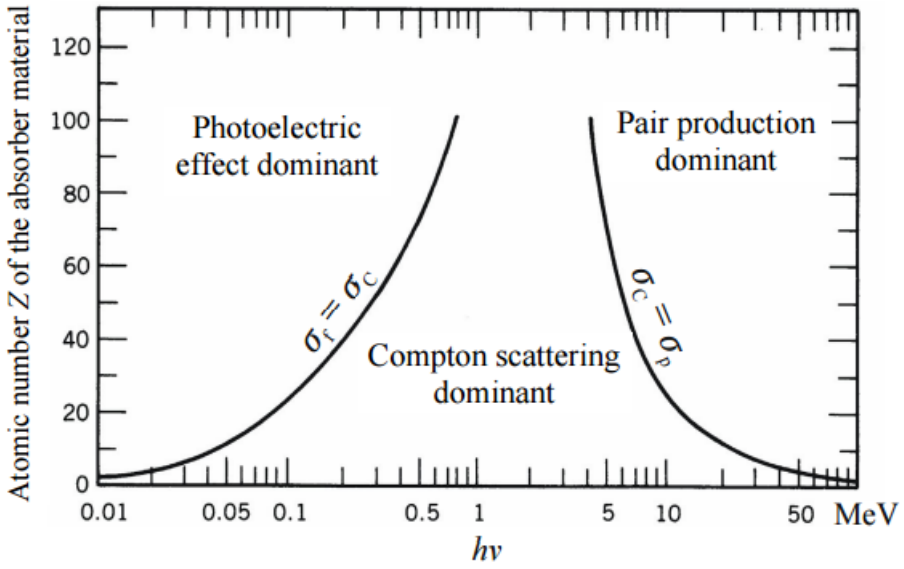

Figure 3.9: Types of photon interaction, at low energy the dominant effect is photoelectric, then at medium energies the Compton effect becomes more important and at high energy, pair production. The process depends also on the Z of the absorber material[171, 172]

states are created when the energy transfer to the molecule is small and the electron jumps to a higher electronic state. Triplet states, on the other hand, are created when the energy transfer is large, and the electron is temporally torn from the molecule. When the ion recaptures an electron, it populates mostly the triplet states [174, 175].

Molecules are excited into their higher electronic singlets S_n or triplets T_n states and rapidly (some picoseconds) decay into the S_1 and T_1 states through radiationless internal conversion. These states have longer mean life time, of some nanoseconds for the S_1 state and larger than tens of nanoseconds (usually ∼100 ns) for the T_1 state.

The main characteristics of scintillators are the scintillation efficiency, light output, emission spectrum and decay time of the scintillation light. The scintillation efficiency is the ratio between the energy emitted as photons and the energy absorbed by the scintillator. The light output is the number of photons produced by MeV of energy absorbed in the scintillator. The decay time usually follows an exponential law. The typical decay time for organic scintillators is of a few nano seconds[169], varying from 0.5 to 100 nanoseconds, depending on the scintillator.

The fraction of the particle energy that is converted into fluorescent light, depends on the type and the energy of the particle. For organic scintillators, the response to electrons is linear for energies roughly above few hundred keV [169]. For heavy particles like neu-

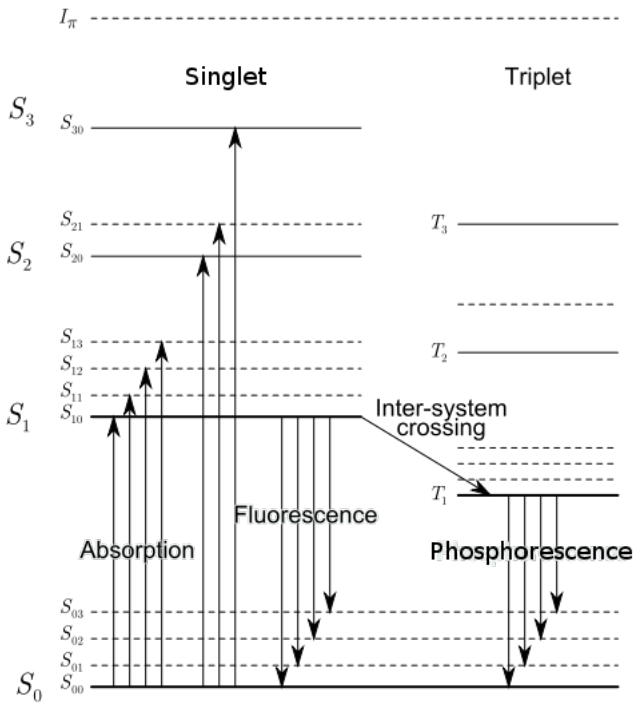

Figure 3.10: Energy levels of a fluorescent molecule [169]. An incident particle can excite an electron into the excited singlet or triplet states. The higher excited states rapidly decay into the lowest excited states S_1 and T_1, which decay emitting light through fluorescence and phosphorescence process respectively.

trons or protons this response is nonlinear up to higher energies.

The response of organic scintillators is the amount of light produced as a function of the kinetic energy of the incident particle. It can be described by a function of dE/dx, linear in a first approximation. For electrons this process is described by the equation 3.7.1. There are however, two main sources of non linearity in the response of the LS: ionization quenching and Cerenkov light emission.

For highly ionizing particles, the light output degrades (this is called quenching). This process occurs at the end of the particle's track, where the mean energy loss dE/dx increases quickly. In the absence of ionization quenching, the light output is proportional to the energy loss. Low energy particles have high dE/dx and thus their light output is significantly quenched. More energetic particles, on the other hand, have smaller dE/dx and this effect is less important. Birks found a semi-empirical model that describes this process [174]

$$\frac{dL}{dx} = \frac{S\frac{dE}{dx}}{1 + k_B\frac{dE}{dx}} \tag{3.7.5}$$

where L is the light output, S is the normal scintillation efficiency, and k_B is called the Birks constant. It is characteristic of the scintillation material used. The Birks constant

describes the strength of the quenching effect for a given particle in a given scintillator. It has to be found experimentally by fitting the data.

The second source of non linearity is the Cerenkov effect. As was already said before, this light is created only if the speed of the incident particle is larger than the speed of light in the medium. For heavy particles (protons or alphas), the Cerenkov effect is only produced for energies above hundreds of MeV, so this effect is of no importance in the STEREO liquid scintillator. For electrons or positrons however, the energy threshold for the production of Cerenkov light is of only hundreds of keV. This energy threshold depends on the refractive index of the medium $n(\lambda)$.

In STEREO, the visible energy threshold of accepted events is expected to be 2 MeV. For a 2 MeV prompt signal, the energy deposited by the positron via ionization (1 MeV) will lead to little non-linearities. The two 511 keV gammas from the annihilation however, convert into plenty of low energy electrons (<200 keV), and their non-linear response becomes important. It needs to be measured and characterized carefully in order to have a good understanding of the energy reconstruction and to reduce the systematic uncertainties associated to these nonlinear effects.

3.7.3 Pulse shape discrimination

The scintillation process since the primary excitation to the light emission happens in a very short period of time (few to hundred nanoseconds). However, the time distribution of the light emission contains valuable information. For most organic scintillators, the prompt or fast fluorescence represents most of the observed light. However a delayed or slow fluorescence is also observed in many cases. This delayed fluorescent emission is the product of the interaction of two molecules in the T_1 state, which leads to one molecule in the S_1 state and the other in the ground state.

The amount of the slow component is dominated by the population of singlet and triplet states. These populations are governed by the mechanism of energy loss dE/dx of the ionizing particle. If dE/dx is small, molecules will be excited into singlet states, while if dE/dx is high, the triplet states will be preferred. Thus, the fraction of light that appears in the slow component depends on the nature of the exciting particle, and this information can be used to separate heavy charged particles from electrons and gammas. This is called pulse shape discrimination (PSD). Good discrimination of electrons and gammas against fast neutrons, that ionize the medium through collisions with protons, can be achieved in this way.

The components of the liquids used in STEREO have been studied and used in other

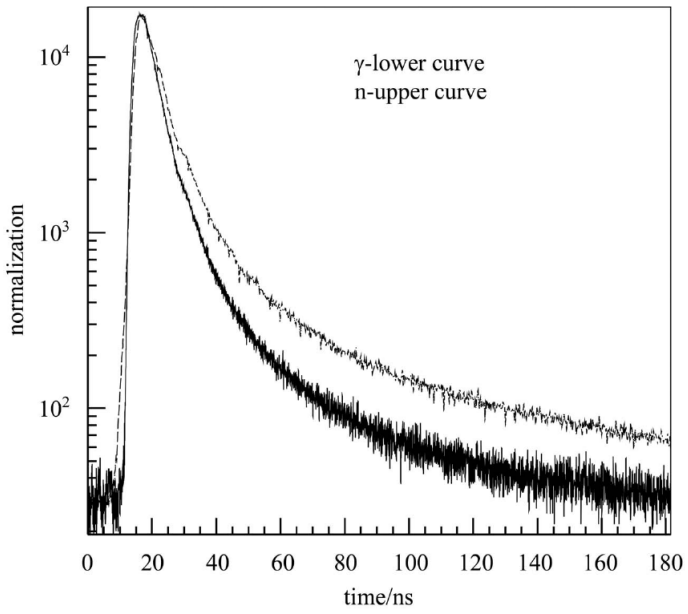

Figure 3.11: Scintillation time profile of a LAB based LS under gamma and fast neutron radiation [176]. For neutrons the slow component is larger than for gammas.

experiments showing that PSD can be successfully exploited [176, 177]. Studies have also shown that in mixtures including DIN as solvent the amount of slow component is larger than in the case of LAB [178]. Then, the use of DIN in the mixture improves the efficiency of the PSD discrimination. Given that STEREO will be placed in a high neutron flux environment, the use of PSD could play an important role in the discrimination of the fast neutrons background.

The particle identification information is thus encoded in the fast and slow components of the collected charge. The most common way of exploiting them is defining the collected charge in a delayed time window (Qtail) and comparing it to the charge collected in the whole trigger time window (Qtot). Figure 3.12 shows the expected performance of the STEREO liquids. The measurements were realized in a small test cell, and showed that electrons can easily be separated from protons. The light collection being somewhat more complicated in the STEREO experiment, the PSD performance will most likely be a little less impressive.

3.8 The STEREO inner detector

The inner detector of STEREO consists of the six cells constituting the detector Target and a Gamma Catcher (GC) surrounding these cells (see figure 3.13). The Target cells are filled with gadolinium loaded liquid scintillator (1.8 m^3), while the outer crown (GC)

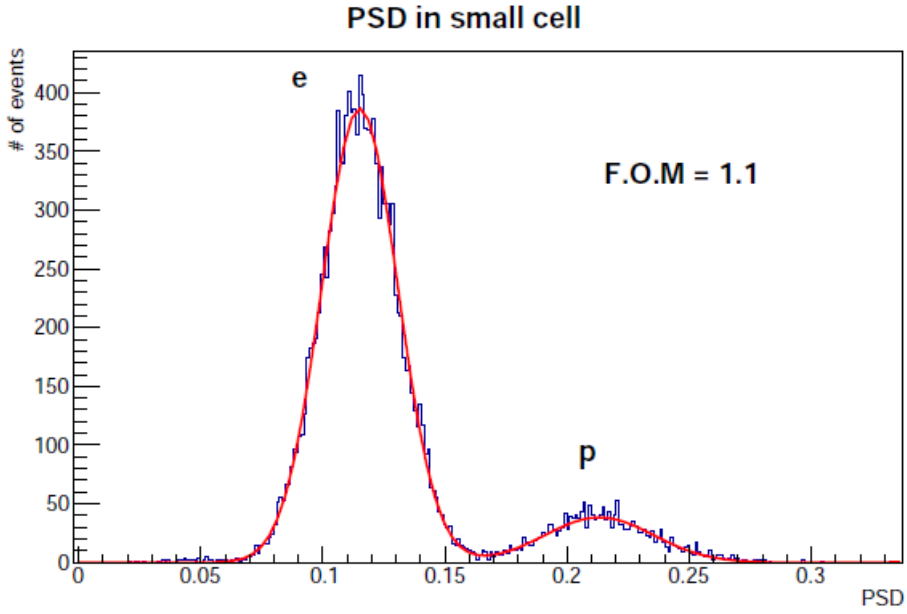

Figure 3.12: PSD in a test cell. The performance of the STEREO liquid to the PSD was studied in a small cell. Electrons and protons can easily be identified.

is filled with a similar liquid scintillator but without gadolinium. To protect the detector from the gamma and neutron ambiance in the casemate PN3 at the ILL, an "internal" shielding composed of polyethylene and lead enclose the inner detector. In addition, a muon veto is placed over the detector, whose function is to identify the passage of a muon to remove the possible cosmic-ray induced background.

3.8.1 Target and Gamma Catcher

The STEREO Target consists in 6 cells filled with LS, whose dimensions are $37\times90\times90\text{cm}^3$, thus segmenting the Target in the direction of the antineutrino's propagation. The cell walls are made of acrylic plates. On the top of each cell, 4 photo-multipliers tubes of 8 inches are placed to collect the light produced in the liquid. An acrylic buffer of 20 cm separates the LS from the PMTs.

The Gamma Catcher is the outer crown surrounding the 6 cells of the Target. Its dimensions are 28 cm in the lateral sides, and 37 cm in the front and in the back of the detector. Its volume is about 2.3 m^3, and the composition is similar to the Target liquid, except that it is not loaded with Gd, and has a lower concentration of PPO (3g/L). As in the cells, an acrylic buffer of 20 cm is placed between the liquid and the PMTs and VM2000 sandwiches are glued to the walls to ensure the optical separation with the Target. The number of PMTs in the Gamma Catcher is 24, 8 in each lateral side, and 4 in the front and back sides, mimicking a Target cell. The idea is to make the detector as invariant under translations along the neutrino's propagation direction as possible.

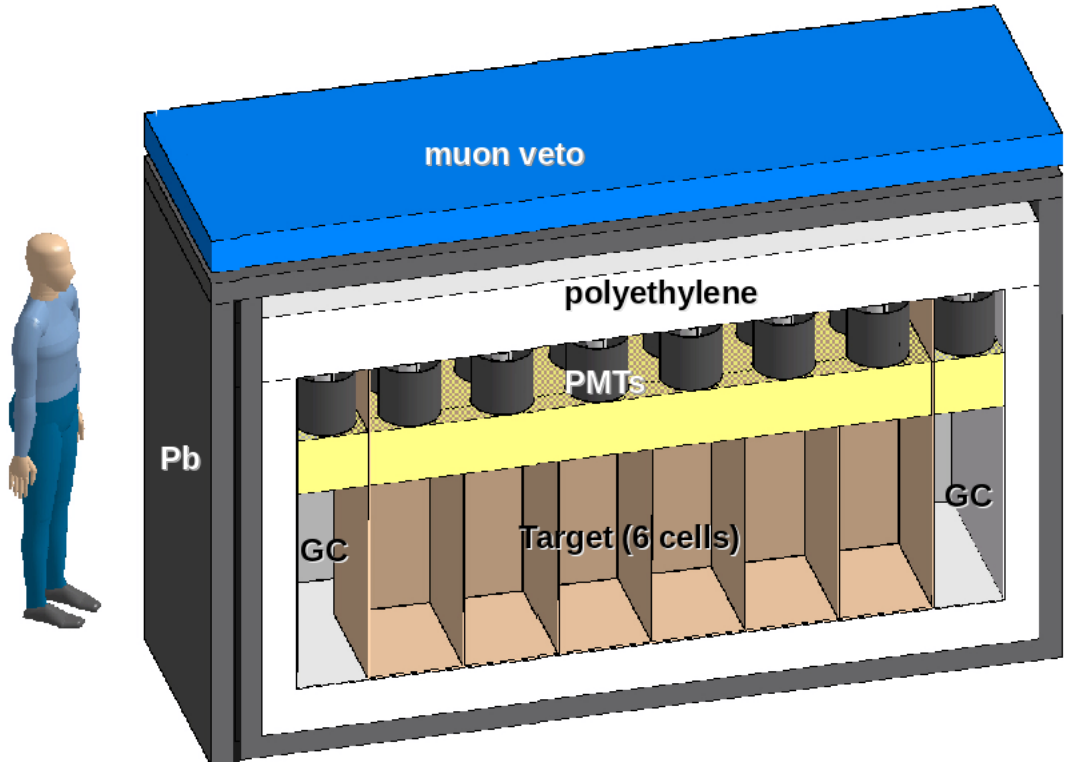

Figure 3.13: The STEREO detector consist in a Target of 6 cells filled with liquid scintillator loaded with Gd and read out by an array of 4 PMT in each cell. Surrounding the Target, there is an outer crown of 30 cm of liquid scintillator without Gd called Gamma Catcher (GC). Enclosing the detector, a shielding composed of polyethylene and lead. On the top of the detector, a muon detector, called muon veto.

The main function of the Gamma Catcher is to improve the energy resolution by recovering some of the 511 keV escaping gammas from the positron annihilation. Moreover, the Gamma Catcher can be used as an active shielding, detecting and stopping gammas and fast neutrons coming from the outside.

3.8.2 Light collection

Once the light is produced in the liquid scintillator, the goal is to collect the largest possible fraction of it. Light is emitted isotropically from the track of the ionizing particle. Two effects degrade the light collection: optical self absorption within the scintillator and losses at the scintillator surface. Self absorption depends on the attenuation length (or mean free path), which is the mean distance traveled by photons before being absorbed, and it depends on the photon wavelength and in the liquid scintillator composition (in STEREO it is expected to be larger than 5 meters). Thanks to the wavelength shifting performed by the fluors, self absorption is not significant, except for large volumes of scintillators.

In STEREO there are PMTs only in the upper side of the cells. This means that a dependence of the amount of light absorbed with the distance between the interaction position and the PMTs is expected. This non-uniformity will degrade the overall energy resolution of the experiment. This non-uniformity will therefore depend strongly on the reflection properties of the walls and floor of the STEREO cells.

In order to homogenize the light collection, the STEREO liquid scintillator is separated from the PMTs by 20 cm thick acrylic buffers, which are transparent, chemically compatible with the LS and have a similar refraction index as the LS. In this way the light collection non-uniformity associated to the vertical position of interaction is reduced. Moreover, to recover the largest possible amount of light, reflectors (VM2000) are glued to the acrylic walls. These are prepared in a kind of "sandwiches" using fine acrylic plates in order to create an air gap between the reflector surfaces and thus obtain total reflection. Thus these wall sandwiches between the Target cells consist in a plate of 2 mm of acrylic + an air gap of 100 μm + a VM2000 foil plus an air gap of 100 μm + plate of 2 mm of acrylic. In order to maintain the air gap between the walls, the borders of these sandwiches are sealed. These sandwiches ensure the optical separation between cells and improve the light collection. Thus, about 90% of light produced in one cell is collected in the same cell.

3.8.3 PMTs

Once the light is produced in the liquid scintillator of the Target and Gamma Catcher, the PMTs detect a fraction of this light. Light in the visible or ultraviolet range liberates electrons from the PMT photo-cathode via the photoelectric effect [179]. Photoelectrons are emitted into the vacuum, and then are accelerated and focused onto the first dynode by electric fields. The accelerated electrons then collide with the dynode and cause the emission of secondary electrons, multiplying the incident charge. The secondary electrons coming from the first dynode get further multiplied at the second dynode and so on. Finally all the electrons are collected by the anode, which outputs the electron current to an external circuit, giving a macroscopic current (mA) from only one incident photon.

The PMTs chosen to the STEREO Target and Gamma Catcher are the 8 inches Hamamatsu R5912-100 [181]. They have a quantum efficiency of 34 % at 400 nm, an average electron transit time of 54 ns and a transit time spread of 2.5 ns, a single photo-electron peak to valley ratio between 2.0-3.6 and a dark rate between 1.1-1.8 KHz. The high voltage can be tuned (typical voltage of 1500 V) to provide a gain of 10^7.

The gain of the PMTs is calibrated via their single photo-electron response. This

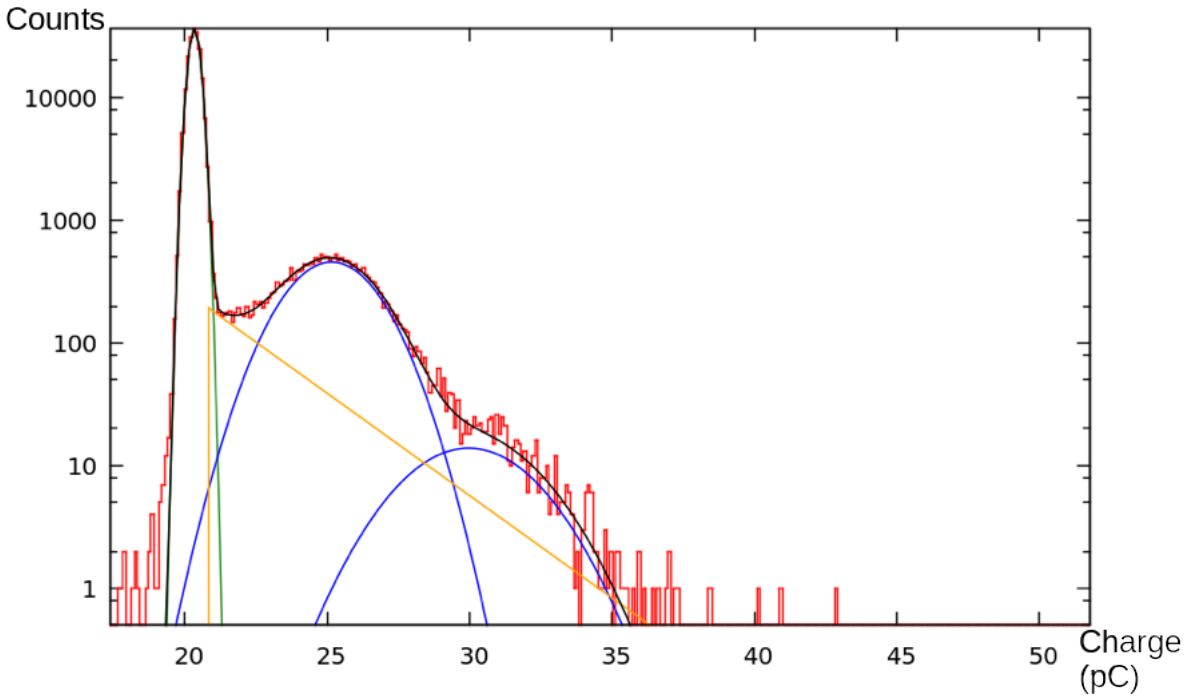

Figure 3.14: Single photo-electron (SPE) response for the PMT SQ0215 measured in Heidelberg at the MPIK [180]. The pedestal is found to be at 20.92 pC, the SPE at 25.74 pC and the charge per PE to be 4.82 pC

response is induced by injecting low intensity light pulses with the LED monitoring system (see Section 3.12.1). Figure 3.14 shows the single photo-electron response of a R5912-100 PMT during a test performed at Heidelberg. Fitting the collected SPE charge distribution allows the determination of the pedestal, and the positions of the one, two, three... photo-electron responses. The number of observed photoelectrons $N_{\text{p.e.}}$ is then obtained by first subtracting the pedestal and then dividing by the gain, which is the difference between the first photo-electron and the pedestal positions:

$$N_{\text{p.e.}} = \frac{Q^{\text{tot}}_{PMT_i} - Q^{\text{pedestal}}_{PMT_i}}{g_{PMT_i}} \tag{3.8.1}$$

3.9 Electronics and acquisition

The STEREO electronics and readout system will have to deal with the signals of 68 PMTs: 24 from the Target, 24 from the GC and 20 from the muon veto. Each PMT can collect up to 1500 photoelectrons. The total duration of the expected signals varies from 100 to 200 ns. In addition, the electronics and readout system should allow a rate as high as 1 KHz in the whole detector with no dead time. Thus, the main task of the readout electronics is to receive and digitize the analog signals from the 68 PMTs and transmit all the relevant information to storage without loss of quality.

The detection of the IBD needs the energy and the time of each event. For electrons above few hundred keV the deposited energy is roughly proportional to the light emitted in the liquid. In a first approximation the light is also proportional to the amount of charge detected by the PMTs. The STEREO requirements on energy scale systematic uncertainties imposes that the non-linearity in the electronics should be at the 1% level.

The variables needed for the data analysis are the charge and the time of each signal in all the 68 PMT. The trigger scheme may be either global or local, and configured with different conditions (coincidence or anti-coincidence). The signal should be processed on board to compute the Q_{tot} and Q_{tail} for pulse shape discrimination (PSD). Taking into account all these considerations, a dedicated electronic in a single microTCA crate has been designed for STEREO, the overview is shown in the figure 3.15.

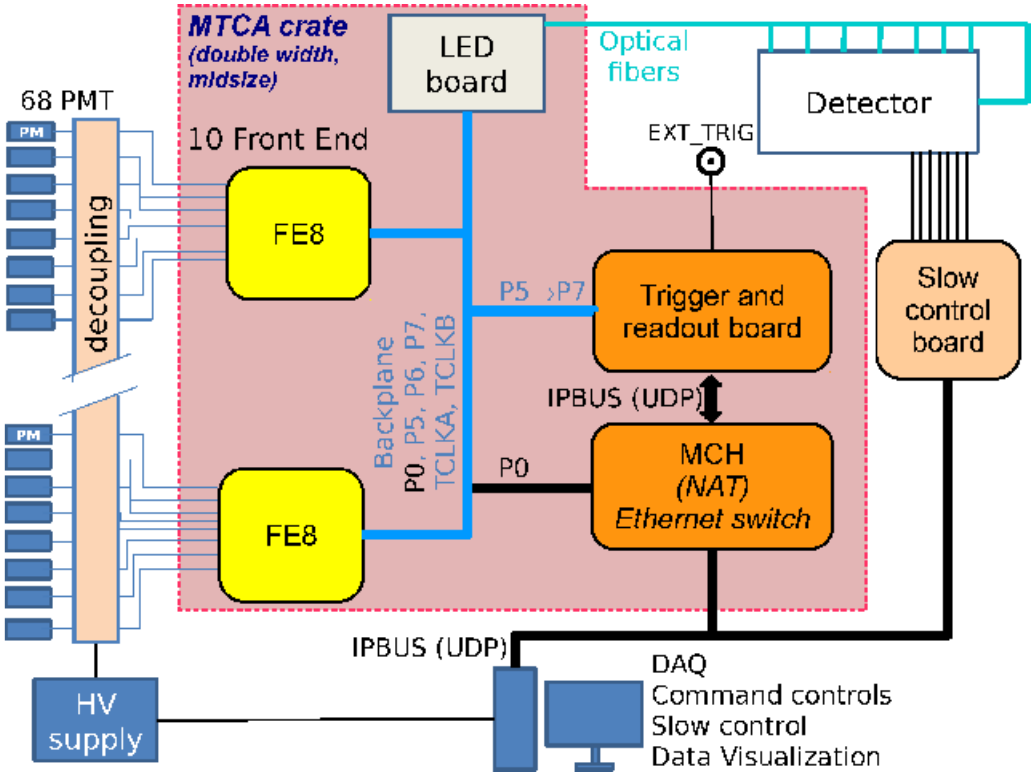

Figure 3.15: The STEREO DAQ electronics overview. The microTCA is equipped with ten 8-channels front-end electronics boards, one LED board to drive the LED boxes and one trigger and readout mezzanine board [182].

The electronics consists in ten 8-channel front-end boards with a first programmable trigger, which will provide the Q_{tot}, Q_{tail} and tCFD[1] in real time. Two different gains are fixed by hardware for the PMTs, one for the single photo-electron calibration ($\times 20$)

[1]The Constant Fraction Discriminator (CFD) is used to found the beginning of the signal

and the other for the normal acquisition periods (×1). The trigger board consists in a programmable second level taking into account in this case the information of the muon veto, the Gamma Catcher and the Target. In this way, triggers in coincidence or anti-coincidence can be performed. Finally a LED board has been designed to inject light using optical fibers for PMT calibration and monitoring (see section 3.12.1). The electronics have been extensively tested using the muon veto detector.

The data acquisition has been developed using NOMAD, which is the standard acquisition software at ILL. Furthermore, a dedicated monitoring and slow control has been designed, allowing to monitor the PMT response at any time. All the acquisition chain has been tested using the LEDs monitoring system.

3.10 Reconstruction software

3.10.1 Pre-processing software

The pre-processing software has been designed to make a fast and automatic analysis of the physics and calibration runs. It converts raw data in a usable ROOT TTree, with the addition of the information of SPE calibration for each PMT. Thus, the Qtot and Qtail can be provided in p.e. units, ready for conversion to energy. This software also performs a first vertex reconstruction by using the charges collected in the Target.

The pre-processing software can also process the information of the simulations to produce a TTree with the same format as pre-processed data.

3.10.2 Reconstruction of the position of interaction

Naively, one would try to reconstruct the interaction vertex position by calculating the average of the positions of the PMTs weighted by the amount of charge collected by each of the PMTs. This is called "the barycenter of charges". This works fine for the charge collected in the Target, since the responses of all cells are relatively similar (see figure 4.19). If, however, the charge collected in the GC has to be used in order to improve the the vertex resolution, the difference in response between the GC and the Target (whose LS are not identical), must be taken into account.

In order to homogenize the detector response of the Target and Gamma Catcher, we propose to normalize it by using the calibration constant (number of observed p.e per deposited MeV, see next chapter) of each cell and each Gamma Catcher. Once normalized the charges, the barycenter is found using all the information of the Target and Gamma

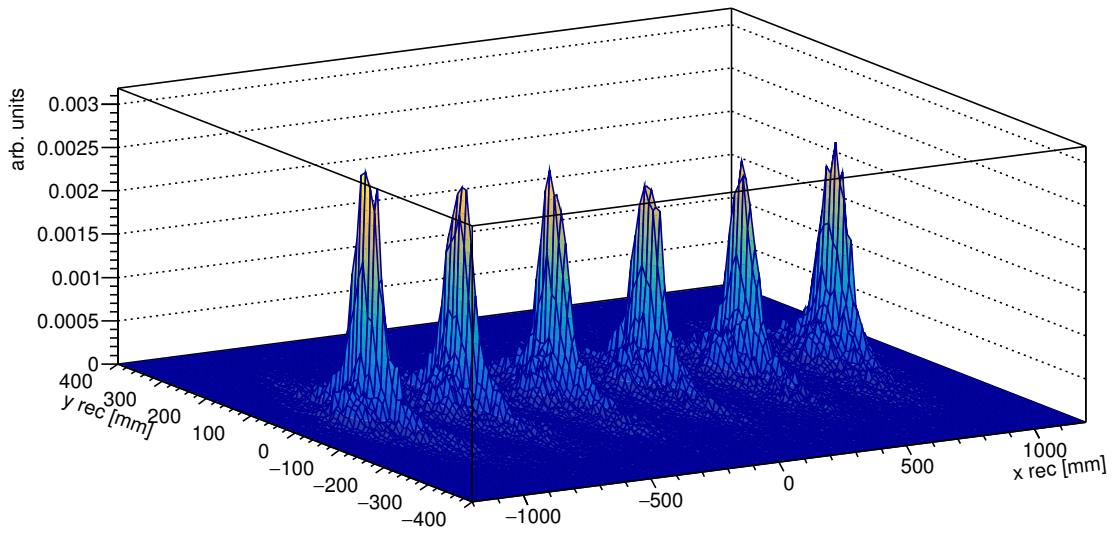

Figure 3.16: The reconstructed vertex for positrons of 1 MeV uniformly distributed in all the Target. Most of the events are reconstructed in the centers of the cells.

Catcher:

$$\vec{X} = \frac{\sum_i^{cell} \frac{1}{C(\vec{X}_{\text{cell}_i})} \sum_j^{\text{PMT}_{\text{cell}_i}} Q_{tot}^{\text{PMT}_j,\text{cell}_i} \times \vec{X}^{\text{PMT}_j,\text{cell}_i}}{\sum_i^{cell} \left(\sum_j^{\text{PMT}_{\text{cell}_i}} Q_{tot}^{\text{PMT}_j,\text{cell}_i} \right) / C(\vec{X}_{\text{cell}_i})} \tag{3.10.1}$$

where $C(\vec{X}_{\text{cell}_i})$, $Q_{\text{tot}}^{\text{PMT}_j\text{cell}_i}$ and $\vec{X}^{\text{PMT}_j,\text{cell}_i}$ are the calibration constant, the charge and position of the PMTs of the cell i (including the Gamma Catcher). The result of this method is shown in the Figure 3.16 for prompt signals. Most of the events are reconstructed in the center of the cells. Note that we are not sensitive to the position within each cell. Figure 3.17 shows the results of the vertex reconstruction for delayed signals. The vertex of delayed signals is more distributed in the cells than the vertex of prompt signals.

The advantage of the inclusion of the charge collected in the Gamma Catcher in the vertex reconstruction algorithm is that it improves the resolution results, especially in the case of the delayed signals, which are characterized by the n-Gd gamma cascade. In this case, more energy can leak to the Gamma Catcher, and the improvement by including it is bigger. Figure 3.18 shows the residual value between the true and the reconstructed vertex in the y axis using only the Target and the Target plus the Gamma Catcher. Thus the RMS can be reduced from 221 mm using only the Target to 193 mm including the Gamma Catcher.

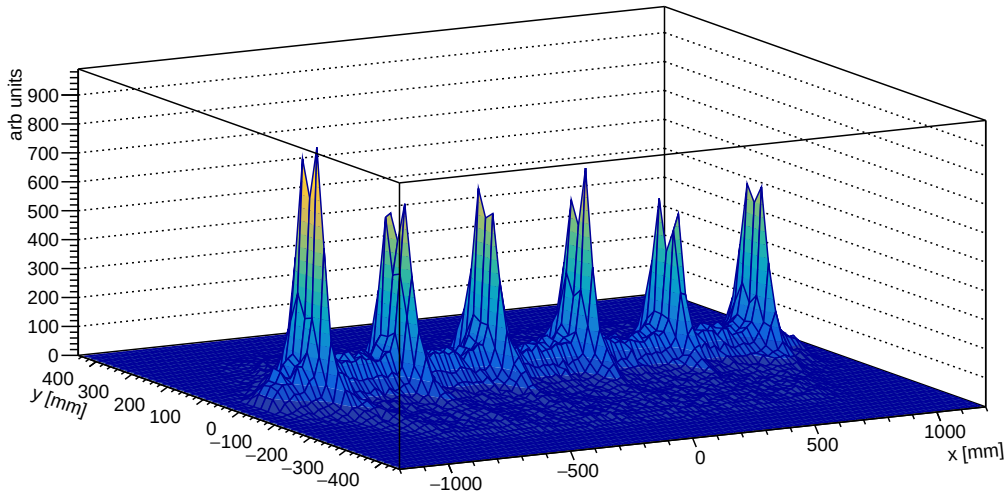

Figure 3.17: Vertex reconstruction of delayed signal. Most of the events are reconstructed in the center of the cells. However the vertex is more distributed in the cells compared with the vertex of prompt signals

3.10.3 Vertex reconstruction in GC

The vertex reconstruction in the Target is performed using the calibration constant-weighted charges of the Target and Gamma Catcher. The reconstruction in the Gamma Catcher needs to use only the Gamma Catcher charge.

Since the light collection changes according to the position of interaction in the long sides of the Gamma Catcher, we propose to use weighted charges in a similar way to the computation of the barycenter in the Target. Thus, the barycenter in the gamma catcher can be found as:

$$\vec{X}^{\mathrm{GC}}_{\mathrm{Bary}} = \frac{\sum_i Q^{\mathrm{PMT}_i}_{tot} \times \vec{X}_{PMT_i}/C(\vec{X}_{PMT_i})}{\sum_i Q^{\mathrm{PMT}_i}_{tot}/C(\vec{X}_{PMT_i})} \tag{3.10.2}$$

where the charges of each PMT are weighted with a calibration constant obtained when the calibration source is placed in front of each PMT by using the external calibration system. If charge is recorded in more than one Gamma Catcher side, the barycenter is taken from the side where most of the charge is collected. In general only one 511 keV gamma escape from the Target to the Gamma Catcher. Nevertheless, in a few events both 511 keV gammas can escape and can be registered in two different sides of the Gamma Catcher. These events only occur when a positron is produced in the corner of the border cells. Thus, one 511 keV gamma can be detected in one short side and the other in one long side of the Gamma Catcher.

The barycenter in the Gamma Catcher is found to be biased towards the center of

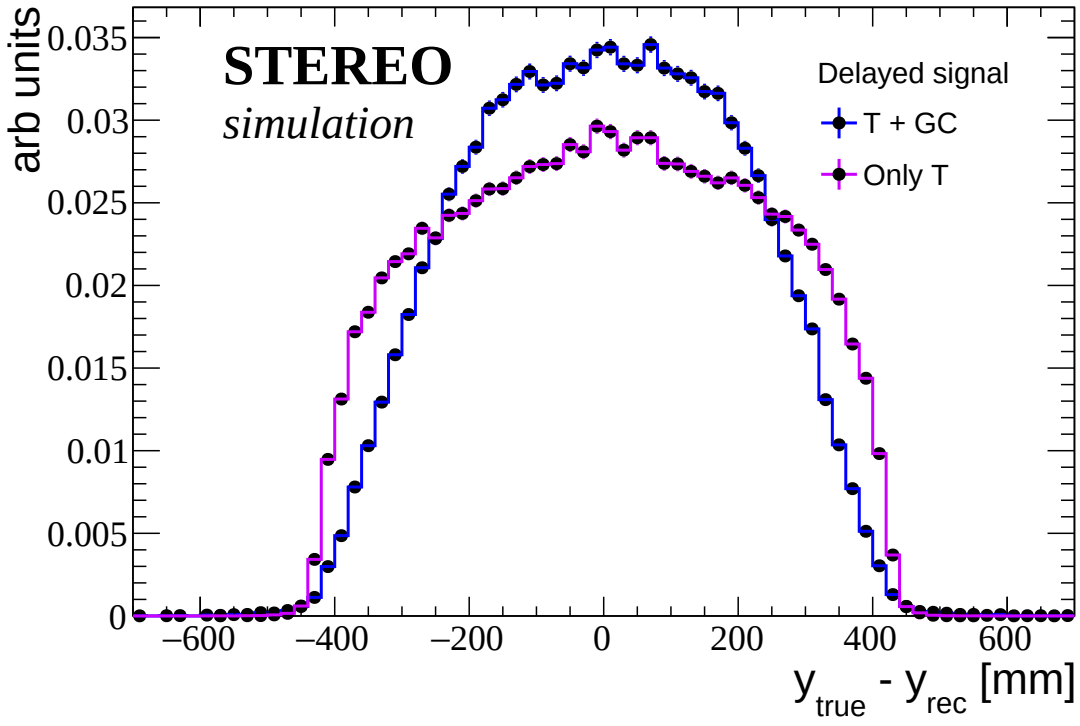

Figure 3.18: Delayed vertex reconstruction resolution. The residual value between the true and reconstructed vertex in the y axis is presented. The violet histogram corresponds to the case in which only the Target is used (σ = 220.8 mm), and the blue histogram corresponds to the case when the gamma has been included (σ = 192.5 mm)

the Gamma Catcher "cells". However, in the long sides of the Gamma Catcher, it can be corrected by using a polynomial function correction. This function can be found by using the external calibration system to place the ^{68}Ge gamma source along the long sides of the Gamma Catcher (see chapter 4). In this way the true vertex can be taken as the position of the calibration source. Then a direct relation between this "true" position and the reconstructed barycenter in the long sides of Gamma Catcher can be found.

Figure 3.20 shows the residual value between the position-corrected reconstructed vertex in the long sides of the Gamma Catcher and the true vertex for 511 keV gammas, which leak from the Target when positrons of 1 MeV uniformly distributed in Target were simulated. The true vertex is taken as the position of the most energetic electron generated by the 511 keV in the Gamma Catcher, in the Monte-Carlo simulation.

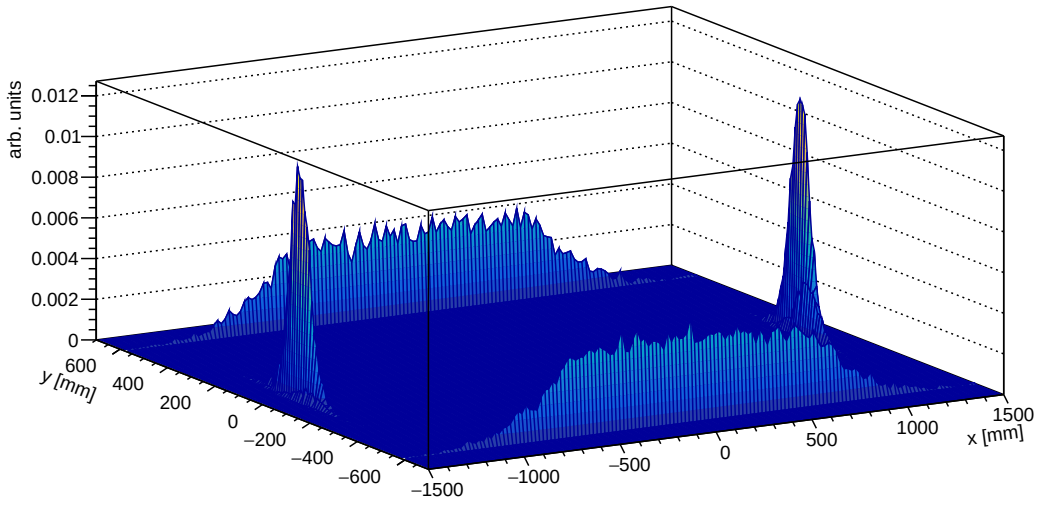

Figure 3.19: Vertex reconstruction in the Gamma Catcher. 1 MeV positrons uniformly distributed in the Target were simulated. When a 511 keV gamma escapes to one side of the Gamma Catcher, a vertex in it is found using equation 3.10.2. The barycenter thus reconstructed is found to be biased towards the center of the Gamma Catcher "cells". In the short sides most of the events are reconstructed in the center, very similar to what happens in the Target cells. In the long sides the bias is smaller given the bigger size of this part of the Gamma Catcher.

3.11 The detector simulation

The detector simulation of STEREO is based on Geant4 [183]. It includes the detector and prototype geometry description, physics processes, and event generators.

An accurate description of the STEREO geometry has been implemented in the detector simulation. It includes: the composition and geometry of liquid scintillator in each cell and Gamma Catcher, the acrylic walls, a detailed implementation of the VM2000 reflective sandwiches and the optical separation between Target cells and between Target and Gamma Catcher, the buffers between that separate the liquid scintillator and the PMTs, the 48 PMTs of the Target cells and Gamma Catcher, the stainless steel double vessel, and the internal shielding composed of polyethylene and lead. Finally, the muon veto and the entire casemate geometry and walls has been included.

The physics process in the STEREO simulation includes electromagnetic, hadronic, ion and optical photon processes, and the optical model for the PMTs. The optical properties of the VM2000 sandwiches have been measured and included in the simulation. The non-linearity between scintillation light and the ionization energy loss due to quenching effects is implemented as well, although the specific parameters are yet to be tuned to match

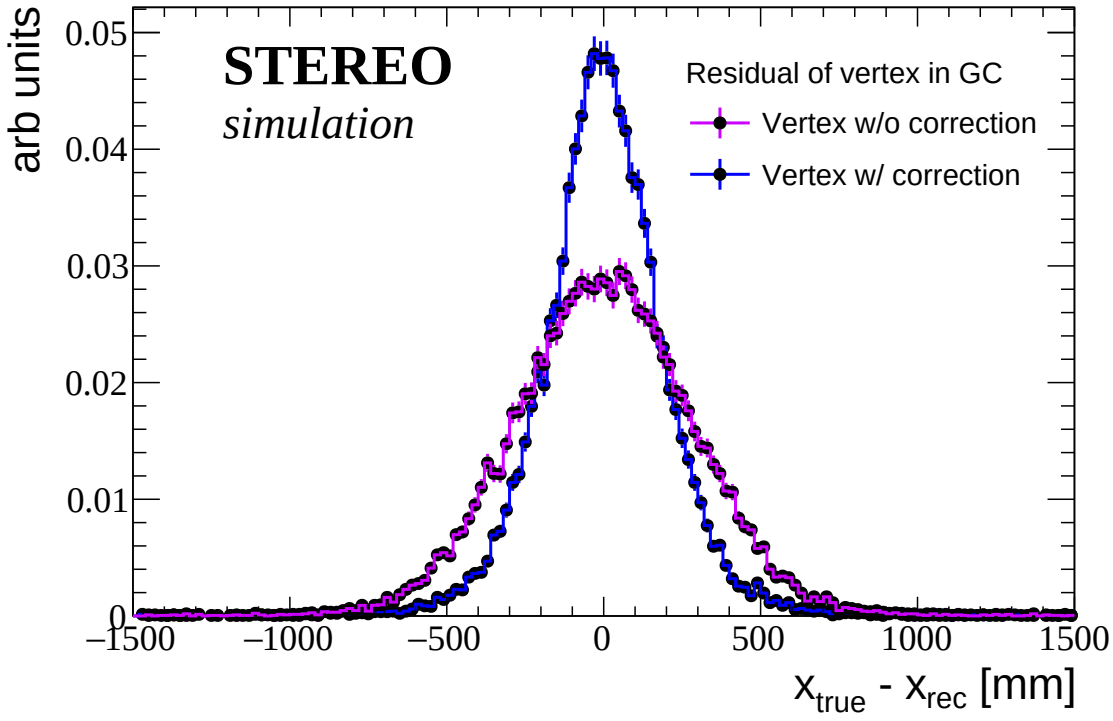

Figure 3.20: Gamma catcher vertex reconstruction resolution. The residual value between the true and reconstructed vertex in the x axis is presented. The violet histogram corresponds to the case in which the vertex without any correction is used (σ = 288 mm), and the blue histogram corresponds to the case when the barycenter is position-corrected (σ = 208 mm)

STEREO's liquids.

In the STEREO simulation, some properties and options are defined in data cards. These cards are read only at run time, which provides flexibility. The STEREO option cards allow the selection of some properties, such as the choice of the liquid and its properties. The optical properties of scintillation like emission, re-emission, light yield, etc can be defined and modified in the cards, too.

The simulation output is given as two root TTrees. The first TTree includes the true Monte-Carlo (MC) information: type of particle, energy, position, time, direction, energy deposited by volume, etc. Using the true MC, the acquisition algorithms are simulated and the second TTree, filled with information on collected charges and times, using the same format as for the experimental data.

The simulation of the STEREO detector has been used for a dedicated study of the development of the radioactive source calibration system and a first look at the selection

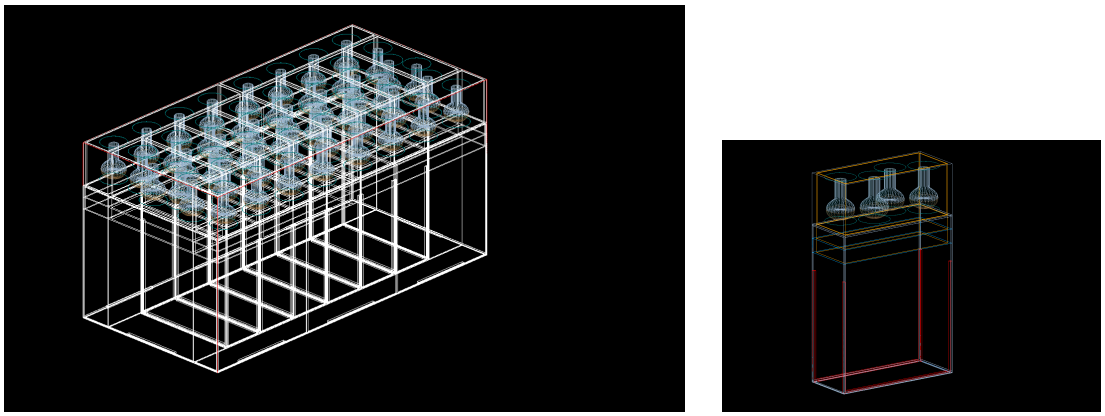

(a) Stereo Target and GC simulation (b) Target cell in STEREO

Figure 3.21: (a) The STEREO Geant4 simulation includes the description of the 6 cells plus GC, and the shielding. (b) Detailed description of the internal geometry of each cell, which includes the implementation of the reflective VM2000 sandwiches.

criteria and the discrimination of backgrounds. These studies are presented in Chapter 4 and Chapter 5.

3.12 The calibration system

Accurate knowledge of the detector response is a crucial parameter of any experiment. The goal in the STEREO experiment is to calibrate the energy response with an uncertainty below the 2% level. For such purpose, the scintillation response, the optical model, non uniformities, energy scale, and PMT gain need to be measured and characterized precisely.

The experiment will be calibrated using the radioactive neutron and gamma sources, and the LED monitoring system.

3.12.1 LED monitoring system

Light produced by 5 independents LED boxes is injected into the cells using optical fibers. The light is injected at 6 different points of the Gamma Catcher and three different vertical distances from the PMTs in each cell of the Target. The point is using these three different vertical positions to characterize and monitor the vertical dependence of the light collection. To calibrate the muon veto, light is injected in 12 different positions at the same vertical position (the vertical dependence is meaningless here).

The LED system is composed of one LED board that controls five remote LED boxes (see figure 3.22). In each LED box there are 6 LED (5 blue +1 UV), 6 LED drivers, and 1 temperature sensor. The advantage of using LEDs is the linearity of the light intensity

with the applied voltage, their fast on-off switching and their stability with time.

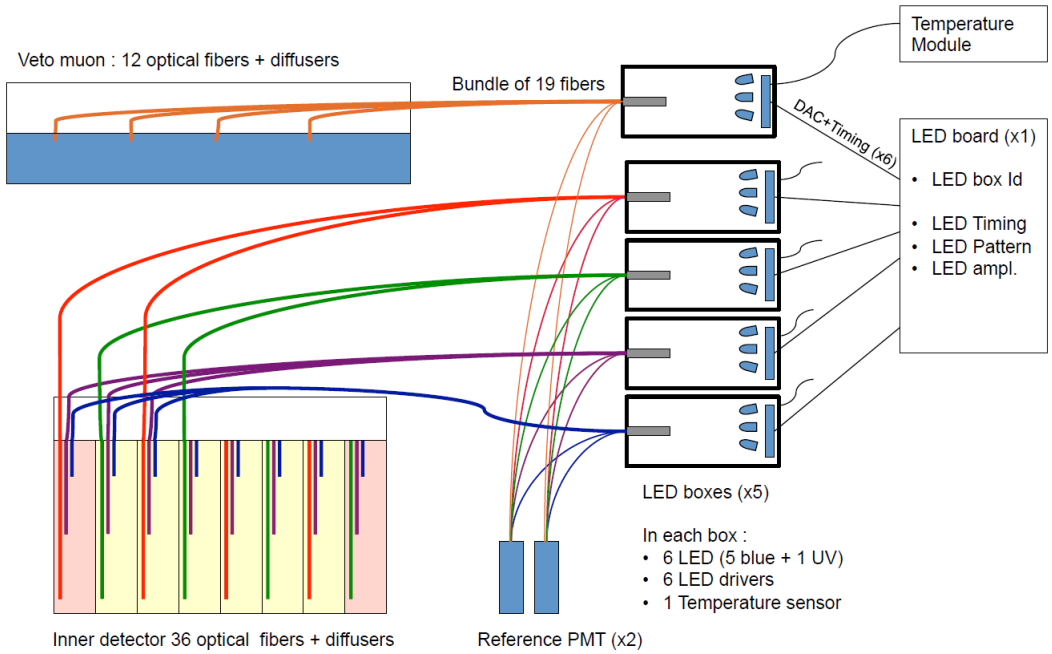

Figure 3.22: The LED calibration system of the STEREO experiment. Optical fibers are used to inject light at three different vertical distances of the PMTs in each cell and at 6 different points of Gamma Catcher. To calibrate the muon veto, light is injected at the same vertical position in 12 different positions. One LED board control five remote LED boxes.

The main role of the LED system is the precise and continuous measuring and monitoring of the PMTs' gains via the SPE method (see section 3.8.3). This allows for a detailed detector response interpolation between two full calibrations of the experiment.

3.12.2 The radioactive source calibration system

The source calibration system has to characterize the energy scale response as well as the neutron capture efficiency in each cell independently. In addition, the system must enable the characterization of the detector response in a broader sense (non-uniformities, non-linearities, etc).

To calibrate the energy scale in each cell, radioactive gamma sources are used: ^{22}Ge (0.511 MeV), ^{137}Cs (0.67 MeV), ^{54}Mn (0.83 MeV), ^{60}Co (1.17+1.33 MeV) and AmBe (4.4 MeV). In addition, neutron captures on H and Fe yield gammas of 2.2 and 7.6 MeV respectively and allow to cover most of the energy range of the electron antineutrino reactor spectrum. To assess the neutron capture efficiency, an AmBe neutron source is used.

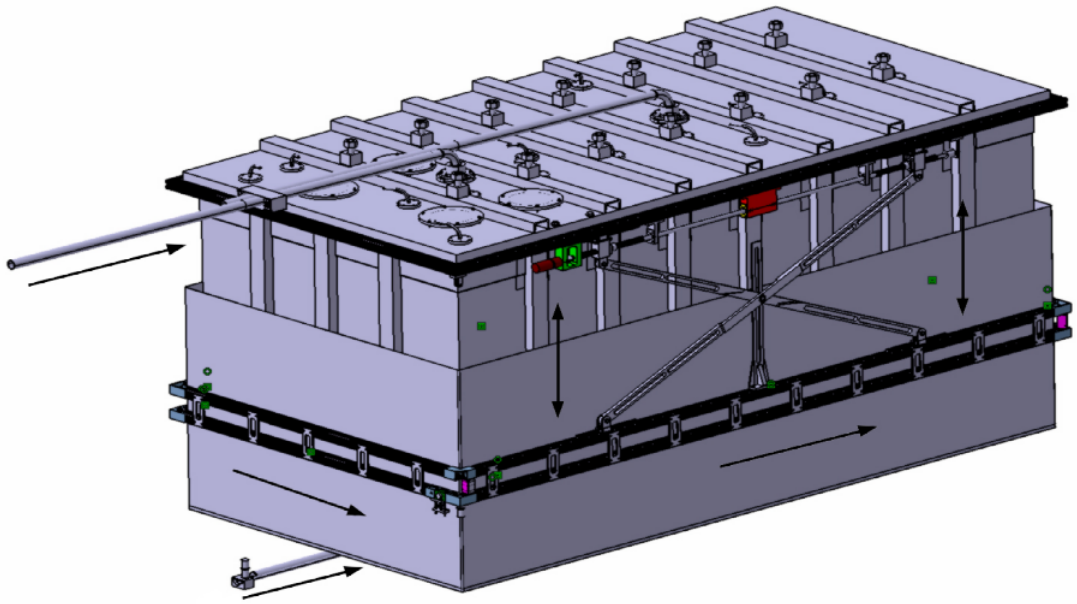

Figure 3.23: The source calibration system of the STEREO experiment. A subsystem to move the gamma sources around the entire detector as well as in the vertical axis has been implemented. In this way the energy scale and non-uniformities in each cell are calibrated. A second system allows to introduce in one central and one border cell a neutron source. This system is devoted to measure the neutron capture efficiency at different positions on the cell, but can also be used to calibrate the energy scale in that cell. Finally a third system is used to move a neutron source under the detector, so that the neutron capture efficiency can be inter-calibrated between all the cells.

The calibration system consists of three subsystems. To calibrate the energy scale in each cell, a first subsystem allows to move the gamma sources around the detector. A collimation device could also be used in order to characterize the vertical dependence of the response. It consists of a scintillating crystal (LYSO) with a PMT and a source of ^{22}Na or ^{68}Ge. In order to measure the neutron capture efficiency at different positions of the cell, a second subsystem is used to introduce an AmBe source in three different cells (two central cells and one border cell). Finally, a third subsystem allows to move an AmBe neutron source under the detector, which inter-calibrates the neutron capture efficiency between all the cells. The details of the development of the source calibration system are presented in the Chapter 4.

3.13 Internal shielding

Given the gamma and neutron ambiance present at the ILL, different shieldings enclose the detector. Starting from the inner part, the first component that can be considered as an (active) shielding is the Gamma Catcher. Even though its main goal is to recover

the escaping gammas of the Target, it can be also used to reject background events (see Chapter 5). If fast neutrons go through the passive shielding, these will be slowed down in the Gamma Catcher and most of them will be captured on H, giving a signal below the threshold of the delayed signal. Covering the vessel that contains the Target and Gamma Catcher, plates of 1.5 mm of mu-metal surround the detector in order to deflect the magnetic lines coming from the IN20 magnet.

Continuing to the outermost layers of shielding, 20 cm of borated polyethylene is used to slow down fast neutrons. The next layer consists in 10 cm of lead, the purpose being to stop gammas coming from the outside. Additional Pb, PE and B4C layers of shielding have been put in place on the walls of the STEREO casemate, as discussed in section 3.6.1.

3.14 Muon veto

A muon detector is placed on the top of the experiment. The function of this detector is to tag the passage of muons through their Cerenkov emission in water in order to stop the acquisition and thus reject background originated by these events. The detector consists in a tank of $396 \times 240 \times 25.9$ cm^3 filled with purified water loaded with fluorescent 4-Methylumbelliferone (4MU) at 6 ppm and read out by an array of 20 PMTs (see figure 3.24). A prototype has been built at the LPSC, the results on the prototype show that the use of 4MU improves the detection efficiency, increasing it up to 98.6% with 4MU instead of 96.8% without 4MU [184]. It's been tested extensively, and has been used to test the electronics and the data acquisition chain. It was moved to the ILL in July 2016.

3.15 STEREO's sensitivity to light sterile neutrinos

STEREO will probe the oscillation probability dependence on the neutrino energy and the baseline (relation 2.4.3). By using a segmented detector, the energy spectrum can be measured at different distances. Then, a bin-to-bin comparison between the non-oscillated and the oscillated spectrum can be done [185], including all the systematic uncertainties.

The number of expected neutrinos to be detected per day is about 400. The detector efficiency is estimated to be 63% through Geant4 simulations. It's dominated by the delayed neutron detection efficiency. The energy resolution is expected to be 12% at 2 MeV, which is dominated at low energy by the energy leaks of the 511 keV gammas from the positron annihilation. To evaluate the detector sensitivity to possible oscillation into a light sterile neutrino state (see Figure 3.25), the following assumptions have been used:

Figure 3.24: The muon veto in the Ariane Hall at the LPSC. Its dimensions are $396 \times 240 \times 25.9$ cm^3 and it's filled with purified water.

- ✓ An energy resolution of 12% at 2 MeV (taken from detailed Geant4 simulations)
- ✓ Six reactor cycles are considered, which gives 300 days of data taking
- ✓ A signal-to-background ratio of 1.5
- ✓ An uncertainty of 2% on the energy scale calibration
- ✓ A threshold on the visible energy of 2 MeV for the prompt signal and 5 MeV for the delayed signal
- ✓ A resolution in the vertex reconstruction of 25 cm
- ✓ An uncertainty of correlated and uncorrelated of of 3.7% and 1.7% respectively in the spectrum normalization
- ✓ A distance between the center of the detector and the center of the reactor core of 10 m

With these assumptions, STEREO's sensitivity to the RAA best fit values allows to confirm or exclude them at more than 5 σ, and exlude a good part of the parameter space around the RAA favored area (see Figure 3.25).

The sensitivity of STEREO to higher values of Δm^2 is dominated by the energy resolution and the background assumptions. On the other hand the sensitivity to constrain small values of $\sin^2 2\theta$ is dominated by the statistics. The cell to cell comparison reduces the detector systematic uncertainties and the reactor spectrum shape uncertainty. A detailed study of the effects of the different assumptions on the detector sensitivity can be found in the PhD thesis of A. Collin [186].

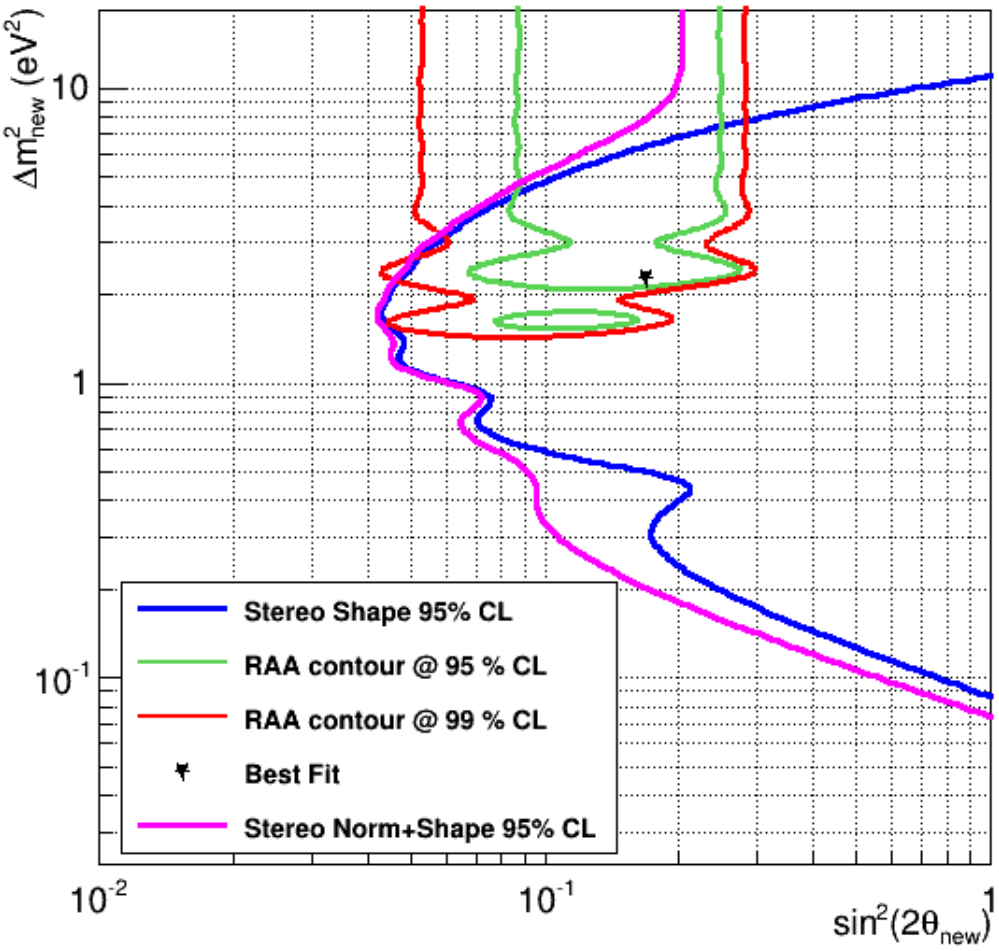

Figure 3.25: Exclusion contours for STEREO at 95 % confidence level. Most of the reactor antineutrino anomaly will be covered by STEREO, in particular the best parameters region at more than 5 sigma.

- Chapter 4 -

Calibration of the STEREO experiment

4.1 Introduction

STEREO's strategy to search for a light sterile neutrino consists in comparing the measured antineutrino energy spectrum and number of signal events among the 6 Target cells. This imposes calibrating each cell independently, in spite of the possible gamma escapes and light leaks from one cell to its neighbors. Also the measurement of the energy of the positron produced in the IBD process is of paramount importance to asses the energy dependence of the oscillation probability. Finally, knowing the neutron capture efficiency is necessary to constrain the oscillation probability with a determination of the emitted flux of antineutrinos. The STEREO physics requirements imposes to know the energy scale better than 2% and the neutron capture efficiency with an uncertainty better than ∼3-4% [187]. In a liquid scintillator, there are two major sources of energy non-linearity. The first one is the intrinsic non-linearity of the liquid, which includes quenching of the scintillation light at low energy and Cerenkov light at higher energy, the dominant effect being the first. The second source of energy non-linearity is introduced by the electronics. This effect has been measured expected to be under the 1% level [188]. Neutron capture efficiency exhibits a strong position dependence due to gamma escapes. This dependence needs to be mapped carefully.

In this chapter, a dedicated simulation study based on the STEREO Geant4 software is presented. It describes the development of the source calibration system, and the ways it can be used to characterize:

- the absolute energy scale

- the liquid scintillator energy non-linearity

- the detector response non-uniformity
- light leaks from one cell to its neighbors
- the neutron capture efficiency

There is also a section on how to use the information provided by the calibration system to reconstruct the deposited energy. To accurately address the study of these parameters, the calibration system must deploy several gamma and neutron sources at different positions in order to calibrate each target cell and Gamma Catcher independently.

The radioactive source calibration system has to provide a good enough knowledge of the detector response that can be translated into a detector model, which in our case will be based on Geant4 simulations. Here is a non-exhaustive list of requirements:

1. Characterize the energy scale response in each cell independently over the whole energy range of the $\overline{\nu_e}$'s energy spectrum (0-8 MeV). Means to study the detector energy non-linearity should be provided.
2. Measure the neutron capture time and assess the absolute neutron capture efficiency at the 3-4% level
3. Allow the neutron capture efficiency inter-calibration among the target detector cells
4. Provide information to the characterization of the PSD by using fast neutrons
5. Enable the characterization of the cell non-uniformity in order to know accurately the detector response
6. The calibration system should be as less intrusive as possible in the active volume, to avoid reducing the amount of active material and degrading the light collection. A system that can be automatized would be a bonus, and would guarantee a repeatability of the positioning of the calibration sources.

How would we go about calibrating the energy scale and reconstructing the deposited energy? As was already said in section 3.7.2, the liquid scintillator response depends on the energy and particle type. Since we have energy non-linearity in the liquid scintillator and since STEREO's prompt signal is the visible energy generated by a positron plus the two 511 keV gammas from its annihilation, the energy scale should be characterized with positrons of different energies. Unfortunately, there are no available β sources that could be used for such calibration, since the positrons or electrons would be stopped in the system that is needed to introduce such a source (in our case, this system is composed of an aluminum capsule and a steel tube, like in figure 4.4) inside the LS. Fortunately, as we saw in section 3.7.1, gamma sources are in a way equivalent to electron sources, since they generate electrons with the known energy spectrum via their interaction with

the LS atoms. Hence, multiple gamma sources at different energies can be used to study the detector response to tune the Monte-Carlo simulations. However, the interaction of gammas in the LS is not exactly equivalent to that of electrons. Gammas convert in the LS in distances much longer ($\sim$ 17 cm for 1 MeV γ's) than electrons ($\sim$ mm), which means that the light generation and collection is different. However, it is worth noting that simulations are needed in order to relate the calibration with gammas to the detector response to positrons.

Given the non-linearity of the detector energy response, we propose to reconstruct a visible energy from the data in a linear way by using a single calibration point from a gamma source, and include the non-linearities in the detector response model that will be applied to theoretical predictions of the $\overline{\nu_e}$ spectrum in order to compare them to data. These detector response model will be extracted from the MC simulations. These simulations will be anchored to several calibration points in order to accurately reproduce all the calibration measurements, concerning both the energy scale and the neutron capture efficiency. Indeed, once simulations have been tuned to reproduce the calibration data, the visible energy spectrum is obtained by convolving the theoretical prediction of the $\overline{\nu_e}$'s spectrum with the simulated detector response model to positrons.

4.2 Light leaks calibration

Although the goal of the STEREO experiment is to compare the energy spectra of the different Target cells, complete independence among the cells is hard to attain and interaction in one cell will often result in some light being collected in other cells. This is both because energy can leak to neighboring cells via Compton scattering, and because completely optical separation is challenging and some light emitted in one cell often leaks to the near cells.

As was already said, the implementation of the VM2000 sandwiches is not possible on the whole surface of the detector cells. Then, the cells are not completely optically separated. The amount of light going to the neighboring cells and Gamma Catcher needs to be measured in order to characterize the detector response.

In figure 4.1(top), the amount of light leaks to the neighboring cells for a ^{54}Mn gamma source deployed inside a given cell is shown. The charge collected in the cell where the source has been deployed is about 95% of the total charge collected in the Target, which means that around 5% of the light emitted in the cell leaks to neighboring cells. The tail on the left side of the distribution is originated by Compton events. By requiring a veto ($\mathrm{Qtot_{cell}}/\mathrm{Qtot_{Target}} \gtrsim 0.93$), most of these events can be removed, which is shown on figure

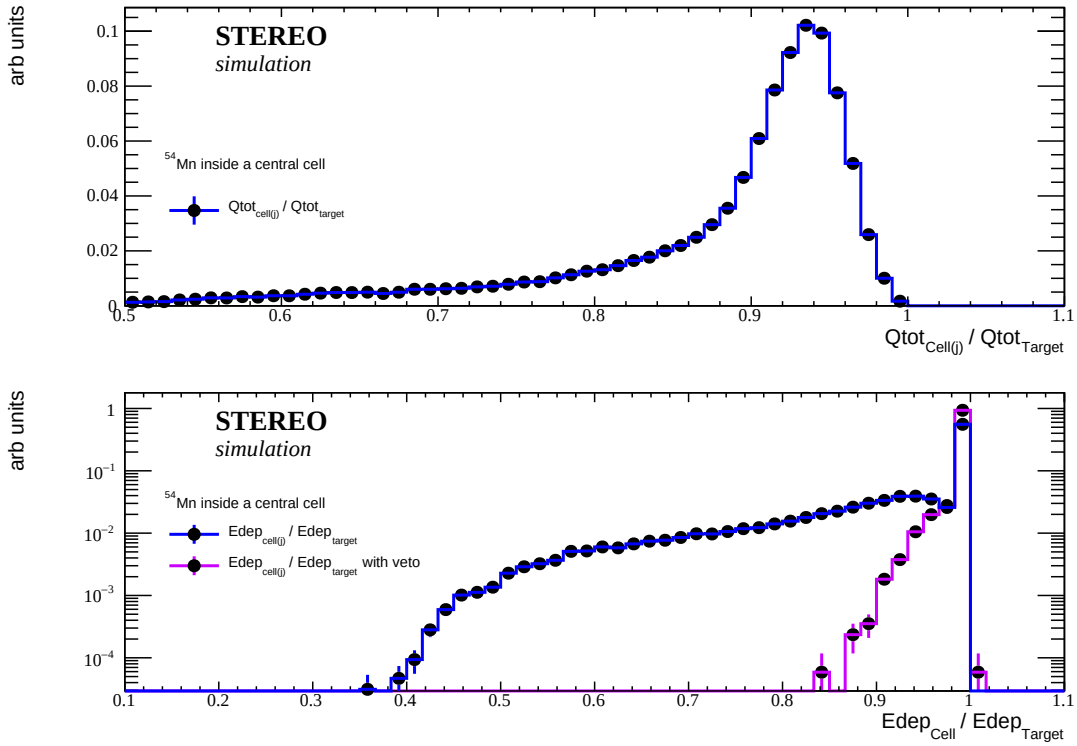

Figure 4.1: (top) Light leaks from the cell 4 to the rest of the target using a ^{54}Mn gamma source inside a cell (placed in the center of the cell). The charge collected in the cell where the source has been deployed is about 95% of the total charge collected in the Target, which means that around 5% of the light emitted in the cell leaks to neighboring cells. On the left tail of the distribution, light leaks and energy leaks are combined (bottom) The amount of energy deposited in the cell predicted by the Monte-Carlo. The blue line shows the amount of energy deposited in the cell for all the events, while the violet line shows the events in which a veto has been imposed. The amount of total light leak is requested to be smaller than 5%. This removes almost all the Compton events.

4.1(bottom). Thus, the light leak from one cell to its neighboring cells can be measured by taking into account the Gaussian part of the distribution.

In figure 4.2, the amount of light leaks to the neighboring cells is shown. The veto discussed above is applied in order to remove Compton events. In this way the amount of deposited energy in the neighboring cells is reduced to only a few keV, which is completely negligible compared with a total deposited energy of the order of MeV.

The amount of light leaks to the neighboring cells has been estimated to be about 5%. Nevertheless, this is an important parameter to be tuned once the detector is operating. The amount of light leak will be affected by the wall properties as the reflectivity, the absorption and transmission.

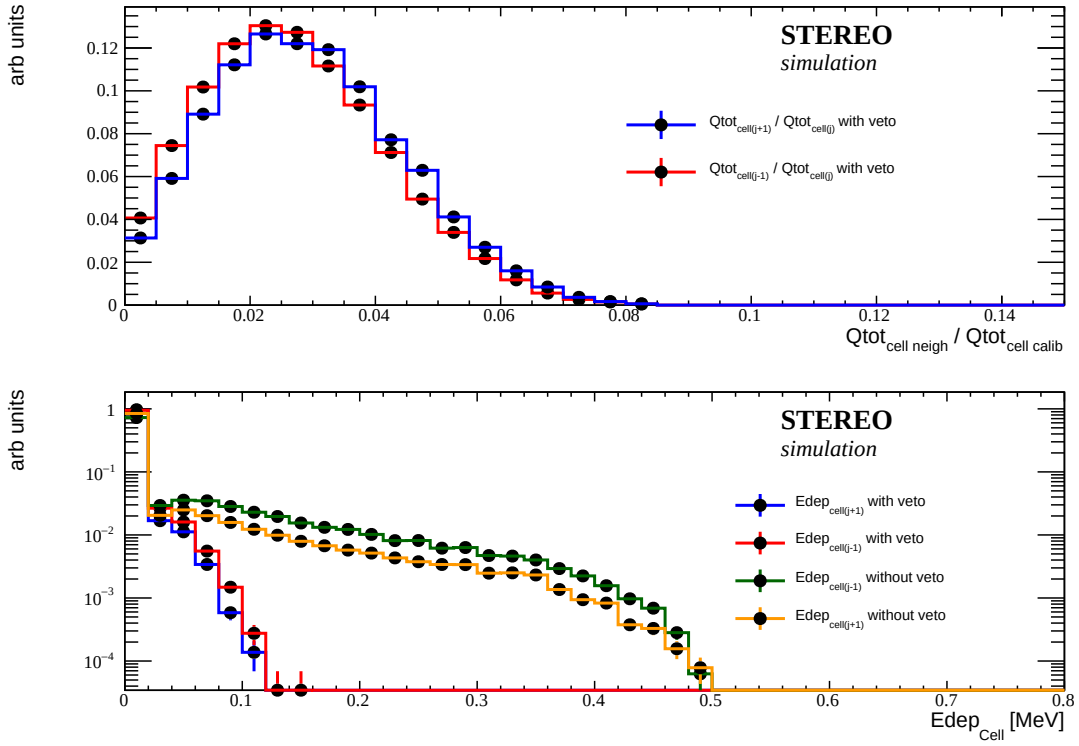

Figure 4.2: (top) Light leaks from the cell under calibration to its neighboring cells using ^{54}Mn inside a cell. In order to separate light leaks from energy leaks, a veto is used, which consists in demand more than 90% of light collected in the Target to be in cell. The amount of light slightly differs from cell$_{j-1}$ to cell$_{j+1}$ because the calibration tubes are not centered in the calibration cell. (bottom) The amount of energy deposited in the neighboring cells with and without vetoes. Using a veto of more than 90% of light collected in the calibration cell, the mean leaked energy goes from ∼290 keV to ∼3 keV.

The calibration tubes are only present in three cells, so the light leaks need to be measured using the external calibration system in the remaining cells. Simulations showed that this procedure can be performed with the external system by using the same vetoes.

4.3 Energy scale calibration

The goal of the energy scale calibration is to translate the charge collected at the PMTs into energy. In order to do so, we need to precisely measure the PMTs response to well known deposits of energy. Radioactive sources with unique, narrow, well known gamma lines will be used for that. At energies below 2 MeV, a variety of sources can be found in commercial catalogs. The situation is much more complicated regarding gamma sources at higher energy, above 2 MeV, where only AmBe is commercially available. The AmBe

sources are neutron sources, which often emit also a 4.4 MeV gamma. The problem to find gamma sources at high energy resides in the very short lifetime of radioisotopes producing high energy gammas. In the best of the cases it is only a few seconds or a few hours, e.g. ^{24}Na (two gammas: 1.4 and 2.8 MeV) has a half life of only 15 hours, ^{16}Ni (6.1 MeV) has a half life of only 7 seconds.

Using neutron sources, gammas can be induced by the excitation of some nucleus through thermal neutron capture. In the liquid scintillator of the STEREO Target most of the neutrons are captured on Gd, and a small fraction on H. Gammas thus produced can be also used to calibrate the energy scale. The gamma sources initially considered for the calibration of the energy scale are presented in the table 4.1.

Source	Yield	Energy (MeV)	Half life
^{68}Ge	1.8	0.511×2	270 d
^{22}Na	1.8	0.511×2 + 1.27	2.6 y
^{137}Cs	0.85	0.667	30 y
^{54}Mn	1	0.83	312 d
^{88}Y	0.99	0.88 + 1.8	107 d
^{65}Zn	0.5	1.12	244 d
^{60}Co	0.99	1.17 + 1.33	5.27 y
Am-Be	6E-5	4.44 + n	432 y
^{252}Cf	0.12	2.2(n-H) 7.6(n-Fe)	2.7 y

Table 4.1: Radioactive neutron and gamma sources initially considered to calibrate the energy scale in STEREO. Below 2 MeV, plenty of gamma sources are available in the catalogs, however above 2 MeV, only AmBe is available, which provides a 4.4 MeV gamma plus a fast neutron. ^{252}Cf will be used to induce neutron captures on H and Fe. The yield is the number of gammas or neutrons emitted per disintegration, in some cases it is larger than 1 (several gammas emitted at the same time) and in others it is lower than one (a disintegration can occur without the emission of gammas).

4.3.1 Overview of the calibration procedure

As seen in section 3.8.2, the SPE method allows to calibrate the gain of the PMTs and hence convert the collected charges to number of observed photoelectrons. We now want to translate the number of observed photoelectrons into the deposited energy. For that, we place a gamma source either inside or outside the liquid scintillator. We then fit the p.e. distribution thus obtained. Then, the mean deposited energy of gamma rays within the liquid scintillator of the cell in question is computed by using the Monte-Carlo through the STEREO Geant4 simulation. The ratio of the p.e. peak mean and the true deposited

energy gives us the conversion factor, the "calibration constant".

Gammas with energies above 0.1 MeV interact within the liquid scintillator mostly by Compton. Therefore some gammas deposit only a fraction of its energy in the LS of the calibration cell. In order to remove Compton events, we apply vetoes asking for no energy leaks in the neighboring cells and Gamma Catcher. In these conditions the peak of the photoelectrons distribution corresponds to the full energy peak.

The calibration process can be summarized as follows:

1. Deploy a gamma source outside or "inside" the liquid scintillator
2. Apply vetoes of no energy leaks in the GC and neighboring cells in order to remove Compton events
3. Perform a Gaussian fit of the p.e. distribution around peak in the distribution of $N_{p.e.}$, and extract the position of the peak $N_{p.e.}^{peak}$
4. Compute through Monte-Carlo simulations the mean deposited energy by the gamma rays $< E_{\gamma}^{MC} >$ around the full energy peak ($\pm$10 p.e.)
5. Compute the calibration constant for a given gamma energy as: $C_{\gamma} = \frac{< E_{\gamma}^{MC} >}{N_{p.e.}^{peak}}$

Figure 4.3 shows the p.e. distribution produced by a ^{137}Cs gamma source when it is placed inside the liquid scintillator. Vetoes of no energy leaks in the neighboring cells and Gamma Catcher are applied. In this way the peak of the distribution is found in 151 p.e., while the deposited energy around this peak ($\pm$ 15 p.e) is found to be 0.652 MeV in the Monte-Carlo simulations. Gammas emitted from a ^{137}Cs source have an energy of 0.667 MeV. However, a small fraction of this energy can be deposited in a neighboring cell or in non-scintillating materials.

4.3.2 Position of the source

The radioactive sources used to calibrate the energy scale or the neutron capture efficiency, can in principle be placed either inside or outside the liquid scintillator. This is possible because the distance of conversion for gammas of a few MeV in the liquid scintillator is of order of $\sim$20 cm. However, this distance depends on the gamma energy, and is smaller for lower energy gammas. In the following, the advantages and disadvantages of each configuration are described.

4.3.2.1 Internal source

The most common and intuitive way to calibrate the energy scale in a detector like STEREO consists in deploying gamma sources inside the liquid scintillator. In this way

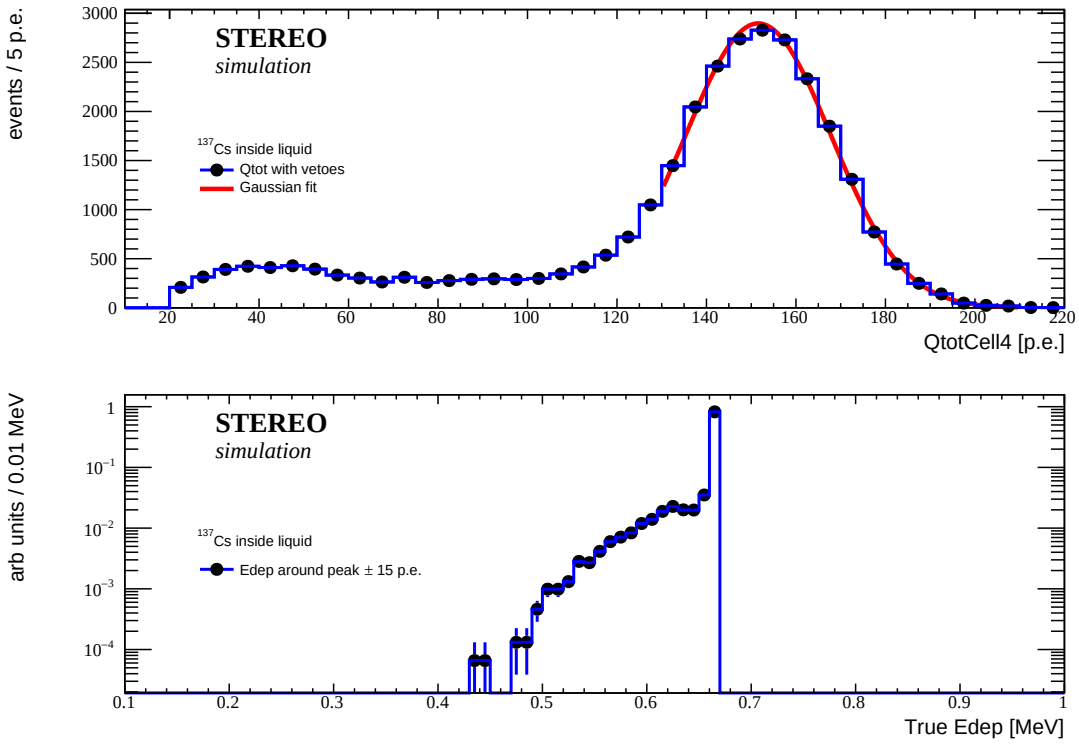

Figure 4.3: ^{137}Cs inside cell 4. The source is deployed manually inside the liquid scintillator using a tube placed inside the cell. To remove Compton events vetoes of no energy leaks in the neighboring cells and Gamma Catcher are applied. The mean energy deposited by gammas around the peak is found using the Monte-Carlo. The mean of the distribution is found by fitting the distribution with a Gaussian function. For this source the peak is found in 151.6±0.2 p.e., while the deposited energy around the peak ± 15 p.e is found 0.652 MeV

gamma rays can "directly" interact within the liquid. However, this is not entirely true, because a mechanical system is needed to introduce the source inside the liquid. Then, gammas need to go through the materials of this system before reaching the liquid scintillator. In STEREO, this mechanical system consist in steel tubes placed inside the cells. An aluminum capsule is used to introduce and move the sources along the tubes. This system is shown in the figure 4.4. The use of steel ensures the compatibility of materials with the liquid scintillator.

The calibration tubes have an internal and external diameter of 18.1 mm and 21.3 mm respectively. On the other hand, the aluminum capsule is 41 mm height and has a radius of about 8 mm. The radioactive sources considered for the STEREO calibration are encapsulated in very compact containers. In general diameters lower than 8 mm and heights lower than 10 mm. Thus, all the sources can be manually introduced inside the cells by using this system without any problem.

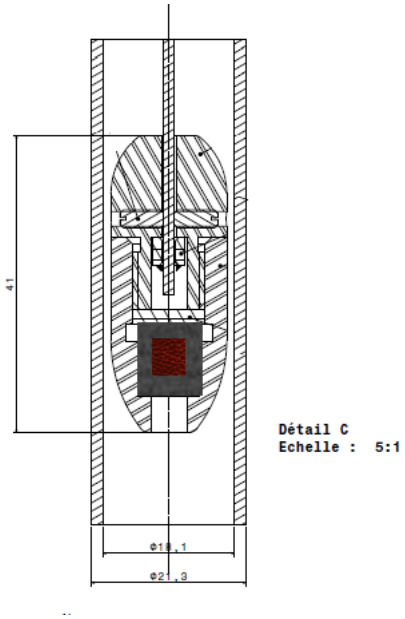

Figure 4.4: Device to deploy calibration sources inside cells. In this configuration, gammas or neutrons need to go through the envelope of the source, the aluminum device and the steel tube until they reach the liquid scintillator. For gammas of high energy, this does not represent any problem, but the device should be carefully simulated in order to reproduce accurately the experimental results.

The automated implementation of such a system in each target cell and gamma catcher is complicated. Nevertheless, this system is ideal during special calibration runs, especially when the reactor is OFF. This system has the advantage of providing direct access to the dependence of detector response with vertical position of interactions. It is an important parameter that needs to be characterized. Furthermore, as we will see in section 4.6.2 the absolute neutron capture efficiency can be directly measured inside the liquid scintillator, which is much more difficult to assess using an external system.

Figure 4.5 shows the p.e. distribution obtained when a ^{54}Mn gamma source is simulated inside the LS in a central cell (4). The violet histogram corresponds to the total charge in this cell without any condition. The blue histogram is obtained when vetoes of no energy leaks in the neighboring cells and Gamma Catcher are applied. These vetoes consist in asking for a number of p.e. in the neighboring cells and Gamma Catcher lower than the amount of light that can be leaked from the calibration cell.

On the negative side, this system is not desirable for radioactive sources where several particles are emitted at the same time and where the rates and energies are not well known. This is the case of the AmBe source (n+γ). The gamma energy spectrum is contaminated by the (unknown) light emitted by protons recoiling from neutron interactions. The neutron energy spectrum is not well known and depends on the way the Am and Be

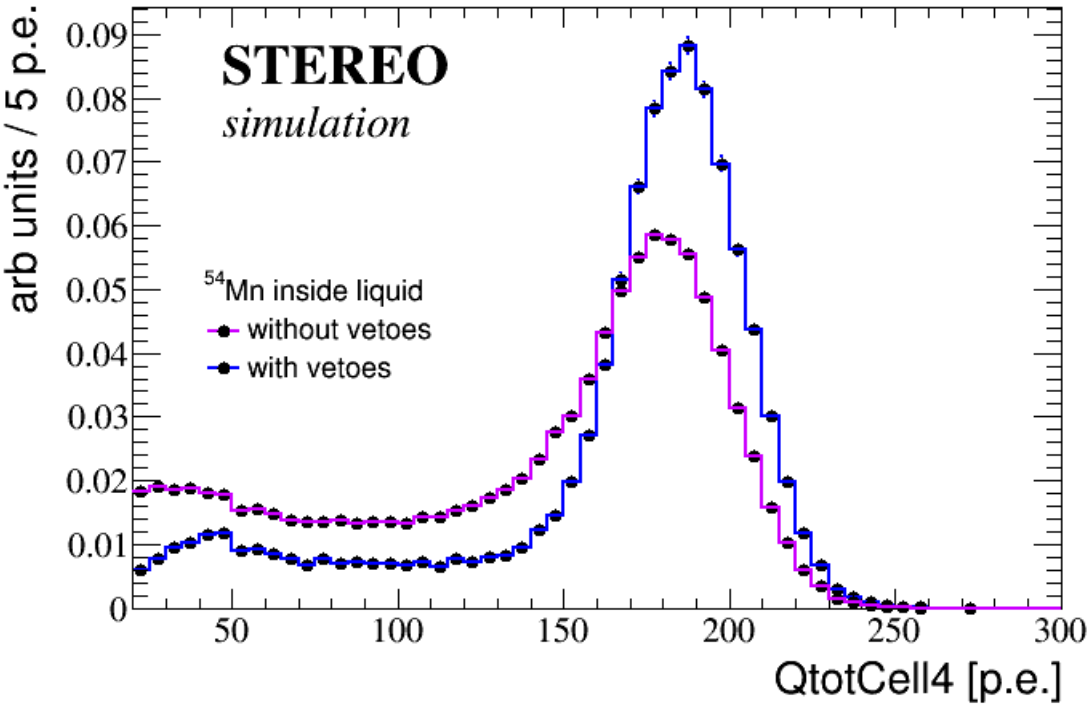

Figure 4.5: Source of ^{54}Mn placed inside cell 4. Without vetoes, Compton events are included in the photoeletron distribution; to remove these events vetoes are used. These vetoes consist of requiring that there are no energy leaks in the neighboring cells and Gamma Catcher

are packed together. Therefore, it is not possible to use AmBe to calibrate the energy response inside these calibration tubes. On the other hand (see section 4.6.1.1), AmBe sources can be used to calibrate the neutron capture efficiency. The 4.4 MeV gamma can be used as prompt signal because it allows to identify the emission of neutron.

4.3.2.2 External source

From the mechanical point of view, an external system capable to move radioactive sources around the detector is much simpler. Moreover, the automation of such a system will be "easier". On the negative side, in this configuration gammas need to traverse the stainless steel vessel, the Gamma Catcher and the acrylics before reaching the target cells liquid scintillator.

For low energy gammas, surviving the voyage through all this material budget is not likely: More than half are lost just due to the solid angle, others are lost in the stainless steel vessel, the acrylics or the Gamma Catcher. Only a small fraction reach the liquid scintillator of the target cells. The fraction of gammas reaching the target cells has been evaluated using simulation and varies from 0.3% to 3% depending on the gamma energy.

Thus, much more intense gamma sources are needed to calibrate the detector in this configuration.

To extract the full energy peak in one target cell, the Gamma Catcher can be used as veto. Requesting no energy deposited in the Gamma Catcher is equivalent to putting the source just outside the acrylic of the target. Gammas arriving to the target without interacting in the Gamma Catcher will deposit most of their energy in the liquid scintillator of the target cells. To avoid energy leaks, once selected the calibration cell, the condition of no energy leaks in neighboring cells and Gamma Catcher can be imposed. These vetoes are defined by the amount of light leaking to the neighboring cells and Gamma Catcher. As was already shown, the amount of light leaks is about 5%, so the vetoes consist in asking less than ∼5% of charge in each neighboring cell. Since the light leaks to the Gamma Catcher is almost negligible, the veto in the Gamma Catcher consists in asking for less than ∼10 p.e. in each side of the Gamma Catcher. Figure 4.6 shows the effect of these vetoes. Without the use of the Gamma Catcher, the extraction of the full energy peak would be very hard.

An additional advantage of this configuration is that the AmBe neutron-gamma source can be used to calibrate the energy scale at 4.4 MeV. Two scenarios are possible in this configuration: The first one is produced when the 4.4 MeV gamma goes in the direction of the target and the fast neutron goes in the opposite direction. In this case, all the charge collected in the target cells and Gamma Catcher is due to only the gamma. The second scenario happens when the 4.4 MeV gamma and the fast neutron both go in the target's direction. In that case, neutrons are slowed down by the hydrogen of the Gamma Catcher. For neutrons of a typical commercial AmBe source, the distance traveled in the liquid scintillator before being captured has been evaluated to about 10 cm (see figure 4.24). Then, most of the time only the 4.4 MeV gamma will deposit energy in one target cell. In this way the 4.4 MeV gamma can be disentangled from the fast neutron which are always emitted at the same time.

4.3.3 Cell non-uniformity

The response of an ideal detector for a same particle of a given energy should be the same independently of the position of its interaction within the detector. However, this is not the case in a real detector because many factors contribute to having a different response according to the position of interaction. In the case of STEREO, light is collected by PMTs placed only on top of the detector cells. To improve the light collection, reflectors (VM2000 sandwiches) are glued to the acrylic walls. However, as the reflectivity of the walls cannot be 100%, some light will be lost here. Then, the amount of light collected

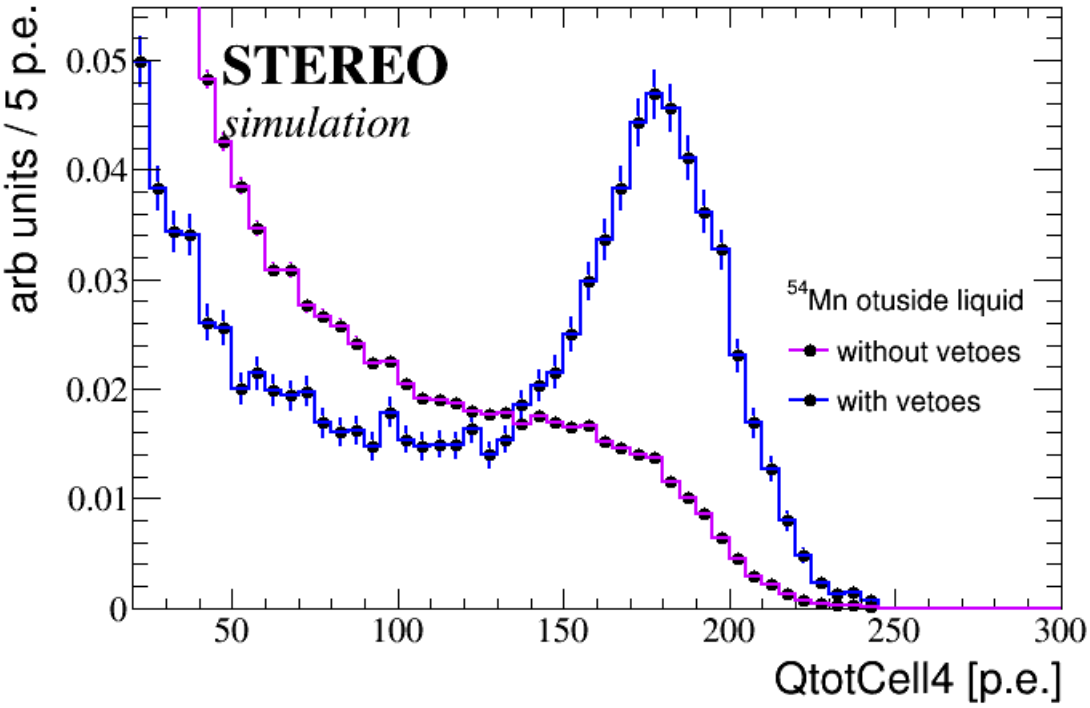

Figure 4.6: Source of ^{54}Mn deployed outside the steel vessel which contains the inner detector. It is placed just in face of the cell under calibration. Without vetoes (violet histogram), Compton events are included in the p.e. distribution. In order to remove them and make the full energy peak visible, vetoes must be used. The condition of no energy leaks in the neighboring cells and Gamma Catcher is imposed. Both histograms are normalized to one.

depends on the distance of the interaction to the PMTs. On the one hand, for events occurring at the bottom of the cells, light undergoes more reflections before arriving to the PMTs. On the other hand, in events produced close to the PMTs more light can arrive directly for detection.

The attenuation length of the liquid scintillator also contributes to this vertical non-uniformity response to the light collection. For events produced at the bottom of the cells, the mean distance traveled by light before reaching the PMTs is larger than the distance traveled by events produced at the top. However, given the small size of the cells (height of 917 mm), and taking into account that the attenuation length is expected to be larger than 5 m, this effect is less important. All these effects contribute to have a non-uniform response to the light collection in the target cells and Gamma Catcher.

To assess the vertical cell non-uniformity response, radioactive neutron and gamma sources will be used in order to measure and characterize this behavior. In cells where calibration tubes can be used, sources can be deployed at different vertical positions. In

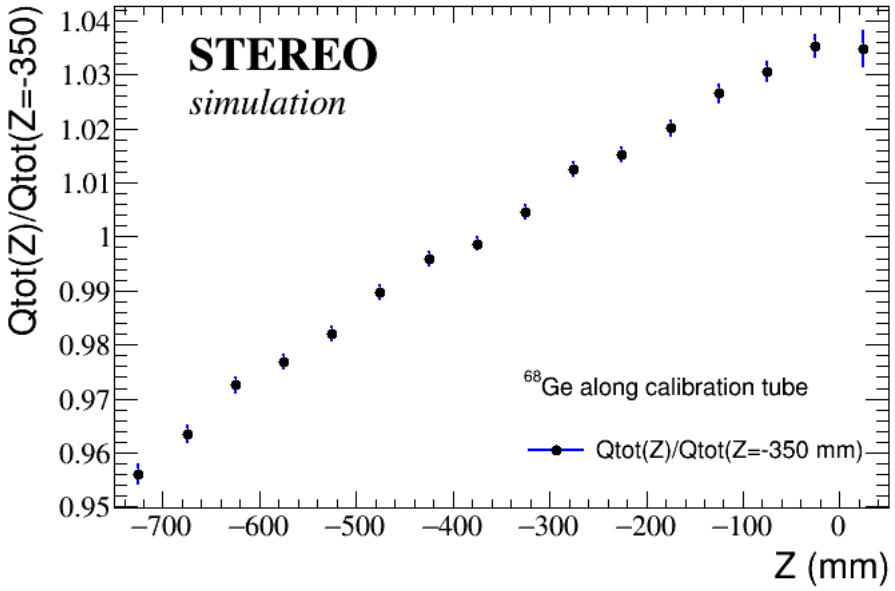

Figure 4.7: ^{68}Ge along calibration tube, the source can be moved in the vertical axis. The number of p.e. increase when the source closer of the PMTs. There is a difference of about 6% between the top and the bottom of the cell.

this way the response at different distances from the PMTs can be measured. Figure 4.7 shows the results of the simulation of a ^{68}Ge source. It is moved along the calibration tube. When the source is closer to the PMTs more light is collected, while when it is in the farthest position at the bottom of the cell, less light is collected. There is a difference of about 6% between the closest and the farthest position. In the cells where it is not possible to use the calibration tubes, this study could be performed by using the external calibration system with a collimation device. This study is presented in the next section.

Another factor of non-uniformity in the cell response is the energy leaks. Events produced in the center of the cells will deposit almost all their energy within the liquid scintillator. Nevertheless positrons produced by the IBD process at the edge of the cells will deposit only a fraction of their energy in the liquid scintillator and the rest in non-scintillating materials.

4.3.4 Collimation device

As we already said the study of the vertical cell non-uniformity response can be addressed with the manual calibration tubes system. However, only in three cells such measurements are possible. Moreover, the same vertical non-uniformity in the Gamma Catcher needs to be studied and characterized.

¿Can the external calibration system be used to measure this non-uniformity response

in the Gamma Catcher and in all the cells? In this configuration gammas are almost uniformly distributed along the vertical axis of the entire cell (by solid angle). Therefore just a global response of the cell can be obtained in this configuration. A solution to this issue might be to use a collimation system. To this end, two possibilities were studied in order to test the viability of such a system.

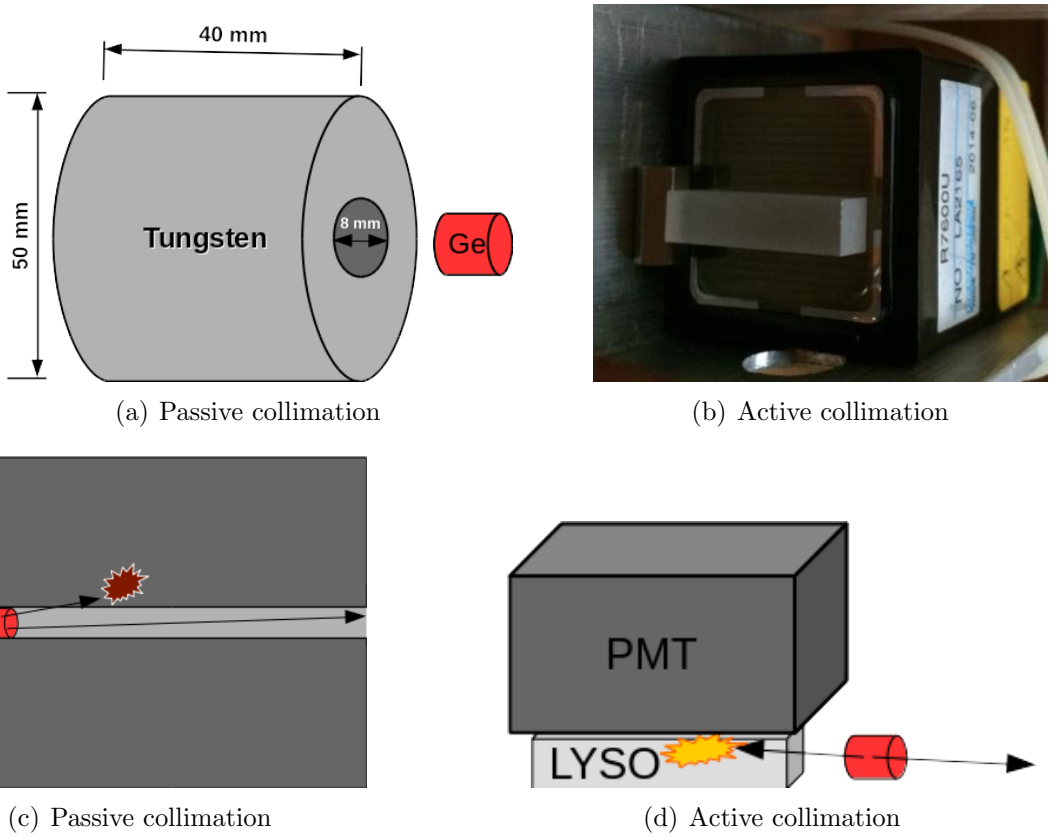

(a) Passive collimation

(b) Active collimation

(c) Passive collimation

(d) Active collimation

Figure 4.8: (a,c) The passive collimation using a tungsten cylinder with an orifice of 8 mm. (b,d) The active collimation system which is composed of a small crystal (LYSO) 5x5x20 mm plus a 1 inch hamamatsu PMT.

The first possibility consists in using a passive collimation (a cylinder with an orifice in the center made of a dense material, see figure 4.8). Several simulations were performed to evaluate the viability of this device using lead or tungsten. Results showed that this system could work for low energy gammas, since in high Z materials they interact mostly by the photoelectric effect. Higher energy gammas ($\gtrsim$1 MeV) interact mostly by Compton scattering, which greatly reduces the collimating power of the device. The optimal dimensions of the cylinder were found as follow: an inner radius of 4 mm, an external radius of 25 mm and a height of 4 cm. The height of the cylinder is limited by mechanical constraints given by the available space between the steel vessel and the shielding ($\sim$5 cm). For high energy gammas, for the reasons discussed above, larger dimensions are needed.

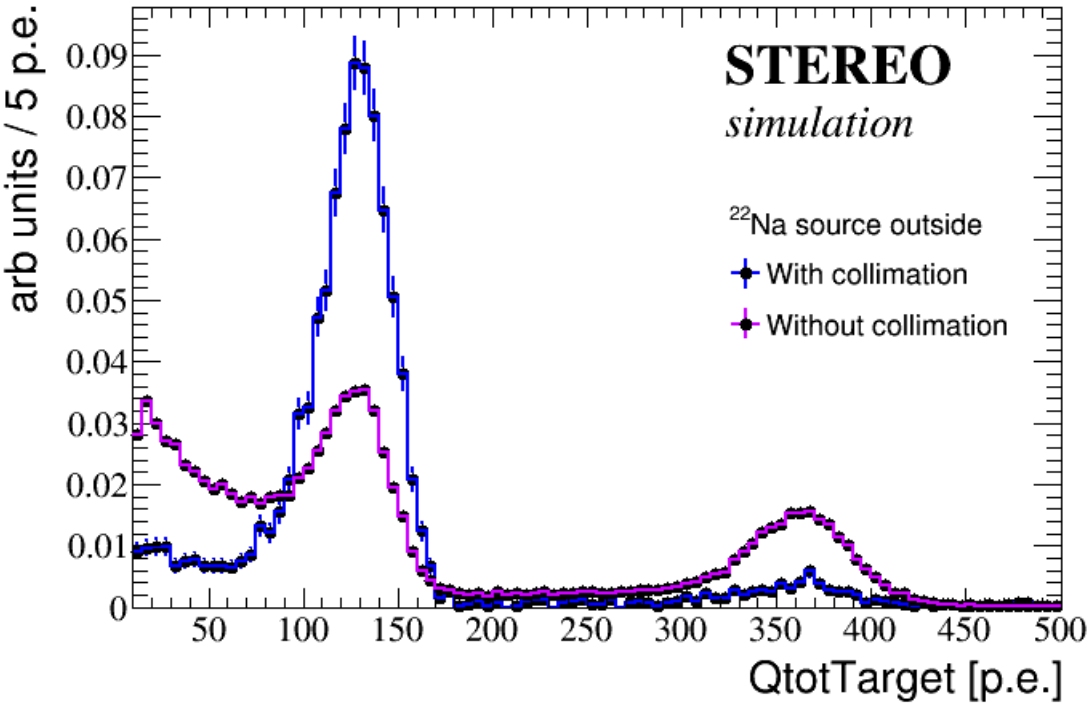

Figure 4.9: ^{22}Na outside the steel vessel. The violet histogram shows the p.e. distribution in the target, for events reconstructed in a cell with the standard vetoes of no energy deposited in the Gamma Catcher and neighboring cells. The distribution is dominated by the 1.27 MeV gamma. The blue histogram shows the effect of having the active collimation in addition to the standard vetoes. The detection of one 511 keV gamma in the crystal is imposed by asking an energy deposit between 0.2-0.52 MeV. Thus most of the 1.27 MeV gammas are suppressed.

The second possibility consists in use a source where gammas are emitted back-to-back. If one of these gammas is detected, the direction of the other one is known. Sources decaying by β^+ produce a positron that quickly annihilates within the source producing two 511 keV back-to-back gammas. A device to detect one of the gammas and trigger in coincidence was studied. It is composed of a small scintillating crystal (LYSO) of dimensions 5x5x20 mm^3, and a 1 inch hamamatsu PMT (see figure 4.8). Two sources were identified as possible candidates for this system: ^{22}Na and ^{68}Ge. These sources have large half life: 2.6 years for the sodium and 270 days for the germanium. Besides the positron, ^{22}Na also emits a 1.27 MeV gamma in coincidence, which could pollute the 511 keV calibration. Nevertheless, it is heavily suppressed with this system because the 1.27 MeV gamma's direction is uncorrelated to the 511 keV gammas, and it's thus disfavored by solid angle when a trigger in coincidence is imposed. On the contrary, this source could be used at the same time to calibrate the energy scale at 1.27 MeV by using the trigger in anti-coincidence.

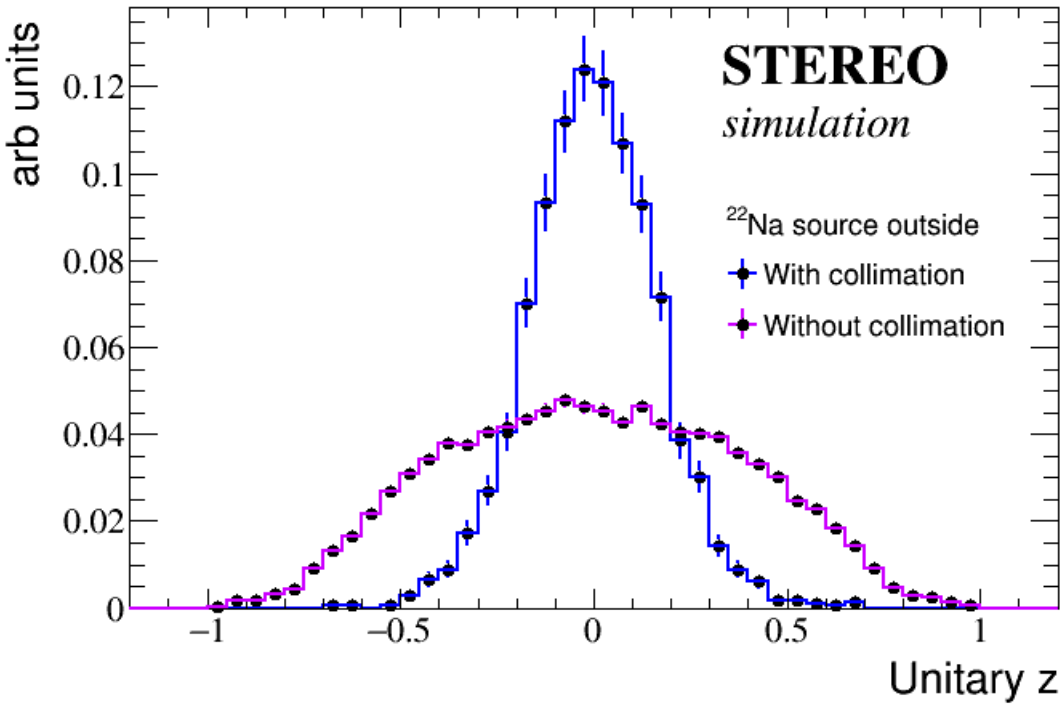

Figure 4.10: Vertical component of ^{22}Na 511 keV gammas direction vector with and without collimation. Without collimation 511 keV gammas are emitted isotropically in all directions, with the collimation most of the selected gammas are emitted orthogonal to the Gamma Catcher and target, and so the study of the light collection with the vertical position is possible with this device.

Simulations showed that the passive collimation (cylinder) requires a very intense ^{68}Ge source ($\sim$ 1.2 MBq). The probability that 511 keV gammas reach the target in this configuration is only 0.046%, and the background is expected to be much higher in this region. Thus at least a 1.2 MBq intensity was estimated under the assumption of having a S/B$\sim$ 1 and supposing a background rate in this region (0.3-0.7 MeV) of about 1 kHz. The active collimation on the other hand works either with ^{68}Ge or ^{22}Na, and activities of the order of $\sim$ 30 KBq are required. By using this system, the vertical response to the light collection in the cells and Gamma Catcher could be performed. Figure 4.9 shows the effect of the active collimation using the ^{22}Na source. By requiring the detection of one 511 keV gamma in the crystal and the other gamma in the target, the 1.27 MeV gamma is almost removed.

Gammas from the ^{22}Na source are emitted isotropically and arrive to the target and Gamma Catcher along the entire vertical axis. However, the detection of one the 511 keV gamma in the crystal implies that the direction of the other 511 keV gamma is constrained. Most of the gammas thus selected are emitted orthogonally to the Gamma Catcher and target cells. Figure 4.10 shows the effect on the vertical direction (z) of using this system.

Moreover, the same device can be used in anti-coincidence to have a clear peak with the 1.27 MeV gamma. Thus, the ^{22}Na source can be used to study the vertical response and the energy scale at two different energies.

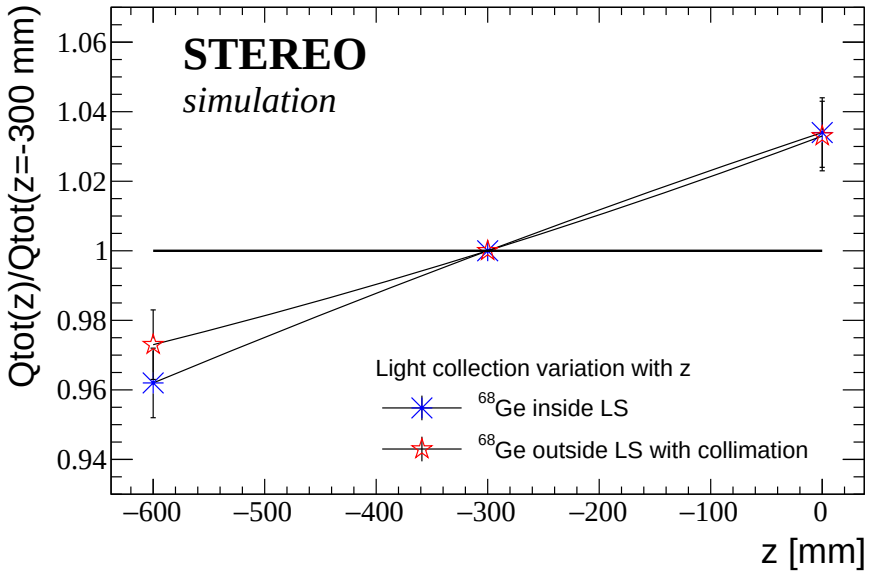

Figure 4.11: The effect of using a collimation system with the external system is presented. The active collimation could produce results that are comparable to introducing the source inside the LS.

Figure 4.11 shows the comparison between the vertical dependence obtained with a source inside the LS and with a source outside the LS coupled to the collimation device. Both solutions seem to be equivalent.

4.3.5 Gammas from n capture

Besides the use of commercial sources, gammas of 2.2 MeV are also produced by neutron captures on the hydrogen of the liquid scintillator. In addition, neutron captures on Gd produce a gamma cascade with a total energy of 8 MeV. The mean energy of these gammas is about 2 MeV, which is very close to the 2.2 MeV from hydrogen. Since the mean energy of the gammas is so close in both neutron captures the liquid scintillator's response will be nearly identical, and any non-linearity would come from the electronics.

Figure 4.12 shows the predicted energy non-linearity in absence of electronic non-linearity. The blue point corresponds to the visible energy to true deposited energy ratio for 2.2 MeV gammas from neutron captures on H. The red point corresponds to the ratio produced by gammas from neutron captures on Gd. Since the mean energy of these gammas is about 2 MeV, both calibration points are almost equivalent. The Monte Carlo

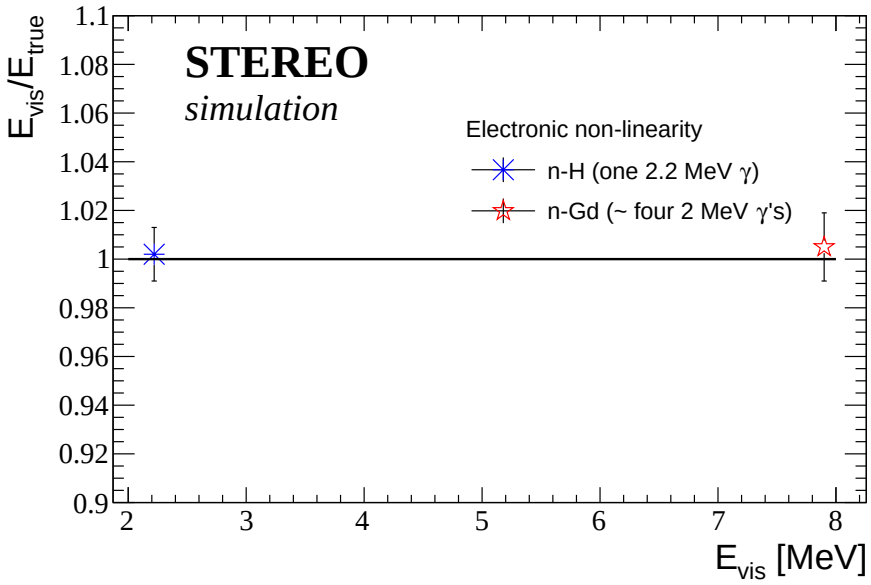

Figure 4.12: The Monte-Carlo prediction of energy non-linearity in absence of electronics non-linearity for the n-H and n-Gd. These two calibration points can be used to cross check the electronics non-linearity by comparing the visible energy to true deposited energy ratios. The mean value is found in 1.00 and 1.01 for n-H and n-Gd respectively

predicts the visible energy without electronic non-linearity effects, and both ratios are almost the same.

4.3.5.1 n-H

In the target liquid scintillator most of the neutron captures are produced on Gd. Only a few captures take place on H. The situation is completely different in the Gamma Catcher because its liquid scintillator is not loaded with Gd. Therefore most of the neutron captures happen on hydrogen, and induce a 2.2 MeV gamma.

Element	E_γ (keV)	σ_γ (barns)	Uncertainty (barns)	GC LS composition (%)	Expected number of n captures (%)
H	2223.2	**0.3326**	**0.0007**	63	99.4
	Total	**0.00351**	**0.00005**	37	0.6
C	1261.8	0.00124	0.00003	-	0.1
	3683.9	0.00122	0.00003	-	0.1
	4945.3	0.00261	0.00005	-	0.4

Table 4.2: The expected number of thermal neutron captures in the Gamma Catcher.

AmBe or ^{252}Cf are common neutron sources that can be used to calibrate the energy scale at 2.2 MeV. The external system is then the ideal choice to this calibration. The Gamma Catcher can be irradiated with neutrons by using one of these sources. Neutrons thus emitted will arrive and thermalize directly in the Gamma Catcher liquid scintillator. Here the ratio H/C is about 1.7. In addition the thermal neutron capture cross section on H is 0.33 barns while on ^{12}C it is only 0.0035 barns (see table 4.2). This means that hydrogen captures almost all(about 99.4%) of the thermal neutrons in the Gamma Catcher, and only a small fraction are captured by C (about 0.6%).

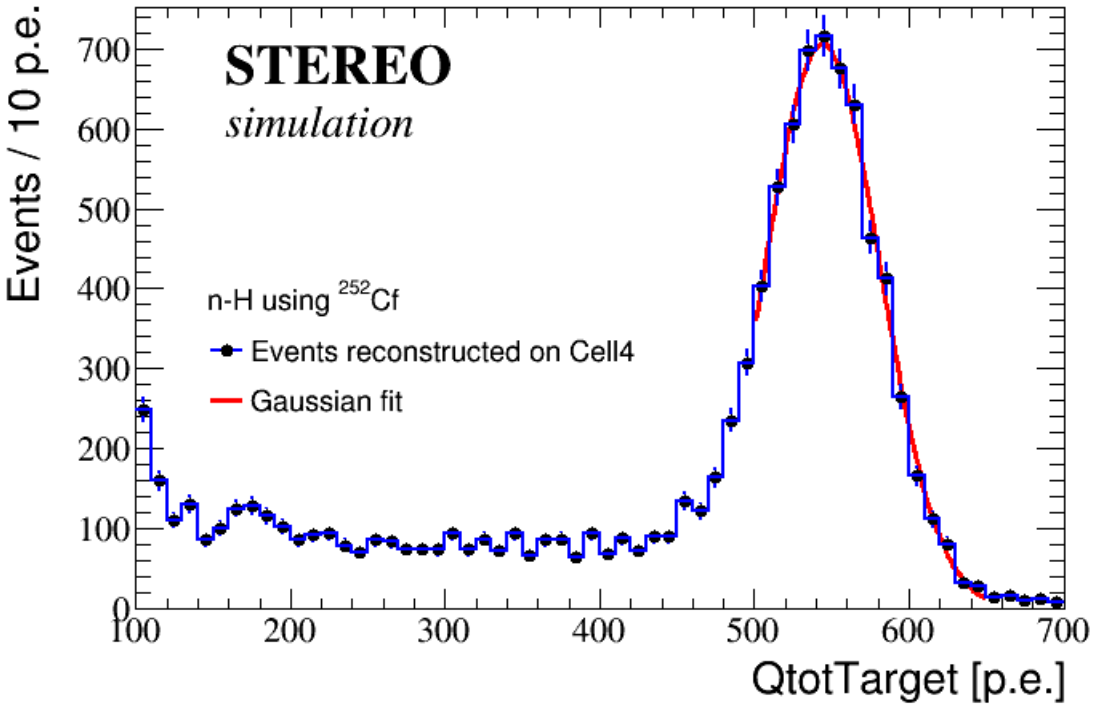

Figure 4.13: Calibration with 2.2 MeV from n-H using a ^{252}Cf source. The source is placed outside the Gamma Catcher between the vessel and the shielding using the external system. For events reconstructed in a central cell, the condition of no energy deposited in the Gamma Catcher and neighboring cells is applied. The distribution is fitted with a Gaussian function.

The 2.2 MeV n-H calibration point is important because it is chosen as the anchor point to determine the absolute energy scale in order to reconstruct the visible energy. Moreover, this point can be used to monitor the time evolution of the liquid scintillator and the detector almost in real time. A lot of fast neutrons are produced by cosmic rays (see section 4.9) that later are captured on the H of the liquid scintillator. Tagging these fast neutrons could provide a clean neutron sample to calibrate and monitor the energy scale at 2.2 MeV.

4.3.6 High energy calibration

Above the 4.4 MeV calibration point from AmBe, there are no commercially available sources. In other experiments as SNO and SuperKamiokande the calibration at high energy was achieved by employing complex systems in order to obtain the 6.1 MeV gamma from ^{16}N [189, 190]. However, such systems are very complicated to implement because the half life of the ^{16}N is only 7.13 s. In addition, ^{16}N needs to be produced via the (n,p) reaction on ^{16}O in the form of CO_2 gas by using 14-MeV neutrons. The gas is then circulated inside the detector liquid. Unfortunately a similar system is not possible in STEREO.

Element	Steel composition (%)	Uncertainty
Fe	71.73	0.50
Cr	18.11	0.19
Ni	8.06	0.04
Mn	1.47	0.45
C	0.02	0.003
Si	0.34	0.09
P	0.04	0.004
S	0.01	0.009
N	0.07	0.02
Co	0.10	0.09

Table 4.3: The composition of the stainless steel vessel which contains the inner detector according to the material composition certificates of the producer. It is composed mostly of Fe, Cr and Ni.

A solution in STEREO could be to excite the materials of the detector itself. The different elements that are found in the structure that compose the inner detector were analyzed. It was observed that the iron of the double steel vessel containing the inner detector could be a good candidate to calibrate at high energy. Indeed, thermal neutron capture on iron produces several gammas above 5 MeV. In the following section, the details of this study are presented.

4.3.6.1 n-Fe

The double steel vessel containing the inner detector is made, according to the material composition certificates of the producer, of 71.73% iron, 18.1% Cr, 8.1% Ni, 2% Mn, Co, Si at the 0.2% level and other materials are present in concentrations lower than 0.1% (see table 4.3). The thermal neutron capture cross section on Fe is 2.56 barns, for Ni it is 4.39 barns and for Cr 3.07 barns. Neutron capture on iron produces several gammas

of high energy, in about 50% of cases it is either a 7.63 or a 7.65 MeV gamma. There are other gamma lines at high energy, but their emission probability is lower. The second most abundant element in the steel vessel is chrome, the most probable emission in case of a neutron capture is a 7.9 MeV gamma (∼13%), other gammas have lower emission probability. Finally, nickel has also several gamma lines above 5 MeV. In about 34% of cases a 8.998 MeV gamma is emitted when it captures a neutron. Taking into account the steel composition, we have that about 31% of neutron captures on the steel vessel lead to a 7.6 MeV gamma emission. Any other gamma has an emission probability lower than 6% as is shown in table 4.4.

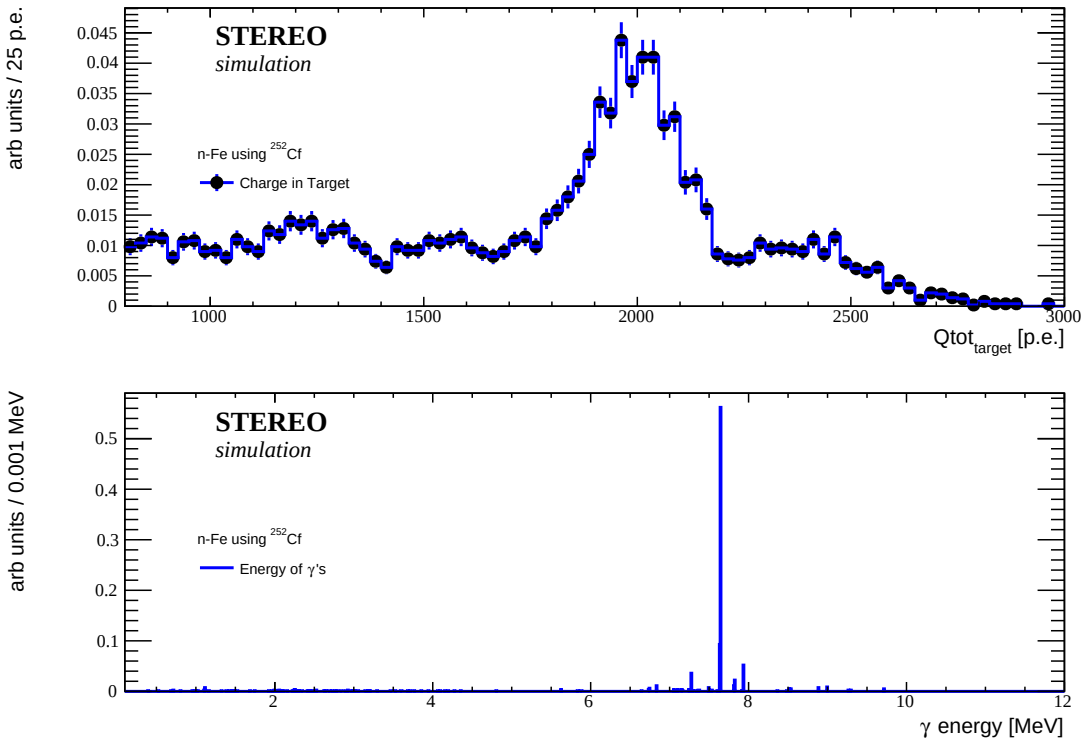

Figure 4.14: (top) Charge in Target produced by 7.6 MeV gammas from n-Fe using a ^{252}Cf source. The source is placed outside the Gamma Catcher between the vessel and the shielding using the external system. For events reconstructed in one of the target cells, the condition of no deposited energy in the Gamma Catcher and neighboring cells is applied. (bottom) The gamma energy for events around the peak (2000 ±150 p.e.) is found to be 7.05 MeV. From the figure it is clear that most of these gammas comes from neutron capture on Fe, the distribution being dominated by the 7.6 MeV gammas.

Once identified a possible solution to calibrate at high energy, the next step was identifying the most suitable neutron source. The easiest option was using the AmBe source inside the liquid, in this way neutrons could thermalize within the liquid and then some of them would be captured on the steel vessel. However, simulations showed that when

putting the source inside the liquid scintillator almost all the neutrons are captured on Gd or H, and the fraction of neutron captures on Fe was too small to separate them from captures on Gd by using a topological selection.

Another possibility tested was putting the source under the detector. However even in this configuration most of the neutrons are absorbed by Gd or H. Moreover, the few neutron captures on Fe are diluted inside the peak produced by neutron captures on Gd, whose total energy (∼8 MeV) is in the same region as the 7.6 MeV gammas. This leads to the idea of placing the source outside the Gamma Catcher. In this way, neutrons will thermalize in the liquid scintillator of the Gamma Catcher and then will be captured on the steel vessel or in the H of the Gamma Catcher. These neutron captures on H do not pollute the calibration peak because their energy (2.2 MeV) is much lower than the 7.6 MeV we seek.

Simulations showed that the irradiation of the steel vessel with neutrons from an AmBe source can indeed produce a peak to calibrate the energy scale at high energy. However, even in this configuration a fraction of the neutrons reach the Target and in consequence are captured on Gd, producing a signal in the same energy range. These neutron captures represent a source of background for this calibration point. Neutrons from the AmBe source can reach the target because they have a mean energy of about 4.2 MeV. This problem could be solved by using neutrons with a lower energy. Another common commercial source of neutrons is ^{252}Cf, this is a fission source which produces in average 4 neutrons per fission with a mean energy of 2 MeV.

Simulations of a ^{252}Cf source showed that even these low energy neutrons can reach the target cells. Nevertheless, the amount of neutrons reaching the target cells is much lower. Using a topological selection the amount of neutron captures on Gd around the peak of the figure 4.14(top) is found to be around 5.5%, and 94 % of them correspond to neutron captures on the steel vessel. Most of the neutrons thermalize and are captured on the hydrogen of the Gamma Catcher. Thus, by using a ^{252}Cf source, two different energy levels can be calibrated (2.2 MeV and ∼7.1 MeV).

The results of irradiating the steel vessel with a ^{252}Cf source are shown in Figure 4.14. The charge in p.e. for events reconstructed in one target cell and satisfying the vetoes of no energy leaks in the Gamma Catcher and neighboring cells is shown on the top. The value of the peak is found to be about 2000 p.e.. This peak is produced mostly by 7.6 MeV gammas as is shown in bottom plot. So the mean deposited energy in the liquid scintillator for these events is about 7.56 MeV, and goes down to 7.05 MeV once the background of lower energy neutron captures gamma lines, such as gadolinium's, is taken into account.

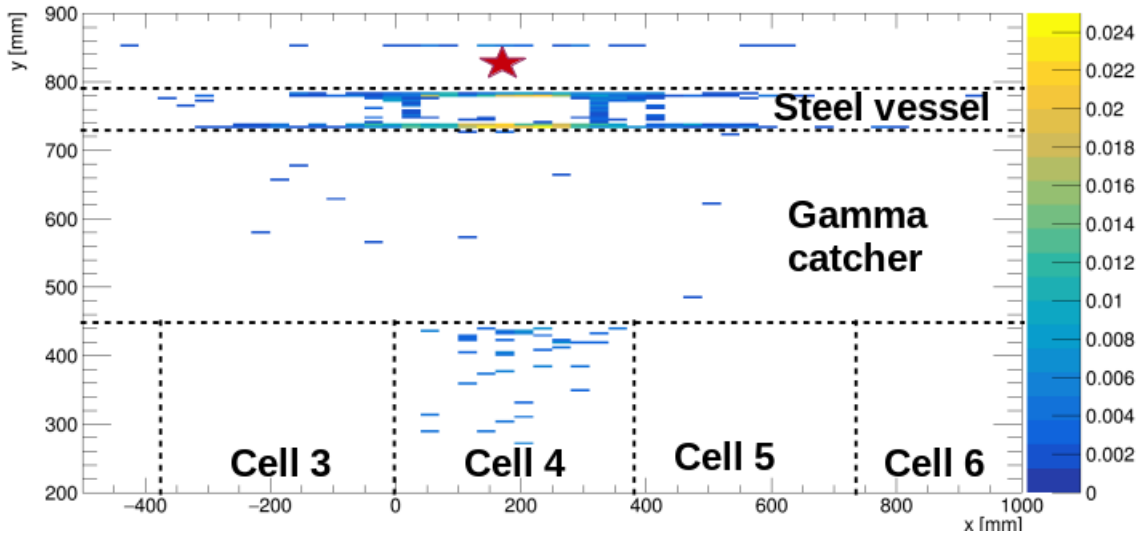

Figure 4.15: Position of origin of gammas produced by ^{252}Cf neutron captures which are around the calibration peak of the figure 4.14. The position of the source is represented by the red star, which is placed between the Gamma Catcher and the shielding using the external calibration system. Most of the neutrons are captured on Fe, however a few neutrons reach the target and are captured on Gd (∼5.4 %).

Figure 4.15 shows the vertex in the XY plane of gammas produced by neutron captures of a ^{252}Cf neutron source placed outside the double steel vessel and whose total reconstructed visible energy in the target is around 8 MeV. Most of these neutrons are captured in the steel vessel, whose double wall structure can be observed in the figure. Its walls are 0.5 cm thick. A few neutrons reach the target and are captured on Gd.

4.3.7 Energy non-linearity and choice of calibration sources

As was already said before, there are two intrinsic sources of non-linearity in the energy response of STEREO. The first one comes from the behavior of the liquid scintillator and depends on the energy and particle type. At the origin of this non-linearity we have quenching and Cerenkov light emission. On the other hand, we have the non-linearity given by the electronics, which is expected to be below 1%. The goal of STEREO is to have an uncertainty in the energy scale below the 2% level, so the non-linearity given by the liquid scintillator has to be known at the ∼1% level.

The effect of the liquid scintillator non-linearity becomes relevant at low energy. For electrons in particular, this effect becomes small above few hundred keV. For positrons however the effect is more important because of the two 511 keV gammas produced by its annihilation with an electron. These gammas produce a lot of low energy electrons by Compton scattering, where quenching is much more important.

Element (% on steel)	E_γ keV	σ_γ barns	Uncertainty barns	Expected n captures (%)
	Total	**2.56**	**0.13**	**67.8**
	4218.3	0.099	0.003	2.6
	5920.4	0.225	0.005	6.0
Fe	6018.5	0.227	0.005	6.0
(72 %)	7278.8	0.137	0.004	3.6
	7631.1	0.653	0.013	17.3
	7645.5	0.549	0.011	14.5
	9297.7	0.0747	0.025	2.0
	Total	**3.07**	**0.15**	**19.7**
	2239	0.186	0.01084	1.2
	6645.6	0.183	0.013	1.2
	7099.9	0.146	0.009	0.9
Cr	7938.5	0.424	0.011	2.7
(18 %)	8482.8	0.169	0.007	1.1
	8510.8	0.233	0.008	1.5
	8884.4	0.78	0.05	5.0
	9719.1	0.26	0.018	1.7
	Total	**4.39**	**0.15**	**12.4**
	6837.5	0.458	0.008	1.3
Ni	7536.6	0.19	0.004	0.5
(8 %)	7819.5	0.336	0.006	0.94
	8533.5	0.721	0.013	2.0
	8998.4	1.49	0.03	4.2

Table 4.4: Steel composition and neutron capture cross sections of the most prominent lines of the most abundant elements in the steel.

Figure 4.16 shows the expected LS energy non-linearity response for gammas of different energies. Below 2 MeV the quenching is more important and the amount of scintillation light drops quickly. So in this region several sources must be used in order to accurately characterize the LS non-linearity in this energy range. Above 2 MeV the variation of the number of p.e./MeV is almost linear.

For the amount of non-linearity present in the simulations[1], the energy non-linearity can be parametrized as follows:

$$C(E_{\text{true}}) = (p_2 + p_3 E_{\text{true}})(1 - p_0 e^{-p_1 E_{\text{true}}}) \tag{4.3.1}$$

[1]The scintillation model in the STEREO simulation is that of Double Chooz. The STEREO LS is expected to have more quenching than the Double Chooz LS

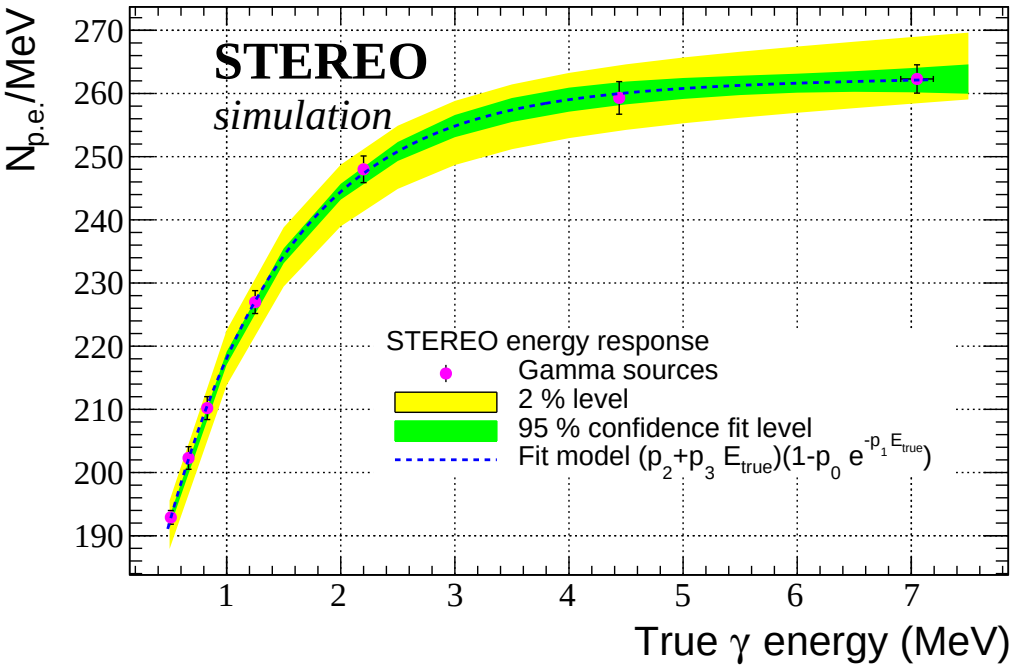

Figure 4.16: The STEREO energy response model. Several radioactive sources are used to study and characterize the energy non-linearity. From the lowest energy we have: ^{68}Ge, ^{137}Cs, ^{54}Mn, ^{60}Co, n-H, AmBe, and n-Fe. As the green band shows, these sources should allow to know the energy scale better than 2%.

where $C(E_{\text{true}})$ is the calibration constant for each source, and E_{true} is the true deposited energy in the liquid scintillator.

In table 4.5, sources that have been used to the calibration of recent reactor antineutrino experiments are shown. Most of these sources yield gammas below 2 MeV. Among the sources that we will use to calibrate the energy scale in STEREO, from the lower energy we have ^{68}Ge. It has a half life of 271 days and decays by electronic capture into ^{68}Ga, which in turn decays into ^{68}Zn by β^+ emission in about 87.5% of the cases [191]. The emitted positron has a maximum energy of 1.9 MeV and quickly annihilates with an electron within the source producing two 511 keV back-to-back gammas. This source is important because it produces the exact visible energy threshold of the prompt neutrino signal, allowing to identify unambiguously this point. Moreover, this source is ideal for the collimation device, since unlike the ^{22}Na, there is (almost) no additional gammas. There are many sources of lower energy but they are out of the energy region of interest for STEREO.

Given that the non-linear effects of the liquid scintillator are more pronounced at lower energies (quenching, specially below 2 MeV, see figure 4.16), it is important to explore

Source	^{68}Ge	^{22}Na	^{137}Cs	^{54}Mn	^{65}Zn	^{88}Y	^{40}K	^{60}Co	n-H	^{208}Tl	AmBe	n-C	n-Fe	n-O	^{252}Cf
Energy (MeV)	0.511x2	0.511x2 1.27	0.667	0.83	1.12	0.88 1.8	1.45	1.17 1.33	2.2	2.6 0.58	4.4 2.2	4.9	7.6 6.1	6.2	7.6 2.2
DayaBay	X		X	X			X	X	X	X	X	X	X	X	X
DoubleChooz	X		X					X	X			X			X
RENO	X							X	X						
BUGEY			X	X	X	X			X		X				
STEREO	X		X	X				X	X		X		X		X

Table 4.5: Selection of sources for the calibration of the STEREO experiment. In recent experiments several gamma sources have been used in order to characterize the energy response in the range of the $\overline{\nu_e}$'s energy spectrum. The goal of STEREO is to cover all the energy range from 0.5 to 8 MeV. By using different neutron and gamma sources, the whole energy range can be covered.

this energy range thoroughly. Thus, ^{68}Ge (0,511x2 MeV), ^{137}Cs (0.667 MeV), ^{54}Mn (0.83 MeV), and ^{60}Co (1.27 MeV and 1.33 MeV) will be used to study the energy response of the liquid scintillator in this region.

^{137}Cs has a half life of 30 years and decays by β^- into ^{137}Ba. In about 5.6 % of cases it goes directly to the ^{137}Ba ground state, while in about 94.4% it goes to its second excited state. Its deexcitation to the ground state emits only one 661.7 keV gamma.

^{54}Mn has a half life of 312 days and decays into the first excited state of ^{54}Cr by electronic capture. It goes to its ground state by emitting a 834.8 keV gamma. ^{60}Co has a half life of 5.27 years and its decay is produced by β^-. In about 99.88% of cases it goes to the third excited state of ^{60}Ni, which in turn goes to its first excited state by the emission of a 1.173 MeV gamma and then to its ground state by the emission of a 1.332 MeV gamma. Detailed decay schemes for these sources are presented in the appendix A.

In order to reduce the uncertainty in the reconstructed visible energy, the entire interval from 0 to 8 MeV must be studied and characterized. Then the AmBe and the n-Fe calibration points at high energy are crucial. These two calibration points can only be achieved by using the external calibration system. Thus, we can have three energy calibration points above 2 MeV. The 2.2 MeV gamma produced by neutron captures on H, the 4.4 MeV gamma from the AmBe source (when it is placed outside the detector), and the 7.6 MeV gamma produced by neutron captures on the iron of the steel vessel when it is irradiated with neutrons from a ^{252}Cf source. The AmBe source is also essential for the measurement of the neutron capture efficiency (see section 4.6).

4.3.8 Energy scale determination systematic uncertainties

The energy scale is crucial in STEREO. The physics requirements impose that its uncertainty should be below 2%. The electronic non-linearity has been tested and is expected to be at the 1% level. Thus the liquid non-linearity uncertainty should be as well around the 1% level. Using the STEREO simulation software, a dedicated study was performed in order to evaluate the systematic uncertainty in the determination of the energy scale. The following factors were evaluated:

Effects of the vetoes (no energy leaks in the GC and neighboring cells): Given the small size of the cells, vetoes are needed to remove Compton events in order to have a clear full energy peak for the calibration. These effects were evaluated by varying the amount of charge detected in the Gamma Catcher and neighboring cells. The vetoes consist in the following conditions: QtotGC$< \alpha$ for the Gamma Catcher and QtotCell$_{i\pm1}$ <QtotCell$_i \times \lambda$ for neighboring cells. The nominal value of α is 20 p.e. and it was changed from 10 to 100 p.e.; at the same time the value of λ was changed from 3 to 10%. Its nominal value is 6%.

For each set of α and λ values, the calibration constant was evaluated. The uncertainty given by the variation of these vetoes was estimated as the square root of the variance of all the values of the calibration constant: $\sigma_{\text{vetoes}} = \sqrt{var(\text{C})}$. The value of σ_{vetoes} depends on the source and ranges from 0.2-0.7%.

Uncertainty in the materials budget (acrylic and steel): Whether the source is placed inside or outside the liquid scintillator, gammas need to go through non-active materials before they interact directly with the liquid scintillator. An imperfect knowledge of the amount of non-active material will thus lead to an uncertainty in the energy deposited in the LS.

To evaluate this contribution, the calibration constant is computed while varying the thickness of the acrylic plates by 0.5 mm (the thickness of acrylic plates of VM2000 sandwiches is 2 mm) and the steel vessel by 1 and 2 mm (the thickness of each plate of the steel vessel is 5 mm). The associated uncertainty is evaluated to $\sigma_{\text{materials}} = 0.4\%$

The photoelectrons peak fit procedure (intervals and bin width): The p.e. distribution is fitted with a Gaussian function in order to find the mean value of its peak. This value can vary slightly depending on the bin width used and the interval taken into account to perform the fit. The effect of the bin width was evaluated varying the width within the range [5-20]p.e. in steps of 1 p.e.

The effect of the fit interval was evaluated by varying it in steps of 5 p.e. around the peak. The contribution of these effects is estimated to $\sigma_{\text{fit}} = 0.06\%$

Interval for the true deposited energy computation: The true deposited energy is

computed using the Monte-Carlo simulations. Once the fit is done, the deposited energy is calculated around the mean of the peak extracted from the fit. The nominal interval used is ±20 p.e.. This interval was varied from 10 to 35 p.e. in steps of 1 p.e.. The value of this effect is estimated to $\sigma_{\text{EdepI}} = 0.07\%$.

Changes of temperature: The expected changes of temperature in the STEREO casemate are ±2°C for normal periods. Exceptionally these changes can reach ±11°C. Changes of temperature can produce changes in the liquid scintillator density, which implies a change in the value of the calibration constant.
Changes in the liquid density produced by changes of temperature have been evaluated for a liquid scintillator based on LAB, which is similar to the STEREO liquid [192]. These changes are expected to be: for $\Delta T = 2$°C a $\Delta\delta = 0.19\%$ and for a $\Delta T = 11$°C a $\Delta\delta = 0.96\%$. This leads to a systematic uncertainty of $\sigma_T = 0.01$ or 0.02 % for a $\Delta T = 2$ or 11°C respectively.

All these effects were evaluated for the two calibration possibilities (source is placed outside the LS using the external system and source inside the LS using the manual calibration tubes). Whereas the effect of the vetoes of no energy leaks is the same in both configurations, the effect of the materials budget uncertainty is bigger when the source is placed outside the liquid. The total systematic uncertainty is

$$\sigma^2_{sys} = \sigma^2_{\text{vetoes}} + \sigma^2_{\text{materials}} + \sigma^2_{\text{fit}} + \sigma^2_{\text{Temperature}} + \sigma^2_{\text{Edep interval}} \tag{4.3.2}$$

The contribution of each factor is shown in the next table, where the example of the ^{137}Cs source is presented:

Source	Position	Fit	Edep interval	Temperature	Materials	Cuts	Total
^{137}Cs	Outside	0.05	0.07	0.02	0.7	0.5	0.9
^{137}Cs	Inside	0.05	0.07	0.02	0.2	0.5	0.5

Table 4.6: Systematic uncertainty for the ^{137}Cs calibration point. The total systematic is dominated by two effects: the vetoes and the material budget. If the source is placed outside the liquid, the uncertainty on the deposited energy in non scintillating materials is bigger.

In the table 4.6 we can see that the systematic uncertainty is dominated by the no energy leaks vetoes and by the material budget uncertainty. The later being the most important contribution when the source is placed outside the LS.

When using the collimation device or for the calibration at high energy with neutron captures on the steel, additional uncertainties must be considered. They are are following:

Collimation: When using the collimation device, an additional contribution needs to be considered in the systematic uncertainty for the 511 keV calibration. The collimation is carried out by demanding the detection of one 511 keV gamma in the scintillating crystal. To fulfill this condition, deposits in the crystal in the range 0.3-0.52 MeV were required. The lower bound of this interval was varied from 0.1 to 0.5 MeV in steps of 0.01 MeV. This leads to an uncertainty of $\sigma_{lyso} = 0.1\%$.

Systematics of the n-Fe calibration: The calibration with 7.6 MeV gammas from n captures on iron is crucial to the evaluation of the detector response at high energy. Nevertheless, the systematics of this calibration point is much more complex to evaluate. On top of all the others effects mentioned above, additional sources of uncertainty were considered, the main ones being: the neutron capture cross section of the iron and the other material present in the steel vessel, the uncertainties in the steel composition, and the amount of neutron captures on Gd.
In order to evaluate this systematic uncertainty the contribution of each gamma line to the deposited energy was varied according to the total uncertainty on the neutron capture cross section and the uncertainty on the steel composition.
For each set of values, the calibration constant was computed and the mean gamma energy was estimated. The effect in the calibration constant is small because the value of the calibration constant at high energy depends very little on energy (see figure of calibration constants). However the energy at which this calibration constant is computed is more uncertain: 7.05 ± 0.06 MeV. The total systematic uncertainty on the calibration constant is thus evaluated to $\sigma_{iron} = 1\%$. The thermal neutron capture cross sections of the elements composing the steel vessel are shown in the table 4.4.

In table 4.7 a summary of the estimated systematic uncertainty for different sources is presented.

4.3.9 Reactor ON calibration and monitoring

The STEREO liquid scintillator is expected to be very stable over time. It is similar to the Double Chooz liquid scintillator, which is very stable with variations of its properties under the 1% level [193]. Nevertheless, the monitoring of the liquid properties over the time is very important. This allows to reduce the systematic uncertainty given by changes on the behavior of the liquid scintillator. Quasi-online monitoring of the detector properties could be achieved by looking at the time evolution of the Gd neutron capture peak.

Concerning the possibility of reactor ON calibration, the use of low energy sources could be difficult since the background at low energy during reactor ON periods is expected to be very high. Calibration during reactor ON periods should then be done with

Source	Energy (MeV)	Constant (pe/MeV)	Sys error (%)
^{22}**Na**	0.511	193	0.9
^{137}**Cs**	0.66	202	0.9
^{54}**Mn**	0.83	210	0.8
^{65}**Zn**	1.12	220	0.5
^{22}**Na**	1.27	223	0.8
n-H	2.22	248	0.8
AmBe	4.44	259	0.9
n-Fe	7.05±0.06†	263	1.1

Table 4.7: Systematic uncertainty for different calibration sources. In all the cases the value of the systematic uncertainty is lower than 1% except for the neutron capture on iron. † the mean energy of γ's from n capture on Fe is polluted with γ's from neutron captures on Gd and others materials, which gives a mean energy of 7.05 instead of 7.6.

the AmBe source (4.4 MeV) or with neutron captures on H (2.2 MeV).

Cosmic rays induced background produce a lot of fast neutrons that later can be captured on the H of the LS (see section 4.9). The muon veto allows to identify the passage of a muon. A 2.2 MeV gamma produced by a neutron capture on H can be searched after the passage of a muon in a time window of ∼200 μs. Rough estimates (see Section 5.1) indicate they could be used to perform a daily monitoring of the detector.

4.4 Gamma catcher calibration

As was already said, the signal searched by STEREO is characterized by two energy deposits. In the prompt signal, most of this energy is deposited in the target cells, but 511 keV gammas can escape and deposit some energy in the Gamma Catcher. In the delayed signal (gamma cascade), more energy deposits are expected in the Gamma Catcher. Thus, the Gamma Catcher needs to be calibrated in order to reconstruct the total visible energy created by the prompt and delayed signals.

As for the Target, the energy scale in the GC can be calibrated with the 2.2 MeV gamma from neutron captures on H. This gamma can be induced either with ^{252}Cf or AmBe neutron sources. Figure 4.17 shows the expected number of photoelectrons produced by an AmBe source placed outside the steel vessel by using the external calibration system. Two peaks can be observed, the first one around 850 p.e. corresponds to the 2.2 MeV gamma, the second peak around 1800 p.e. corresponds to the 4.4 MeV gamma

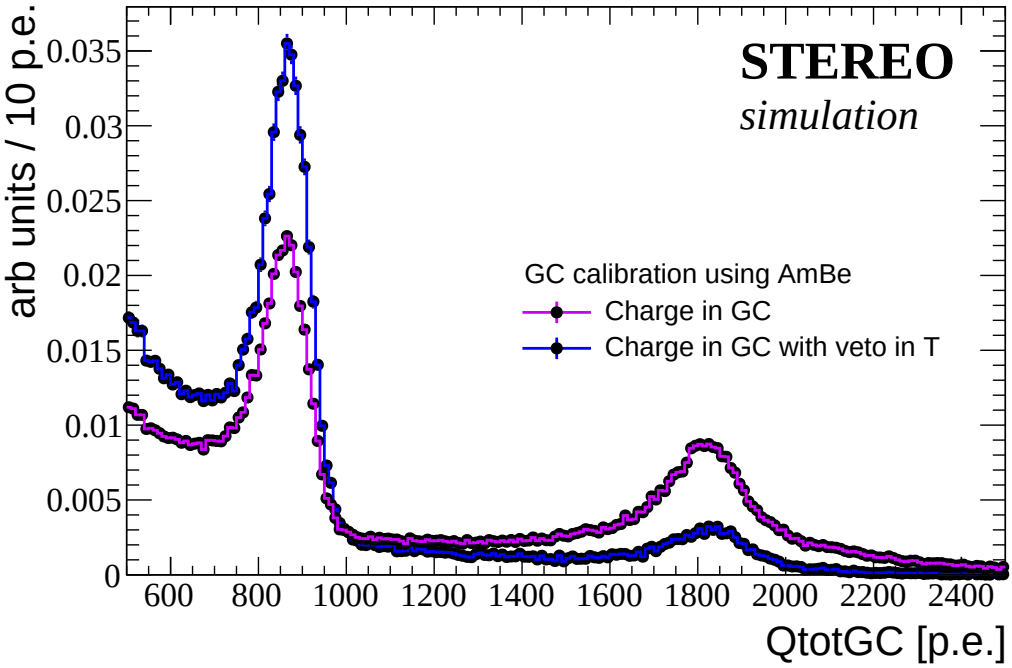

Figure 4.17: Calibration constant in GC with AmBe. The absolute p.e to MeV scale factor in each side of the Gamma Catcher can be found using the 2.2 MeV n-H peak with the AmBe or ^{252}Cf neutron sources. The sources can be placed next to each side of the Gamma Catcher by using the external calibration system.

polluted by proton recoil. In order to clean the full energy peak of the 2.2 MeV, the Target can be used as an anti-Compton device, the violet histogram shows the expected charge in the GC without using the Target information, while the blue histogram shows the effect of selecting events requiring less than 10 p.e. in the Target. To have a clean 4.4 MeV peak in the GC, the AmBe source can be put in the manual calibration tubes.

In the short sides of the Gamma Catcher (cell-like) the response is expected to be similar to the target cells, and non-uniformities within the short GC sides can not be corrected since we do not have the resolution to reconstruct the vertex with precision inside the cells. Nevertheless, as was showed in section 3.10.3, in the long sides of the Gamma Catcher a better reconstruction of the vertex of interaction is possible. In consequence, corrections of non-uniformity are possible in these long sides. This non-uniformity response can be addressed with the external calibration system, variations of about 2% between the center and the end of the Gamma Catcher are expected (see figure 4.19).

Since in the Gamma Catcher we do not have calibration tubes, the only way to study the vertical dependence of the light collection is the external calibration system. Figure 4.18 shows this response for a ^{54}Mn gamma source placed just outside the steel vessel at

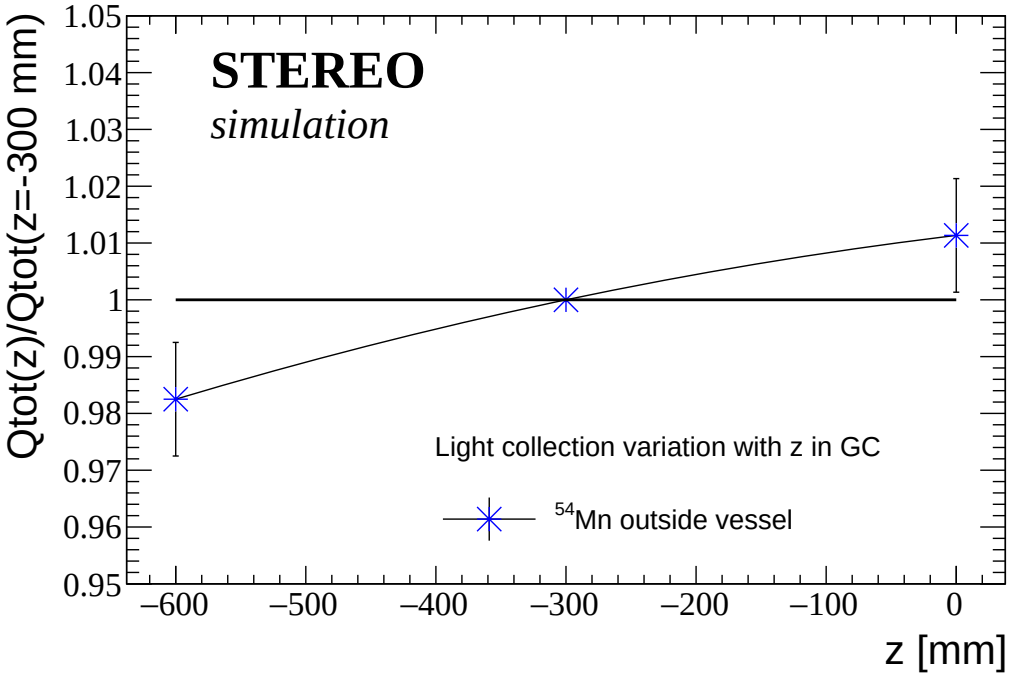

Figure 4.18: Calibration of the vertical dependence for the light collection in GC.

three different heights. A difference of about ∼3% can be measured by using the external calibration system.

4.5 Visible energy reconstruction

In this section we present our proposal for the reconstruction of the visible energy. The initial idea of STEREO was to have completely optically separated cells. In that scenario, our (linear) reconstructed visible energy (see discussion on section section 4.1) could be easily computed as

$$E_{\text{vis}}^{\text{Total}} = \sum_i N_{\text{p.e.}}^{\text{cell}_i} \times C_{e^+}^{\text{cell}_i} \tag{4.5.1}$$

with $N_{\text{p.e.}}^{\text{cell}_i}$ and $C_{e^+}^{\text{cell}_i}$ the number of observed p.e. and the calibration constant in each cell of the Target or Gamma Catcher for a chosen energy calibration point (2.2 MeV for instance). However, as was already said in the introduction, measuring a calibration constant for positrons is not possible. In addition, the optical separation between cells is not perfect and some light produced in one cell leaks to neighboring cells. These problems render equation 4.5.1 irrelevant. The first problem can be approximately solved by considering positrons as "electrons with two 511 keV gammas attached", and using gamma sources to constrain the response to electrons (see section 3.7.1). This is shown in figure 4.19, where the 2.2 MeV gammas are used on all Target cells and a few points in the GC to compute a position-dependent energy scale. It is worthy to note that: 1) a calibration

constant per cell suffices since the vertexing is not sensitive to the position within one cell (see section 3.10.2) and 2) the value of the calibration constants vary slowly within the Target, and likewise within the GC. Small non-uniformity corrections are thus needed.

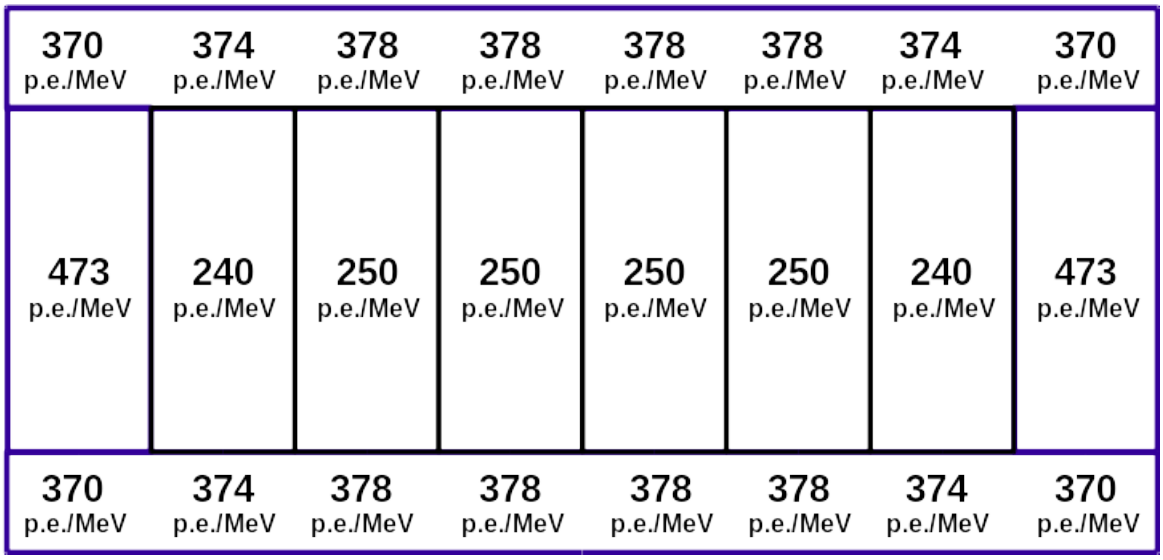

Figure 4.19: Calibration constant per cell. The absolute p.e to MeV scale factor in each cell is found using 2.2 MeV n-H peak with the AmBe or ^{252}Cf neutron sources. The source can be placed facing each cell using the external calibration system.

What about the light leaks problem? Given the small variation of the calibration constant from one cell to another (<5%), and the small fraction of light that leaks (<10%), the overall mistake incurred in using the wrong calibration constant is well below 1%. Sizeable differences in the values of the energy scales are found between the Target and the GC, but the light leaks between them are very small (<1% [194]), giving a total error well below 1% once more. A similar argument can be applied to 511 keV energy. Thus we conclude that the position dependence of the energy and light leaks can be safely ignored. We then propose to compute a calibration constant per cell including the light leaks to neighboring cells, i.e. summing over the observed p.e. of the whole Target to compute the denominator $C_{\gamma}^{\mathrm{cell}_i} = \frac{<E_{\gamma}^{\mathrm{MC,cell}_i}>}{N_{\mathrm{p.e.,\ Target}}^{\mathrm{peak}}}$. This is equivalent to considering the Target as a single scintillating volume (because there is no 100% effective optical separation among the cells). Thus the use of one single calibration constant depending on the position of reconstruction is equivalent to the non-uniformity corrections used in other experiments like Double-Chooz.

The approach proposed in this section consist in adding the light leaks to the computation of the calibration constant. Thus for one event a single calibration constant can be used to the computation of the visible energy. Since the energy leaks originated by the 511 keV are just a small fraction of energy compared with the total detected energy, and given that the calibration constants among cells are expected to be very similar, this effect

can be neglected.

Thus, we now reconstruct the visible energy as:

$$E_{\text{vis}}^{\text{Target}} = N_{\text{p.e.}}^{\text{Target}} \times C_{\text{n-H}}(\vec{X}) \times f_T(t) \tag{4.5.2}$$

where $N_{\text{p.e.}}^{\text{Target}}$ is the total number of p.e. in the Target, $C_{\text{n-H}}(\vec{X})$ is a position-dependent calibration constant obtained with the 2.2 MeV gamma, which varies from cell to cell and includes the light leaks, and $f_T(t)$ is a time evolution factor which interpolates the calibration constant value between two consecutive calibration runs. It may be possible to evaluate $f_T(t)$ thanks to cosmic ray induced neutrons. Similarly, the visible energy in each optically separated part of the Gamma Catcher can be reconstructed as:

$$E_{\text{vis}}^{\text{GC}_i} = N_{\text{p.e.}}^{\text{GC}_i} \times C_{\text{n-H}}(\vec{R}) \times f_{\text{GC}_i}(t) \tag{4.5.3}$$

Leading to a total visible energy as

$$E_{\text{vis}} = E_{\text{vis}}^{\text{Target}} + \sum_i E_{\text{vis}}^{\text{GC}_i} \tag{4.5.4}$$

Since the calibration constant is for a fixed, unique energy (here, 2.2 MeV), non-linear effects are ignored in the reconstructed E_{vis} for the data. All the non-linear effects will be included however ,in the simulations and hence in the E_{vis} response model for an antineutrino of a given energy. Thus the visible energy of the MC should include an extra non-linearity correction, leading to

$$E_{\text{vis}}^{\text{M.C.}} = E_{\text{vis}}^{\text{Target}} f_{\text{nl}}^{\text{T}} + \sum_i E_{\text{vis}}^{\text{GC}_i} f_{\text{nl}}^{\text{GC}} \tag{4.5.5}$$

where f_{nl}^{T} and $f_{\text{nl}}^{\text{GC}}$ are non-linearity corrections (LS non-linearity and electronics non-linearity), which can be parametrized as a function of the true deposited energy in a similar fashion as was done in section 4.3.7.

Since the energy scale factor varies from one cell to another and along the GC, the first step to the visible energy reconstruction consists in the reconstruction of the vertex of the events. To this end, we propose to use the weighted barycenter of charges described in section 3.10.2.

Figure 4.20 shows the reconstructed visible energy using equation 4.5.4 for 1 MeV positrons uniformly distributed in the target before (top) and after (bottom) non-uniformity corrections. The visible energy is reconstructed in all cells, after the non-uniformity correction are statistically compatible, which is STEREO's goal: all cells should be equivalent

in order to limit the systematics in the comparison of their respective energy spectra. The validity of this approach to the energy reconstruction will be cross-checked cell by cell using calibration data.

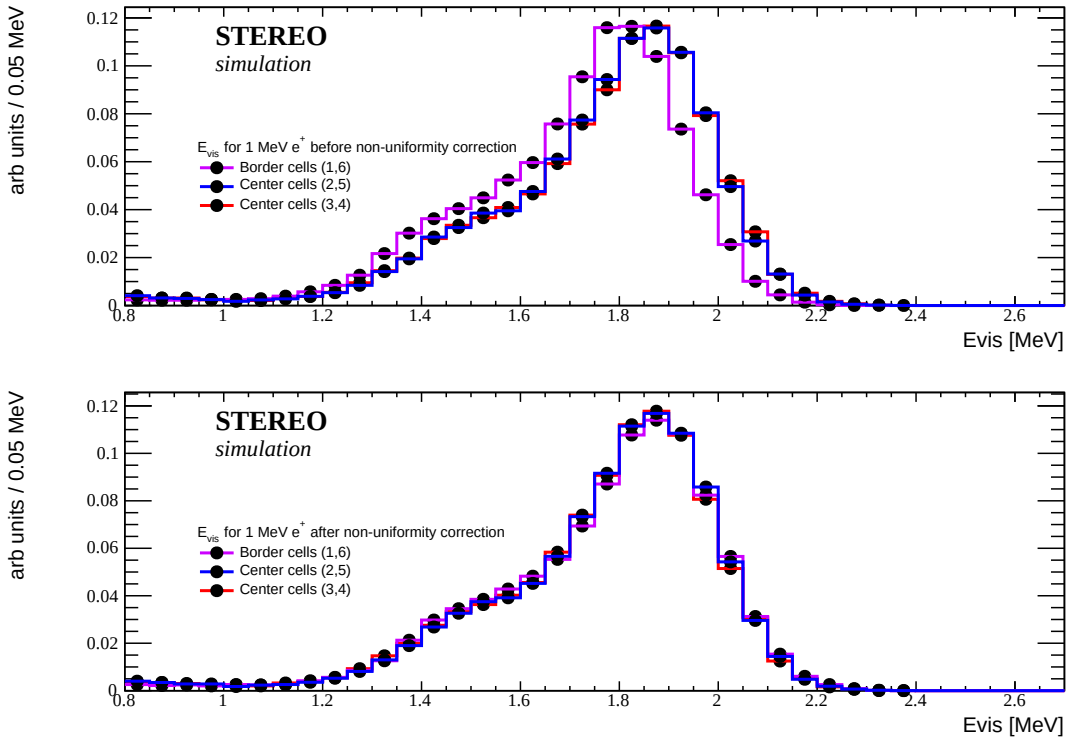

Figure 4.20: (top) The reconstructed visible energy before non-uniformity corrections by the position for positrons of 1 MeV uniformly distributed in all the target. (bottom) Visible energy after non-uniformity correction. A calibration constant as a function of the cell where the events are reconstructed is used. There are almost no difference between the cells. Before the non-uniformity correction, the mean of the visible energy in the border cell is found to be about 1.74 MeV with a RMS of 0.21, while for the center cells the mean value is found to be 1.80 MeV with a RMS of 0.21. After non-uniformity correction the mean value of all the cells is found to be 1.78 with a RMS of about 0.21.

A similar crosscheck can be carried out with IBD events generated across the whole detector according to the expected antineutrino energy spectrum, instead of using 1 MeV positrons as in Figure 4.20. This is done in figure 4.21. STEREO's baseline selection cuts have been applied to the IBD sample (see section 5.3). Compatible E_{vis} spectra are reconstructed in the different cells of the detector with an IBD sample whose size is comparable to the expected data total size. In the presence of a light sterile neutrino, the energy spectrum will be different in each cell. If this oscillation pattern is observed, STEREO will be able to exploit this information to extract the oscillation parameters.

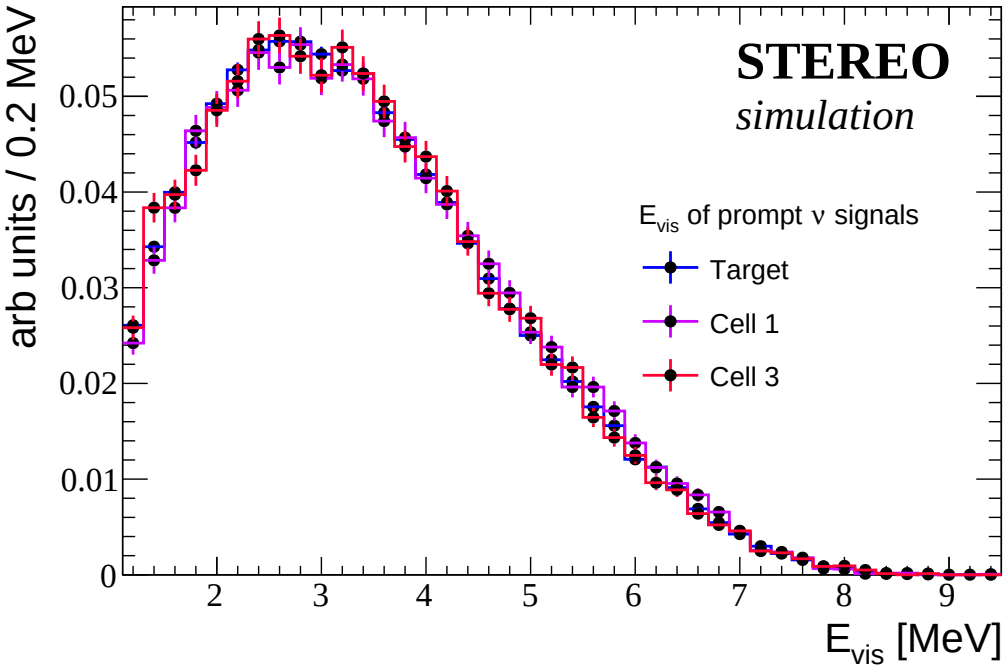

Figure 4.21: Expected prompt visible energy of ν candidates once STEREO's baseline selection cuts are applied (see section 5.3): Barycenter inside the target, $\mathrm{E}_{\mathrm{vis}}^{\mathrm{Prompt}} > 1.1$ MeV, $\mathrm{E}_{\mathrm{vis}}^{\mathrm{Delayed}} > 5$ MeV, $\Delta t < 50\mu s$, $\mathrm{E}_{\mathrm{vis}}^{\mathrm{GC\ Prompt}} < 1$MeV, and $E_{\mathrm{T}} > E_{\mathrm{GC}}$ (using a calibration constant for each cell and GC). The blue line corresponds to the total visible energy in the entire target, while the violet and red correspond to the prompt visible energy in a border and a central cell, respectively.

4.6 Neutron capture efficiency

In STEREO, electron antineutrinos are detected via the inverse beta decay reaction: $\bar{\nu_e} + p \rightarrow e^+ + n$. The delayed signal of this signature is associated to the neutron capture on Gd some $\sim 15\mu$s after the prompt signal. A precise determination of the neutron capture efficiency is needed to characterize the detector response to IBD neutrons. Specifically, this efficiency has to be known at the level of $\sim$3% in order to avoid it being the limiting factor when comparing the observed number of $\overline{\nu_e}$ events to the expectations from reactor flux calculations, which further constrains the reactor antineutrino anomaly.

Several neutron sources are available to calibrate the neutron capture efficiency. In recent experiments, the sources that have been used are: ^{252}Cf in Double Chooz and RENO [195, 196], and ^{241}Am-^{13}C in Daya Bay [197]. These sources produce fast neutrons, which, due to quenching produce a small quantity of light. Nevertheless in general fast neutrons can be identified and tagged by using the PSD information. Once identified the emission of a neutron, its later thermal capture can be searched in a time window

of a few microseconds. The low energy background in STEREO is expected to be much higher than in these experiments, which means that this technique could be perturbed by the background, particularly during reactor ON periods. So another technique must be implemented in order to measure accurately the neutron capture efficiency even during reactor ON periods.

The STEREO constraints impose to know the neutron capture efficiency at the 3% level. Nevertheless, in most of the commercial sources, the neutron flux is only known at the 15% level. Suppliers can provide at best a certificated neutron source with a flux known at the 5% level. The sources initially considered for the STEREO neutron efficiency calibration were AmBe and ^{252}Cf. The former has a clear, systematics free, 4.4 MeV gamma emission in about 59 % of neutron emissions which allows a simple, clean tagging of neutron emission. ^{252}Cf, on the other hand, emits simultaneously to neutron emission gammas from a fission spectrum. In addition, several neutrons are emitted on each ^{252}Cf fission, the average being 4. Clearly the 4.4 MeV signal is the simplest way to tag neutrons, also during reactor ON periods, and we choose as calibration source for the neutron capture efficiency the AmBe source. In the following we describe the details of this study.

4.6.1 AmBe neutron source

In an AmBe source, radioactive ^{241}Am which has a half life of 432 years, decays via α emission into an intermediate excited ^{237}Np state. It goes into its ground state through gamma emission. In about 35.8 (2.4)% of the cases, the emission of a 0.060 (0.26) MeV gamma is produced. The ^{237}Np ground state has a half life of over two million years. Fast neutrons are produced when the α particle, whose energy is about 5.5 MeV, interacts with ^{9}Be, and results in an excited ^{13}C nucleus. The latter decays giving a fast neutron and an excited ^{12}C. If it is in its first excited state, it promptly decays to the ground state via the isotropic emission of a 4.438 MeV gamma [198, 199, 200]. Generally in the AmBe neutron energy spectrum, peaks are observed around 3.1, 4.8, 6.6, 7.7 and 9.8 MeV. The maximum energy of this free neutron can reach 11 MeV as is shown in the figure 4.22. However, the fine details of the neutron energy spectrum structure depends on how the mixture of Americium and Beryllium is fabricated and encapsulated. Thus the neutron energy spectrum change from one source to another. The AmBe reaction can be summarized as follows:

$$\begin{aligned} ^{241}\mathrm{Am} &\rightarrow ^{237}\mathrm{Np} + \alpha \\ \alpha + ^{9}\mathrm{Be} &\rightarrow ^{13}\mathrm{C}^{*} \\ ^{13}\mathrm{C}^{*} &\rightarrow ^{12}\mathrm{C}^{**} + n \\ ^{12}\mathrm{C}^{**} &\rightarrow ^{12}\mathrm{C} + \gamma(4.438\mathrm{MeV}) \end{aligned} \tag{4.6.1}$$

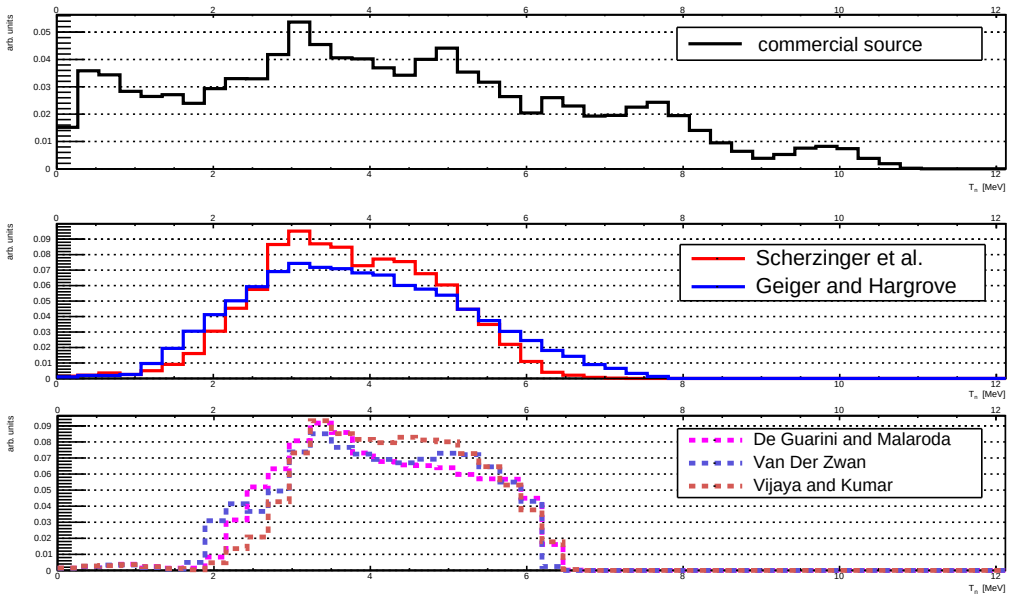

Figure 4.22: Top: Energy n spectra for a typical AmBe commercial neutron source, several peaks can be observed around 3.1, 4.8, 6.6, 7.7 and 9.8 MeV. The details of this shape can change depending on the source fabrication process but the spectra remain similar. The most important variations happen in the low energy region [198]. Middle and bottom: the measured and predicted neutron energy spectrum when a 4.4 MeV gamma is emitted [199, 201, 202, 203, 204, 205].

The $^{12}C^{**}$ denotes the first excited state of this nucleus, which is the most populated. The 4.438 MeV gamma ray to total neutron ratio $R = S_\gamma/S_n$ is an important parameter of an AmBe source. Nevertheless, its values change from one source to another depending on the source fabrication. Several authors have measured R to be approximately 0.6 [206, 207, 200, 208].

Figure 4.22 shows the total energy spectrum of a typical commercial AmBe source. In addition, the predicted and measured energy spectrum when a 4.4 MeV gamma is emitted is shown. The mean energy of these neutrons is about 4 MeV.

4.6.1.1 Neutron capture efficiency definition with AmBe

The strategy we have adopted consists in tagging fast neutrons emission using the 4.438 MeV gamma. In this way a clear signal is produced and even during reactor ON periods the neutron capture efficiency can be assessed.

Figure 4.23 shows the visible energy for all triggers when an AmBe neutron source is introduced inside a central cell by using the manual calibration tubes. Three peaks can be observed: the first one correspond to the 2.2 MeV gamma from neutron captures on

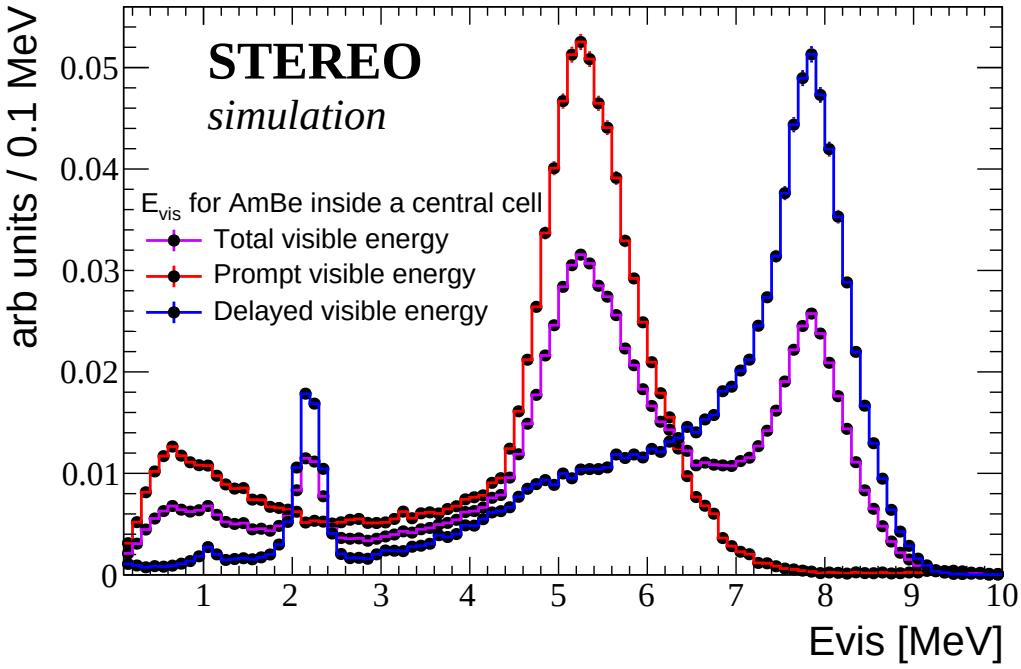

Figure 4.23: Visible energy for an AmBe source inside a central cell. The violet line shows the visible energy for all triggers when the source is placed inside the cell using the manual calibration tubes. The red line shows the prompt visible energy, which is obtained by asking for no events events in the previous 100 μs. The delayed visible (blue line) energy is obtained by requiring a prompt and a delayed coincidence in a time window of 50 μs. All the histograms are normalized to 1 for visual purposes. However the violet histogram contains both the prompt and delayed events ($\sim$ 50% each one after time cut)

hydrogen. Next we have another peak around 5 MeV, which is originated by the 4.4 MeV gamma plus the (quenched)proton recoil produced by the simultaneous emission of a fast neutron and interaction in the same cell. Finally we have a last peak around 8 MeV which is generated by the gamma cascade ($\sim$8 MeV) when neutrons are captured on Gd.

Thus we are led to define the following cuts for the neutron tag: a visible energy between 4 and 7 MeV, and no previous events observed in a time window of 100 μs. Fast neutrons thus emitted have a mean energy of about 4 MeV. Once a neutron has been tagged, a delayed signal with a total visible energy larger than 5 MeV is searched for in a time window of 50 μs. Then, the neutron capture efficiency is defined as the number of coincidences between prompt and delayed signals over the number of prompt signals:

$$\epsilon_n = \frac{\mathrm{N(Prompt\ \&\ Delayed)}}{\mathrm{N(Prompt)}} \tag{4.6.2}$$

For a delayed energy cut of 5 MeV and a time window of 50 μs, the neutron capture

efficiency is estimated to be ∼74% when the source is placed at the middle of the cell. Fast neutrons thermalize, diffuse and are captured close to its original position; an RMS of about 10 cm between the initial position and the point of capture is found (see figure 4.24).

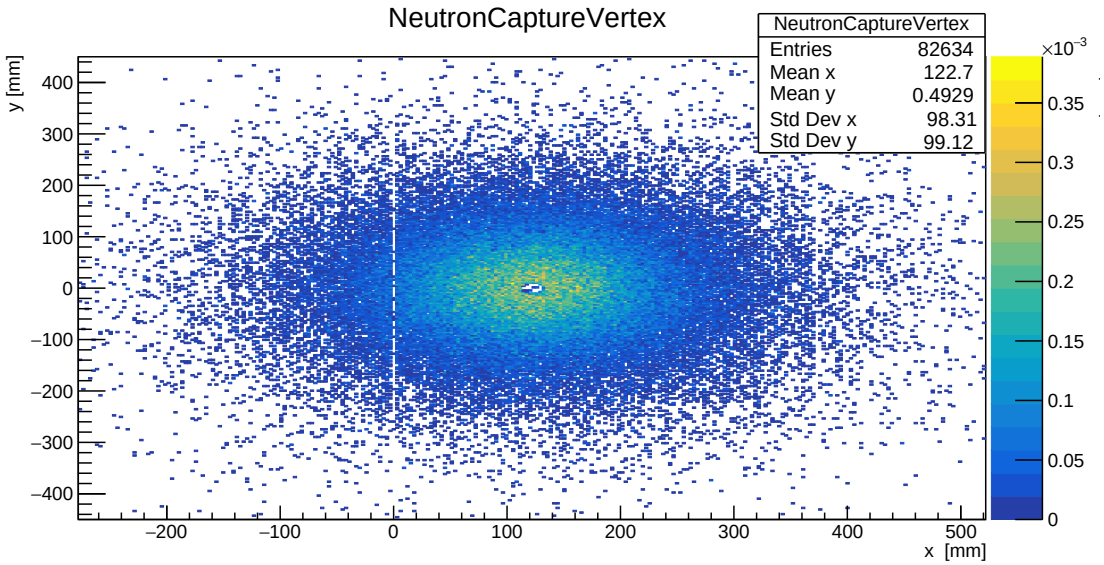

Figure 4.24: Position of AmBe neutrons capture. Fast neutrons from an AmBe source are thermalize in a few microseconds. They diffuse until they are captured, most of the times by Gd. The distance traveled by fast neutrons before being captured is about 10 cm.

The neutron capture efficiency is dominated by the energy cut in the delayed signal. The 50 μs time window has a small effect, only 5% of neutrons are captured after this time (see figure 4.25). However, about 21% of neutron captures produce a visible energy below 5 MeV. Two reasons are at the origin of this behavior: the first one is that neutron captures on Gd produce a gamma cascade with a total energy of 8 MeV, and not a single 8 MeV gamma. Some of these gammas of the cascade can escape or deposit energy in non scintillating materials, giving rise to signals with a total visible energy lower than 5 MeV. The second cause is that some neutrons are captured on H ($\sim$ 7 %), and these events produce only a 2.2 MeV gamma.

Figure 4.25 shows the expected time of neutron capture for fast neutrons from an AmBe source. The data associated to this calibration will provide information about the time of thermalization of fast neutrons, will allow to crosscheck the correct modelization of these physical processes in the Monte-Carlo simulations, and can be used to estimate systematic uncertainties on the neutron capture efficiency.

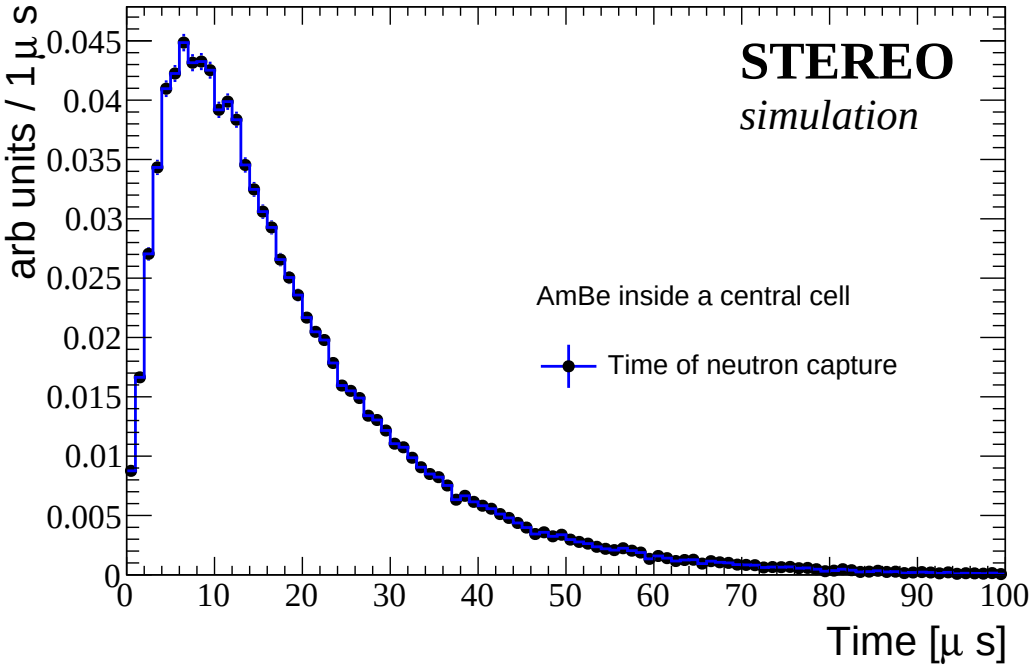

Figure 4.25: Time of neutron capture for AmBe neutrons. Most of then are captured in less than 50μs. About 5% are captured after this time

4.6.2 Geometrical neutron efficiency dependence in one cell

Since the neutron capture efficiency has a strong geometrical dependence due to gamma leaks, it needs to be measured at different positions in the cell. The manual calibration tubes system can provide a few such measurement points. By using this system, the AmBe source can be introduced in three different cells at different heights.

Figure 4.26 shows the neutron capture efficiency measurements for an AmBe source simulated at different vertical positions[2]. The highest value of the neutron capture efficiency is found when the source is placed in the middle of the cell. At this point, gamma leaks are the lowest. In the figure we can clearly observe that the neutron capture efficiency decreases when the source moves away from the center of the cell. In the vicinity of the cell center the decrease is small, but further on it drops quickly. Close to the center of the cell, the most important effect that contributes to the neutron capture in efficiency is the gamma leaks. However, when the source is close to the edge of the cell, more neutrons begin to escape from the cell. These neutrons are often captured on H, being thus lost.

As the calibration tubes are present only in three cells, a method to calibrate at least

[2]In the cell coordinates used to produce this figure, the closest point of the liquid scintillator to the PMTs correspond to ∼+100 mm, while the farthest point to ∼-700 mm

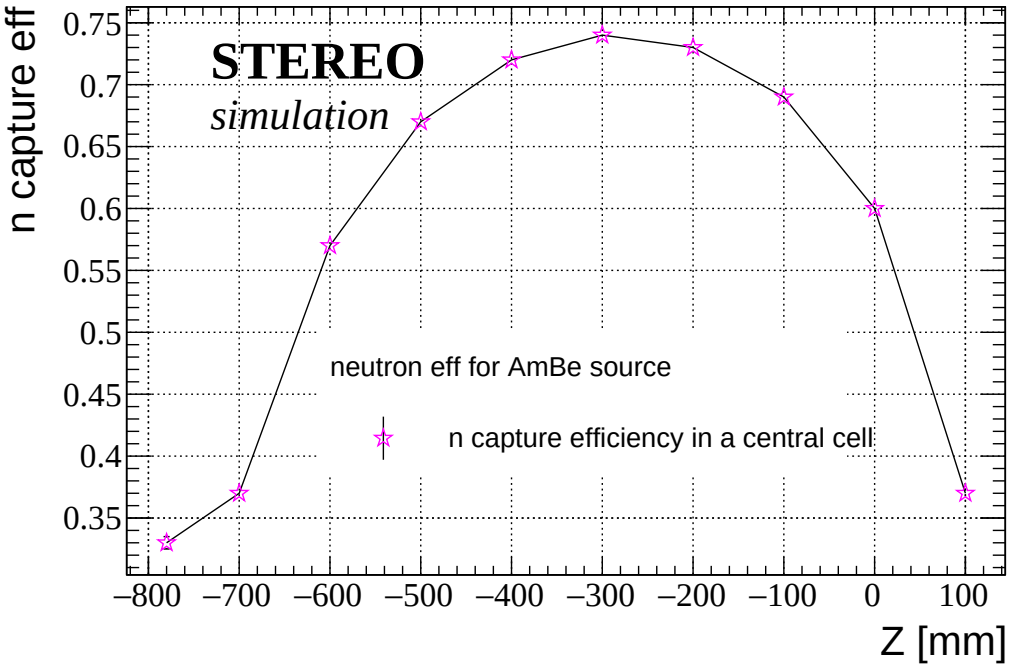

Figure 4.26: Neutron capture efficiency for AmBe source inside a central cell. The source is simulated at different vertical position along the calibration tube.

one referential point in each cell needs to be found.

Since, was we can see in figure 4.24, the typical distance in LS between the point of neutron emission and its capture is ∼10 cm, neutron fired from the side of the steel vessel with the external calibration system will not be useful for neutron efficiency calibration purposes. We can, however, test the viability of calibrating the neutron capture efficiency from under the detector. This corresponds to the point around ∼-780 mm in the figure 4.26. Even if the neutron capture efficiency is lower in this point and not representative of the overall neutron capture efficiency, it can be used to inter-calibrate all the cells. To this end, an additional system to move the AmBe source under the detector will be implemented.

To calibrate the neutron capture efficiency with the AmBe source placed under the detector, the condition to tag neutrons needs to be modified. Since the gamma and neutron emission by the AmBe source is isotropic, and their directions are not correlated, detecting a 4.4 MeV gamma doesn't guarantee that the neutron has also entered the detector. Thus the criteria for the neutron tag is modified here to the total visible energy corresponding to the 4.4 MeV gamma plus the proton recoil. This spectrum can be measured by inverting an AmBe source in the lowest possible position of a manual calibration tube. Then the visible energy of the 4.4 MeV gamma in presence of a proton recoil can be accurately

identified.

4.6.3 Neutron efficiency inter-calibration: central vs border cell

The neutron capture efficiency is expected to be the same in all but the first and last cell, which have a bigger surface of contact with the Gamma Catcher. On one hand, the gamma leakage is different because there is only the Gamma Catcher in one side (short Gamma Catcher) to contain the gamma leakage of these border the cells. In contrast, in central cells gammas need to traverse the equivalent of at least two cells. Thus the probability of gammas to escape the detector is bigger in the border cells. On the other hand, in central cells neutrons can escape to one neighboring cell, where they are also captured on the Gd. In the border cells, this can happen only in one direction. It means that more neutrons can escape to the Gamma Catcher (∼1% more than in the central cells) where they are captured on hydrogen, and produce a visible energy of 2.2 MeV, well below the delayed energy requirement of 5 MeV.

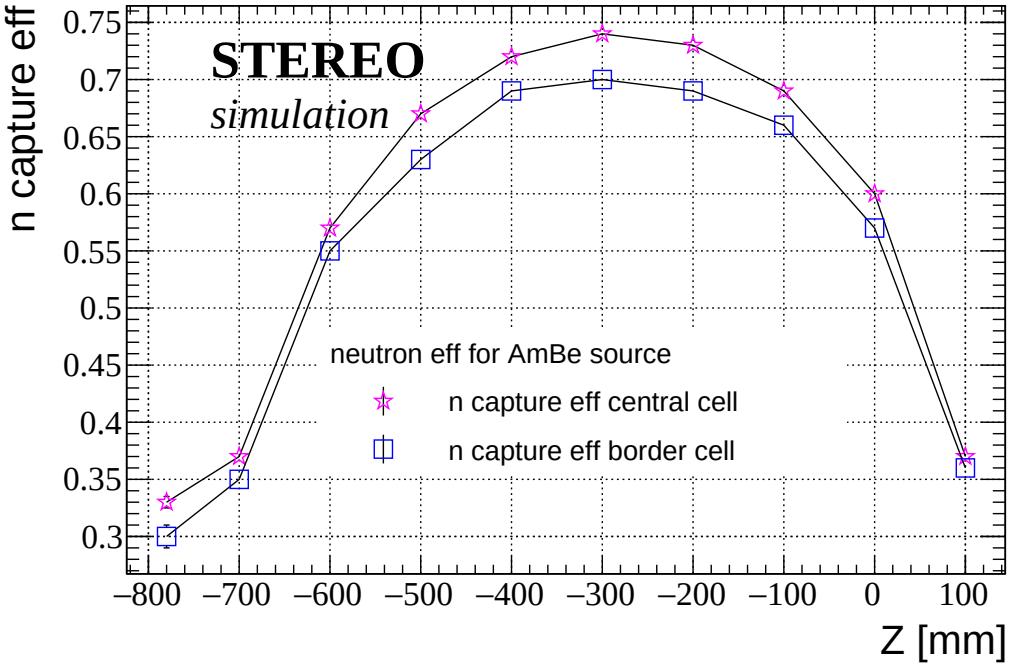

Figure 4.27: Neutron capture efficiency for AmBe: border versus central cell. A difference of about 4% is observed between a central and a border cell.

Figure 4.27 shows the results of an AmBe source simulated in a central and a border cell. A difference of about 4% is observed. When the source is placed under the detector, a difference of about 3% is found. Thus, we confirm that calibrating with the AmBe source below the detector is sensitive to the differences in neutron capture efficiency among the

cells and conclude that they can be inter-calibrated like this.

4.6.4 Systematic uncertainties in the neutron capture efficiency determination

The STEREO physics requirements impose to know the absolute neutron capture efficiency at the 3% level. In order to evaluate the systematic uncertainty on this observable, the following parameters were considered:

The uncertainty in the neutron energy spectrum: As was already said, the neutron energy spectrum of an AmBe source depends on the fabrication process. Different measurements and theoretical predictions have been done of the neutron energy spectrum with and without the 4.4 MeV gamma emission [199, 201, 202, 203, 204, 205].

Since we propose to use the 4.4 MeV gamma to tag fast neutron emission, simulations have been carried out varying the neutron energy spectrum. The results are presented in the figure 4.28, where 6 different cases were taken into account. The differences found in the neutron capture efficiency are small when the source is deployed inside the LS. However, they are bigger when the source is placed under the detector as big as 4 %. Since the calibration source will be the same for all the cells, this variation has no importance for the inter-calibration, because the only goal is to have a relative measure between the cells. Averaged over the cell, a systematic of σ_{spectrum} ~0.6% is found, being about 0.4 % when the source is placed in the middle of the cell, and about 0.8% when it is placed at the bottom.

The delayed energy cut: In STEREO the delayed signal will be searched in a time window of 50μs, requiring a visible energy bigger than 5 MeV. An uncertainty on the exact point of the energy spectrum where this cut happens is induced by the systematic uncertainty on the energy scale. Since the energy scale is expected to be known at the 2% level, the efficiency was computed varying randomly the delayed cut around 5 MeV using a Gaussian distribution with a sigma of 2%. Thus, a systematic $\sigma_{\text{E scale}}$= 1.3% was found.

Changes in temperature: As we saw for the energy scale, changes in temperature can alter the liquid scintillator properties. Temperature can change the LS density, modifying the way of neutrons and gammas interacts within it. A systematic of $\sigma_{\text{temperature}} = 0.1\%$ for changes of temperature of $\pm 2°$C was found. The parameters that were altered by this temperature change are the following: the distance of gamma conversion varied ~0.4%, the fraction of neutron captures on Gd changed by

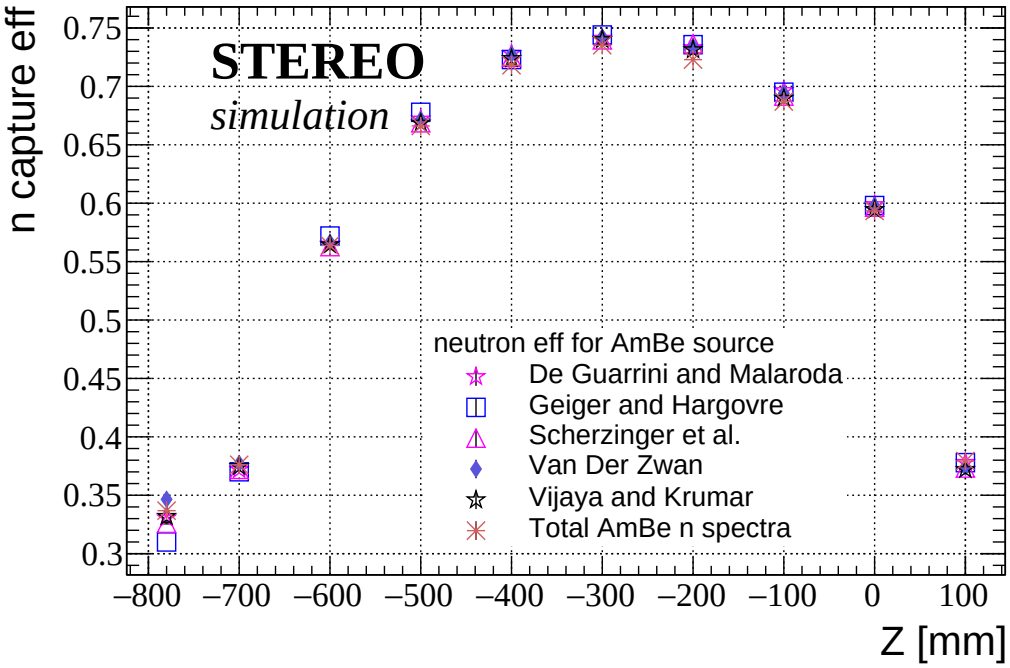

Figure 4.28: Neutron capture efficiency for different AmBe spectrum. The predictions and measurement shown in the figure 4.22 were used to simulate the neutron spectrum of the AmBe source. The neutron capture efficiency was evaluated for each case.

about ∼0.1% and the distance traveled by neutrons before being captured changed by ∼0.1%.

Finally, the total systematic uncertainty in the neutron capture efficiency is estimated to be 1.4%. This value is dominated by the uncertainty coming from the energy scale.

Source	Cut in energy	Temperature	n energy spectrum	Total
AmBe	1.3	0.1	0.4	1.4

Table 4.8: Systematic uncertainty in the neutron capture efficiency. The systematic is dominated by the uncertainty in the energy scale, which is assumed to be known at the 2% level.

4.7 Fast neutron characterization sample and PSD calibration

Besides the use of neutron sources to calibrate the neutron capture efficiency, another important function is to characterize the PSD capabilities of the detector. It is a key

parameter to be measured and studied because it should allows the discrimination of background produced by fast neutrons.

As was already said, in the AmBe source a 4.4 MeV gamma is always emitted with fast neutrons. This gamma can be also used to have a sample of fast neutrons with a known energy. In this case, the mean energy of these neutrons is about 4 MeV. Since the interaction length of the 4.4 MeV gamma is larger than the neutron, it can escape from the calibration cell to one neighboring cell. Ask for this condition is equivalent to demanding for a deposited energy of 4.4 MeV in the closest neighboring cell. Thus, only the interaction of the proton recoil will be produced in the calibration cell. Figure 4.29 shows the total charge in p.e. of the prompt signal in the calibration cell (blue) and neighbor cell (orange) when the AmBe source is deployed inside the calibration cell by using a calibration tube. If we ask for the observation of the 4.4 MeV gamma in the neighboring cell (violet), a sample of fast neutrons is selected in the calibration cell (red). In this way the liquid scintillator response to a fast neutrons of a mean energy of 4 MeV can be characterized. The light leaks associated to the 4.4 MeV gamma that will always pollute the proton recoil sample can be measured with the AmBe source outside the detector and subtracted from the (polluted) proton recoil sample.

4.8 Calibration system concept

As was already said before, the STEREO physics requirements impose that the energy scale must be known at the 2% level in each cell independently, and the neutron capture efficiency at the 3% level. Using the STEREO Geant4 software, we proposed, studied and validated a concept for the radioactive source calibration system. To fulfill all the STEREO physics requirements, it consists of three subsystems:

Automated subsystem to move radioactive sources around the inner detector: This system will allow to move radioactive neutron and gamma sources around the stainless steel vessel which contains the inner detector. Thus, the energy scale and light leaks can be calibrated in all the target cells and Gamma Catcher volumes independently. Moreover, the calibration points at 4.4 MeV (AmBe), and ∼7.1 MeV (n-Fe) can only be obtained in this configuration. In addition, this subsystem could provide access to the monitoring of the vertical detector response to the light collection by using a collimation device.

Automated subsystem to move AmBe source under the detector: The main function of this system will be to inter-calibrate the neutron capture efficiency among the cells by exposing the bottom of the inner detector to an AmBe source. In this way the neutron capture efficiency can be assessed in one point of reference in each

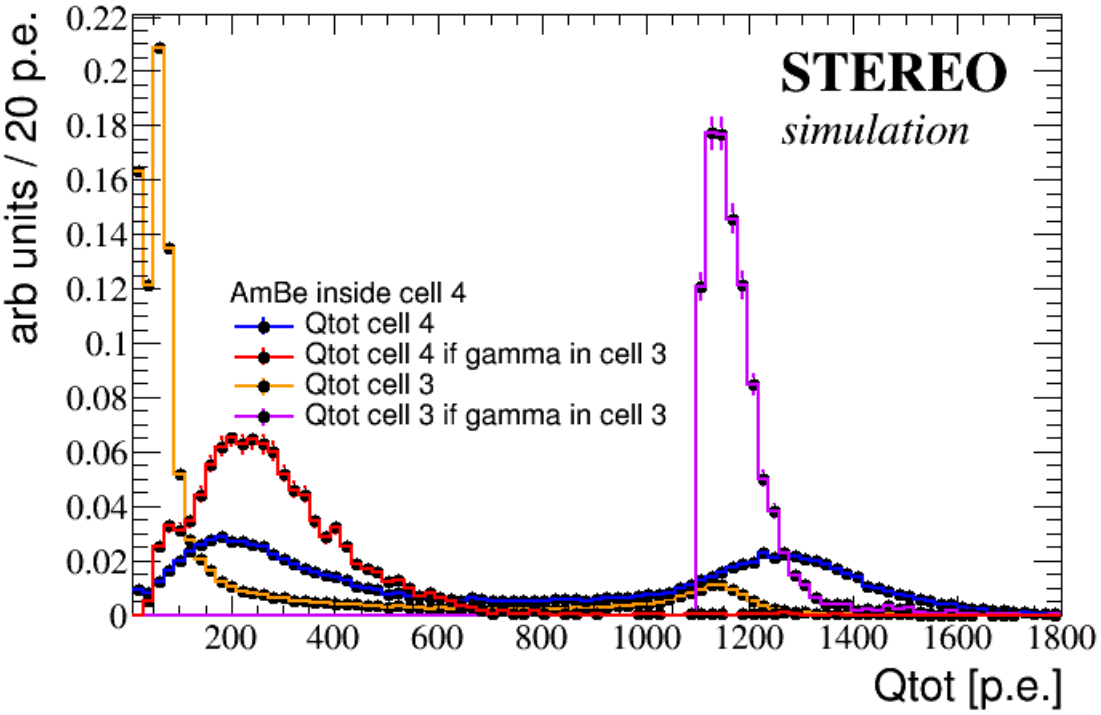

Figure 4.29: Fast neutron sample using the prompt signal of the AmBe source. In order to have only the proton recoil in one cell, the 4.4 MeV gamma is asked to be observed in one neighboring cell. The blue and orange lines shows the total charge when no condition is asked, while the violet (cell 3) and red (cell 4) shows the total charge when the condition is imposed.

cell. In addition this system can be used to calibrate the PSD response in all the cells.

Manual calibration tubes in three cells: The main goal of this system will be to provide access to the absolute neutron capture efficiency within the liquid scintillator in three different cells. In this way the neutron capture efficiency can be measured at different vertical positions. At the same time, the energy scale at low energy, the vertical response to the light collection and the light leaks can be studied. Finally, this system can be used to characterize the PSD with fast neutrons in a few cells.

The final design of the source calibration system which we have seen to meet the STEREO's goals is presented in figure 4.30. A device with two motors moves the external system in the vertical axis. By using a "trolley" mechanism, the sources can be easily introduced and changed through a small door in the internal shielding at the detector rear. Under the detector, an automated system is used to move the AmBe source. Finally, sources can be manually deployed inside the liquid scintillator of three cells using the calibration tubes.

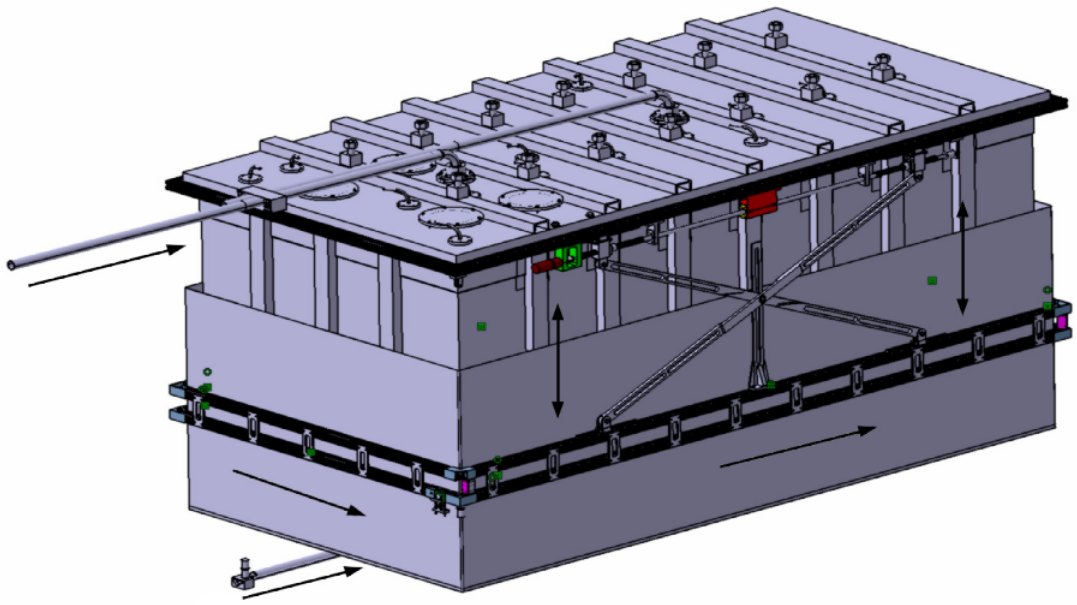

Figure 4.30: The source calibration system of the STEREO experiment. A subsystem to move the gamma sources around the entire detector as well as in the vertical axis has been implemented. In this way the energy scale and non-uniformities in each cell are calibrated. A second system allows to introduce in one central and two border cells (one border cell in this figure) the neutron source. This system is devoted to measure the neutron capture efficiency at different positions on the cell, but can also be used to calibrate the energy scale in these cells. Finally a third system is used to move the neutron source under the detector, using this system the neutron capture efficiency can be inter-calibrated among all the cells.

The external calibration system has already been fabricated at LAPP (Annecy) as can be observed in figure 4.31. During the summer (2016) tests to validate the automation calibration cycles were carried out in order to guarantee that no source will get stuck close to the detector vessel while operating it. Each automated calibration cycle consists in the movement of the "trolley" around the detector at three different heights, stopping in all the expected calibration points (28x3 calibration points in total, in front of each position of the PMTs). About 80 cycles were performed in total. No worrying malfunctions were observed. The system has been moved to the ILL and is ready for the installation.

4.9 Calibration using cosmic-ray induced radioisotopes

The expected muon rate at the STEREO casemate is about 500 Hz. The main product of muon related interactions in a liquid scintillator detector are fast neutrons [159, 209, 210]. In the case of STEREO, we might be able to use them to calibrate and monitor the LS

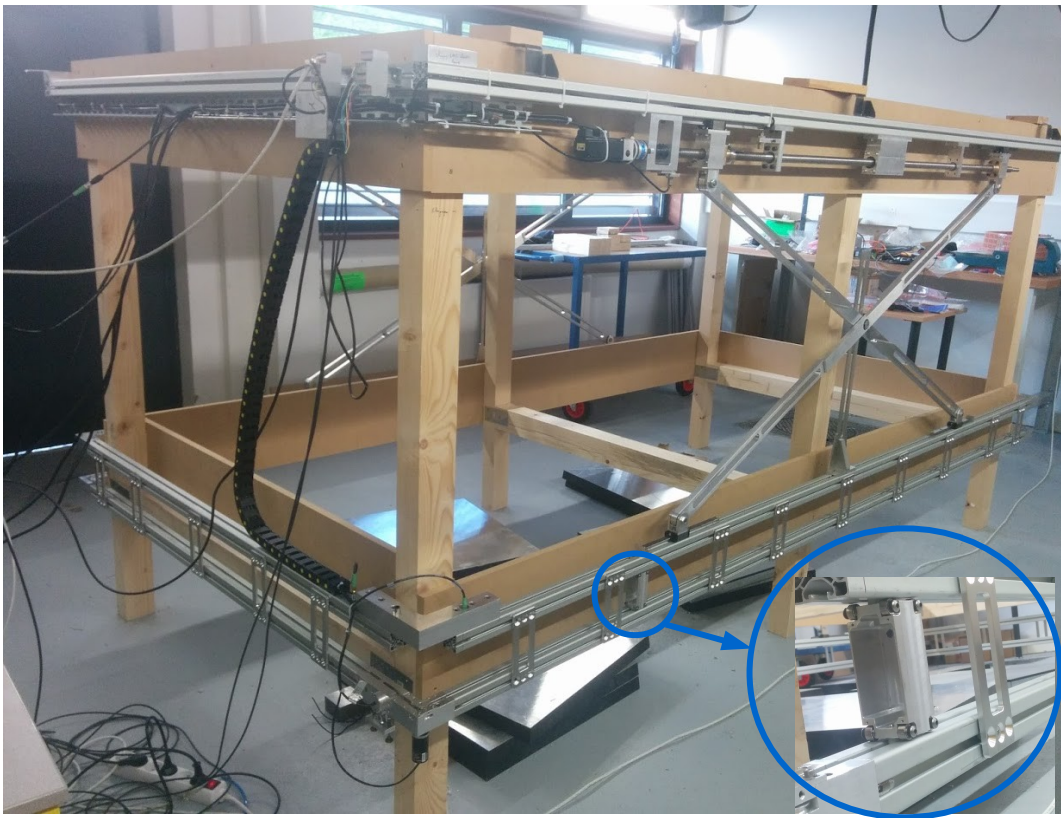

Figure 4.31: The external calibration system of the STEREO experiment. This automated system allows to move gamma and neutron sources around the entire detector as well as in the vertical axis.

evolution throughout the time, as it has been already mentioned.

One of the most abundant products of muon spallation is ^{12}B. It has a half life of about 20 ms and decays by β^- emission with an energy up to 14 MeV. Electrons thus emitted could be used to crosscheck the energy scale response to electrons. Recent works [160, 159] have shown that Geant4 can predict the correct cosmogenic radioisotopes production by muon spallation within a factor of two. In order to estimate the yield of ^{12}B in STEREO, vertical muons with an energy of about 2 GeV were simulated with Geant4. The yield of ^{12}B is expected to be $\sim 2 \times 10^{-5}/\mu$, which leads to about $\sim$ 1000 events per day. The yield of fast neutrons on the other hand is estimated to be $\sim 2 \times 10^{-4}/\mu$, which leads to about $\sim$ 7000 fast neutrons per day. Since the mean energy of muons reaching the earth's surface is about 4 GeV [211], and given that STEREO has an overburden of of about 18 m.w.e., the real muon energy in STEREO is expected to be higher, so these values can be considered as underestimated.

In bigger experiments as Daya-Bay or Double-Chooz the use of ^{12}B to calibrate the detector response to electrons was achieved. However, given the small volume of the

STEREO liquid scintillator and the expected background rate (1 KHz), this calibration technique is very challenging because of the long life time of the ^{12}B. Fast neutrons, however, should be a possibility to monitor the detector performance and check the time dependence of the calibration daily.

4.10 Conclusions

We have proposed a concept for the calibration of all the relevant parameters of the experiment: the energy scale, the neutron capture efficiency, the non-uniformity response of the detector, PSD and fast neutron response, and the light leaks among the different optically separated volumes. Using STEREO's Geant4 geometry model and simulation software, we have studied and validated it, by showing that STEREO's goals for the energy scale and neutron efficiency will be attained. Thus, to fulfill STEREO's physics requirements, it integrates three subsystems which are mutually complementary.

The energy scale calibration can be performed either with sources inside or outside the liquid scintillator by using the appropriate vetoes to extract the full energy peak. Above 2.2 MeV (n-H) only the external system provides a mechanism to calibrate at 4.4 MeV with the AmBe source. In addition, this system allows the use of neutron captures on the iron of the steel vessel in order to calibrate the detector energy response at high energy ($\sim$7.1 MeV).

The vertical response to the light collection can be studied with the internal system. However, this response could be also studied if a collimation mechanism is implemented in the external system. Light leaks can be measured either with the internal or the external system.

The absolute neutron capture efficiency inside the cells can be only assessed with the manual calibration tubes. For this purpose, a procedure using the 4.4 MeV gamma from AmBe source has been defined. Finally, using a system to move sources under the detector, the inter-calibration of the relative neutron capture efficiency between cells can be addressed by exposing the bottom of each cell to an AmBe source. Either this system or the manual calibration tubes can be used to study the proton recoils due to fast neutrons and to measure the γ/n separation capabilities of the PSD.

The proposed automated subsystems have been fabricated and tested at LAPP during the summer of 2016, and have been transported to the ILL for installation of the STEREO experiment.

- Chapter 5 -

Characterization of the neutrino signal and the gamma background, and methods to reject this background

5.1 Introduction

This chapter is devoted to the characterization of the neutrino signal and the gamma background. To this end, the STEREO Geant4 software was used to simulate both signal and background. Neutrino events were generated using the STEREO neutrino generator [212], while gamma background was injected using the measured gamma spectrum at the PN3 casemate [156]. One characteristic that makes STEREO different from current reactor experiments as Double Chooz, Daya Bay or RENO is its segmentation. Thanks to this, the prompt and delayed signals exhibit different signatures. It is characterized by the 511 keV gamma leakage to the neighboring cells in the prompt signal and a bigger gamma leakage to the neighbors in the delayed signal. More importantly, the same segmentation also gives a handle for background reduction, as we will see in section 5.6.

In the next sections, prompt, delayed and gamma background topologies are studied separately, and the effect of the selection criteria and its efficiency on the gamma background rejection are analyzed. Then, a method to reject gamma background at high energy is presented, which is based on the topology of the charge distribution. The effect of the selection criteria on the prompt energy resolution is studied. Finally, a proposal to get small samples with improved resolution is presented.

5.2 Cosmic ray induced background

As was already discussed in section 4.9, fast neutrons induced by spallation interactions of muons on the material surrounding the detector vessel (most notably the Pb shielding) are one of the most abundant sources of correlated background. In STEREO, the rate of fast neutrons is expected to be higher than 7000 n/day (see section 4.9). Most of the background generated by these fast neutrons can be suppressed by tagging the passage of the muon or its shower in the muon veto or the detector itself. Nevertheless if the muon is not detected, fast neutrons produced in the detector shielding or in the surrounding materials can reach the target and produce a correlated background. In this case, fast neutrons can be identified by using the PSD capabilities of the STEREO LS.

Common cosmogenic radioisotopes also produced by spallation are ^{8}He and ^{9}Li, which have lifetimes of 257 ms and 172 ms respectively, much longer than the expected muon veto of STEREO ($\sim 100\mu$s). They undergo β decay followed by neutron emission, which makes them obvious correlated background candidates. Since we simulated 300000 muons traversing STEREO for calibration purposes (see section 4.9), we decided to try and estimate the abundance of these correlated backgrounds. The simulations yielded 0 of these radioisotopes for 300 000 muons going through the STEREO LS (Target and GC). Thus an upper limit in the number of ^{8}He/^{9}Li events per day lower than 150 at 95% confidence level is found. This value is not negligible with respect to the expected number of $\overline{\nu_e}$ events observed per day ($\sim$400), and a bigger statistical sample should be simulated to better asses the importance of this background.

5.3 Selection criteria

The selection criteria aim to extract signal rejecting most of the background. The gamma background is expected to be originated by neutron captures within and in the vicinity of the STEREO detector. The majority of gammas coming from the outside will be stopped in the internal shielding. Nevertheless a small fraction can traverse the shielding and reach the inner detector. In this scenario, the Gamma Catcher can be put to use as a veto and will play a crucial role in the rejection of background coming from the outside.

The baseline STEREO selection criteria are:

- Both prompt and delayed vertices reconstructed in the target
- $E_{vis}^{Prompt} > 2$ MeV
- $E_{vis}^{Delayed} > 5$ MeV

- $\Delta t < 50 \mu s$
- $E_{\text{vis}}^{\text{T}} > E_{\text{vis}}^{\text{GC}}$

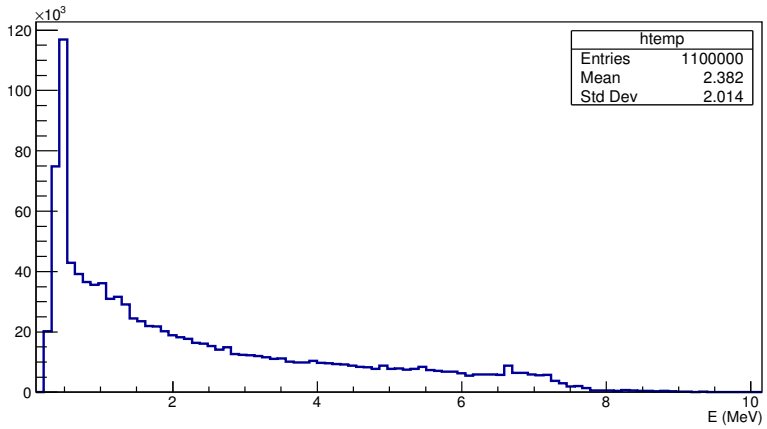

Figure 5.1: Gamma background spectrum. It was measured using a germanium detector at the PN3 casemate in 2014. New shielding has been installed in and around the STEREO casemate, which will decrease the gamma count and change the spectrum shape. A new measurement campaign is ongoing.

In the next sections we will refer to these cuts as the "baseline selection criteria". If one of these cuts is modified, it will be explicitly indicated. $\overline{\nu_e}$ events were generated using the STEREO neutrino generator. Thus, a sample of 620 000 $\overline{\nu_e}$ events (IBD) was generated in the whole detector. In order to evaluate and characterize the gamma background, γ's with an energy spectrum following Figure 5.1 were simulated uniformly distributed in the four sides outside the still vessel which contains the inner detector and with an orthogonal direction to the vessel walls (see figure 5.2). This spectrum was measured at the PN3 casemate in 2014 using a germanium detector. The estimated rates of prompt and delayed gamma backgrounds were 240 Hz and 64 Hz respectively [213], leading to an accidental rate of ∼60 000 events/day, which is much higher than the STEREO physics requirements (∼400 events/day). In order to reduce the accidental rate produced by gammas, additional shielding has been installed at the PN3 casemate, which includes borated polyethylene (to avoid neutron captures on steel structures) and lead (10 or 5 cm depending on the direction). However, since the gamma background is diffuse, it is not clear at the moment the real effect of these improvements. We should then improve the selection criteria to reduce as much as possible these rates. The goal of STEREO is to have a delayed background rate lower than 1 Hz, therefore special attention should be given to the reduction of delayed background. The gamma background spectrum that STEREO will see will likely be shifted towards lower energies by the passage through the extra shielding. A new, ongoing measurements campaign will inform us soon. In the meantime, the choice of Figure 5.1 represents a pessimistic estimate. In table 5.1 the effect of the

baseline selection criteria on the signal and gamma background is shown. The efficiency of signal detection is dominated by the prompt and delayed energy cuts of 2 MeV and 5 MeV respectively.

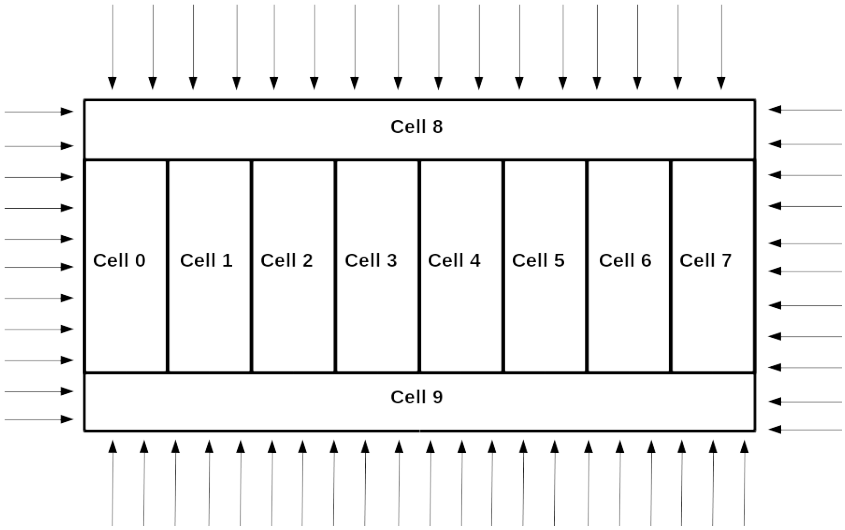

Figure 5.2: Gamma background direction. Gammas were generated uniformly distributed outside the inner detector and with an orthogonal direction to the target. To study the effect of the gamma's direction, the border cells were used taking into account all the events and only events coming from the short sides (section 5.6).

For the prompt neutrino signal the selection criteria should include an upper energy bound on the Gamma Catcher given by the energy leaks originated by the two 511 keV gammas. Since we have the back-to-back 511 keV gamma condition, if one of the two gammas points outwards, the other one will be pointing inwards and it is highly improbable to lose the two 511 keV gammas. This only occurs in less than 1% of the events. In general only one of these can escape and be detected in one side of the Gamma Catcher. Furthermore, only in the border cells both 511 keV gammas can escape to two different Gamma Catcher volumes. This upper energy bound can accurately be measured in each part of the Gamma Catcher by using the ^{68}Ge gamma source with the external calibration system.

Figure 5.3 shows the expected visible energy in the Gamma Catcher for a ^{68}Ge gamma source placed outside the steel vessel by using the external calibration system. The peak of the distribution produced by 511 keV gammas is found close to 0.35 MeV. This low value is a consequence of the liquid scintillator non-linearity, 511 keV gammas produce a visible energy below 0.55 MeV in about 99.9% of cases. Consequently, prompt signals reconstructed in one central cell should have a visible energy in one long Gamma Catcher below 0.55 MeV. What's more, prompt signals reconstructed in a border cell can satisfy at the most the same condition in two different Gamma Catcher volumes: a 511 keV gamma

Selection requirement	Efficiency (%) ν signals	Efficiency (%) γ background
$E^{total}_{vis\ prompt} > 2MeV$	80.2	24.9
$E^{T}_{vis\ prompt} > E^{GC}_{vis}$	80.0	8.2
Prompt vertex in Target	79.9	8.2
$E^{total}_{vis\ delayed} > 5$ MeV	54.8	7.8
$E^{T}_{vis\ delayed} > E^{GC}_{vis\ delayed}$	49.8	2.9
Delayed vertex in Target	49.2	2.9
$\Delta t < 50\mu s$	47.1	-

Table 5.1: Efficiency of the selection criteria on the signal.

in one long side and the other in a short side of the GC. Thus a trivial addition to our selection criteria is $E^{GC_i}_{vis\ prompt} < 0.55$ MeV, which reduces the prompt gamma background from 7.8 to 5.8 %, and it only reduces the signal from 79.9 to 79.6 %. In the next sections we study the prompt and delayed gamma signals in order to explore different methods to improve the background rejection effectiveness of the selection criteria.

5.4 Prompt topologies

Prompt signals in STEREO will be generated by positrons with kinetic energies ranging from 0 to 9 MeV. Positrons deposit their energy almost instantaneously in a few millimeters of the LS and then annihilate with an electron producing two back-to-back 511 keV gammas.

When the IBD process takes place in the center of the cells, almost all the energy (both the positron's kinetic energy and the two annihilation gammas) is deposited within the liquid scintillator of only one cell. Nevertheless, if the IBD process happens within ∼10 cm of the edge of the cells, at least one 511 keV gamma can easily escape to one neighboring cell or the Gamma Catcher. It can also be completely lost when it interacts in non-scintillating materials, such as the acrylic walls separating the cells and Gamma Catcher.

Figure 5.4(top) shows the true deposited energy for positrons of 1 MeV uniformly

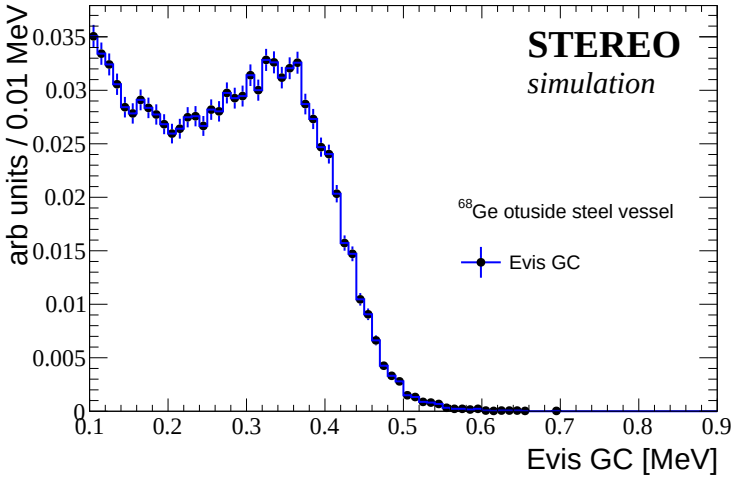

Figure 5.3: Gamma catcher visible energy for ^{68}Ge placed outside the steel vessel.

distributed in a central cell. In most events at least one 511 keV gamma escapes from the cell of interaction (in $\sim$ 70% of events more than 250 keV are deposited in other volumes, both active or inactive). Nevertheless, in general it is recovered in the neighboring cells or Gamma Catcher (in $\sim$ 50% of events more than 250 keV are deposited in neighboring cells or the Gamma Catcher). Thus, prompt signals at low energy are characterized for a concentration of charge in one cell with a shoulder on the left side as can be observed in the figure 5.4(bottom). The shoulder on the left correspond to the leakage of one 511 keV gamma. Thus, for positrons below 1 MeV, the deposited energy is dominated by the two 511 keV gammas, and the charge is distributed in at least two cells. However, this effect becomes less important for positrons of higher energy, where the energy carried by the leaked gammas ($\lesssim$500 keV) represents a small fraction of the total deposited energy. This effect is shown in figure 5.5, where we can observe that the amount of collected charge in the cell of interaction increases with the positron energy.

5.5 Delayed topologies

The delayed signal of the IBD process in STEREO is produced by the neutron capture on Gd. It gives rise to a gamma cascade with a total energy of about 8 MeV. On average 4 gammas are emitted in each cascade, leading to a gamma mean energy of about 2 MeV.

Since the $\sim$ 4 gammas are emitted isotropically an their conversion length is higher than the 511 keV gamma's, most often the deposited energy of delayed events is distributed in three cells and/or the Gamma Catcher. The charge of delayed signals is thus much more distributed than the prompt signals. Figure 5.6(top) shows the distribution of the deposited energy for delayed events reconstructed in a central cell. There are only a few

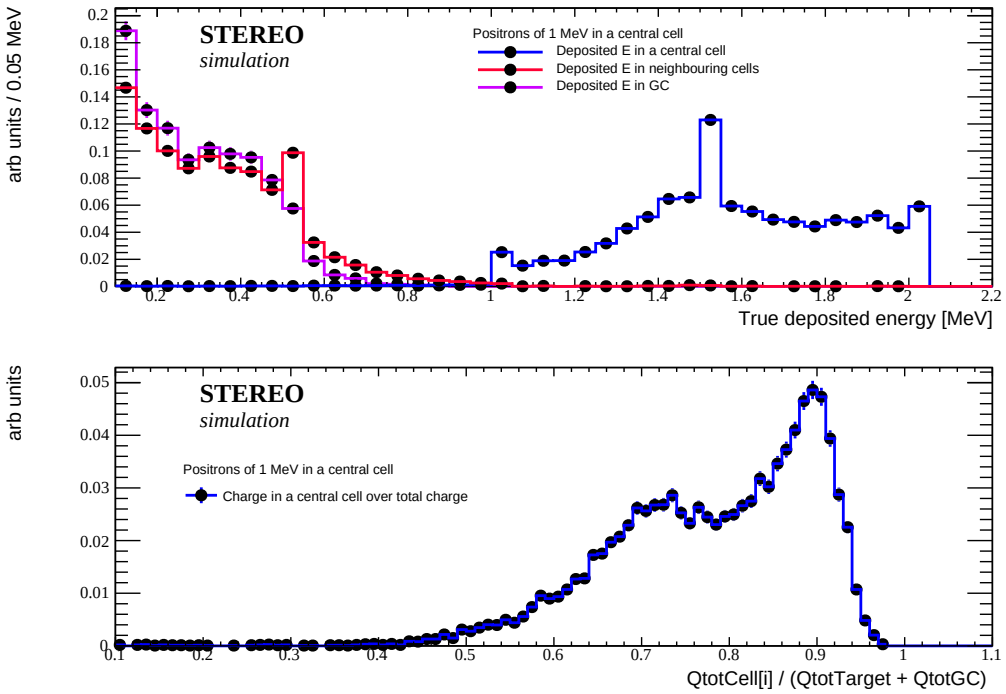

Figure 5.4: (top) Deposited energy for positrons of 1 MeV uniformly distributed in a central cell. In most cases at least one 511 keV gamma leaks to the neighboring cells or GC. (bottom) Collected charge in cell of interaction for positrons of 1 MeV. Most of the charge is collected in the same cell, while in neighboring cells a 511 keV gamma can be registered.

events where the whole energy is deposited in the same cell. This fact is reflected in the figure 5.6(bottom), where the collected charge in the cell of reconstruction over the total charge in the Target plus the GC is presented. A long shoulder on the left side is observed.

The distribution of charge has a direct influence in the vertex reconstruction. On one hand, the charge of prompt events is concentrated in one cell and so the vertex is usually found in the center of the cells. On the other hand, in delayed events the charge is distributed in at least three cells, and the vertex is more dispersed in all the cells. Figure 5.7 shows the vertex reconstruction for prompt and delayed events. Prompt signals are reconstructed in the center of the cells, while delayed events are reconstructed more uniformly. Thus, it is highly unlikely to have prompt events reconstructed around the walls (±100 mm) between cells.

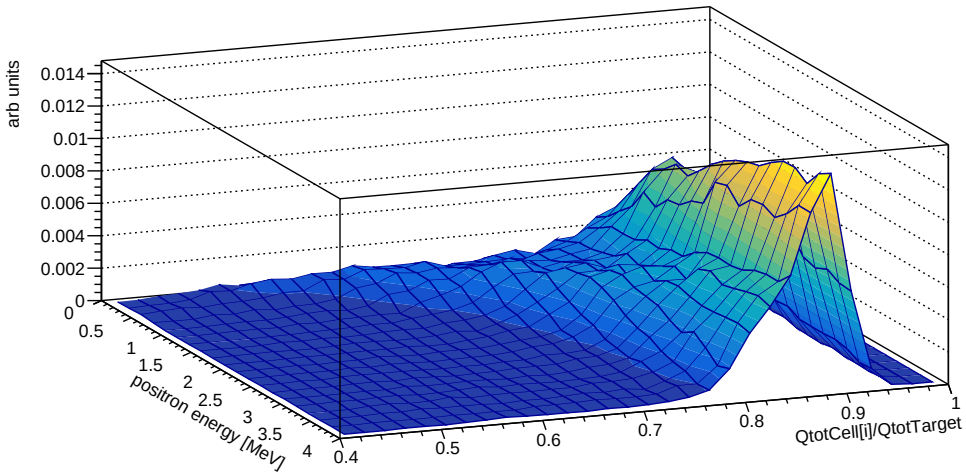

Figure 5.5: Charge distribution for positrons with energies from 0 to 4 MeV. The fraction of collected charge in the cell of interaction increases with the positron's energy.

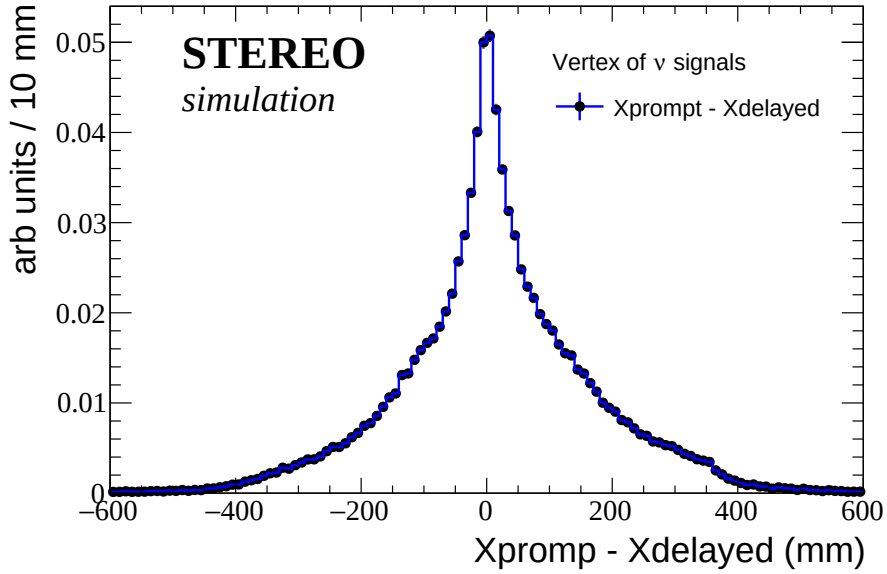

Figure 5.8: Distance from prompt to delayed vertex. Neutrinos are produced using the STEREO ν generator. Events passing all the expected vetoes are reconstructed using the barycenter of charge. The distance of both vertex is found lower than the size of a cell in about 98.4% of cases.

Prompt and delayed signals are correlated in time and position. On one hand, positrons lose their energy just in a few millimeters and then annihilate with an electron. On the other hand, neutrons thermalize and diffuse some centimeters ($\sim$10 cm) before they are captured some $\sim 15\mu s$ later. Most of prompt signals will be reconstructed in the same cell where the the IBD took place, while delayed signals can be reconstructed in the neigh-

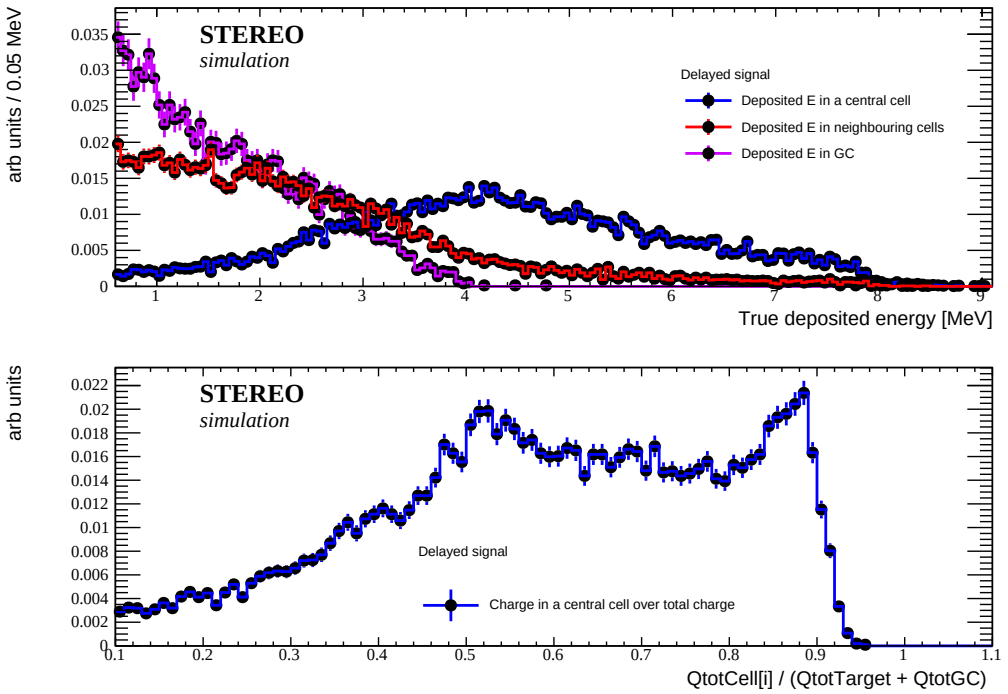

Figure 5.6: (top) Deposited energy for delayed signals in a central cell. The energy is most often deposited in at least 3 cells plus the Gamma Catcher. The condition of having more energy in the target than in the Gamma Catcher and a cut of 4 MeV have been applied. (bottom) Charge distribution in the Target of delayed signals reconstructed in a central cell with the same cuts as for the plot on the top.

boring cells. Both signals should then, be reconstructed nearby. Indeed, in about 98.4% of events, the distance of separation between the reconstructed vertex of both signals is lower than the size of a cell $\sim$ 374 mm (see figure 5.8). In addition, in about 75.6% of events both signals are reconstructed in the same cell.

5.6 Gamma background discrimination

As we have seen in section 5.3, the gamma background is much too high in STEREO, in spite of making the GC play the role of an active veto ($E^{\mathrm{T}}_{\mathrm{vis}} > E^{\mathrm{GC}}_{\mathrm{vis}}, E^{\mathrm{GC}}_{\mathrm{vis}} < 0.55\mathrm{MeV}$). This lead us to consider handles to reduce this background. Can the reconstructed vertex position of any help? What about the charges are distributed among the cells and GC?

Besides the cut on the deposited energy in the Gamma Catcher, a requirement on the reconstructed vertex can be applied. Indeed, prompt neutrino signals are reconstructed in the center of the cells, while gamma background is biased to the border of the cells. In fact, 99.6 % of prompt signal is located $\pm$ 200 mm around the center of the cells. The

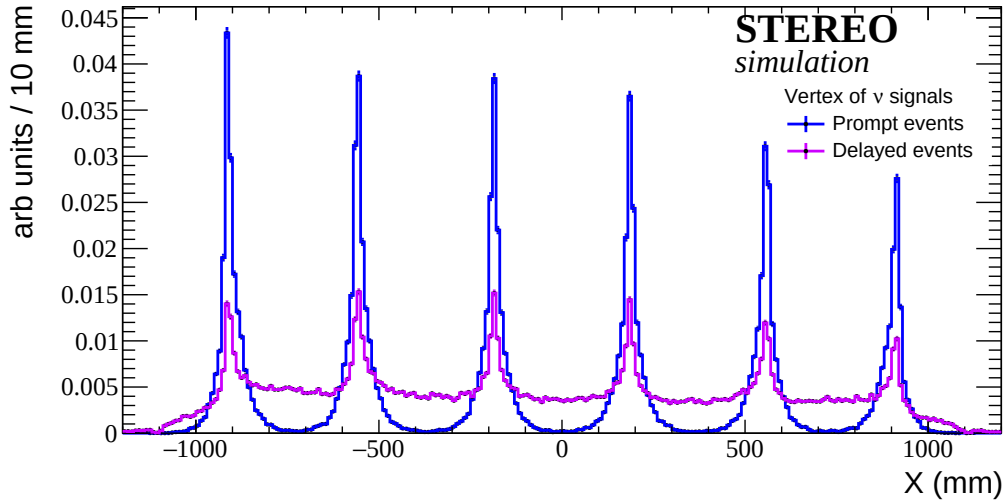

Figure 5.7: Reconstructed vertex of ν signals (selection criteria being $E_{vis}^{Prompt} > 1.1$ MeV, $E_{vis}^{Delayed} > 4$ MeV). The blue line corresponds to the prompt events, where all the charge is concentrated in one cell and the vertex is usually reconstructed in the center of the cells. The violet line correspond to the delayed signals, where the charge is more dispersed.

barycenter of prompt signals and background can be observed in the figure 5.9.

Figure 5.9(top) shows the barycenter of prompt signal and gamma background simulated by placing a ^{60}Co gamma source outside the detector and reconstructed in the target. The conditions of having a total visible energy of more than 1.1 MeV and a visible energy in the target larger than the Gamma Catcher were applied. The blue histogram shows the barycenter of prompt signal while the red corresponds to background originated by a ^{60}Co gamma source. An upper bound on the energy in the Gamma Catcher of 0.55 MeV can be applied, which decreases the background by 19% (violet histogram). If an additional cut on the barycenter (<200 mm) is added, the background reduction reaches 30%.

However, the effectiveness of these cuts depends strongly on energy. In order to study this dependence, neutron captures on the H of the Gamma Catcher can be used to simulate 2.2 MeV gamma background, and an AmBe source to simulate gamma background above 4 MeV. The vertex reconstruction of this background is presented in figure 5.9(middle and bottom). It is found to be less biased than for low energy gammas. The conditions of having a total visible energy larger than 2 MeV (2.2 MeV gamma from n-H) and 3 (4..4 MeV gamma from AmBe) MeV and a visible energy in the target larger than the Gamma Catcher were imposed. Thus, the most effective cut in these case is asking for a deposited energy in the Gamma Catcher lower than 0.55 MeV. This reduces the background by 16% and 37% respectively. Adding an extra cut on the barycenter (y <200 mm) only improves

the result by ∼1% and ∼0.1% respectively.

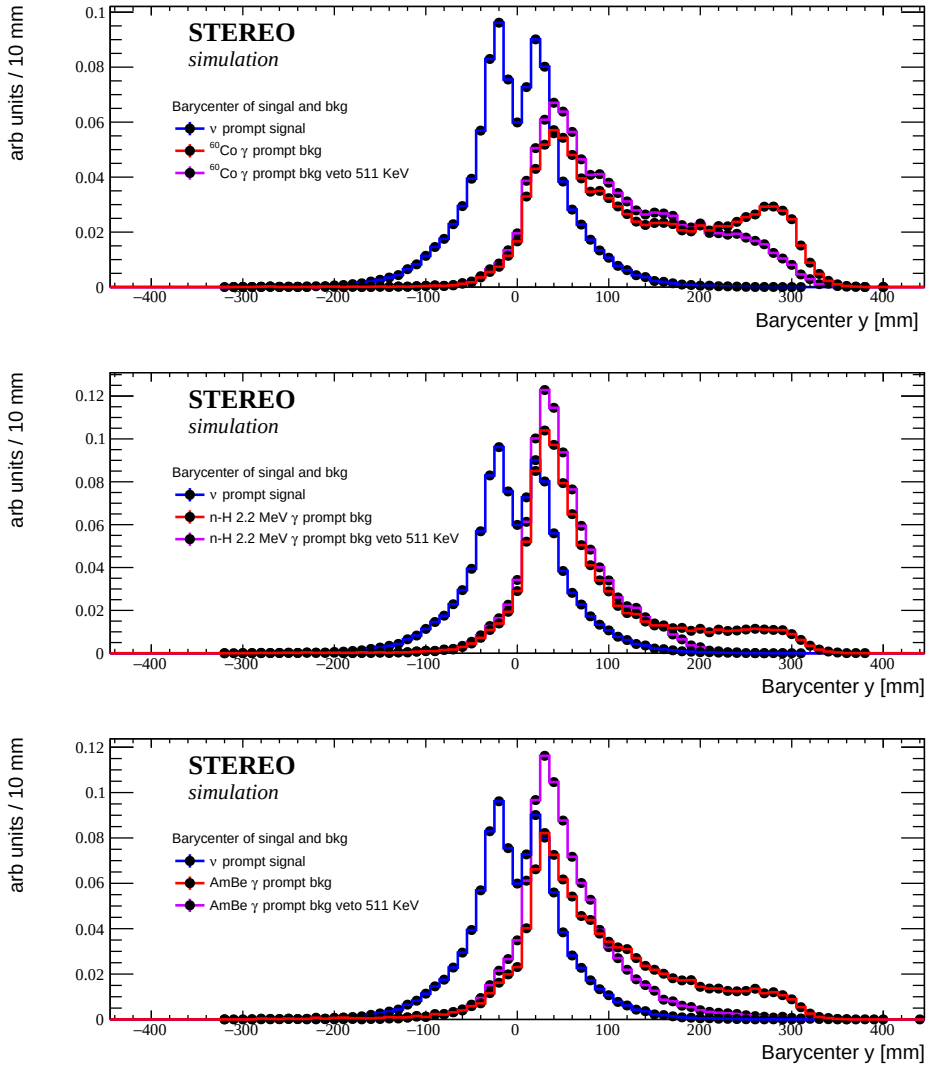

Figure 5.9: (top) Barycenter of gamma background simulated by placing a ^{60}Co gamma source outside the detector. Gammas from ^{60}Co have energies of about 1.25 MeV. Barycenter of events generating a total visible energy above 1 MeV and with a visible energy in the target larger than the Gamma Catcher is shown in red. The violet histogram shows events when an additional cut on the deposited energy (<0.55 MeV) in the Gamma Catcher is used. (middle) Barycenter of 2.2 MeV gamma background simulated by neutron captures on the H of the Gamma Catcher. (bottom) Barycenter of gamma background simulated by using an AmBe source. The most effective cut in this case is the cut on the deposited energy in the Gamma Catcher.

The vertex reconstruction of events satisfying the baseline selection criteria is shown in Figure 5.10. In this scenario, border cells are the most exposed to this background as is shown in table 5.2. Thus in border cells the probability of have a gamma background

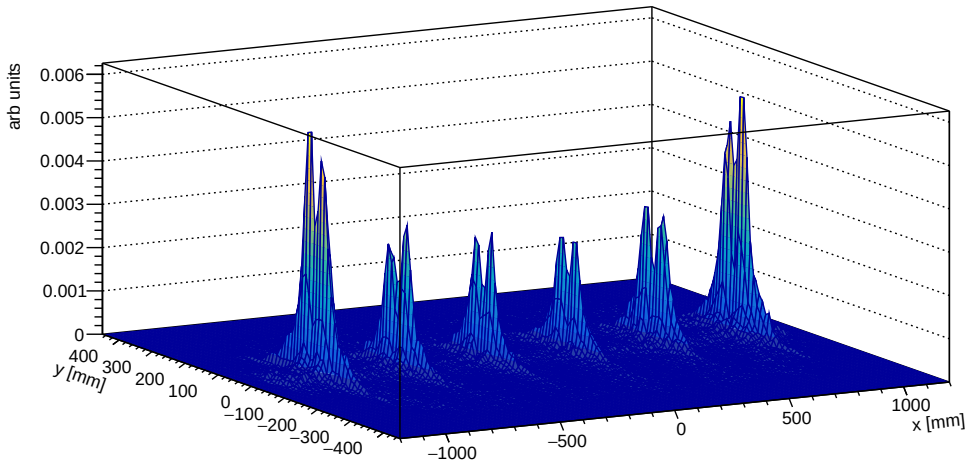

Figure 5.10: Barycenter of gammas coming from the outside which satisfy the baseline selection criteria. Gammas are generated outside the steel vessel with an orthogonal direction to the vessel walls.

is about 21% while for center cells this probability is only ∼13%. As was shown in section 5.5, the vertex of prompt and delayed signals are correlated in position, and this information can be used to reject accidental background. Using the information of table 5.2, the probability of having two consecutive events in the same cell is estimated to be ∼21% for the border cells and ∼13% for the center cells, which implies the rejection of 69 and 87 % of accidental background while keeping 75.6% of signal if we demand the prompt and delayed to happen in the same cell. A closer cut is demanding the same cell or the intermediate neighbors. In this case, the background rejection attains about 50% while keeping 98.5% of signal.

Cell	P (γ bkg)
1	21.4%
2	15.8%
3	12.6%
4	12.9%
5	15.9%
6	21.5%

Table 5.2: Normalized probability of gamma background, for gammas generated outside the steel vessel with an orthogonal direction to the vessel walls. Border cells are the most exposed to gamma background coming from the outside

Since the probability of gamma background faking a delayed signal is particularly high with respect to the goals for such background, and the reconstructed vertex does not help

very much, we can look at the topology of the charge distribution. Indeed, in general gamma background is produced by an only gamma, while delayed signals are originated by a gamma cascade. Thus, gammas producing a delayed background are in general converted in only one cell, whereas the gamma from the Gd cascade are likely to escape to neighboring cells or the GC.

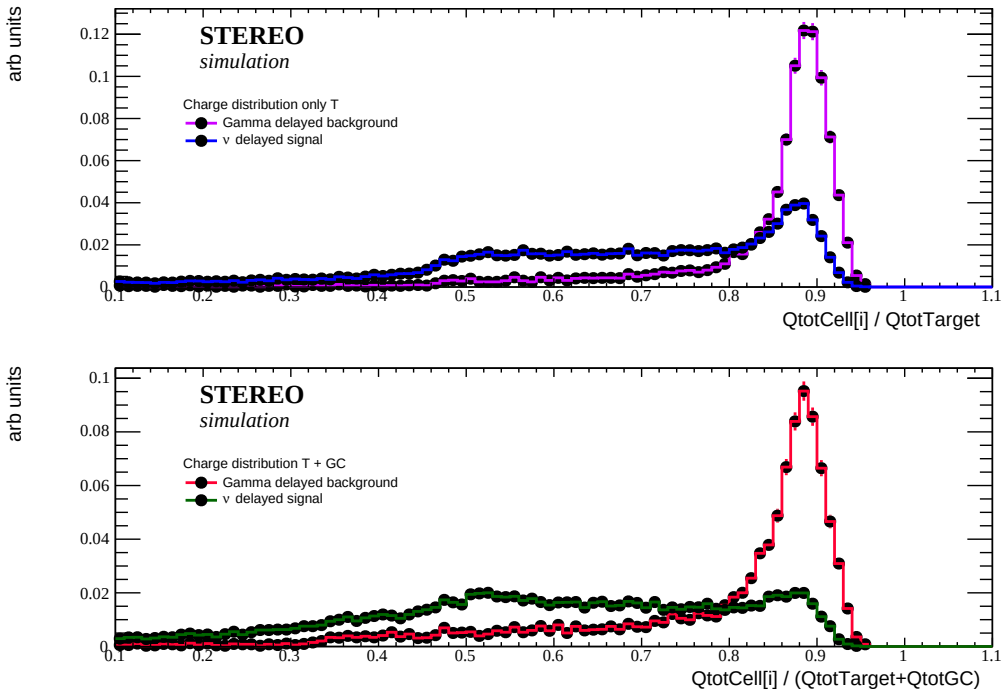

Figure 5.11: (top) Charge distribution of the gamma background compared to the neutrino delayed signal considering only the charge of the Target (bottom) Charge distribution of the gamma background compared to the neutrino delayed signal and considering the total charge collected in the Target plus the GC.

Figure 5.11 shows the distribution of charge for gamma background and delayed signals. The charge of gamma delayed background is concentrated in one cell which differs from delayed signals where in general it is distributed in at least three cells and/or the Gamma Catcher. In this way a fraction of gammas producing delayed background and which meet the baseline selection criteria can be discriminated.

Figure 5.12 shows the potential of use the distribution of charge to gamma background discrimination. The use of the the distribution of charge in the target plus Gamma Catcher instead of only the target produces improved results. Thus, it could be possible to reject about 50% of background while keeping 90% of signal.

A difference of about 2% between central and border cells is observed. At the origin

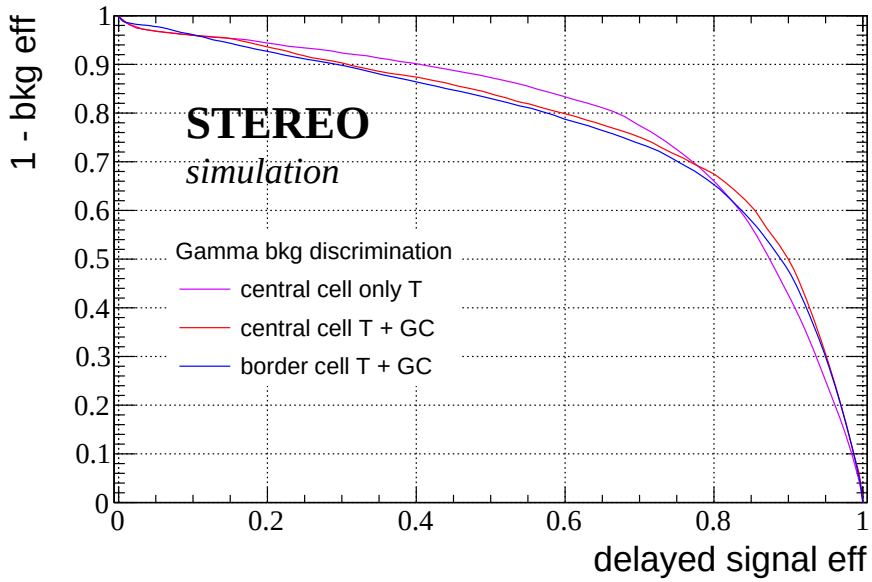

Figure 5.12: Gamma background rejection in a central cell taking into account only the charge in the target (violet) and taking into account the charge in the target plus the Gamma Catcher (red). Gamma background rejection in a border cell taking into account the distribution of charge in the target and Gamma Catcher (blue).

of this difference is the gamma background direction. Gammas coming from the long sides of the Gamma Catcher have about 90 cm of liquid scintillator of one cell to convert (the cell width). However, gammas coming from the short sides of the Gamma Catcher can interact in two cells because they only see 37 cm of LS (the cell length). Thus, for border cells it is more likely that gammas traverse the first cell and interact in a second cell.

To study the effect of the gamma direction, events reconstructed in the border cells (1 and 6) and coming only from one short side of the Gamma Catcher were used. Even in the most unfavorable case, it could be possible to reject more than 40% of background while keeping 90 % of signal, as shown in figure 5.13. In this case gammas were generated only in the short side of the Gamma Catcher with an orthogonal direction to the cell 1. In this way gammas can traverse the 37 cm of liquid scintillator of cell 1 and interact in the liquid scintillator of cell 2.

After the last measurements campaign, efforts have been made to reduce neutron capture on iron structures close to STEREO in order to reduce the high energy component of the STEREO gamma background. The ongoing measurements campaign will determine how much these efforts have reduced the gamma background. The goal of these measurements is to validate the STEREO background requirements and identify the origin and direction of the remaining neutron and gamma background. With such measurements, a better description of the gamma background will be implemented. With this new infor-

mation, the same study should be performed again in the next months.

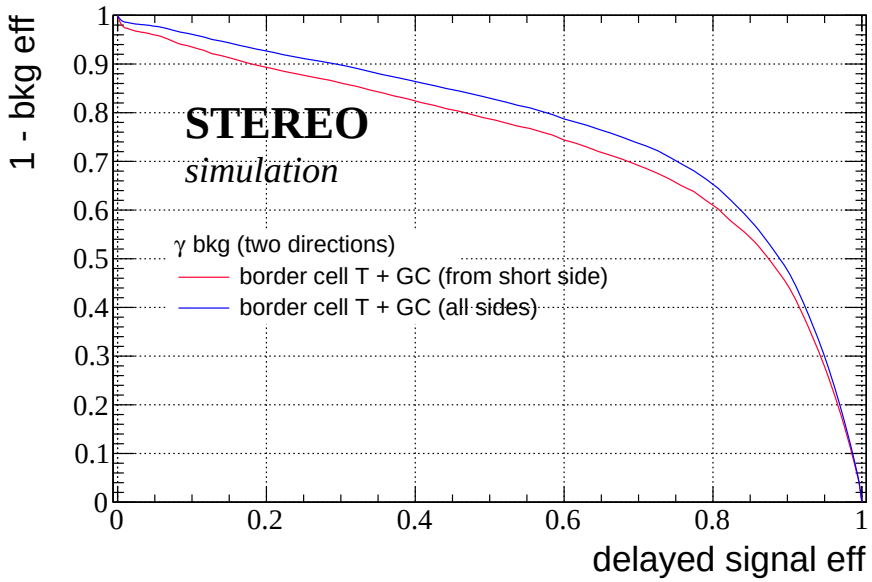

Figure 5.13: Gamma background rejection in a border cell. The direction of gammas has an influence on the rejection efficiency, being smaller when gammas come orthogonal from the short side of the Gamma Catcher (red line), which can be considered as the most unfavorable case.

Table 5.3 shows the efficiency of the selection criteria, including all the improvements proposed in this section. The probability of prompt background is estimated to be $\sim$ 7.1 % (8.2% before), and the probability of delayed background $\sim$0.7% (2.9 % before). Thus, the accidental rate can be improved by a factor 5, while only reducing the signal by 14%.

5.7 Improved resolution samples

The STEREO resolution for positrons of low energy is dominated by the 511 keV gamma leaks. At higher energy, the 511 keV gamma leak becomes a small effect when comparing with the intrinsic resolution of the detector. Separating the low resolution sample from the high resolution can lead to gains in the determination of the oscillation parameters by the fit. Thus we can use STEREO's segmentation to identify cases were one 511 keV gamma escape to a neighboring cell or Gamma Catcher. Crucially, in these cases the back-to-back condition ensures the other gamma cannot escape and we end up with a sample that has virtually no undetected 511 keV gamma.

At low energy the leakage of 511 keV gammas can easily be identified by looking for the charge in the neighboring cells or Gamma Catcher. Figure 5.14 shows the energy

Selection requirement	Efficiency (%) ν signals	Efficiency (%) γ background
$E^{total}_{vis\ prompt} > 2MeV$	80.2	24.9
$E^{T}_{vis\ prompt} > E^{GC}_{vis}$	80.0	8.2
Prompt vertex in Target	79.9	8.2
$\lvert Y^{Prompt}_{rec}\rvert < 200$ mm	79.8	7.7
$\lvert E^{Prompt}_{GC_i}\rvert < 0.55$ MeV	79.6	7.1
$E^{total}_{vis\ delayed} > 5$ MeV	54.8	7.8
$E^{T}_{vis\ delayed} > E^{GC}_{vis\ delayed}$	49.8	2.9
Delayed vertex in Target	49.3	2.9
$\Delta t < 50\mu s$	46.6	-
$\lvert X^{Prompt}_{rec} - X^{Delayed}_{rec}\rvert < 372$ mm	45.4	1.5
Topological charge distribution cut	40.86	0.7

Table 5.3: Efficiency of the improved selection criteria on the signal and the accidental gamma background.

resolution for positrons of 1 MeV generated uniformly distributed in the target (green). Taking into account the whole sample a resolution of 10.32% is found. This value can be improved by asking for an energy deposit in the Gamma Catcher or neighboring cells produced by one 511 keV gamma. Thus, asking for a deposited energy in the Gamma Catcher or neighboring cells of more than 200, 300 and 400 keV, the resolutions obtained are 9.3, 8.9 and 8.3 % respectively. However, the size of the sample is also reduced to 50, 36 and 22 % respectively.

The improvement on the energy resolution for positrons of higher energy is smaller. Thus, for positrons of 2 MeV, the resolution can only be improved from 10.75% to 10%. This is due to the small contribution of the 511 keV gammas to the total deposited energy as can be observed in the figure 5.14(bottom), which makes the shoulder on the left side which is originated by 511 keV gamma leaks smaller for positrons of 2 MeV than for positrons of 1 MeV. The resolution for positrons of 2 MeV is found to be 7.8% when the energy threshold of the accepted visible energy is taken as 2 MeV. In this scenario the

resolution could be improved to 7.1% by asking a deposited energy in the Gamma Catcher or neighboring cells larger than 400 keV.

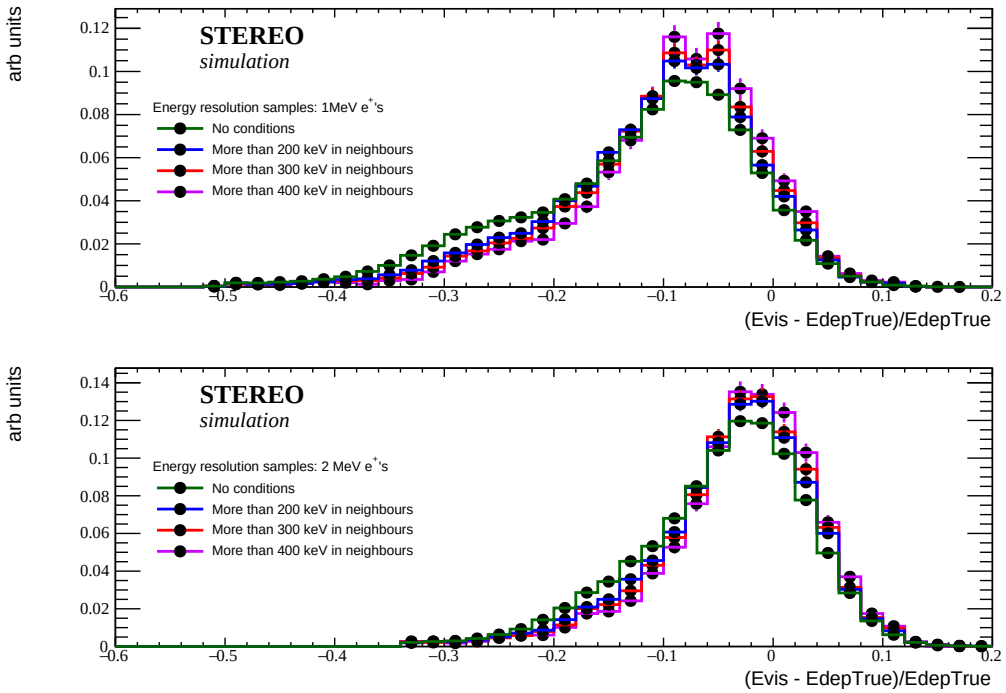

Figure 5.14: (top) Energy resolution for positrons of 1 MeV for different topologies. The green histogram shows the expected resolution for the total sample (10.32%), while blue (9.3%), red (8.9%) and violet (8.3%) histograms shows the expected energy resolution for samples where the condition of an energy deposit larger than 200, 300, and 400 keV in the Gamma Catcher or neighboring cells is imposed. (bottom) Energy resolution for positrons of 2 MeV for different topologies.

Another factor that needs to be taken into account, is the impact of the delayed energy cut on the prompt energy resolution. Events produced at the edge of the cells generally have problems to satisfy the delayed energy threshold of 5 MeV because of the gamma leaks. Since the neutron from the IBD process is captured close to the $\overline{\nu_e}$ interaction point, a strong delayed energy cut induces a geometrical selection on the delayed signal position and thus affects the prompt signal position. Indeed, the 511 keV gamma leaks are bigger when the IBD is produced at the edge of the cells. Nevertheless, this effect seems to be small, being bigger when a small time window is used. This can be observed in the figure 5.15(top), where the influence of the delayed energy cut is presented for two different time windows: 20 and 50 μs. A clear dependence can be observed between the prompt energy resolution and the delayed energy cut. However the slope of this curve is small.

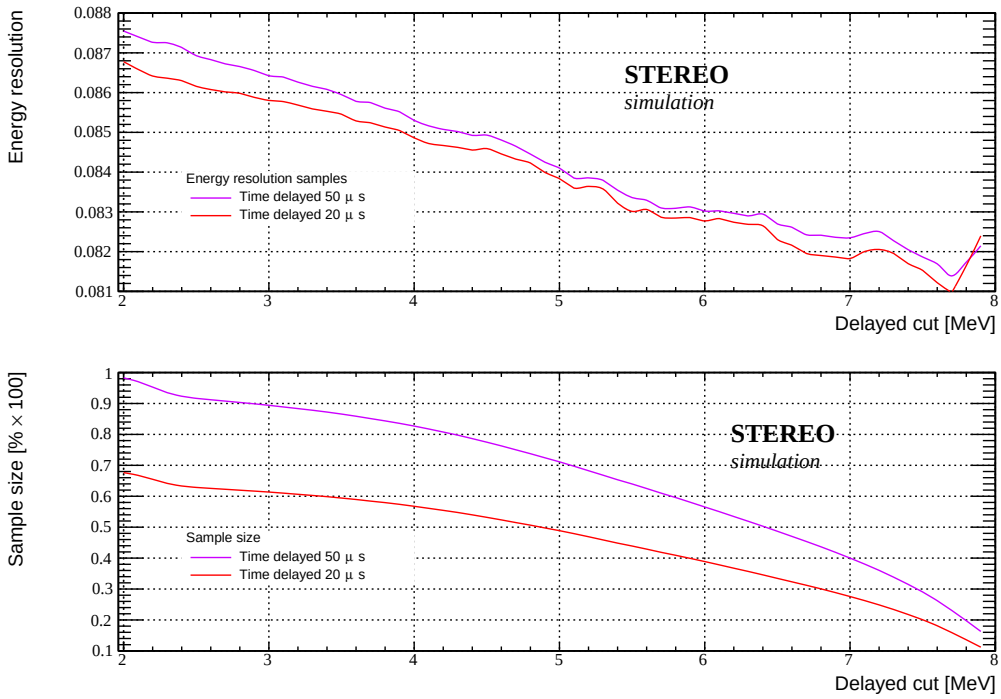

Figure 5.15: (top) Energy resolution dependence with the energy delayed cut for two different time windows: 20 (red) and 50 (violet) μs. The delayed energy threshold has a slight influence on the energy resolution. (bottom) Variation of the sample size according to the delayed energy threshold. Thus, an improvement on the energy resolution could be possible at the expense of the statistics.

5.8 Conclusion

Neutrino signals have been characterized using a sample obtained by using the STEREO neutrino generator. In addition, samples of positrons uniformly distributed in the target were used to study the detector energy resolution. At low energy, energy resolution for the prompt signal is dominated by the 511 gamma leaks. At higher energies this effect is smaller. In general, only one of the two 511 keV gammas escapes because of the back-to-back condition. The energy resolution could thus be improved using the information of the 511 keV gamma leakage. Best results are obtained at low energy. Extra improvements can be achieved using the delayed energy cut which has a slight influence in the energy resolution of the prompt signal.

The delayed signal is due to the n-Gd 8 MeV gamma cascade which features on average, four 2 MeV gammas. Therefore, its energy deposits and charge are distributed in at least three cells and/or the Gamma Catcher. This information can be used to reject high energy gamma background, whose charge is concentrated in one cell. Using all this and other cuts that I have proposed in this chapter, the accidental rate can be reduced by a factor 5.

As a concluding remark, the progress shown in this chapter in background discrimination and signal energy resolution proves that exploiting the topological information of the charge distribution among the cells and the GC is a fruitful approach that should be pursued further.

- Chapter 6 -

General conclusions and perspectives

Using the STEREO Geant4 software a dedicated simulation study was performed in order to define a calibration system based on radioactive sources. Thus, to fulfill all the STEREO physics requirements, it integrates three subsystems which are mutually complementary. A first automated subsystem which allows to move radioactive sources around the inner detector. A second automated subsystem allows the movement of radioactive sources under the inner detector. Finally three manual calibration tubes provide access inside the liquid scintillator in three different cells.

The first calibration subsystem allows to calibrate the energy scale in each cell and gamma catcher independently. This external system provide a mechanism to calibrate at 4.4 MeV with an AmBe source. In addition, a calibration point at $\sim$7.1 MeV can be achieved by irradiating the steel vessel which contain the inner detector with a ^{252}Cf neutron source. Moreover this subsystem can be used to characterize the gamma background and to accurately measure the efficiency of the vetoes to the gamma background rejection.

The goal of the second automated subsystem is to inter-calibrate the neutron capture efficiency among the cells. This can be achieved by exposing the bottom of the cells to an AmBe source.

The main objective of the manual calibration tubes is to assess the absolute neutron capture efficiency inside the cells at different positions. For such purpose, the AmBe source can be deployed inside the liquid scintillator. This system can be used at the same time to calibrate the energy scale with gamma sources at low energy.

A proposal to the reconstruction of the visible energy based on a single scintillating volume was done. We have shown that this method fulfills STEREO's physics require-

ments of having the same reconstructed visible energy for positrons of the same energy, independently of the position of interaction.

The neutrino signals and gamma background were studied and characterized. Improved selection criteria have been proposed. They take advantage of the topological information of the charge distribution among the cells and the GC for the delayed signal and high energy gamma background. They also require a correlation in the reconstructed vertex position between prompt and delayed signal. These improved selection criteria increase the accidental background rejection by a factor of 5.

Finally, a method to obtain improved energy resolution samples by using the peculiarities of the prompt topologies was proposed. Additional improvements can be achieved by using a stronger delayed cut.

Perspectives

Future research work will primarily focus on the validation of the simulation study presented in this manuscript by using the STEREO detector and the calibration system once it is operating. An important part of the calibration work that has barely been touched on this manuscript is the tuning of the MC simulation parameters to match the calibration data. Particular care should be taken in the understanding of the PSD, the non-linearities of the detector, and the vertical dependence of the light collection.

Further study of cosmic induced fast neutron should be made in order to assess their adequacy for online monitoring and calibration.

Once the detector calibrated, my research will focus on the exploitation of data. A more precise and complete study should be performed in order to improve the gamma background rejection. The basis of this study will be the improved selection criteria presented in chapter 5. The proposed discrimination variables could be included in a more complete multivariate analysis. The possible improvements in the extraction of the oscillation parameters by separating the neutrino data in the categories of improved energy resolution and purity that I have proposed should be investigated.

References

[1] Henri Becquerel. On the rays emitted by phosphorescence. *Compt. Rend. Hebd. Seances Acad. Sci.*, 122(8):420–421, 1896.

[2] J. Chadwick. The intensity distribution in the magnetic spectrum of beta particles from radium (B + C). *Verh. Phys. Gesell.*, 16:383–391, 1914.

[3] C. Ellis and W Wooster. The Average Energy of Disintegration of Radium E. *Nature*, 119:563–567, 1927.

[4] W. Pauli. Dear radioactive ladies and gentlemen. *Phys. Today*, 31N9:27, 1978.

[5] Carlo Giunti and Chung W. Kim. *Fundamentals of Neutrino Physics and Astrophysics*. 2007.

[6] J. Chadwick. Possible Existence of a Neutron. *Nature*, 129:312, 1932.

[7] S. M. Bilenky. Neutrino. History of a unique particle. *Eur. Phys. J.*, H38:345–404, 2013.

[8] Enrico Fermi. Tentativo di una teoria dell'emissione dei raggi beta. *Ric. Sci.*, 4:491–495, 1933.

[9] M. Perrin. Spectres continus beta. *Comptes Rendus*, 197:1625, 1933.

[10] Frederick Reines and Clyde L. Cowan. The neutrino. *Nature*, 178:446–449, 1956.

[11] T. D. Lee and Chen-Ning Yang. Question of Parity Conservation in Weak Interactions. *Phys. Rev.*, 104:254–258, 1956.

[12] C. S. Wu, E. Ambler, R. W. Hayward, D. D. Hoppes, and R. P. Hudson. Experimental Test of Parity Conservation in Beta Decay. *Phys. Rev.*, 105:1413–1414, 1957.

[13] R. P. Feynman and Murray Gell-Mann. Theory of Fermi interaction. *Phys. Rev.*, 109:193–198, 1958.

[14] M. Goldhaber, L. Grodzins, and A. W. Sunyar. Helicity of Neutrinos. *Phys. Rev.*, 109:1015–1017, 1958.

[15] B. Pontecorvo. Electron and Muon Neutrinos. *Sov. Phys. JETP*, 10:1236–1240, 1960. [Zh. Eksp. Teor. Fiz.37,1751(1959)].

[16] G. Danby, J. M. Gaillard, Konstantin A. Goulianos, L. M. Lederman, Nari B. Mistry, M. Schwartz, and J. Steinberger. Observation of High-Energy Neutrino Reactions and the Existence of Two Kinds of Neutrinos. *Phys. Rev. Lett.*, 9:36–44, 1962.

[17] Jose Bernabeu. On the history of the PMNS Matrix... with today's perspective. *Nuovo Cim.*, C037(03):145–154, 2014.

[18] F. J. Hasert et al. Observation of Neutrino Like Interactions Without Muon Or Electron in the Gargamelle Neutrino Experiment. *Phys. Lett.*, B46:138–140, 1973.

[19] D. Decamp et al. Determination of the Number of Light Neutrino Species. *Phys. Lett.*, B231:519, 1989.

[20] K. Kodama et al. Observation of tau neutrino interactions. *Phys. Lett.*, B504:218–224, 2001.

[21] S. Schael et al. Precision electroweak measurements on the Z resonance. *Phys. Rept.*, 427:257–454, 2006.

[22] John N. Bahcall and M. H. Pinsonneault. Standard solar models, with and without helium diffusion and the solar neutrino problem. *Rev. Mod. Phys.*, 64:885–926, 1992.

[23] John N. Bahcall, Aldo M. Serenelli, and Sarbani Basu. New solar opacities, abundances, helioseismology, and neutrino fluxes. *Astrophys. J.*, 621:L85–L88, 2005.

[24] Raymond Davis, Jr., Don S. Harmer, and Kenneth C. Hoffman. Search for neutrinos from the sun. *Phys. Rev. Lett.*, 20:1205–1209, 1968.

[25] Vernon D. Barger, R. J. N. Phillips, and K. Whisnant. Long wavelength vacuum neutrino oscillations and the solar neutrino deficit. *Phys. Rev. Lett.*, 65:3084–3087, 1990.

[26] K. S. Hirata et al. Experimental Study of the Atmospheric Neutrino Flux. *Phys. Lett.*, B205:416, 1988. [,447(1988)].

[27] Andy Acker, John G. Learned, Sandip Pakvasa, and Thomas J. Weiler. A Single solution to the atmospheric and solar neutrino anomalies. *Phys. Lett.*, B298:149–153, 1993.

[28] Samoil M. Bilenky and B. Pontecorvo. Again on Neutrino Oscillations. *Lett. Nuovo Cim.*, 17:569, 1976.

[29] Samoil M. Bilenky and B. Pontecorvo. Lepton Mixing and Neutrino Oscillations. *Phys. Rept.*, 41:225–261, 1978.

[30] S. Fukuda et al. Determination of solar neutrino oscillation parameters using 1496 days of Super-Kamiokande I data. *Phys. Lett.*, B539:179–187, 2002.

[31] Q. R. Ahmad et al. Direct evidence for neutrino flavor transformation from neutral current interactions in the Sudbury Neutrino Observatory. *Phys. Rev. Lett.*, 89:011301, 2002.

[32] Th. A. Mueller et al. Improved Predictions of Reactor Antineutrino Spectra. *Phys. Rev.*, C83:054615, 2011.

[33] Patrick Huber. On the determination of anti-neutrino spectra from nuclear reactors. *Phys. Rev.*, C84:024617, 2011. [Erratum: Phys. Rev.C85,029901(2012)].

[34] G. Mention, M. Fechner, Th. Lasserre, Th. A. Mueller, D. Lhuillier, M. Cribier, and A. Letourneau. The Reactor Antineutrino Anomaly. *Phys. Rev.*, D83:073006, 2011.

[35] José Wagner Furtado Valle and Jorge C Romao. *Neutrinos in high energy and astroparticle physics*. Wiley-VCH, Weinheim, 2015.

[36] F. Englert and R. Brout. Broken Symmetry and the Mass of Gauge Vector Mesons. *Phys. Rev. Lett.*, 13:321–323, 1964.

[37] Peter W. Higgs. Broken Symmetries and the Masses of Gauge Bosons. *Phys. Rev. Lett.*, 13:508–509, 1964.

[38] G. S. Guralnik, C. R. Hagen, and T. W. B. Kibble. Global Conservation Laws and Massless Particles. *Phys. Rev. Lett.*, 13:585–587, 1964.

[39] T. W. B. Kibble. Symmetry breaking in nonAbelian gauge theories. *Phys. Rev.*, 155:1554–1561, 1967.

[40] R. N. Mohapatra et al. Theory of neutrinos: A White paper. *Rept. Prog. Phys.*, 70:1757–1867, 2007.

[41] James Barry, Werner Rodejohann, and He Zhang. Light Sterile Neutrinos: Models and Phenomenology. *JHEP*, 07:091, 2011.

[42] B. Pontecorvo. Neutrino Experiments and the Problem of Conservation of Leptonic Charge. *Sov. Phys. JETP*, 26:984–988, 1968. [Zh. Eksp. Teor. Fiz.53,1717(1967)].

[43] Abdus Salam. On parity conservation and neutrino mass. *Nuovo Cim.*, 5:299–301, 1957.

[44] T. D. Lee and Chen-Ning Yang. Parity Nonconservation and a Two Component Theory of the Neutrino. *Phys. Rev.*, 105:1671–1675, 1957.

[45] L. D. Landau. On the conservation laws for weak interactions. *Nucl. Phys.*, 3:127–131, 1957.

[46] Ettore Majorana. Theory of the Symmetry of Electrons and Positrons. *Nuovo Cim.*, 14:171–184, 1937.

[47] J. Schechter and J. W. F. Valle. Neutrino Masses in SU(2) x U(1) Theories. *Phys. Rev.*, D22:2227, 1980.

[48] J. Schechter and J. W. F. Valle. Neutrino Decay and Spontaneous Violation of Lepton Number. *Phys. Rev.*, D25:774, 1982.

[49] S. M. Bilenky and S. T. Petcov. Massive neutrinos and neutrino oscillations. *Rev. Mod. Phys.*, 59:671–754, Jul 1987.

[50] Samoil M. Bilenky, J. Hosek, and S. T. Petcov. On Oscillations of Neutrinos with Dirac and Majorana Masses. *Phys. Lett.*, B94:495, 1980.

[51] Shalom Eliezer and Arthur R. Swift. Experimental Consequences of electron Neutrino-Muon-neutrino Mixing in Neutrino Beams. *Nucl. Phys.*, B105:45, 1976.

[52] Harald Fritzsch and Peter Minkowski. Vector-Like Weak Currents, Massive Neutrinos, and Neutrino Beam Oscillations. *Phys. Lett.*, B62:72, 1976.

[53] Samoil M. Bilenky, A. Bottino, C. Giunti, and C. W. Kim. Neutrino oscillations in the framework of three generation mixings with mass hierarchy. *Phys. Lett.*, B356:273–281, 1995.

[54] S. Abe et al. Precision Measurement of Neutrino Oscillation Parameters with KamLAND. *Phys. Rev. Lett.*, 100:221803, 2008.

[55] K. S. Hirata et al. Observation of B-8 Solar Neutrinos in the Kamiokande-II Detector. *Phys. Rev. Lett.*, 63:16, 1989.

[56] Vernon D. Barger, R. J. N. Phillips, and K. Whisnant. Long wave length oscillations and the GALLEX solar neutrino signal. *Phys. Rev. Lett.*, 69:3135–3138, 1992.

[57] J. N. Abdurashitov et al. Measurement of the solar neutrino capture rate with gallium metal. III: Results for the 2002–2007 data-taking period. *Phys. Rev.*, C80:015807, 2009.

[58] A. I. Abazov et al. Search for neutrinos from sun using the reaction Ga-71 (electron-neutrino e-) Ge-71. *Phys. Rev. Lett.*, 67:3332–3335, 1991.

[59] G. Aardsma et al. A Heavy Water Detector to Resolve the Solar Neutrino Problem. *Phys. Lett.*, B194:321–325, 1987.

[60] T. Araki et al. Measurement of neutrino oscillation with KamLAND: Evidence of spectral distortion. *Phys. Rev. Lett.*, 94:081801, 2005.

[61] S. P. Mikheev and A. Yu. Smirnov. Resonance Amplification of Oscillations in Matter and Spectroscopy of Solar Neutrinos. *Sov. J. Nucl. Phys.*, 42:913–917, 1985. [Yad. Fiz.42,1441(1985)].

[62] Thomas Schwetz, M. A. Tortola, and Jose W. F. Valle. Three-flavour neutrino oscillation update. *New J. Phys.*, 10:113011, 2008.

[63] T. Stanev and T. K. Gaisser. Atmospheric neutrino fluxes at low energy. *AIP Conf. Proc.*, 126:277–282, 1985.

[64] T. J. Haines et al. Calculation of Atmospheric Neutrino Induced Backgrounds in a Nucleon Decay Search. *Phys. Rev. Lett.*, 57:1986–1989, 1986.

[65] Masayuki Nakahata et al. Atmospheric Neutrino Background and Pion Nuclear Effect for Kamioka Nucleon Decay Experiment. *J. Phys. Soc. Jap.*, 55:3786, 1986.

[66] G. Battistoni et al. Fully Contained Events in the Mont Blanc Nucleon Decay Detector. *Phys. Lett.*, B118:461, 1982.

[67] Christoph Berger et al. Study of Atmospheric Neutrino Interactions with the Frejus Detector. *Phys. Lett.*, B227:489, 1989.

[68] Y. Fukuda et al. Evidence for oscillation of atmospheric neutrinos. *Phys. Rev. Lett.*, 81:1562–1567, 1998.

[69] Y. Ashie et al. A Measurement of atmospheric neutrino oscillation parameters by SUPER-KAMIOKANDE I. *Phys. Rev.*, D71:112005, 2005.

[70] Y. Ashie et al. Evidence for an oscillatory signature in atmospheric neutrino oscillation. *Phys. Rev. Lett.*, 93:101801, 2004.

[71] S. H. Ahn et al. Detection of accelerator produced neutrinos at a distance of 250-km. *Phys. Lett.*, B511:178–184, 2001.

[72] D. G. Michael et al. Observation of muon neutrino disappearance with the MINOS detectors and the NuMI neutrino beam. *Phys. Rev. Lett.*, 97:191801, 2006.

[73] N. Agafonova et al. Discovery of τ Neutrino Appearance in the CNGS Neutrino Beam with the OPERA Experiment. *Phys. Rev. Lett.*, 115(12):121802, 2015.

[74] K. Abe et al. Observation of Electron Neutrino Appearance in a Muon Neutrino Beam. *Phys. Rev. Lett.*, 112:061802, 2014.

[75] D. V. Forero, M. Tortola, and J. W. F. Valle. Neutrino oscillations refitted. *Phys. Rev.*, D90(9):093006, 2014.

[76] A. B. Balantekin and D. Yilmaz. Contrasting solar and reactor neutrinos with a non-zero value of theta(13). *J. Phys.*, G35:075007, 2008.

[77] G. L. Fogli, E. Lisi, A. Marrone, A. Palazzo, and A. M. Rotunno. Hints of θ_{13} ¿ 0 from global neutrino data analysis. *Phys. Rev. Lett.*, 101:141801, 2008.

[78] Y. Abe et al. Indication for the disappearance of reactor electron antineutrinos in the Double Chooz experiment. *Phys. Rev. Lett.*, 108:131801, 2012.

[79] F. P. An et al. Observation of electron-antineutrino disappearance at Daya Bay. *Phys. Rev. Lett.*, 108:171803, 2012.

[80] J. K. Ahn et al. Observation of Reactor Electron Antineutrino Disappearance in the RENO Experiment. *Phys. Rev. Lett.*, 108:191802, 2012.

[81] P. Adamson et al. Electron neutrino and antineutrino appearance in the full MINOS data sample. *Phys. Rev. Lett.*, 110(17):171801, 2013.

[82] F. Capozzi, E. Lisi, A. Marrone, D. Montanino, and A. Palazzo. Neutrino masses and mixings: Status of known and unknown 3ν parameters. 2016.

[83] M. C. Gonzalez-Garcia, Michele Maltoni, and Thomas Schwetz. Global Analyses of Neutrino Oscillation Experiments. 2015.

[84] G. L. Fogli, E. Lisi, A. Marrone, D. Montanino, A. Palazzo, and A. M. Rotunno. Global analysis of neutrino masses, mixings and phases: entering the era of leptonic CP violation searches. *Phys. Rev.*, D86:013012, 2012.

[85] Harald Fritzsch and Zhi-Zhong Xing. Lepton mass hierarchy and neutrino oscillations. *Phys. Lett.*, B372:265–270, 1996.

[86] Rabindra N. Mohapatra and Goran Senjanovic. Neutrino Mass and Spontaneous Parity Violation. *Phys. Rev. Lett.*, 44:912, 1980.

[87] Stephen F. King and Christoph Luhn. Neutrino Mass and Mixing with Discrete Symmetry. *Rept. Prog. Phys.*, 76:056201, 2013.

[88] Guang Yang. Neutrino mass hierarchy determination at reactor antineutrino experiments. In *12th Conference on the Intersections of Particle and Nuclear Physics (CIPANP 2015) Vail, Colorado, USA, May 19-24, 2015*, 2015.

[89] E. Fermi. An attempt of a theory of beta radiation. 1. *Z. Phys.*, 88:161–177, 1934.

[90] K. S. Krane. *INTRODUCTORY NUCLEAR PHYSICS*. 1987.

[91] A. Osipowicz et al. KATRIN: A Next generation tritium beta decay experiment with sub-eV sensitivity for the electron neutrino mass. Letter of intent. 2001.

[92] Ch. Kraus et al. Final results from phase II of the Mainz neutrino mass search in tritium beta decay. *Eur. Phys. J.*, C40:447–468, 2005.

[93] V. M. Lobashev et al. Direct search for mass of neutrino and anomaly in the tritium beta spectrum. *Phys. Lett.*, B460:227–235, 1999.

[94] K. Assamagan et al. Upper limit of the muon-neutrino mass and charged pion mass from momentum analysis of a surface muon beam. *Phys. Rev.*, D53:6065–6077, 1996.

[95] R. Barate et al. An Upper limit on the tau-neutrino mass from three-prong and five-prong tau decays. *Eur. Phys. J.*, C2:395–406, 1998.

[96] S. Tremaine and J. E. Gunn. Dynamical Role of Light Neutral Leptons in Cosmology. *Phys. Rev. Lett.*, 42:407–410, 1979.

[97] Benjamin W. Lee and Steven Weinberg. Cosmological Lower Bound on Heavy Neutrino Masses. *Phys. Rev. Lett.*, 39:165–168, 1977.

[98] Julien Lesgourgues and Sergio Pastor. Massive neutrinos and cosmology. *Phys. Rept.*, 429:307–379, 2006.

[99] Steen Hannestad. Neutrino masses and the number of neutrino species from WMAP and 2dFGRS. *JCAP*, 0305:004, 2003.

[100] P. A. R. Ade et al. Planck 2013 results. XVI. Cosmological parameters. *Astron. Astrophys.*, 571:A16, 2014.

[101] V. Kopeikin, L. Mikaelyan, and V. Sinev. Reactor as a source of antineutrinos: Thermal fission energy. *Phys. Atom. Nucl.*, 67:1892–1899, 2004. [Yad. Fiz.67,1916(2004)].

[102] B. Xin et al. Production of electron neutrinos at nuclear power reactors and the prospects for neutrino physics. *Phys. Rev.*, D72:012006, 2005.

[103] G. Mention. The reactor antineutrino anomaly. *J. Phys. Conf. Ser.*, 408:012025, 2013.

[104] P. Anselmann et al. First results from the Cr-51 neutrino source experiment with the GALLEX detector. *Phys. Lett.*, B342:440–450, 1995.

[105] W. Hampel et al. Final results of the Cr-51 neutrino source experiments in GALLEX. *Phys. Lett.*, B420:114–126, 1998.

[106] Dzh.N. Abdurashitov et al. The Russian-American gallium experiment (SAGE) Cr neutrino source measurement. *Phys. Rev. Lett.*, 77:4708–4711, 1996.

[107] J. N. Abdurashitov et al. Measurement of the response of the Russian-American gallium experiment to neutrinos from a Cr-51 source. *Phys. Rev.*, C59:2246–2263, 1999.

[108] John N. Bahcall. Gallium solar neutrino experiments: Absorption cross-sections, neutrino spectra, and predicted event rates. *Phys. Rev.*, C56:3391–3409, 1997.

[109] D. Krofcheck et al. GAMOW-TELLER STRENGTH FUNCTION IN GE-71 VIA THE (P, N) REACTION AT MEDIUM-ENERGIES. *Phys. Rev. Lett.*, 55:1051–1054, 1985.

[110] Carlo Giunti and Marco Laveder. Statistical Significance of the Gallium Anomaly. *Phys. Rev.*, C83:065504, 2011.

[111] S. Gariazzo, C. Giunti, M. Laveder, Y. F. Li, and E. M. Zavanin. Light sterile neutrinos. *J. Phys.*, G43:033001, 2016.

[112] A. Aguilar-Arevalo et al. Evidence for neutrino oscillations from the observation of anti-neutrino(electron) appearance in a anti-neutrino(muon) beam. *Phys. Rev.*, D64:112007, 2001.

[113] B. Armbruster et al. Search for anti-nu/mu –¿ anti-nu/e oscillations with KARMEN2. *Nucl. Phys.*, A663:803–806, 2000.

[114] B. Armbruster et al. Upper limits for neutrino oscillations muon-anti-neutrino —¿ electron-anti-neutrino from muon decay at rest. *Phys. Rev.*, D65:112001, 2002.

[115] A. A. Aguilar-Arevalo et al. Improved Search for $\bar{\nu}_\mu \to \bar{\nu}_e$ Oscillations in the MiniBooNE Experiment. *Phys. Rev. Lett.*, 110:161801, 2013.

[116] S. Gariazzo, C. Giunti, and M. Laveder. Light Sterile Neutrinos in Cosmology and Short-Baseline Oscillation Experiments. *JHEP*, 11:211, 2013.

[117] Carlo Giunti. Light Sterile Neutrinos: Status and Perspectives. 2015.

[118] Joachim Kopp, Pedro A. N. Machado, Michele Maltoni, and Thomas Schwetz. Sterile Neutrino Oscillations: The Global Picture. *JHEP*, 05:050, 2013.

[119] Samoil M. Bilenky, C. Giunti, and W. Grimus. Neutrino mass spectrum from the results of neutrino oscillation experiments. *Eur. Phys. J.*, C1:247–253, 1998.

[120] G. Boireau et al. Online Monitoring of the Osiris Reactor with the Nucifer Neutrino Detector. 2015.

[121] M. Pequignot. The Nucifer and Stereo reactor antineutrino experiments. *Nucl. Part. Phys. Proc.*, 265-266:126–128, 2015.

[122] Stéphane Zsoldos. Search for a sterile neutrino with the STEREO detector at ILL. In *Proceedings, 50th Rencontres de Moriond Electroweak interactions and unified theories*, 2016.

[123] Nick Ryder. First results of the deployment of a SoLid detector module at the SCK-CEN BR2 reactor. In *Proceedings, 2015 European Physical Society Conference on High Energy Physics (EPS-HEP 2015)*, 2015.

[124] Daniel Saunders. Muon Calibration at SoLid. 2016.

[125] Danielle Norcini. Development of PROSPECT detectors for precision antineutrino studies. In *Meeting of the APS Division of Particles and Fields (DPF 2015) Ann Arbor, Michigan, USA, August 4-8, 2015*, 2015.

[126] J. Ashenfelter et al. The PROSPECT Physics Program. 2015.

[127] Ba Ro Kim et al. Development and Mass Production of a Mixture of LAB- and DIN-based Gadolinium-loaded Liquid Scintillator for the NEOS Short-baseline Neutrino Experiment. 2015.

[128] Mikhail Danilov. Sensitivity of DANSS detector to short range neutrino oscillations. 2014.

[129] I. Alekseev et al. DANSSino: a pilot version of the DANSS neutrino detector. *Phys. Part. Nucl. Lett.*, 11:473–482, 2014.

[130] A. P. Serebrov et al. NEUTRINO4 experiment: preparations for search for sterile neutrino at 100 MW Reactor SM-3 at 6-12 Meters. 2012.

[131] A. P. Serebrov et al. Neutrino-4 experiment on the search for a sterile neutrino at the SM-3 reactor. *J. Exp. Theor. Phys.*, 121(4):578–586, 2015. [Zh. Eksp. Teor. Fiz.148,no.4,665–674(2015)].

[132] A. V. Derbin, A. S. Kayunov, and V. N. Muratova. Search for Neutrino Oscillations at a Research Reactor. 2012.

[133] In Sung Yeo et al. Development of a gadolinium-loaded liquid scintillator for the Hanaro short baseline prototype detector. *J. Korean Phys. Soc.*, 64(3):377–381, 2014.

[134] P. Vogel and John F. Beacom. Angular distribution of neutron inverse beta decay, anti-neutrino(e) + p —¿ e+ + n. *Phys. Rev.*, D60:053003, 1999.

[135] Denys H. Wilkinson. ANALYSIS OF NEUTRON BETA DECAY. *Nucl. Phys.*, A377:474–504, 1982.

[136] M. B. Chadwick et al. ENDF/B-VII.1 Nuclear Data for Science and Technology: Cross Sections, Covariances, Fission Product Yields and Decay Data. *Nucl. Data Sheets*, 112(12):2887–2996, 2011.

[137] US National Nuclear Regulatory Commission. Basic plant design, 2005.

[138] Niels Bohr and John Archibald Wheeler. The Mechanism of nuclear fission. *Phys. Rev.*, 56:426–450, 1939.

[139] Petr Vogel, Liangjian Wen, and Chao Zhang. Neutrino Oscillation Studies with Reactors. *Nature Commun.*, 6:6935, 2015.

[140] Jun Cao. Determining Reactor Neutrino Flux. *Nucl. Phys. Proc. Suppl.*, 229-232:205–209, 2012.

[141] V. Kopeikin, L. Mikaelyan, and V. Sinev. Components of anti-neutrino emission in nuclear reactor. *Phys. Atom. Nucl.*, 67:1963–1968, 2004. [Yad. Fiz.67,1987(2004)].

[142] Thomas Mueller. *Expérience Double Chooz : simulation des spectres antineutrinos issus de réacteurs*. PhD thesis, U. Paris-Sud 11, Dept. Phys., Orsay, 2010.

[143] K. Schreckenbach, H.R. Faust, F. von Feilitzsch, A.A. Hahn, K. Hawerkamp, and J.L. Vuilleumier. Absolute measurement of the beta spectrum from 235u fission as a basis for reactor antineutrino experiments. *Physics Letters B*, 99(3):251 – 256, 1981.

[144] F. Von Feilitzsch, A. A. Hahn, and K. Schreckenbach. EXPERIMENTAL BETA SPECTRA FROM PU-239 AND U-235 THERMAL NEUTRON FISSION PRODUCTS AND THEIR CORRELATED ANTI-NEUTRINOS SPECTRA. *Phys. Lett.*, B118:162–166, 1982.

[145] K. Schreckenbach, G. Colvin, W. Gelletly, and F. Von Feilitzsch. DETERMINATION OF THE ANTI-NEUTRINO SPECTRUM FROM U-235 THERMAL NEUTRON FISSION PRODUCTS UP TO 9.5-MEV. *Phys. Lett.*, B160:325–330, 1985.

[146] A. A. Hahn, K. Schreckenbach, G. Colvin, B. Krusche, W. Gelletly, and F. Von Feilitzsch. Anti-neutrino Spectra From ^{241}Pu and ^{239}Pu Thermal Neutron Fission Products. *Phys. Lett.*, B218:365–368, 1989.

[147] N. Haag, A. Gütlein, M. Hofmann, L. Oberauer, W. Potzel, K. Schreckenbach, and F. M. Wagner. Experimental Determination of the Antineutrino Spectrum of the Fission Products of ^{238}U. *Phys. Rev. Lett.*, 112(12):122501, 2014.

[148] H. Kwon, F. Boehm, A. A. Hahn, H. E. Henrikson, J. L. Vuilleumier, J. F. Cavaignac, D. H. Koang, B. Vignon, F. Von Feilitzsch, and R. L. Mossbauer. Search for Neutrino Oscillations at a Fission Reactor. *Phys. Rev.*, D24:1097–1111, 1981.

[149] Petr Vogel. Evaluation of reactor neutrino flux: issues and uncertainties. In *NuPhys2015: Prospects in Neutrino Physics (NuPhys) London, UK, December 16-18, 2015*, 2016.

[150] Emilio Ciuffoli, Jarah Evslin, Marco Grassi, and Xinmin Zhang. Measuring θ_{12} despite an uncertain reactor neutrino spectrum. *Nucl. Phys.*, B903:1–9, 2016.

[151] A. Hoummada, S. Lazrak Mikou, G. Bagieu, J.F. Cavaignac, and Dy. Holm Koang. Neutrino oscillations i.l.l. experiment reanalysis. *Applied Radiation and Isotopes*, 46:449–450, 1995.

[152] V. Helaine. Impact of the IN20 magnet on STEREO PMTs. Technical report 01, LPSC, 2015.

[153] F. Kandzia. Magnetic Field Measurements at the STEREO Site. Technical report 02, ILL, 2015.

[154] Denise B. Pelowitz et al. MCNPX 2.7.0 Extensions. *Los Alamos National Laboratory*, 11:2295, 2011.

[155] Pequignot Maxime. *Les expériences Nucifer et Stereo : étude des antineutrinos de réacteurs à courte distance*. PhD thesis, Université Paris Sud - Paris XI, 2015.

[156] M. Pequignot. Measuremnts at the ILL Reactor. Technical report 03, Université Paris Sud - Paris XI, 2012.

[157] R. S. Carter, H. Palevsky, V. W. Myers, and D. J. Hughes. Thermal neutron absorption cross sections of boron and gold. *Phys. Rev.*, 92:716–721, Nov 1953.

[158] S.A.R. Wynchank, A.E. Cox, and C.H. Collie. The thermal neutron capture cross section of a natural boron. *Nuclear Physics*, 62(3):491 – 496, 1965.

[159] S. Abe et al. Production of Radioactive Isotopes through Cosmic Muon Spallation in KamLAND. *Phys. Rev.*, C81:025807, 2010.

[160] G. Bellini et al. Cosmogenic Backgrounds in Borexino at 3800 m water-equivalent depth. *JCAP*, 1308:049, 2013.

[161] D. Gonzalez et al. Pulse shape discrimination in the IGEX experiment. *Nucl. Instrum. Meth.*, A515:634–643, 2003.

[162] H. O. Back et al. Pulse-shape discrimination with the counting test facility. *Nucl. Instrum. Meth.*, A584:98–113, 2008.

[163] H. Bethe. Theory of the Passage of Fast Corpuscular Rays Through Matter. *Annalen Phys.*, 5:325–400, 1930. [Annalen Phys.397,325(1930)].

[164] F. Bloch. On the Stopping of Fast-Moving Particles in Passage through Matter. *Annalen Phys.*, 408:285–320, 1933.

[165] G. Musiol, J. Ranft, R. Reif, and D. Seeliger. *NUCLEAR AND ELEMENTARY PARTICLE PHYSICS. (IN GERMAN)*. 1988.

[166] Handel Davies, H. A. Bethe, and L. C. Maximon. Theory of Bremsstrahlung and Pair Production. 2. Integral Cross Section for Pair Production. *Phys. Rev.*, 93:788–795, 1954.

[167] P. A. Cerenkov. Visible radiation produced by electrons moving in a medium with velocities exceeding that of light. *Phys. Rev.*, 52:378–379, 1937.

[168] PIERRE MARMIER and ERIC SHELDON. Chapter 12 - nuclear particles and their interactions. In PIERRE MARMIER and ERIC SHELDON, editors, *Physics of Nuclei and Particles*, pages 811 – 1018. Academic Press, 1970.

[169] Glenn F. Knoll. *Radiation Detection and Measurement, 3rd ed.* John Wiley and Sons, New York, 2000.

[170] S. B. Gunst and L. A. Page. Compton Scattering of 2.62-Mev Gamma Rays by Polarized Electrons. *Phys. Rev.*, 92:970–973, 1953.

[171] Claus Grupen and Boris Schwartz. *Particle detectors*. 2008.

[172] J. Beringer et al. Review of Particle Physics (RPP). *Phys. Rev.*, D86:010001, 2012.

[173] D. L. Horrocks. *Applications of Liquid Scintillation Counting*. 1974.

[174] John B. Birks. *The Theory and practice of scintillation counting*. 1964.

[175] C. Aberle, C. Buck, B. Gramlich, F. X. Hartmann, M. Lindner, S. Schonert, U. Schwan, S. Wagner, and H. Watanabe. Large scale Gd-beta-diketonate based organic liquid scintillator production for antineutrino detection. *JINST*, 7:P06008, 2012.

[176] Xiao-Bo Li, Hua-Lin Xiao, Jun Cao, Jin Li, Xi-Chao Ruan, and Yue-Kun Heng. Timing properties and pulse shape discrimination of lab-based liquid scintillator. *Chinese Physics C*, 35(11):1026 – 1032, 2011.

[177] T. Kogler, R. Beyer, E. Birgersson, R. Hannaske, A. R. Junghans, R. Massarczyk, A. Matic, A. Wagner, and K. Zuber. Light yield and n-γ pulse-shape discrimination of liquid scintillators based on linear alkyl benzene. *Nucl. Instrum. Meth.*, A701:285–293, 2013.

[178] Paolo Lombardi, Fausto Ortica, Gioacchino Ranucci, and Aldo Romani. Decay time and pulse shape discrimination of liquid scintillators based on novel solvents. *Nucl. Instrum. Meth.*, A701:133–144, 2013.

[179] HAMAMATSU. *Photomultiplier Tubes: Basics and Applications, 3rd ed.* HAMAMATSU PHOTONICS, Hamamatsu, 2007.

[180] C. Roca. Results of PMT testing. Technical report 01, MPI, 2016.

[181] HAMAMATSU. *LARGE PHOTOCATHODE AREA PHOTOMULTIPLIER TUBES*. HAMAMATSU PHOTONICS, Hamamatsu, 2016.

[182] O. Bourrion et al. Trigger and readout electronics for the STEREO experiment. In *Proceedings, Topical Workshop on Electronics for Particle Physics (TWEPP15)*, 2015.

[183] S. Agostinelli et al. GEANT4: A Simulation toolkit. *Nucl. Instrum. Meth.*, A506:250–303, 2003.

[184] F. Montanet and M. Heusch. STEREO : First measurements with 4-Methylumbelliferone as a wavelength shifter for the muon veto Cherenkov counter. Technical report 01, LPSC, 2014.

[185] Patrick Huber, M. Lindner, T. Schwetz, and W. Winter. Reactor neutrino experiments compared to superbeams. *Nucl. Phys.*, B665:487–519, 2003.

[186] Antoine Collin. *Étude des antineutrinos de réacteurs : mesure de l'angle de mélange leptonique θ_{13} et recherche d'éventuels neutrinos stériles*. PhD thesis, Orsay, 2014.

[187] D. Lhuillier et al. Proposal of a search for sterile neutrinos at ILL: the STEREO experiment.

[188] T. Salagnac. Frond end tests and pmt linearity. Presented at the STEREO general meeeting, Grenoble, France, 2015.

[189] M. R. Dragowsky et al. The N-16 calibration source for the Sudbury Neutrino Observatory. *Nucl. Instrum. Meth.*, A481:284–296, 2002.

[190] E. Blaufuss et al. N-16 as a calibration source for Super-Kamiokande. *Nucl. Instrum. Meth.*, A458:638–649, 2001.

[191] E. Schönfeld, U. Schötzig, E. Günther, and H. Schrader. Standardization and decay data of 68ge/68ga. *Applied Radiation and Isotopes*, 45(9):955 – 961, 1994.

[192] Xiang Zhou, Qingmin Zhang, Qian Liu, Zhenyu Zhang, Yayun Ding, Li Zhou, and Jun Cao. Densities, isobaric thermal expansion coefficients and isothermal compressibilities of linear alkylbenzene. *Phys. Scripta*, 90(5):055701, 2015.

[193] Y. Abe et al. Improved measurements of the neutrino mixing angle θ_{13} with the Double Chooz detector. *JHEP*, 10:086, 2014. [Erratum: JHEP02,074(2015)].

[194] L. Bernard. Light leakages characterization in the detector without scintillator liquid. Presented at the STEREO simulation meeeting, Grenoble, France, 2016.

[195] Y. Abe et al. Reactor electron antineutrino disappearance in the Double Chooz experiment. *Phys. Rev.*, D86:052008, 2012.

[196] J. K. Ahn et al. RENO: An Experiment for Neutrino Oscillation Parameter θ_{13} Using Reactor Neutrinos at Yonggwang. 2010.

[197] J. Liu, R. Carr, D. A. Dwyer, W. Q. Gu, G. S. Li, R. D. McKeown, X. Qian, R. H. M. Tsang, F. F. Wu, and C. Zhang. Neutron Calibration Sources in the Daya Bay Experiment. *Nucl. Instrum. Meth.*, A797:260–264, 2015.

[198] J.W. Marsh, D.J. Thomas, and M. Burke. High resolution measurements of neutron energy spectra from ambe and amb neutron sources. *Nuclear Instruments and Methods in Physics Research Section A: Accelerators, Spectrometers, Detectors and Associated Equipment*, 366(2–3):340 – 348, 1995.

[199] J. Scherzinger et al. Tagging fast neutrons from an ^{241}Am/^{9}Be source. *Appl. Radiat. Isot.*, 98:74–79, 2015.

[200] S. Croft. The use of neutron intensity calibrated 9be(alpha, n) sources as 4438 kev gamma-ray reference standards. *Nuclear Instruments and Methods in Physics Research, Section A (Accelerators, Spectrometers, Detectors and Associated Equipment)*, A281(1):103 – 116, 1989.

[201] E. Lorch. Neutron spectra of 241Am-B, 241Am-Be, 241Am-F, 242Cm-Be, 238Pu-13C and 252Cf isotopic neutron sources. *Int. J. Appl. Radiat. Isot.*, 10:585–591, 1973.

[202] A. D. Vijaya and A. Kumar. The neutron spectrum of AmBe neutron sources. *Nuclear Instruments and Methods*, 111:435–440, sep 1973.

[203] L. Van der Zwan. Calculated neutron spectra from 9be(alpha, n) sources. *Canadian Journal of Physics*, 46(13):1527–1536, 1968.

[204] K.W. Geiger and C.K. Hargrove. Neutron spectrum of an am241-be(alpha, n) source. *Nuclear Physics*, 53:204 – 208, 1964.

[205] F. De Guarrini and R. Malaroda. Two different technique measurements of the neutron spectrum of an ambe source. *Nuclear Instruments and Methods*, 92(2):277 – 284, 1971.

[206] Zhenzhou Liu, Jinxiang Chen, Pei Zhu, Yongming Li, and Guohui Zhang. The 4.438 mev gamma to neutron ratio for the am–be neutron source. *Applied Radiation and Isotopes*, 65(12):1318 – 1321, 2007.

[207] A.A. Mowlavi and R. Koohi-Fayegh. Determination of 4.438 mev gamma-ray to neutron emission ratio from a 241am-9be neutron source. *Applied Radiation and Isotopes*, 60(6):959 – 962, 2004.

[208] Isao Murata, Iehito Tsuda, and Ryotaro Nakamura. Neutron and gamma-ray source-term characterization of ambe sources in osaka university. *Progress in nuclear science and technology*, 4:345–348, apr 2014.

[209] C. Zhang and D. M. Mei. Measuring Muon-Induced Neutrons with Liquid Scintillation Detector at Soudan Mine. *Phys. Rev.*, D90(12):122003, 2014.

[210] Y. Zhang et al. First measurement of radioactive isotope production through cosmic-ray muon spallation in Super-Kamiokande IV. *Phys. Rev.*, D93(1):012004, 2016.

[211] J. F. Ziegler. Terrestrial cosmic ray intensities. *IBM Journal of Research and Development*, 42(1):117–140, Jan 1998.

[212] T. Salagnac. Neutrino generator. Presented at the STEREO general meeeting, Grenoble, France, 2016.

[213] A. Stutz. Simulation of the shielding attenuation. Presented at the STEREO simulation meeeting, Grenoble, France, 2014.

[214] Bé M. et al. Table of radionuclides vol 1-7 A=1 to 245. In *Monographie Table of radionuclides, Bureau international des poids et mesures.*

Appendices

- Appendix A -

Appendix to Chapter 4

Decay schemes

In this appendix, the decay schemes of the radioactive isotopes of the calibration sources considered in this manuscript are presented. For reasons of clarity, only the relevant branches of the decays are plotted. These schemes are based on reference [214].

Most of the sources can be considered as monochromatic. However, some sources need to be studied in more detail, especially sources which decay by multiple gamma emission. It is the case of the ^{22}Na for example.

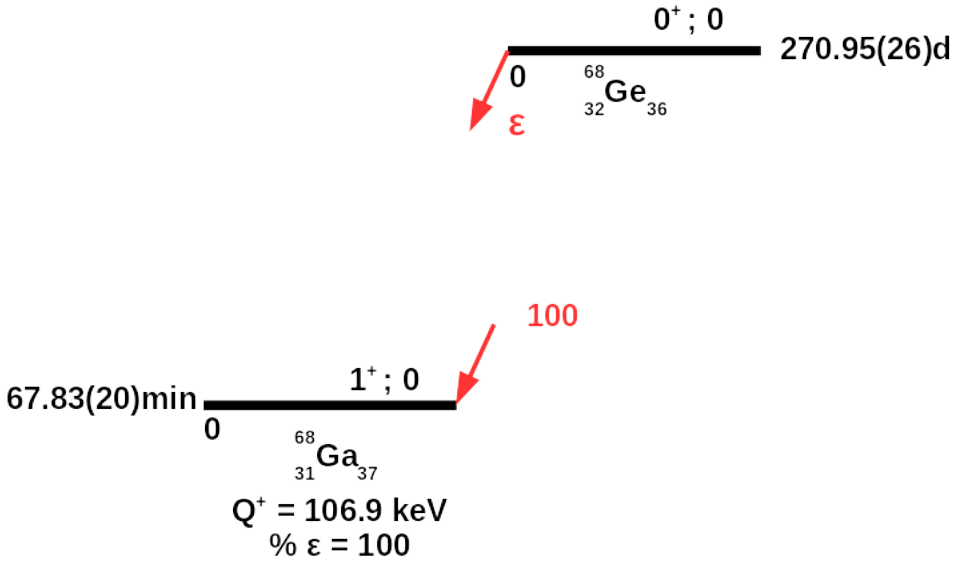

Figure A.1: The decay scheme of ^{68}Ge, which has a half life of 270 days and is 100 % produced by electronic capture going into ^{68}Ga.

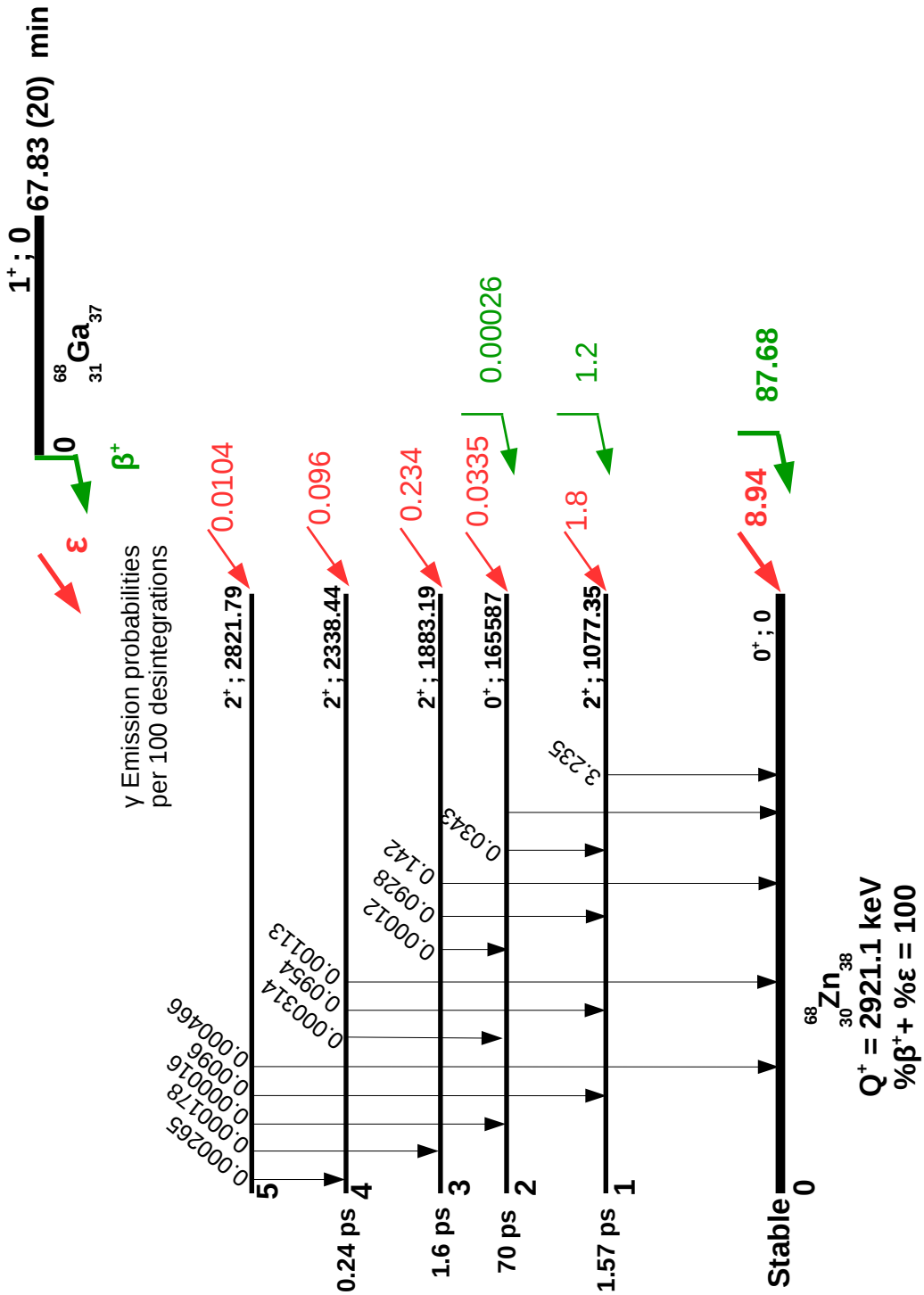

Figure A.2: ^{68}Ga decay scheme, which has a half life of 67.8 minutes and decay mostly by β^+(89%) into ^{68}Zn, while in about 11% it is produced by electronic capture.

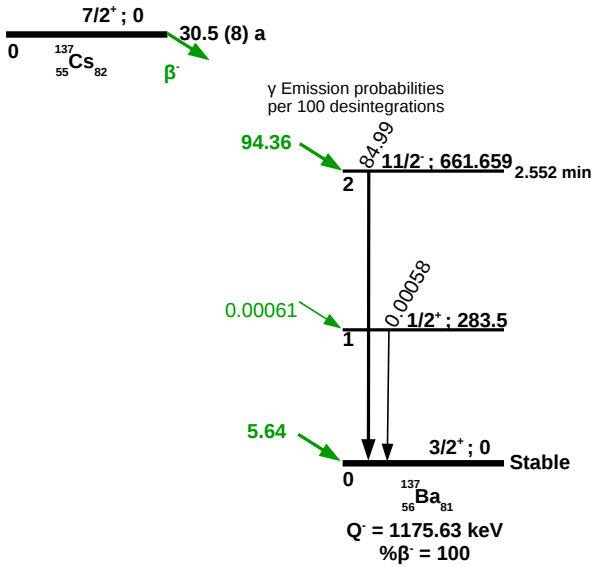

Figure A.3: ^{137}Cs decay scheme, which is produced by β^- emission. In 94.6% of decays it goes to the second excited state of ^{137}Ba whose energy level is 661.66 MeV and has a half life of 2.5 minutes. In about 5.6 % ^{137}Cs goes directly to the ground state of the ^{137}Ba

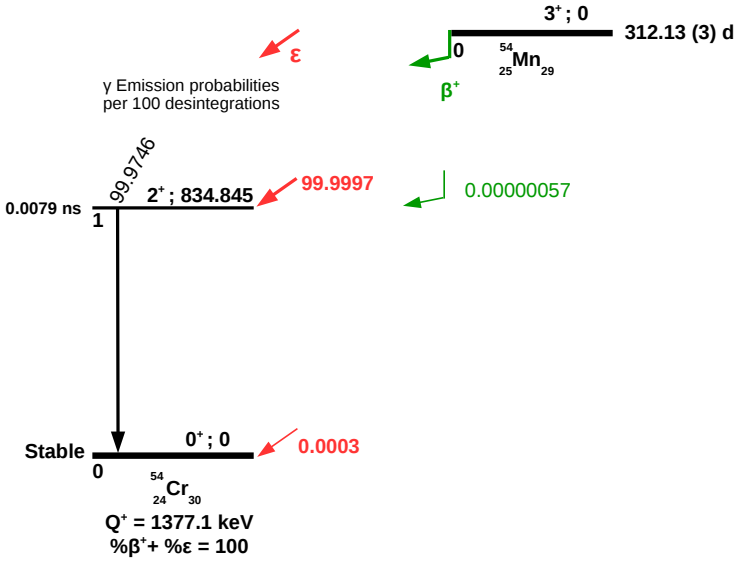

Figure A.4: ^{54}Mn decay scheme, which is produced by electronic capture going to the first excited state of ^{54}Cr. It goes to its ground state by emitting a 834.8 KeV gamma

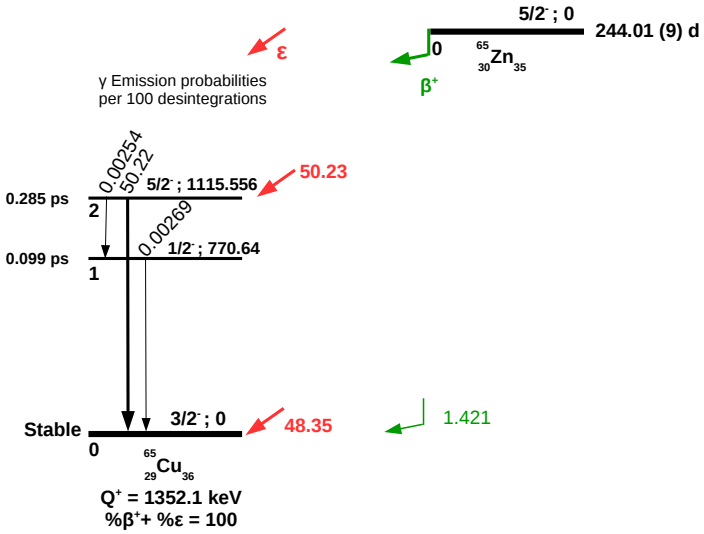

Figure A.5: ^{65}Zn decay scheme, which is produced in almost 100% by electronic capture, going to ^{65}Cu. In about 50.2 % of cases it goes to the second excited state of ^{65}Cu and then it goes to its ground state by the emission of a 1.115 MeV gamma

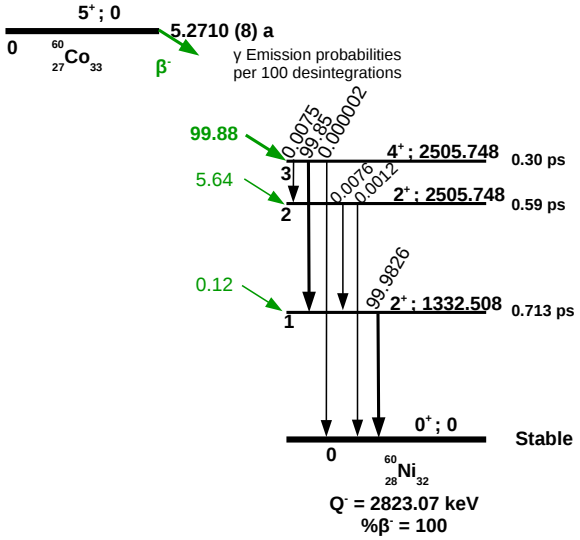

Figure A.6: ^{60}Co decay scheme, which is produced by β^-. In 99.88 of cases it goes to the third excited state of ^{60}Ni, which in turn goes to its first excited state by the emission of a 1.173 MeV gamma and then to its ground state by the emission of a second gamma of 1.332 MeV.

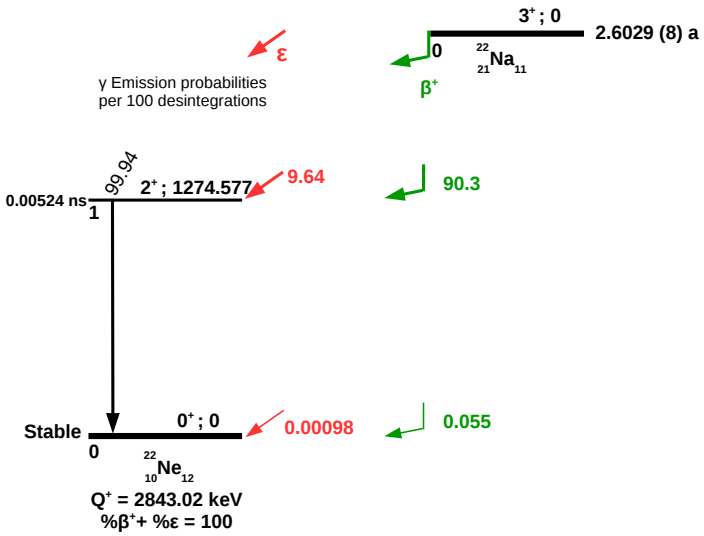

Figure A.7: ^{22}Na decay scheme, which is produced by β^+ (90.4%) and electronic capture (9.64%) into ^{22}Ne. In almost 100% of teh cases ^{22}Na goes into the first excited state of ^{22}Ne which has an energy of 1.27 MeV

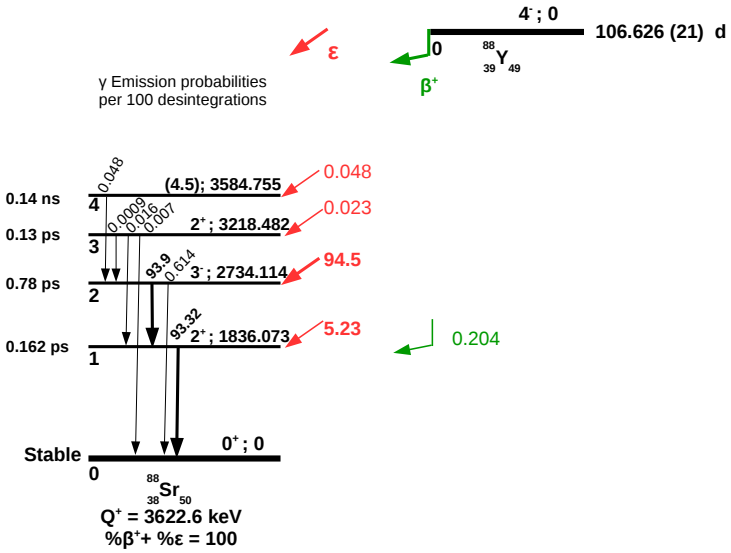

Figure A.8: ^{88}Y decay scheme, which is produced mostly by electronic capture, going to the second (first) excited state of ^{88}Sr in about 94.5% (5.23%). Then it goes to its ground state producing the emission of a 0.898 MeV (93.9%) and a 1.836 MeV (99.32%) gammas